IRIDIUM NANOPARTICLES FOR MULTICHANNEL LUMINESCENCE LIFETIME IMAGING, MAPPING LOCALIZATION IN LIVE CANCER CELLS

By

SIOBHAN MARIE KING

A thesis submitted to
The University of Birmingham
for the degree of
DOCTOR OF PHILOSOPHY

School of Chemistry
University of Birmingham
Edgbaston

May 2020

In loving memory of my father, Duncan King.
Without your love and guidance, I would not be the person I am today and for that I am forever grateful.

Until we meet again

ABSTRACT

The development of long-lived luminescent nanoparticles for multiphoton lifetime imaging is of high interest in cancer research especially for *in vivo* experiments which allows for quantification of angiogenesis and cancer metastasis. Multiphoton imaging can reach up to several millimetres in depth detection, thus providing invaluable information on tumour vasculature and the microenvironment of the tumour. Detection of luminescence lifetimes is extremely sensitive to local environmental changes and is independent of probe concentration. Luminescent cyclometalated iridium(III) complexes were conjugated onto gold nanoparticles to produce novel multiphoton lifetime imaging nanoprobes. These nanoprobes show characteristic long luminescent lifetimes from the iridium(III) complex in the range of hundreds of nanoseconds and a short-lived signal on the scale of picoseconds from the gold, allowing for multichannel detection of these nanoprobes through lifetime imaging. This is the first report of multichannel phosphorescence and fluorescence lifetime imaging being applied to functionalised gold nanoparticle within cancer cells. The sensitivity of the iridium signal on the local environment of the cell was used to successfully map localisation within HeLa cells. The combination of the sensitivity of the iridium signal to the cellular environment together with the targeting nanoscaffold to guide delivery, offer opportunities for iridium nanoparticles to be used for targeting and tracking in *in vivo* models. The ability for these nanoprobes to selectively target cancer cells was investigated by conjugating monoclonal antibodies and SiRNA. Multiphoton lifetime imaging revealed uptake of these nanoprobes into cancer cells, and detection of luminescence lifetimes were sensitive to local changes in the environment. These

functionalised nanoprobes were investigated in applications for selectively targeting angiogenesis in cancer.

ACKNOWLEDGMENTS

I would like to thank my supervisors Zoe Pikramenou and Roy Bicknell for all their help and support throughout my PhD. I really appreciate all the support and guidance throughout my PhD, and I felt like I chose a great research group to be a part of. I would especially like to thank Zoe Pikramenou for taking me into the ZP group and teaching me about the world of nanotechnology. I would like to thank every member of the ZP group that I worked with both before and after my time in the group. I am especially grateful to Shani Osborne, John Lilley and Chris Stepanek for taking me under their wings and helping me get started with my PhD. A special thanks to Sunil Claire for all his witty jokes, funny memes and of course amazing cakes. Not only that, but for all his help with nanoparticle preps and imaging in general. I would like to thank Abiola for all her help with cell biology, and for taking the time out of her busy schedule to come with me to RAL for all the lifetime microscopy experiments.

I could not have done my PhD without my friends and family. Becky and Holly made my days in chemistry fun and exciting and we always had a laugh. They have always been so supportive and helped me through some tough times. A big shout out to my fellow chemistry buddies who made my time in Birmingham special; Greg, Will, Ashley, Phil, Louise, Shani, John, Rodolfo and Laura. I would like to thank my fellow PSIBS buddies (Sophie, Nat, Rich, Iggy, Suzie, Mo and Prema) for all the laughs and games nights throughout my PhD. My family who have been unconditionally supportive throughout my PhD, and I owe them more than just a simple thanks. They are my world and I am forever grateful for what they have done for me. A very special

thanks goes to my parents who have supported me the most throughout my PhD, I wouldn't be where I am today without them. I also must thank them for helping me proofread my thesis, even though I know it bored them! Then I must give a big thanks to Liam McWade who I cannot thank enough for all his love and support. He made some hard times, good and the good times even better. I could not have asked for a better person to meet during my PhD, and I owe him more than a thank you!

I would like to acknowledge Stanley Botchway from Rutherford Appleton Laboratories (RAL) for teaching me how to use the two-photon lifetime microscope and for all his advice on microscopy in general. I learnt a lot from my time at RAL and it was a great experience for me to learn more about microscopy. I would like to acknowledge EPSRC, PSIBS, the School of Chemistry and the University of Birmingham for my financial support. A special thanks to the analytical facility in Chemistry for all their help; Jackie Deans, Chi Tsang, Cecile Le Duff, Neil Spenser and Louise Male. I would like to thank Theresa Morris and Paul Stanley for all their help with electron microscopy over in the Metallurgy and Material department.

CONTENTS

LIST OF ABBREVIATIONS

^{13}C NMR	Carbon Nuclear Magnetic Resonance
^{1}H NMR	Hydrogen Nuclear Magnetic Resonance
AbH	Modified monoclonal antibody
ADC	Acetonedicarboxylate
AuNCs	Gold nanoclusters
AuNP	Gold Nanoparticle
Bpy	2,2'-bipyridine
BSA	Bovine Serum Albumin
DHLA	Dihydrolipoic acid
DLS	Dynamic Light Scattering
DMEM	Dulbecco's Modified Eagle's Medium
EC	Endothelial Cells
ECM	Extensive Extracellular Matrix
EDL	Electric Double Layer
EDC	1-Ethyl-3-(3-dimethylaminopropyl)carbodiimide
EDTA	Ethylenediaminetetraacetic Acid
EPR	Enhanced Permeability and Retention Effect
FBS	Fetal Bovine Serum
FDA	Food and Drug Administration
FLIM	Fluorescence Lifetime Imaging Microscopy
H_2O	Water
GM	Goeppert-Mayer (10^{-50} cm^4 s $molecules^{-1}$ $photon^{-1}$)

HEPES	4-(2-hydroxyethyl)-1-piperazineethanesulfonic acid
HUVEC	Human Umbilical Vein Endothelial Cells
HSA	Human Serum Albumin
ICP-MS	Inductively Coupled Plasma Mass Spectrometry
LPS	Lipopolysaccharide
MCTS	Multicellular Tumour Spheroids
MRI	Magnetic Resonance Imaging
mRNA	Messenger RNA
MS	Mass Spectrometry
NHS	N-Hydroxysuccinimide
OLED	Organic Light-emitting Diode
PBS	Phosphate Buffer Saline
PEG	Polyethylene glycol
PET	Positron Emission Tomography
PDI	Polydispersity Index
PFA	Paraformaldehyde
PLIM	Phosphorescence Lifetime Imaging Microscopy
PMA	Phorbol 12-myristate 13-acetate
RAL	Rutherford Appleton Laboratories
rhES	Recombinant Human Endostatin
RISC	RNA-induced silencing complex
RNA	Ribonucleic Acid

ROI	Region of Interest
TEM	Transmission Electron Microscopy
TEMs	Tumour Endothelial Markers
TIRF	Total Internal Reflectance Fluorescence
Ti: Sapp	Titanium Sapphire
TP	Two-Photon
TPA	Two-Photon Absorbance
TPL	Two-photon luminescence
SiRNA	Small interfering Ribonucleic Acid
SPECT	Single-photon emission computed tomography
SPR	Surface Plasmon Resonance
UCNP	Upconverting nanoparticles
UV	Ultraviolet
VEGF	Vascular endothelial growth factor
Vis	Visible spectrum
ζ-potential	Zeta Potential
λ_{max}	Wavelength with Maximum Intensity
λ_{em}	Emission Wavelength
λ_{exc}	Excitation Wavelength
τ	Luminescence Lifetime
ϕ	Luminescence Quantum Yield

CHAPTER 1. INTRODUCTION

1. 1 Iridium(III) complexes for imaging applications

1. 1. 1 Luminescence imaging

Fluorescence based microscopy has revolutionised the way scientists visualise complex biological systems for biomedical applications. These optical imaging techniques have improved over the past few decades due to synthesis of imaging probes which enhance fluorescence signal for improved visualisation.[1] The design of these fluorescent complexes are important and a lot of research has been carried out to optimise these probes over the past few decades. The factors that need to be considered in the design of a fluorescent probe are photophysical properties, uptake into cells, toxicity and solubility in biological media.[2] Small-molecule organic probes have traditionally been used for *in vitro* imaging of cellular structures and biological events. This is because these probes can be easily modified for the selective targeting of specific organelles and proteins within cells.[3, 4] However, these organic dyes can suffer from photobleaching, poor absorptivity and solubility in biological medium.[5] In recent years research has shifted towards using heavy-metal transition metal complexes as biological imaging probes as they have many advantages over conventional organic dyes.[6, 7] Transition metal complexes have favourable photophysical and electrochemical properties which makes them ideal candidates for optical and time-resolved imaging applications. There are several reasons why these luminescent transition metal complexes are desirable for bioimaging applications. Firstly, these complexes have extremely high photostability in comparison to organic

dyes which prevents photobleaching throughout prolonged exposure to irradiation. This is favourable for experiments requiring long-term observation of a biological specimen.[8, 9] Secondly, they display intense and long-lived emission with a large Stokes shift in the visible region, which reduces the ability for these complexes to undergo self-quenching.[10, 11] Many of these transition metal complexes display long-lived phosphorescence with luminescence lifetimes on the time scale of nanoseconds to microseconds.[12-14] Such long lifetimes can be utilised for eliminating background autofluorescence from biological samples by using time-resolved based techniques.[15] These techniques are extremely sensitive in comparison to emission-based microscopy methods.[16] Lastly, these complexes have good solubility in water and high luminescence quantum yields. These transition metal complexes can be readily functionalised with ligands to selectively target organelles[17, 18] and DNA[19, 20] within cells.

Many transition metal complexes have been studied as biological imaging reagents. The most commonly studied have been d^6 heavy metal complexes based on Ru(II), Ir(III), Re(I) and Rh(III) centres and d^8 heavy metal complexes based on Pt(II) centres.[21] Iridium(III) cyclometalated complexes are popular luminescent probes for biological imaging,[22] as their luminescent signal can be tuned by modification of their ligand framework,[23] which also influences localisation in cell organelles.[24,25] In comparison to other d^6 heavy metal complexes, luminescent iridium(III) complexes have longer luminescent lifetimes[26], higher quantum yields and the iridium(III) metal centre can be functionalised with a wide range of cyclometalating ligands to tune their photophysical properties.[27-30] These make iridium(III) complexes desirable for applications in fluorescence and time-resolved microscopy.

There are lots of examples in the literature of iridium(III) complexes being used as bioimaging probes. Huang *et al.* showed uptake of cationic iridium(III) complexes into the cytoplasm of living cells. This was the first example of an iridium(III) complex being used as a live cell imaging stain.[31] The luminescence imaging showed that these cationic iridium(III) complexes had specificity for staining the cytoplasm of the cells over other organelles such as the nucleus and further analysis of the iridium luminescence revealed little to no signal localised within the nucleus (Figure 1.1).

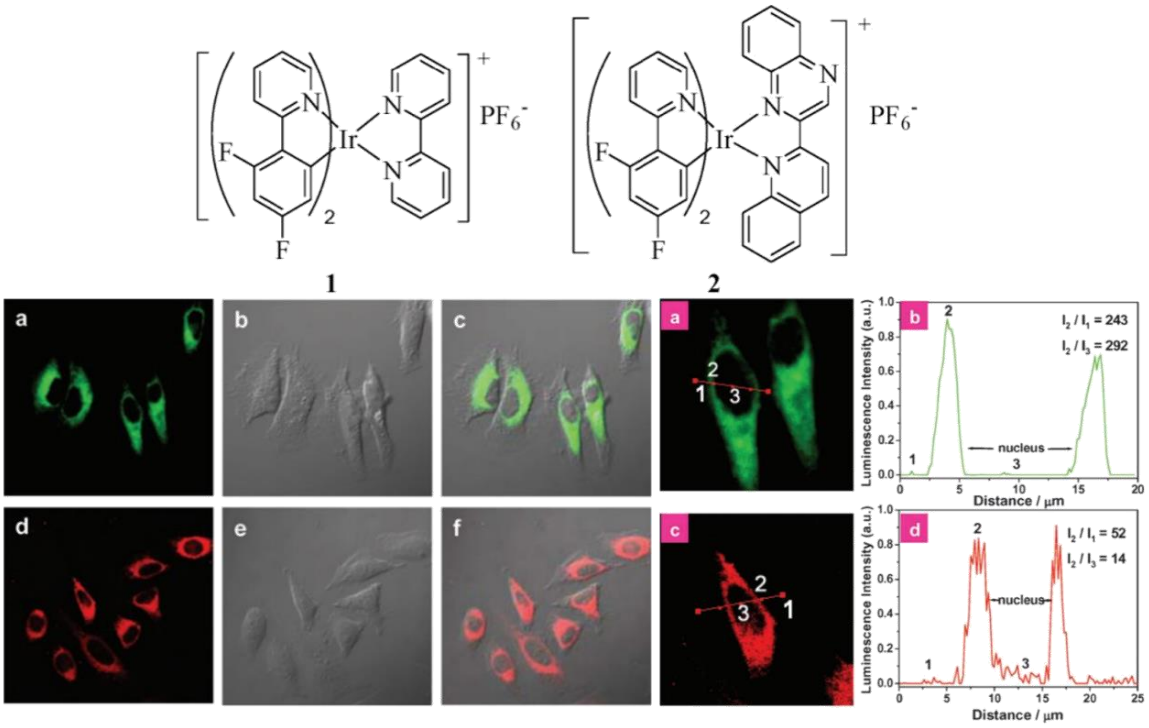

Figure 1.1. (Top) Chemical structure of iridium(III) complexes 1 and 2. (Bottom, left) Luminescence images (a and d) and bright-field images (b and e) of living HeLa cells incubated with 20 mM 1 (top) and 2 (bottom) in DMSO/PBS (pH 7, 1 :49, v/v) for 10 min at 25 °C. (c and f) merged imaging of iridium signal and bright-field images. λ_{ex} = 405 nm. (Bottom, right) Luminescence images and luminescence intensity profiles (across the lines shown in (a and c) of HeLa cells incubated with 20 mM 1 or 2 in DMSO/PBS (pH 7, 1 :49, v/v) for 10 min at 25 °C. Signal-to-noise ratios (I_2/I_1) and cytoplasm-to-nucleus ratios (I_2/I_3) shown in the right hand column.[31]

Iridium(III) complexes have also been used to target specific biomolecules and substrates within cells, through the functionalisation of the iridium(III) centre with targeting ligands. This was seen in the research carried out by Lo *et al.* who developed the first luminescent iridium(III) polypyridine complexes as labelling reagents for biological substrates.[32] They showed successful labelling of BSA and holo-transferrin present in human serum albumin to give luminescent bioconjugates. The group went onto study the interactions of iridium(III) polypyridine indole complexes with BSA and saw an emission enhancement and lifetime extension upon binding to BSA for all the complexes. Luminescence studies revealed that uptake of iridium(III) complexes (3a) mainly localised around the perinuclear region of HeLa cells (Figure 1.2, B).

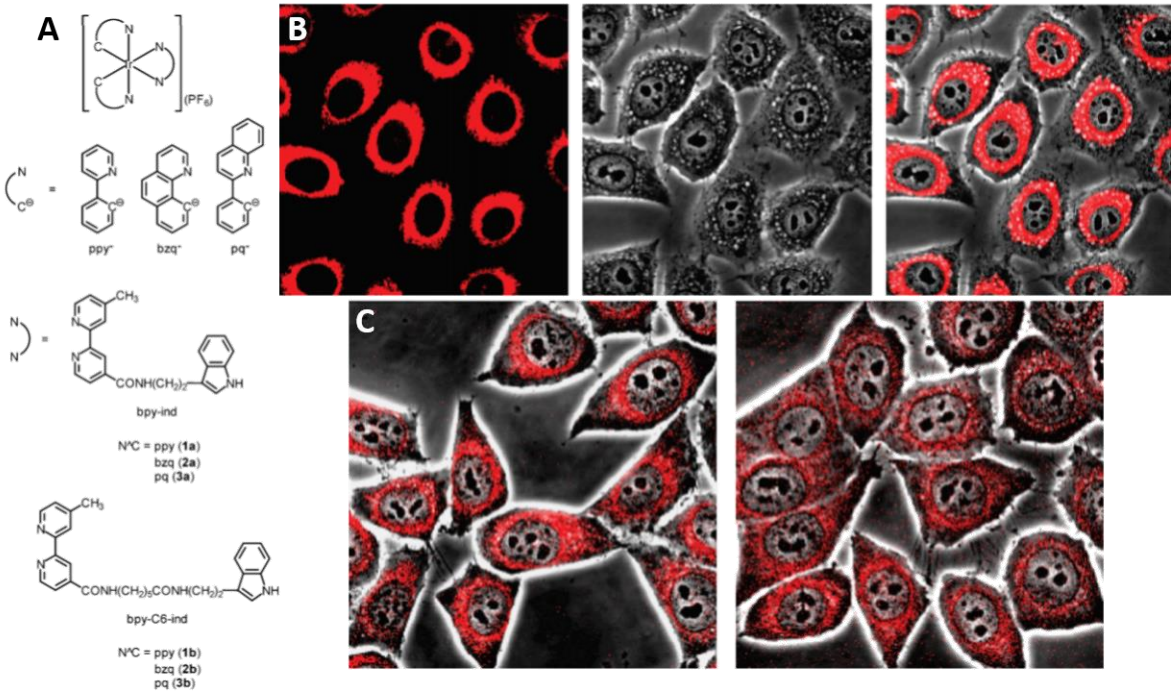

Figure 1.2. (A) Chemical structures of cyclometalated iridium(III) indole complexes. (B) (Left) Fluorescence, (Middle) Brightfield and (Right) overlaid images of HeLa cells incubated with complex 3a (5 μM) at 37 °C for 1 hour. (C) Confocal images of HeLa cells incubated with (Left) Ir-BSA and (Right) Ir-TF at 37 °C for 1 hour.[32]

To understand the mechanism of uptake, BSA was labelled with an amine specific luminescent iridium(III) polypyridine isothiocyanate complex (Ir-BSA). The luminescence images showed that uptake of Ir-BSA complex was mainly confined to the perinuclear region which was the same pattern of uptake as previously seen for complex 3a (Figure 1.2, C). Since the uptake of BSA into cells occurs through receptor mediated endocytosis[33, 34], it was concluded that the iridium(III) polypyridine indole complexes follow the same mechanism of uptake. Since these cyclometalated iridium(III) complexes have desirable photophysical properties and have shown to be taken up readily into cells, studies have been done to investigate whether these complexes can be used to specifically target cellular organelles. Lo *et al.* designed a luminescent cyclometalated iridium(III) polypyridine poly(ethylene glycol) complex that localised within the mitochondrial region of HeLa cells (Figure 1.3).

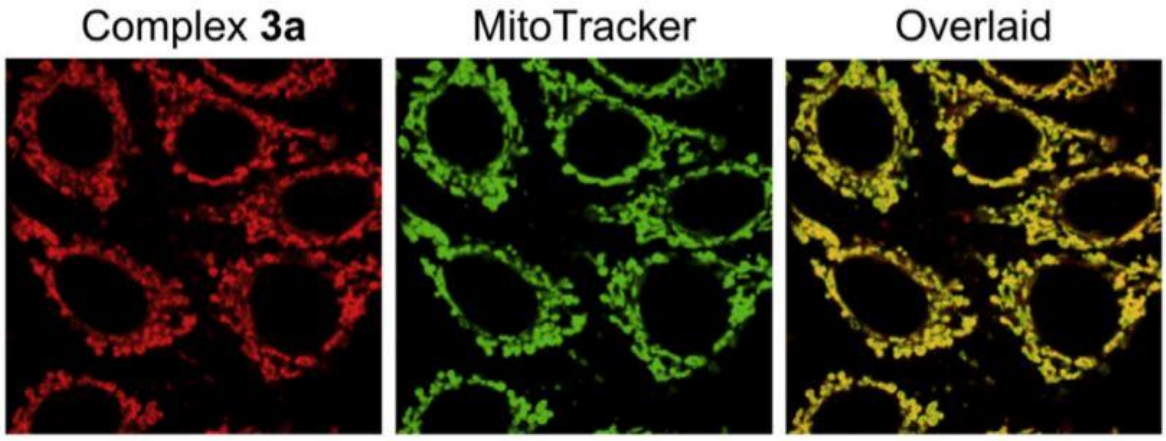

Figure 1.3. (Left) Luminescence images of HeLa cells incubated with complex 3a (100 μM, λ_{ex} = 405 nm) at 37 °C for 2 hour followed by incubation with (Middle) MitoTracker™ Deep Red (100 nM, λ_{ex} = 633 nm) for 20mins at 37 °C. (Right) Merged images of iridium signal and MitoTracker Deep red luminescence signal.[35]

This was confirmed by co-incubating HeLa cells with the iridium(III) complex (100 μM, 2 hours, λ_{ex} = 405 nm) and Mitotracker™ Deep Red (100 nM, 2 hours, λ_{ex} = 633 nm). A high accumulation of iridium(III) PEG complex was found within the mitochondria which was seen through the co-localisation of the iridium signal and Mitotracker™ deep red signal in the luminescence images.[35] Iridium(III) complexes have often been synthesised to target the mitochondria within cells and to track mitochondrial dynamics. Chao *et al.* synthesised four phosphorescent iridium(III) complexes (**Ir1**-**Ir4**) which showed high specificity for targeting mitochondria in live and fixed cells (Figure 1.4).

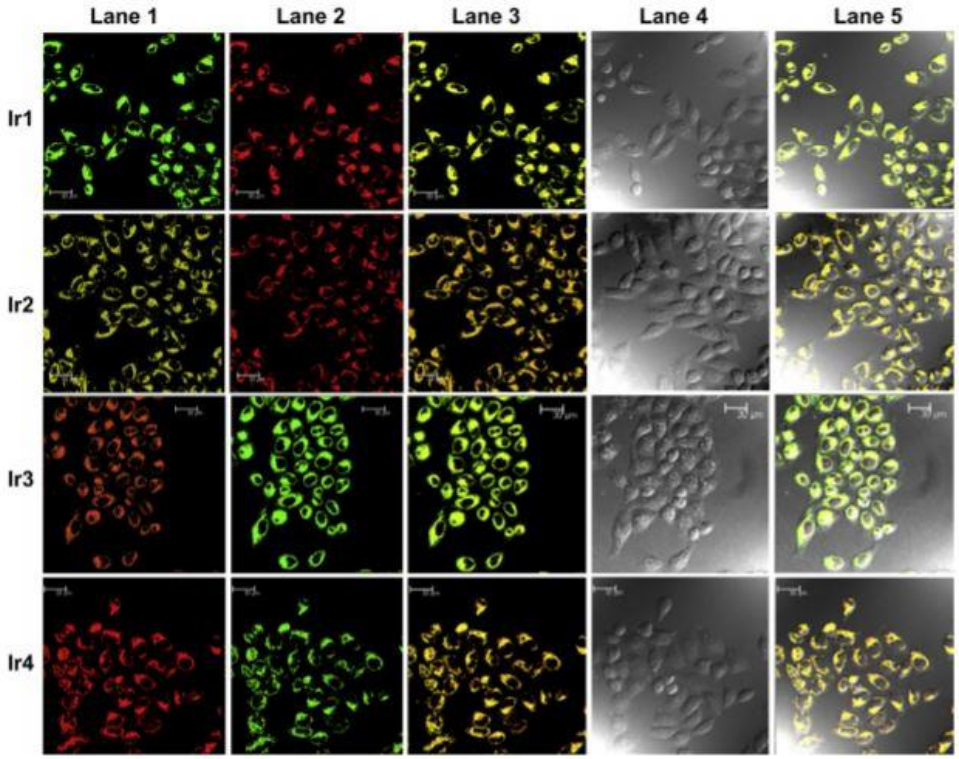

Figure 1.4. Luminescence images of live HeLa cells incubated with 5 μM Ir1-Ir4 in DMSO and PBS for 1 hour at 37 °C, followed by 50 nM MitoTracker Red (Ir1 and Ir2) and MitoTracker green (Ir3 and Ir4), respectively. Lane 1, luminescence images of Ir1-Ir4. Lane 2, luminescence images of MitoTracker Red and MitoTracker Green. Lane 3, merged images of iridium luminescence and MitoTracker luminescence. Lane 4, bright-field images and Lane 5 merged images of iridium signal, MitoTracker luminescence and bright-field.[36]

It was found that the emission properties could be tuned by modifying the ligands around the iridium(III) centre whilst retaining the specificity in targeting mitochondria in live cells. All the iridium(III) complexes were taken up into the mitochondria of the cells, which was identified through co-localisation of the iridium signal and Mitotracker™ red/green signals respectively which was seen in the luminescence images. ICP-MS revealed uptake of iridium(III) complexes was 80% into the mitochondria in comparison to other areas of the cell (cytoplasm and nucleus), indicating strongly of mitochondrial staining.[36] The group furthered this research by synthesising mitochondria specific probes based on iridium(III) imidazo[4,5-f][1-10]phenanthroline derivatives which excelled at staining the mitochondria in comparison to commercially available mitochondrial stains (Figure 1.5). These iridium(III) complexes showed excellent photostability and selectively for staining the mitochondria during short incubation times.[37] This work identifies the benefits of using transition metal complexes as luminescence and cell specific probes in biomedical applications. The desirable photophysical properties and selectivity for mitochondria led to these iridium(III) complexes being investigated as two-photon imaging probes which will be discussed in the following subchapter.

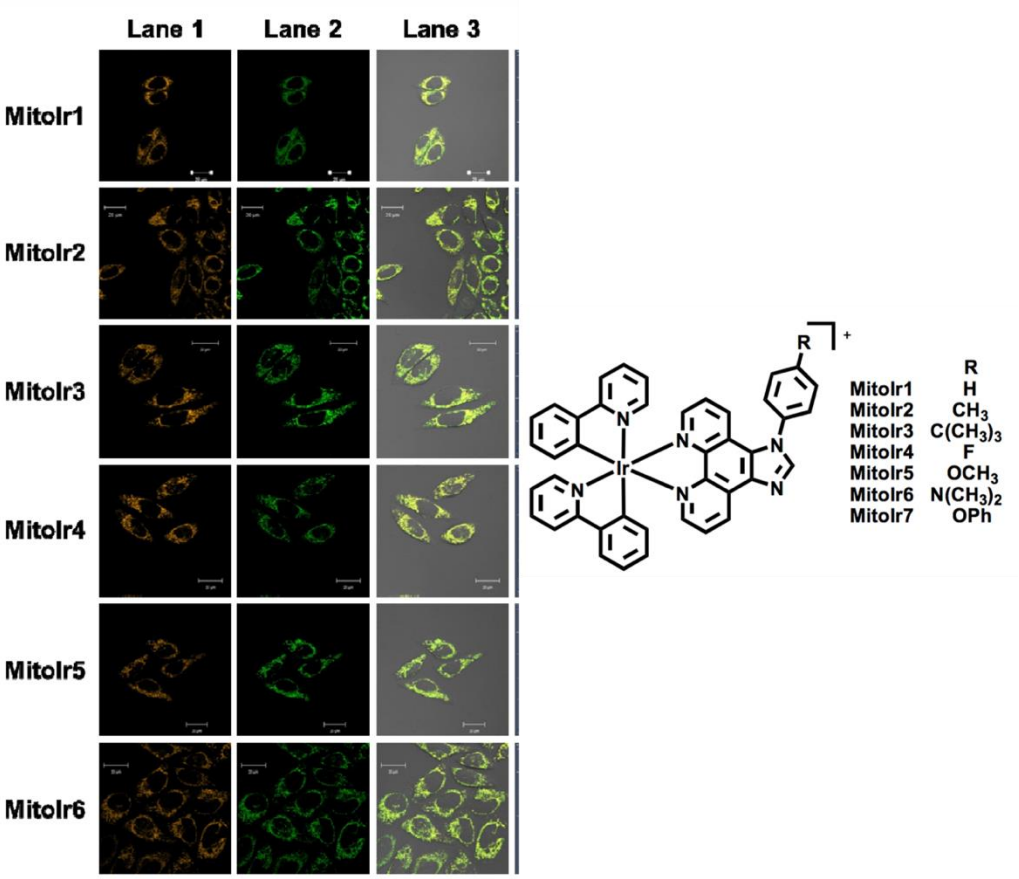

Figure 1.5. Luminescence images of living HeLa cells incubated with 0.5 mM of MitoIr1-MitoIr6 in DMSO and DMEM for 15 minutes at 37 °C followed by 50 nM of MTR. Lane 1 luminescence images of MitoIr1-MitoIr6; lane 2 luminescence images of MTR and Lane 3 overlay of lane 1 and 2 and brightfield. Excitation wavelength: 405 nm (for all Ir(III) complexes) and 488 nm (for MTG).[36]

Iridium(III) complexes have also been investigated for their abilities to selectively target and stain the nucleus of cells. Most commercially available nuclear dyes often suffer from photobleaching and the use of irradiation in the UV range (405 nm) which can cause damage to the cells after prolonged irradiation. These iridium(III) complexes can overcome these limitations as cells can be dosed with lower concentrations of the iridium(III) probes, they have shown to be highly photostable and irradiation can be done at longer visible wavelengths. Li *et al.* showed this by designing non-emissive

iridium(III) complexes that specifically light-up when binding to the nuclei of living cells (Figure 1.6, a).[38]

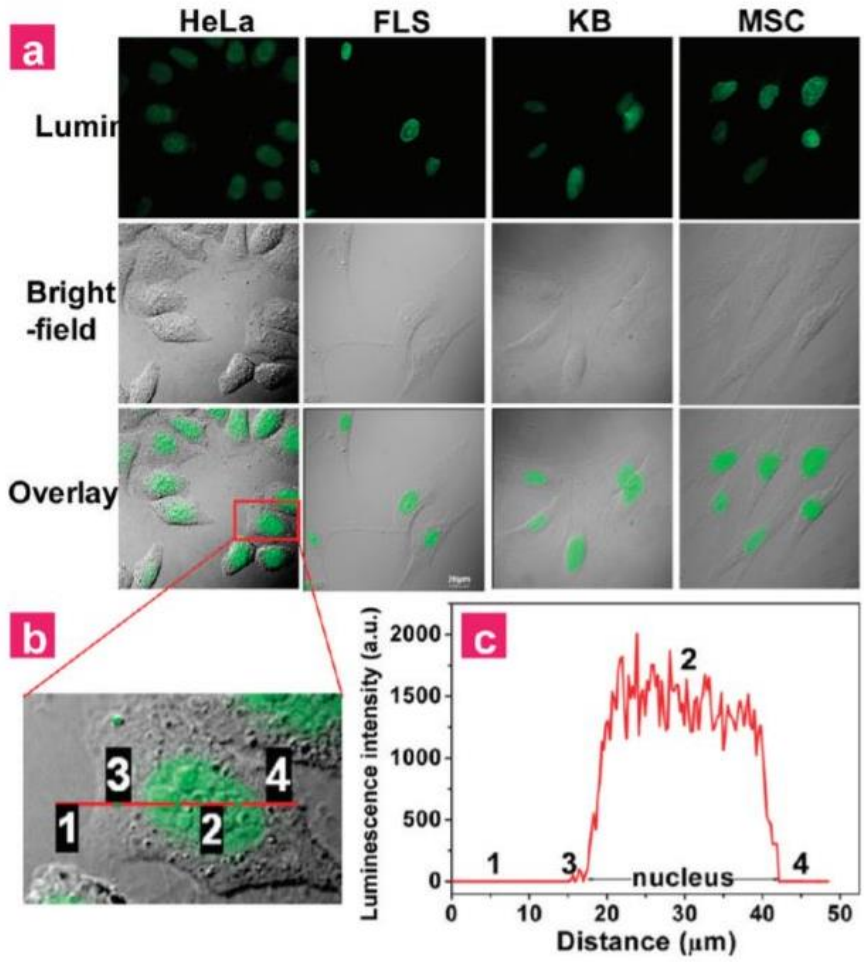

Figure 1.6. (a) Luminescence images of living HeLa, FLS, KB and MSC cells incubated with 10 μM LIr1 in DMSO/PSB PBS (pH 7.4, 1:99, v/v) for 10 min at 37 °C (λ_{ex} = 488 nm, λ_{em} = 520 nm). (b) Intensified luminescence images (inset). (c) Luminescence intensity profile across the line shown in panel b corresponding to extracellular region (1), nuclear region (2) and cytoplasm (3 and 4).[38]

They identified that the iridium(III) complex reacts with histidine and histidine-containing proteins to form a luminescent emission product when localised in the nucleus of living cells. High specificity and accumulation was seen in the nucleus after only 10 minutes of incubation with iridium(III) complex, this was evident from the

luminescence intensity profile going across the whole cell (Figure 1.6, b and c) which showed iridium signal only present within the nucleus of the cells. This shows how selective these transition metal complexes can be in targeting organelles and DNA within cells by modifying the ligands that surround the metal core.

1. 1. 2 Multiphoton imaging

As discussed, emission based imaging methods such as standard fluorescence microscopy has been on the forefront for imaging biological samples with a variety of luminescence probes. However, the use of one-photon excitation presents many disadvantages for imaging thicker biological samples. This is because visible light is highly scattered within biological samples and tissues which limits the depth it can penetrate whilst still providing enough power to excite a fluorophore. Therefore, the field has moved to multiphoton microscopy which has become an invaluable tool in cancer research for *in vivo* applications such as studying angiogenesis and cancer metastasis, where these thick tissues are insufficiently studied by single-photon techniques.[39,40]. Hence, the design of luminescent probes that can undergo multiphoton excitation is of great interest in biomedical imaging and drug-delivery applications.

Multiphoton microscopy uses fluorophores that are excited by the simultaneous absorption of two or more low energy photons. This differs from single-photon excitation which uses one high energy photon for excitation of a fluorophore. For two-photon microscopy; the photons have half the energy needed for excitation in comparison to single-photon excitation and therefore light of twice the wavelength is used (Figure 1.7).[41]

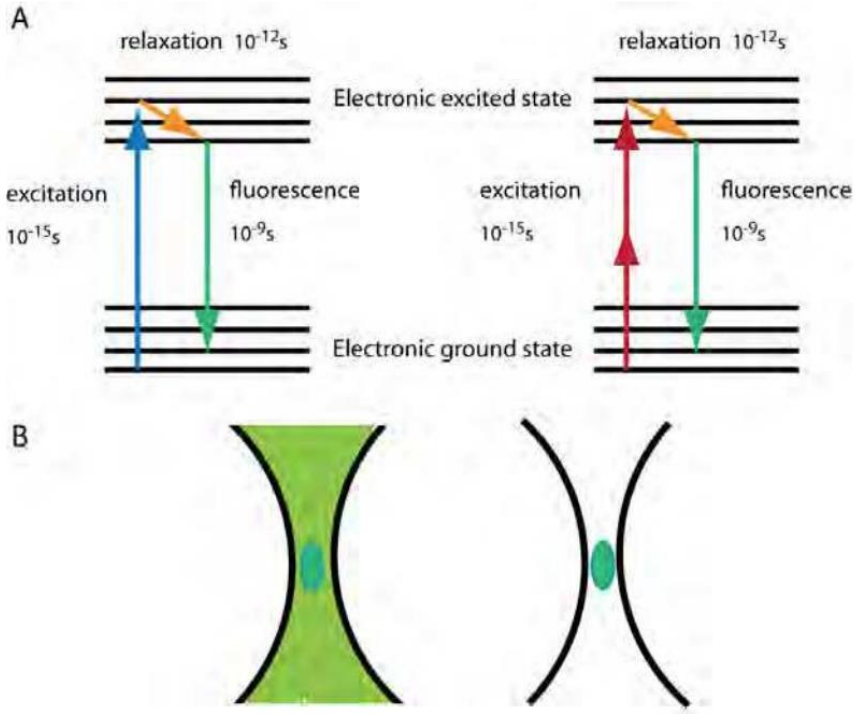

Figure 1.7. Jablonski diagrams for (A) single-photon excitation and two-photon excitation. (B) Schematics of one-photon versus two-photon fluorescence emission.[42]

The use of low energy photons over high energy photons provides many advantages of using multiphoton excitation over single-photon excitation. In multiphoton microscopy, excitation occurs in a small focal plane in thick samples as this focal point has a high enough photon density for the simultaneous absorption of two photons. Effectively, this means that out-of-focus fluorescence is significantly reduced which leads to less photobleaching and phototoxicity in cells.[43] In comparison to single-photon excitation which occurs throughout the sample both above and below the focal plane and generates more out-of-focus fluorescence which increases photobleaching and phototoxicity in cells (Figure 1.8, A).[44] The use of longer, near infrared wavelengths allows for better depth of penetration in tissues. This is because visible light is often scattered in biological tissues which limits the depth of penetration, whereas biological

compounds absorb and scatter light significantly less at these longer near infrared wavelengths which are used in multiphoton excitation (Figure 1.8, B).[45]

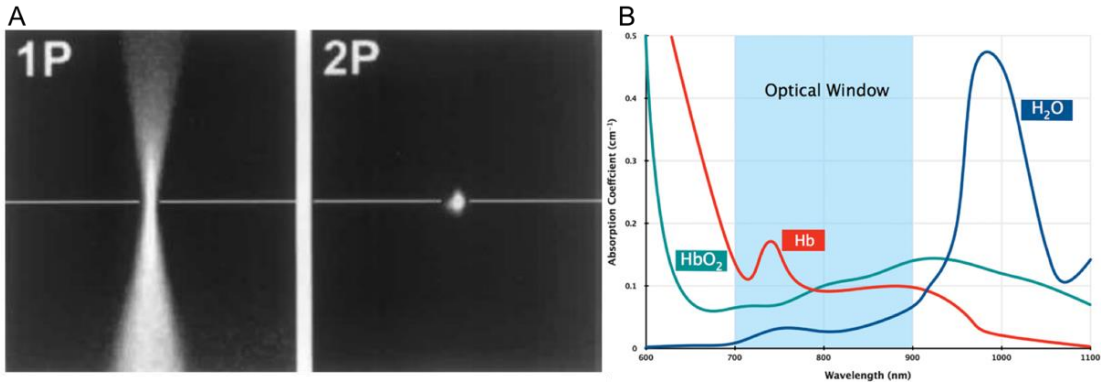

Figure 1.8. Advantages of multiphoton excitation in comparison to single-photon excitation. (A) Reduced out-of-focus light occurs in multiphoton excitation due to the small focus volume. For 1P, the excitation occurs above and below the focal plane whereas for 2P only occurs in a highly-localised area.[44] (B) The biological optical window showing significantly less absorption between 700 – 900 nm wavelengths from biological molecules within cells.[45]

The design of fluorescent probes for multiphoton applications relies on fluorophores with the ability to undergo two-photon excitation and have a high two-photon absorption cross-section (σ_2). This is the probability for a compound to undergo two-photon absorption (TPA).[46] There have been significant developments in this field over the past couple of decades for designing two-photon absorbing materials with large two-photon absorption cross-sections.[47] For this reason organic compounds are often used in multiphoton imaging, although these organic probes suffer for many limitations such as low photostability and poor solubility. Due to these limitations transition metal complexes have been investigated as multiphoton probes due to their desirable photophysical properties and cellular selectivity in addition to having large two-photon absorption cross-sections. Studies have shown that metal complexes based on Pt(II)[48-50], Ru(II)[51-53] and Ir(III)[53-55] can undergo multiphoton excitation with large two-photon

cross-sections. Iridium complexes have been extensively studied for their uses as multiphoton imaging probes as they have shown to exhibit desirable non-linear absorption properties and have rich photochemical properties. Additionally, these iridium complexes have long excited state lifetimes making them excellent candidates for lifetime imaging applications whilst still being able to benefit from multiphoton excitation.[56-58] Another desirable property of iridium(III) complexes is the ability to readily modify the cyclometalated ligands to enhance their two-photon absorption cross-sections. Fan *et al.* showed that a series of triscyclometalated iridium complexes with different oligofluorene-substituted ppy ligands, displayed a range of high two-photon absorption cross-sections (Figure 1.9).[59]

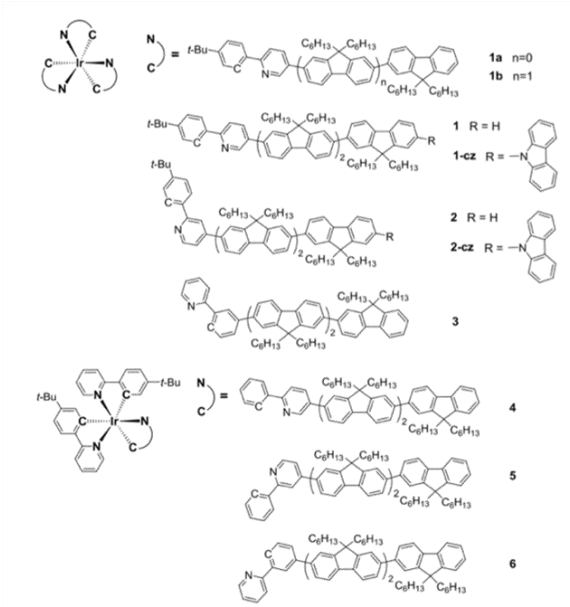

Complex	σ_{2PA} /GM
1a	2.1 x10^2
1b	4.5 x10^2
1	6.9 x10^2
1-cz	1.1 x10^3
2	7.3 x10^2
2-cz	1.2 x10^3
3	6.2 x10^2
4	1.4 x10^2
5	1.3 x10^2
6	1.2 x10^2

Figure 1.9. (Left) Iridium(III) complexes studied for multiphoton absorption experiments. (Right) Two-photon absorption cross-sections calculated for each iridium(III) complex. TPA cross sections (1 GM = 10^{-50}) were measured with a comparative method based on the emission intensity using Rhodamine B as the reference.[59]

Amongst all the iridium(III) complexes, **2-cz** displayed the highest TPA cross-section. This is to be expected with the iridium(III) complex containing three carbazole-terminated trifluorenyl ppy ligands. This shows that the structural design of the ligands around the metal centre can have a major impact on the TPA properties. Edkins *et al.* went on to analyse the TPA cross-sections of neutral iridium(III) complexes with variations in the cyclometalating ligand, 2-phenylpyridine, and ancillary ligands. The results showed that these iridium(III) complexes displayed high TPA cross-sections at 800 nm (Figure 1.10).[60]

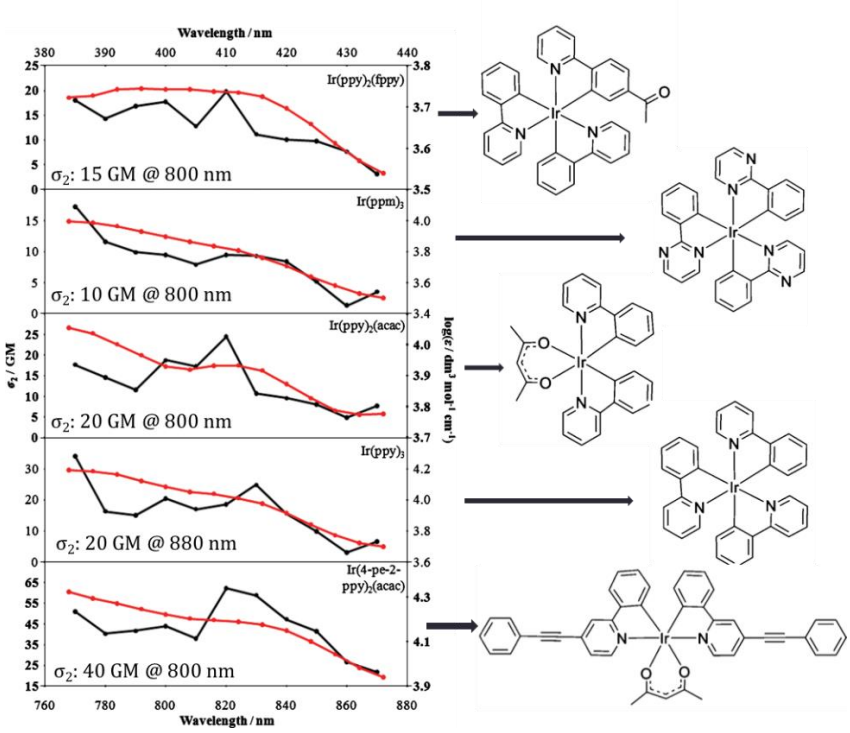

Figure 1.10. (Left) Two-photon absorption spectra (black, bottom abscissa, left ordinate) and single-photon (UV-Vis) spectra (red, top abscissa, right ordinate). Graphs have been annotated showing two-photon absorption cross-sections at 800 nm. (Right) Corresponding structure of iridium(III) complex studied for these experiments.[60]

There were little differences seen in TPA cross-sections between the iridium(III) complexes with the range being between 10 – 20 GM. This was improved by

implementing structural features known to increase the TPA in organic material.[61] Therefore, extending the π network conjugation within the framework of a molecule led to the synthesis of Ir(4-pe-2-ppy)$_2$(acac) which displayed a TPA cross-section of 44 GM at 800 nm. This was more than double the TPA cross-section recorded for Ir(ppy)$_2$(acac), which was found to be 20 GM at 800 nm. This research showed that careful design of these iridium(III) complexes can lead to high TPA cross-section whilst still retaining desirable photophysical properties for a range of biomedical imaging applications. The ability to improve the TPA properties of these transition metal complexes through rational design of the conjugated ligands, would prove invaluable for multiphoton applications.

A range of iridium(III) complexes have been designed for multiphoton microscopy and found to have high multiphoton absorption properties. Additionally, their ligands can be tuned for the selective targeting for organelles and biomolecules within cells. Wong *et al.* developed a heteroleptic iridium(III) complex that could specifically target the Golgi Apparatus *in vitro* using multiphoton microscopy. The results showed high accumulation of the phosphorescent iridium(III) complex within the Golgi Apparatus, which could be seen through complete co-localisation of the iridium signal with the Golgi stain using two-photon excitation (Figure 1.11). TPA cross-section was taken and found to be 340 GM at 750 nm, which is one of the highest recorded values for iridium(III) complexes.[62]

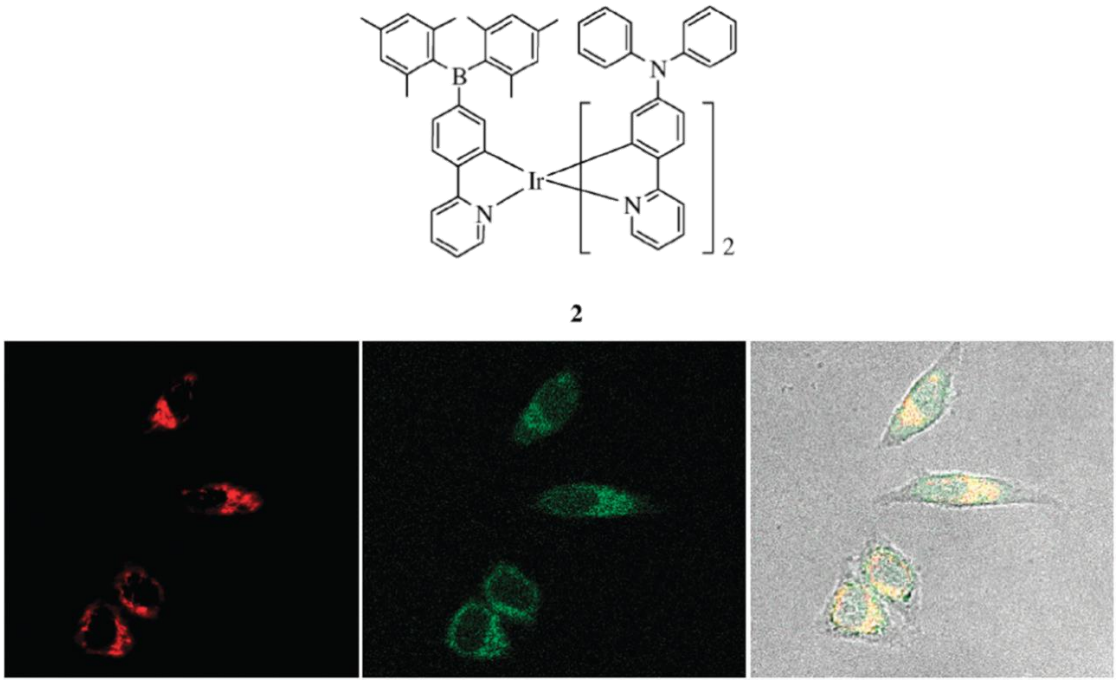

Figure 1.11. (TOP) Structure of Iridium(III) complex (2). (Bottom) (Left) Golgi marker Alexa Fluor 647 conjugates of HPA (Invitrogen L32452) (λ_{ex}= 647 nm, band pass filter = 650 – 750 nm, 10 min exposure) in HeLa cells; (Middle) two-photon microscopy images (λ_{ex} = 700 nm, band pass filter = 500 – 640 nm; (Right) merged image.[62]

Additionally, selectively targeting mitochondria is of high importance due to its proposed role in many diseases. This was demonstrated by Chao *et al.* when two-photon phosphorescent iridium(III) probes for detecting hypochlorite ions (ClO^-) in mitochondria were developed. Multiphoton excitation is sought out for these applications because of the increased penetration depths achieved and reduced out-of-focus fluorescence within the cells, making it easier to visualise mitochondria dynamics. The synthesised iridium(III) complex contained a diaminomaleonitrile group which specifically reacted with ClO^- to form a carboxylate product (Figure 1.12, Top).[63] Studies have shown that abnormal levels of ClO^- is linked to many diseases and therefore this shows the importance of developing probes that can specifically detect this reactive species within mitochondria.[64-66] When this reaction occurred a significant

enhancement in phosphorescence intensity was observed under one-photon (405 nm) and two-photon (750 nm) excitation, with a TPA cross-section (σ_2) of 78.1 GM being recorded. MitoTracker™ Green was used for co-localisation experiments between the Mitotracker and iridium signal. The results showed high specificity and sensitivity for detecting ClO^- in the mitochondria through the fluorescence response of the iridium(III) probe (Figure 1.12, Bottom).

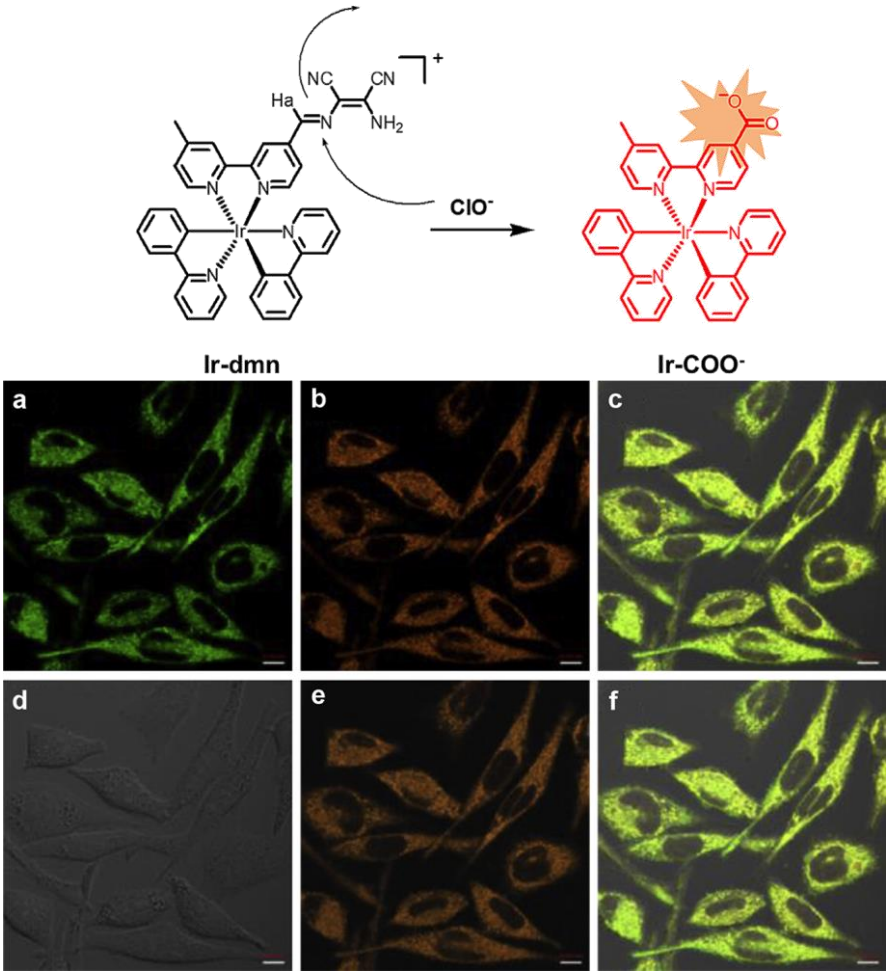

Figure 1.12. (Top) Reaction mechanism of Ir-dmn with ClO^-. (Bottom) Single-photon and Two-photon microscopy images of exogenous ClO^- in HeLa cells. (a) OPM of cells incubated with MitoTracker Green for 30 min, λ_{ex} = 488 nm, λ_{em} = 500 – 540 nm; OPM (b) and TPM (e) image of cells pre-treated with NaClO (10 μM) for 1 h and then treated with Ir-dmn (10 μM) for another 1 h, λ_{ex} = 405 nm (OPM)/750 nm (TPM), λ_{em} = 580-620 nm; (d) Bright-field image of cells; (c) Overlay image of (a), (d) and (b); (f) Overlay image of (a), (d) and (e). Scale bar: 10 μm.[63]

Chao *et al.* went on to develop iridium(III) complexes that could visualise and track mitochondria within living cells using multiphoton microscopy. Understanding the dynamics and functions of mitochondria could help answer many questions relating to diseases such as cancer, neurological disorders and aging. Single-photon and two-photon fluorescence showed localisation of these iridium(III) complexes in the mitochondria by co-localisation of the iridium signal and MitoTracker™ Green signal. This was confirmed by ICP-MS which showed 80 – 90 % of the iridium(III) complexes localised within the mitochondria of the cells in comparison to other areas (cytoplasm or nucleus). The TPA cross-sections were found to be 60 – 65 GM at 750 nm, which is extremely high for iridium(III) complexes. However, the most important aspect of this work was to show the power of using two-photon excitation for imaging thick tissues, since the two-photon penetration depth is greater than that achieved through single-photon excitation. To prove this, they used a 3D multicellular spheroid that contained an extensive extracellular matrix (ECM) (Figure 1.13).

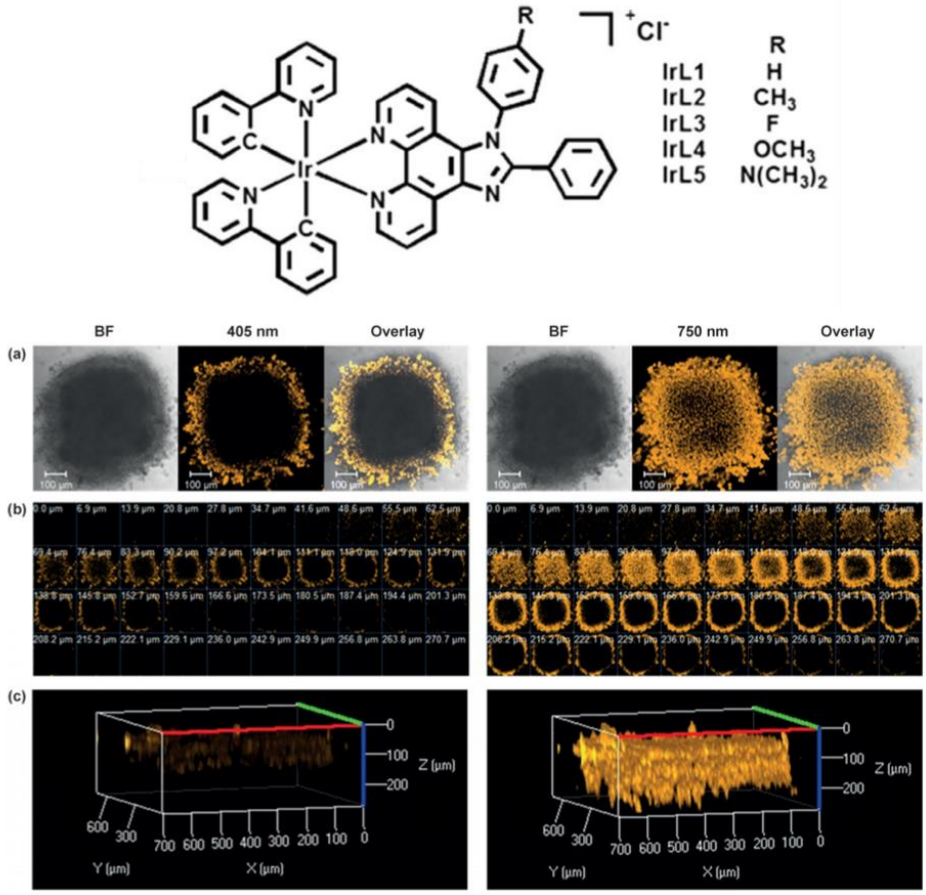

Figure 1.13. (Top) Iridium(III) complexes; IrL1 – IrL5. (Bottom) (a) Single-photon microscopy (left) and two-photon microscopy (right) images of 3D multicellular spheroids after incubation with IrL2 (500 nM) for 0.5 hours. (b) Z-stack images were taken every 7 μm sections along the Z-axis of an intact spheroid. (c) The merged images of Z-stack images of an intact spheroid. Excitation is 405 nm for single-photon excitation and 750 nm for two-photon excitation. Scale bar = 100 μm.[67]

They found that with complex **IrL2**, luminescence signal could be seen down to depths of 90 μm using single-photon excitation and 250 μm using two-photon excitation. Two-photon excitation allowed for strong phosphorescence signal to be detected deep within the spheroid which was not achievable with single-photon excitation, showing the importance of having a carefully designed probe for multiphoton imaging of tissues.[67] This group then went on to investigate the uptake of iridium(III) complexes

specifically into mitochondria which was monitored by phosphorescence lifetime imaging, due to their desirable photophysical properties. Combining lifetime based imaging with multiphoton excitation has become a widely sought out tool for bioimaging due to its sensitivity of detection and complete elimination of background autofluorescence. Transition metal complexes are often used for multiphoton lifetime applications because they emit a long-lived excited state and are known to have high TPA cross-sections making them desirable candidates for this technique.

1. 1. 3 Lifetime imaging

Multiphoton lifetime imaging works by detecting the luminescence lifetimes of the transition metal probes which offers a more sensitive method of detection in comparison to emission based techniques. Fluorescence lifetime imaging microscopy (FLIM) detects the short-lived fluorescence lifetimes of a fluorophore within a sample. FLIM probes have been developed and are traditionally based on organic probes with short nanosecond lifetimes. There are a few examples of iridium(III) complexes being used as FLIM probes within cells. This was demonstrated in a peptide-iridium complex which was designed to selectively target CXR4 receptors on the surface of tumour cells, and could be visualised using fluorescence lifetime imaging (Figure 1.14).[68] The FLIM images revealed clear specificity of these peptide conjugated iridium(III) complexes to the receptor of tumour cells, in comparison to unconjugated probes which showed no specificity to tumour cells.

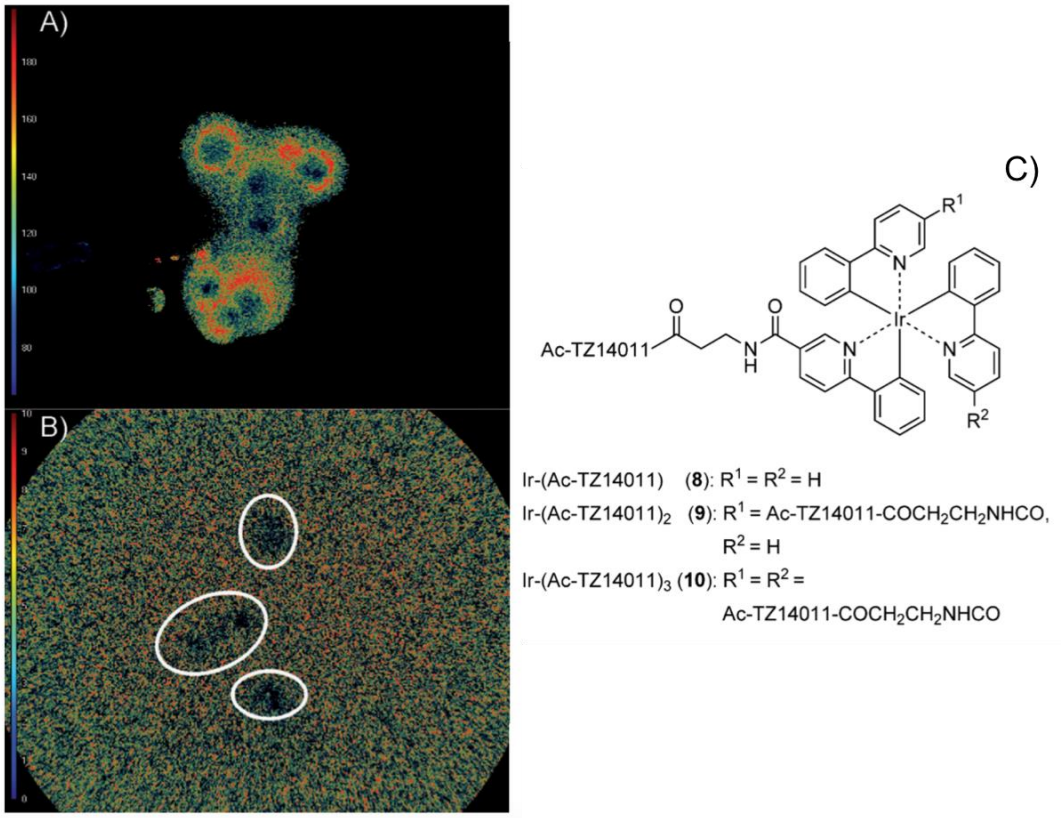

Figure 1.14. (A) FLIM image of MDAMB231^{CXCR4+} cells incubated with 1 μm of peptide functionalised iridium(III) complex (8). The scale bar indicates the lifetime range (60 ns to 200 ns). (B) FLIM images of MDAMB231^{CXCR4+} cells without conjugates (8). The scale bar indicates lifetime range of 0 – 10 ns detected. [68]

Analysis of the lifetimes within the FLIM images revealed lifetimes of 60 – 200 ns for the conjugated probes and 0 – 10 ns for unconjugated probes. This can be seen visually within the FLIM images where the peptide iridium(III) complex can be seen accumulated around the cell membrane of cancer cells, whereas the unconjugated probe is dispersed on the bottom of the coverslip with no uptake into cells. One of the disadvantages of FLIM is detection of these nanosecond lifetimes are in the same range as the lifetimes detected from cellular autofluorescence (1 – 20 ns) which limits the probes' sensitivity.[69, 70] The advantage of using iridium(III) complexes is the ligands can be tuned for specific applications. Furthermore, most iridium(III) complexes exhibit

long-lived luminescence lifetimes which can extend into the millisecond range making them ideal candidates for phosphorescence lifetime imaging microscopy (PLIM). PLIM detects these long-lived lifetimes which can be completely gated from short-nanosecond lifetimes associated with autofluorecence, expanding sensitivity and signal detection for these transition-metal complexes.[71] Furthermore, this technique can be combined with multiphoton excitation which is advantageous for deep tissue imaging, as mentioned previously. Iridium(III) complexes are known to have long-lived phosphorescence lifetimes and can be excited by two-photon excitation to produce large TPA cross-sections. The power of detection by lifetime imaging of metal complexes[72] has been demonstrated in iridium(III) complexes for biomedical applications such as imaging cellular organelles, cancer metastasis and hypoxia.

Two-photon lifetime imaging has been demonstrated using iridium(III) complexes containing diphosphine ligands that could selectively target mitochondria for anticancer therapeutic applications.[73] These iridium(III) complexes were shown to accumulate within the mitochondria of A549 cells which was confirmed by confocal microscopy, lifetime imaging and ICP-MS. It was found that the iridium(III) complexes have viscosity dependent lifetimes which allowed for detection of changes in the mitochondria microenvironment with high sensitivity. The viscosity changes within the mitochondria has shown to affect protein-protein interactions and has been associated with diseases such as diabetes and atherosclerosis. Being able to monitor the changes in mitochondrial viscosity has remained a challenge using other fluorescence microscopy techniques. The results showed the average luminescence lifetimes recorded within the mitochondria for **Ir6** increased from 1,410 ns to 1,792 ns upon increase in mitochondrial viscosity (Figure 1.15, B). It is known that each separate mitochondrion

within the same cell can respond differently to external stimuli[74, 75], but detecting these individual organelles responses is extremely difficult and often limited.

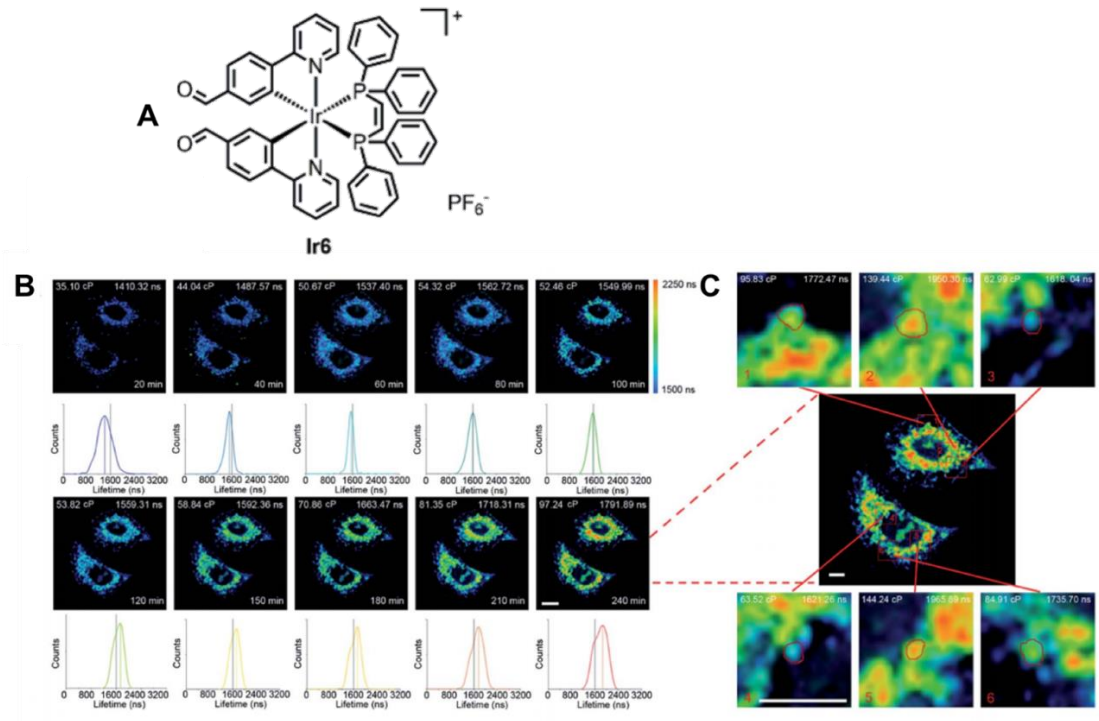

Figure 1.15. (A) Structure of iridium(III) complex, Ir6. (B) Mitochondria viscosity for Ir6-treated A549 cells detected by two-photon PLIM. The cells were treated with Ir6 (20 mm) and imaged at different time intervals. (C) Determination of mitochondria heterogeneity. A549 cells treated with Ir6 (20 mM) for 4 hours. The enlarged images are from the red boxes. The lifetime and viscosity are calculated from the spots in the red circle. λex = 750 nm (Ir6); λem = 550 (Ir6).[73]

Since PLIM is sensitive to local changes in environment, it can be used to determine the heterogeneity of mitochondria (Figure 1.15, C). The results revealed differences in lifetimes detected from the **Ir6** complex in different areas within the mitochondria, this is highlighted in the insets which correspond to the red boxed present on the lifetime images. This shows how sensitive two-photon lifetime imaging can be for detecting small changes in the local microenvironment at a subcellular level. Iridium(III) complexes have the potential to be used as multiphoton lifetime imaging probes for *in*

vivo applications due to their high TPA cross-sections and long-luminescence lifetimes. The power of detection by lifetime imaging of metal complexes has been demonstrated in iridium(III) complexes in tumour imaging for cancer metastasis[76] and hypoxia.[77] For these iridium(III) complexes to be successfully used for *in vivo* applications, their luminescence lifetimes need to be detected in thick samples, which requires a deeper penetration depth of the excitation light. This was demonstrated by Chao *et al*. in which the penetration depth of multiphoton excitation allowed for imaging of 3D spheroids and phosphorescence lifetime imaging was sensitive enough to detect iridium(III) complexes within the mitochondria and multicellular tumour spheroids (MCTS) with complete elimination of background autofluorescence (Figure 1.16).[78]

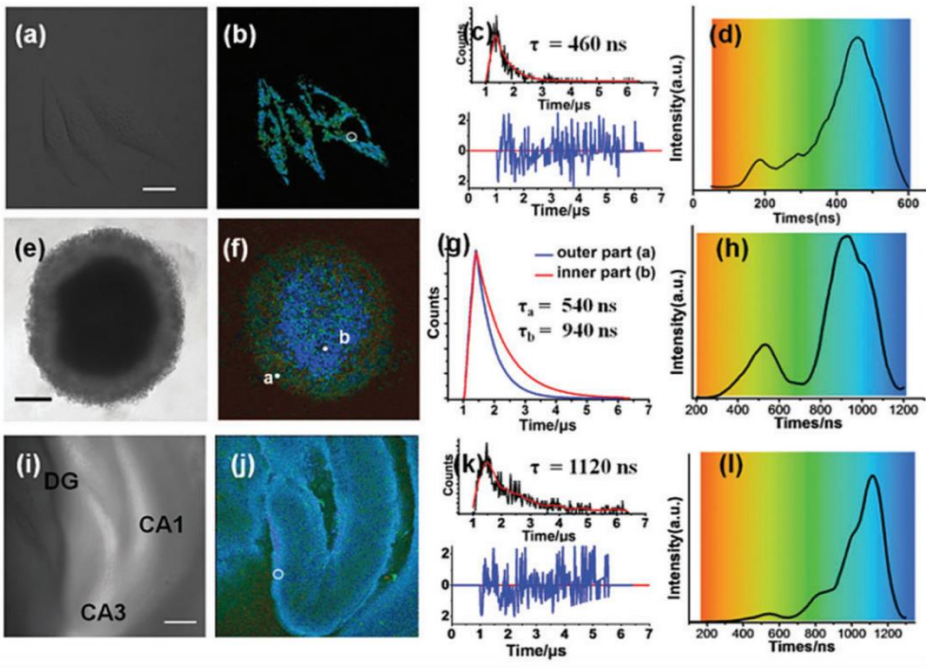

Figure 1.16. (a, e and i) Brightfield and (b, f and j) Two-photon excited PLIM images of iridium(III) complex in cells, 3D MCTSs and hippocampus slice. (c, g and K) kinetic traces from the selected regions of (b), (f) and (j). (d, h and l) Lifetime distribution for Ir(III) complexes = 730 nm. Scale bar = 20 μm (a) and 200 μm (e and i).[78]

The images revealed a high accumulation of iridium(III) complexes into the mitochondria of cells which can be seen in cyan on the lifetime images (Figure 1.16, b). Long-luminescence lifetimes of around 460 ns were detected and found to be evenly distributed throughout the mitochondria. MCTSs were used as a model in these experiments to mimic the extracellular matrix of tumours. This is a more accurate representation of the tumour microenvironment and in understanding how the iridium probes behaves in this complex environment. The results showed that the lifetimes recorded for the iridium(III) complex seems to vary throughout the spheroid. This was to be expected as the oxygen levels within the spheroid change throughout (Figure 1.16, f). The results showed that phosphorescence lifetime microscopy can be used for applications in oxygen sensing as well as tissue imaging. Since the aim of this work was to characterise these probes for tissue imaging, PLIM was carried out on iridium(III) complexes taken up in rat hippocampus tissue slices (Figure 1.16, j). PLIM could resolve the structural details of the tissue regions in much higher resolution than the corresponding wide-field image (Figure 1.16, j). The lifetime detected were found to be 1120 ns, which could be differentiated from the lifetimes recorded in cells (460 ns), showing not only sensitivity to local environment changes but also selectively to different cell types.

1. 2 Gold Nanoparticles for imaging applications

1. 2. 1 Luminescence imaging

Another novel area of research is looking at using nanoparticles and their applications in fluorescent bioimaging.[79, 80] These nanoparticle probes have received a lot of interest for bioimaging because of their unique photophysical properties, ease of

synthesis and tuneable optical properties.[81-83] Nanoparticles can be synthesised in various shapes and sizes and their surface can be functionalised with various ligands for selective targeting and drug delivery applications.[84] There are many advantages for using nanoparticles over molecular probes. Most nanoparticles, such as gold nanoparticles, do not suffer from photobleaching, which is an inherit property of molecular dyes and they have shown to be non-toxic within cells.[85] Nanoparticles can easily accumulate within cells and tissues and can be used to target specific molecular sites.[86-88] The biggest advantage of using nanoparticles is that their surface can be used as a scaffold for the conjugation of biomolecules and synthetic ligands. The nanoparticles can be conjugated with luminescent probes for bioimaging applications,[89, 90] biomolecules for selective targeting of specific receptors[91, 92] or drug compounds for targeted delivery of these compounds into cells.[93, 94] Nanoparticles have been used for many applications in biomedicine, from imaging to diagnostics to targeted cancer therapies.[95, 96] To date a range of nanoparticles have been used including carbon nanotubes[97-99], quantum dots[100, 101], magnetic nanoparticles[102, 103] and gold nanoparticles.

Gold nanoparticles (AuNPs) have often designed for biomedical imaging applications because they are readily taken up by cells with low cytotoxicity, tuneable optical and electrochemical properties and their surface can be easily modified with imaging probes[104, 105] and biomolecules for targeting.[106, 107] Whereas, in comparison to other nanoparticles such as upconverting nanoparticles[108, 109] or Quantum Dots, the synthesis for these nanoparticles is often difficult and they have shown to exhibit high cytotoxicity within cells. The internalisation of gold nanoparticles has been investigated

by multiple microscopy techniques such as two-photon luminescence, scattering, lifetime imaging, electron microscopy and fluorescence microscopy.

The most common technique employed is electron microscopy which provides high resolution imaging of gold nanoparticles to show localisation within cells. However, the drawback of this technique is the sample preparation which requires cells to be fixed and only thin sections are imaged. This means that this technique cannot be used for real-time imaging of cells *in vivo*, which is a major drawback. Optical based techniques overcome these limitations and can view nanoparticles within cells in real-time. Gold nanoparticles have been employed for optical imaging because of their unique fluorescence induced by single and two-photon excitation. Gold nanoparticles have a characteristic surface plasmon resonance (SPR) which can change based on the shape, size and surface coating of the nanoparticles. This SPR scattering properties allows these nanoparticles to be detected by both fluorescence and reflectance microscopy techniques using both single and multiphoton excitation wavelength.[110, 111] This was demonstrated by Ren *et al.* where 38 nm gold nanoparticles (AuNPs) were efficiently taken up into cancer cells, and the luminescence signal could be detected to identify single gold nanoparticles (surface not functionalised with any luminescent probes) within cells using confocal microscopy. (Figure 1.17).[112]

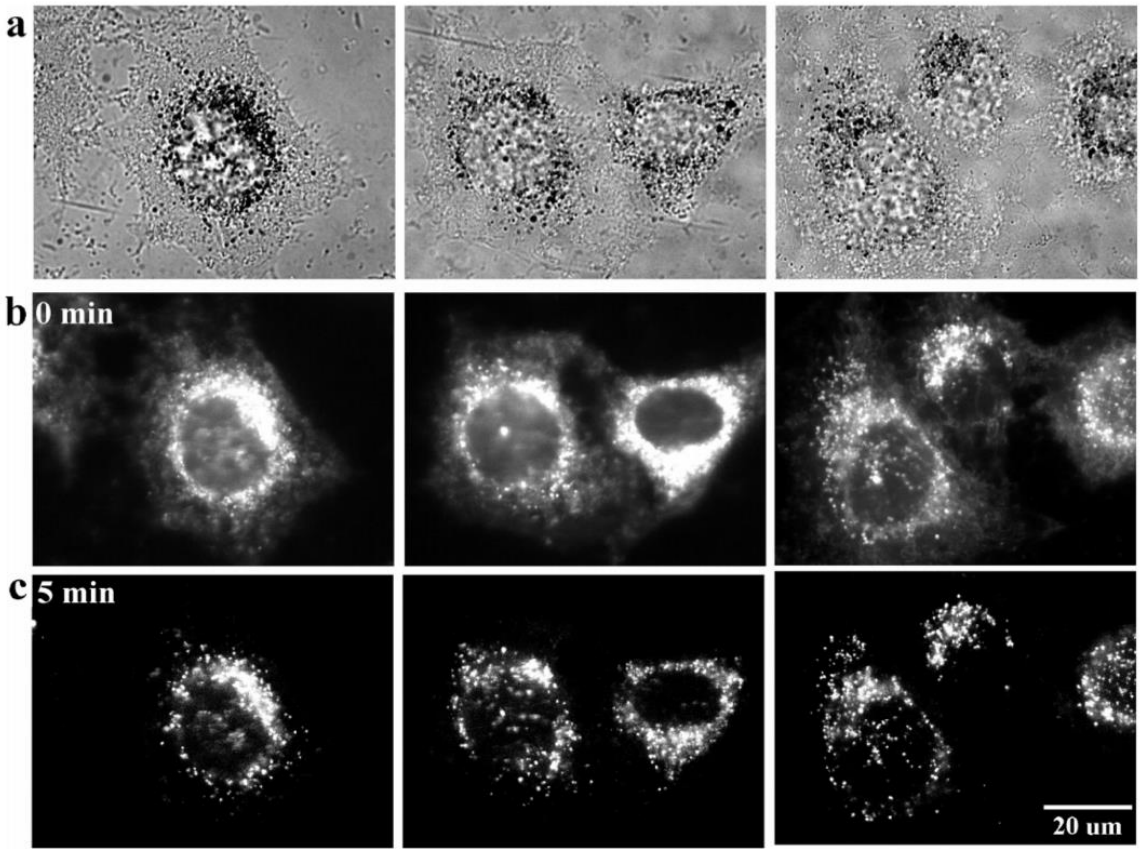

Figure 1.17 Bright-field images (a) and fluorescence images of HeLa cells incubated with 38 nm GNPs (b) before and (c) after 5 min photobleaching. The other two images in the same row for each imaging condition are shown to test reproducibility. Exposure time: 5 s.[112]

The results showed that after photobleaching with a high laser intensity, the AuNPs could still be detected within cells and suffered no photobleaching. Irradiation with high laser powers meant that cell autofluorescence was removed, to leave only the luminescence signal of the gold nanoparticles within cells, which allowed for single particles to be detected over background signal. This would not be possible with many organic and inorganic probes which suffer from photobleaching during laser irradiation. However, even though the intrinsic luminescence of gold nanoparticles can be detected by reflectance microscopy, the emissive properties are sensitive to the size, shape and morphology of these particles making it difficult to predict its luminescence

in vitro and *in vivo* for their uses as reliable imaging probes. Therefore, research has shifted to developing luminescent nanoprobes by modifying the gold surface with luminescent probes which allows for bimodal imaging using the unique signature from the gold and the luminescence signal from the bioimaging probe. The large surface area of AuNPs allows for hundreds to thousands of luminescent agents to be attached to the surface. Often metal complexes are functionalised onto the gold surface for medical imaging such as positron emission tomography (PET), magnetic resonance imaging (MRI), single-photon emission computed tomography (SPECT) and fluorescence imaging. As discussed previously, transition metal complexes have desirable photophysical properties and their ligands can be easily modified with thiol containing groups for attachment onto gold nanoparticles. Our group have demonstrated the successful coating of AuNPs with transition metal complexes based on ruthenium(II) and iridium(III) centres for imaging applications.[113, 114] This was demonstrated using ruthenium(II) coated gold nanoparticles which showed high accumulation into cancer cells after 24 hours incubation (Figure 1.18).[115]

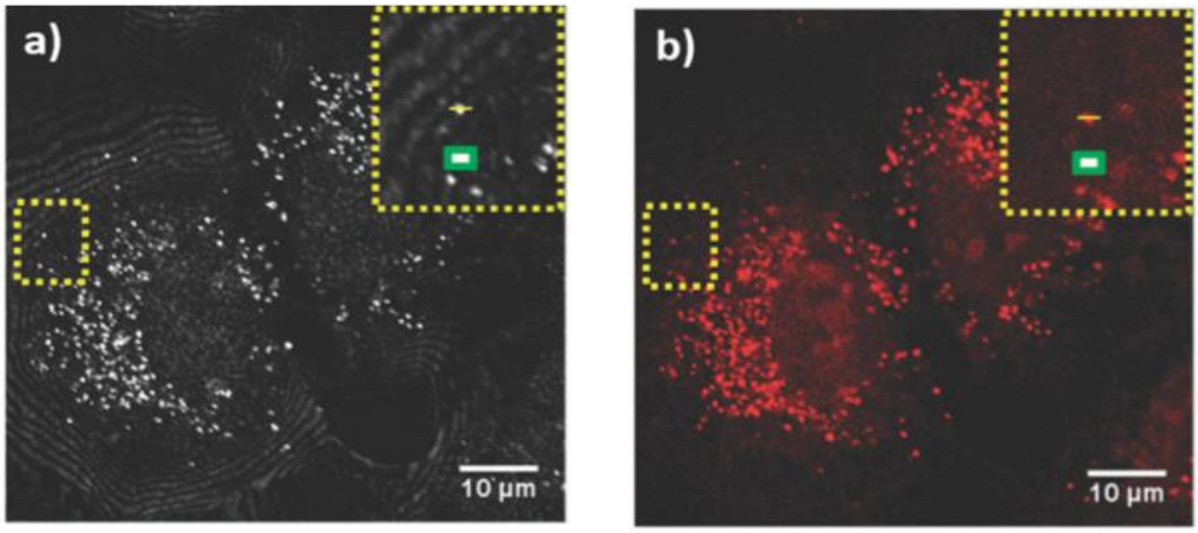

Figure 1.18. (a) Confocal reflection microscopy image λ_{exc} = 488 nm, λ_{em} = 478-498 nm and (b) confocal luminescence microscopy of ruthenium λ_{exc} = 453 nm, λ_{em} = 555-800 nm.[115]

It was found that the unique signal for the gold SPR band could be detected by confocal reflectance microscopy and was found to completely co-localise with the fluorescent signal from the ruthenium(II) complex. After a 24 hour incubation single non-aggregated particles were observed within the cancer cells showing the high stability of these nanoparticles within cells after internalisation. These results led to the development of more luminescent ruthenium(II) complexes for attachment onto gold nanoparticle and their cellular fate was investigated.[116] Transition metal complexes based on iridium(III) centres have been functionalised onto the surface of gold nanoparticles and the applications for *in vivo* imaging of blood flood investigated. Iridium(III) coated nanoparticles have shown to produce brighter nanoparticles in comparison to ruthenium(II) coated nanoparticles, therefore making them ideal candidates for imaging in flow systems.[117] However, the excitation wavelength of iridium(III) complexes is usually in the UV range making them less suitable for single photon techniques due to the high cellular autofluorescence present at these

wavelengths. Since these iridium(III) complexes have shown to excite using multiphoton excitation with high two-photon absorption cross-sections, iridium(III) functionalised nanoprobes have the potential to be effective multiphoton imaging probes for *in vivo* applications. Not only is the excitation in the near infrared range desirable for *in vivo* applications but the long-lived luminescence lifetimes of iridium(III) complexes would allow multiphoton lifetime imaging applications. At present, functionalising gold nanoparticles with iridium(III) complexes for multiphoton lifetime imaging has not be explored.

1. 2. 2 Multiphoton imaging

It has been found that gold nanoparticles can exert strong photoluminescence which is enhanced under two-photon excitation. Research has found that photoluminescence can be enhanced by a factor greater than 1 million by exciting the surface plasmon resonance band of gold nanorods[118]. Utilising this phenomenon has made these gold nanoparticles attractive contrast agents for two-photon imaging, which is a powerful technique that is becoming a widely sought out technique for *in vivo* experiments specifically for cancer diagnostics and detection. This technique can non-invasively image up to several millimetres in depth, which allows for deep tissue imaging of sub-cellular structures providing us insight into cancer and cancer processes. Nanoparticles that can undergo two-photon excitation have been used for many applications to label free contrast agents[119, 120], photodynamic therapy[121, 122] and targeting cancer cells[123]. Gold nanorods are attractive options as two-photon luminescence (TPL) contrast agents because their rod like shape provides a characteristic longitudinal plasmon resonance which can be excited in the near-

infrared region to provide enhanced photoluminescence.[110, 124] Excitation in this region makes them suitable candidates for imaging thick tissue samples for *in vivo* applications due to the greater depths achieved in the NIR region with these techniques. Wang *et al.* demonstrated the use of single gold nanorods for *in vivo* imaging of blood vessels through the strong two-photon luminescence signal from the gold (Figure 1.19).[124]

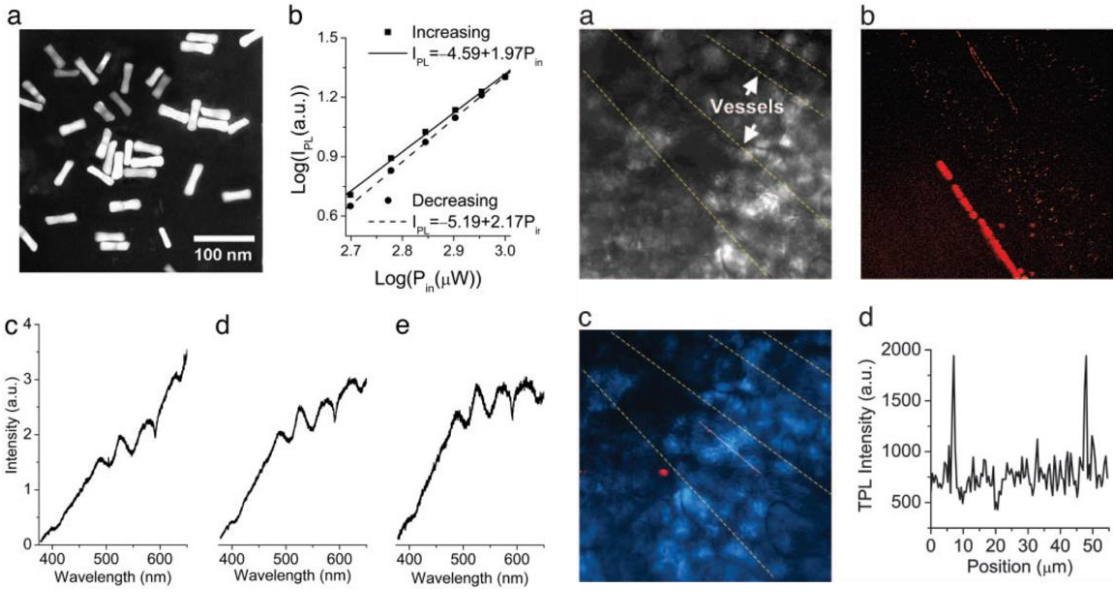

Figure 1.19. (Left) Properties of two-photon luminescence from gold nanorods (a) TEM image, (b) Power dependence studies and (c – e) Photoluminescence spectra from solution of gold nanorods at excitation 730 (c), 780 (d) and 830 (e) nm. (Right) *In vivo* imaging of single gold nanorods in mouse ear blood vessels (a) Transmission imaging highlighting two blood vessels. (b) Two-photon luminescence image of gold nanorods (red dots) in flow. (c) Overlay of transmission image (light blue) and a single-frame TPL image. (d) TPL intensity profile from the linescan in c.[124]

The results showed that the two-photon luminescence recorded from a single gold nanorod was ~58 times brighter than the two-photon luminescence from a single dye molecule such as Rhodamine 6G. These gold nanorods displayed extremely high two-photon absorption cross-sections of 2,320 GM at 830 nm, in comparison to Rhodamine

6G which has a two-photon absorption cross section of 40 GM at 830 nm excitation. This high TPA cross section combined with the lack of photobleaching makes these gold nanorods superior contrast agents for two-photon imaging for *in vivo* applications. The strong two-photon luminescence emitted by these gold nanorods meant they could be detected *in vivo* without interference from background autofluorescence. These single gold nanorods were presented throughout the blood vessel appearing as individual red dots which were rapidly cleared by 30 minutes of imaging (Figure 1.19, right, b). This work showed a great example of the enhanced two-photon intensity present from gold nanorods and how this effect can be utilised in biomedicine for imaging under two-photon excitation.

Another advantageous property of gold nanoparticles is their surface can be functionalised with biomolecules for selective targeting of cancer receptors. Durr *et al.* synthesised antibody coated gold nanorods that could selectively targeted cancer cells overexpressing EGFR, which could be detected through strong two-photon luminescence. The two-photon images showed accumulation of these antibody coated gold nanorods around the cell membrane of cancer cells overexpressing EGFR, which is where EGFR proteins are present, showing a high degree of specificity. When compared to unlabelled cells, two-photon signal from the antibody coated gold nanorods could be seen throughout the cytoplasm of the cells with no specificity for the outer membrane (Figure 1.20). The two-photon luminescence signal detection allowed for imaging up to depths of 75 μm, confirming their suitability of *in vivo* applications.[123]

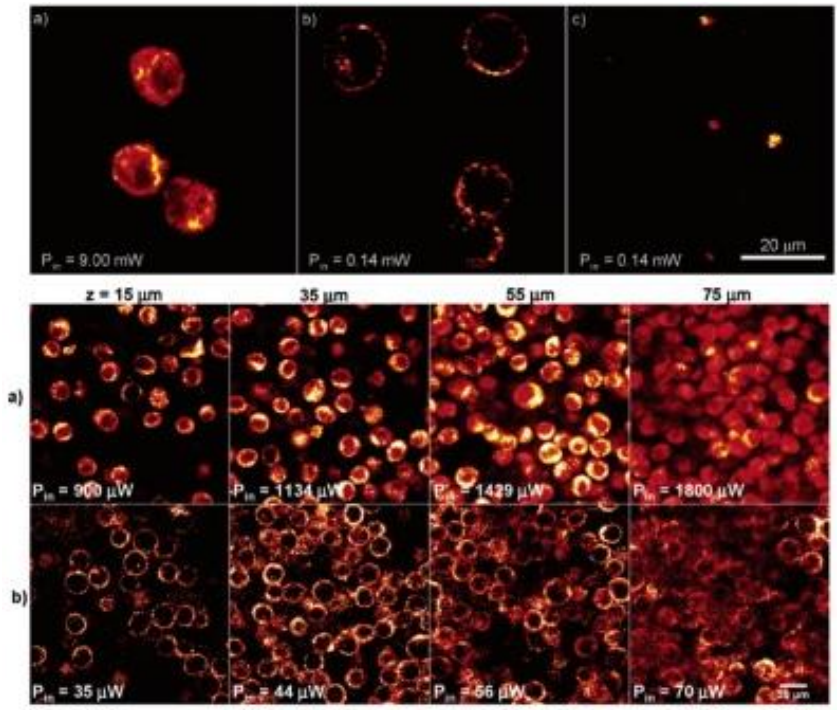

Figure 1.20. (Top) Two-photon images of cancer cells placed on a coverslip from a cell suspension. (a) TPL image of unlabelled cells. (b) TPL image of nanorod-labelled cells. (c) TPL image of non-specifically labelled cells. (Bottom) Two-photon imaging of cancer cells embedded in a collagen matrix at increasing depths. (a) TPL imaging of unlabelled cells and (b) TPL imaging of nanorod-labelled cells. Both samples require the same excitation power increase of 26% at each 20 μM depth increment to maintain constant emission intensity.[123]

Quantum dots have been used for multiphoton imaging due to their larger two-photon absorption cross-sections, however they suffer from disadvantages of high cytotoxicity and photo blinking.[125, 126] Gold nanoparticles with their many shapes and sizes have often been investigated as two-photon contrast agents because of their strong two-photon photoluminescence (TPPL) and high multiphoton absorption cross-sections. When compared to organic fluorophores, gold nanoparticles excel as an imaging agent as they do not photobleach under multiphoton excitation. They have proven to be biocompatible in cells and are non-toxic, making them perfect candidates for biomedical imaging applications. Many different types of gold nanoparticles have been

studied for two-photon luminescence applications including gold nanorods (AuNRs), nanocages (AuNCs), nanotriangles (AuNT) and nanospheres (AuNS). This has been demonstrated using spherical gold nanoparticles of various sizes where strong two-photon luminescence (TPL) could be detected within 3D spheroids (Figure 1.21).[127]

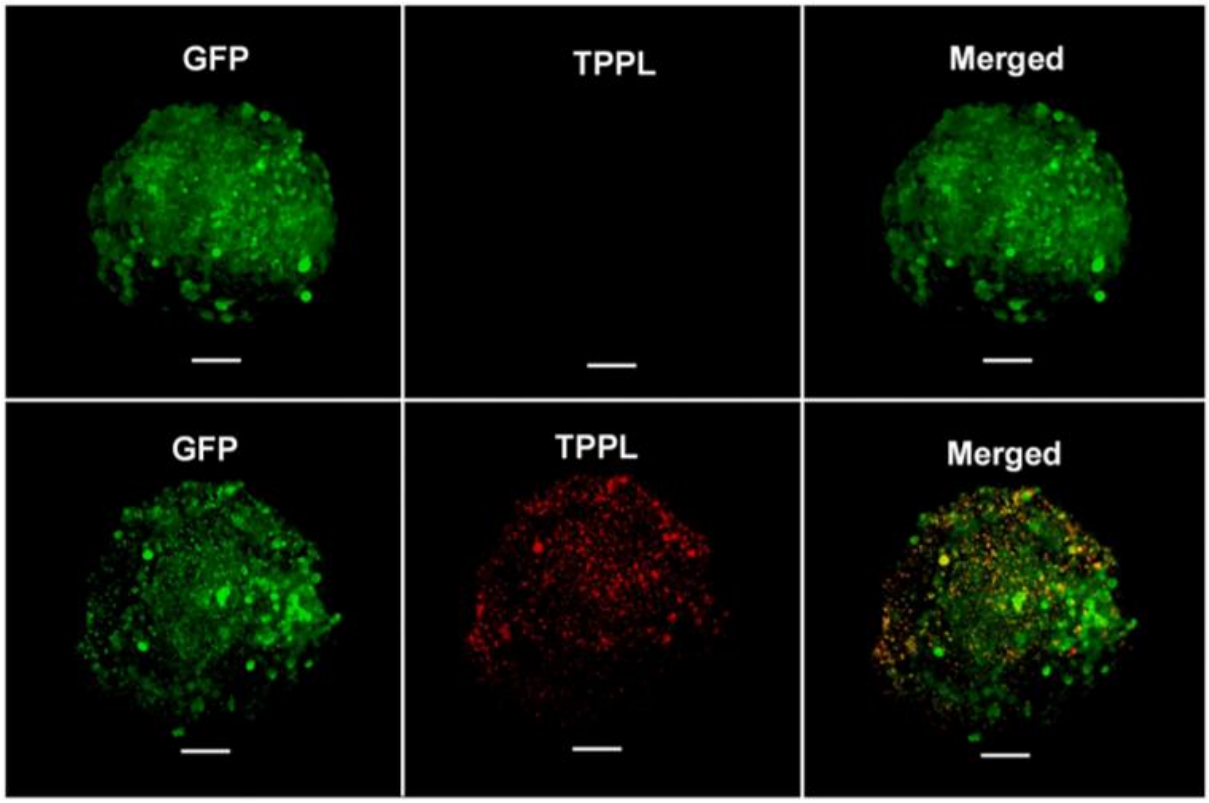

Figure 1.21. Two-photon images of HCT116 cell spheroids used for estimation of AuNP uptake in cell spheroids. (Top) control spheroid (Bottom) cell spheroid incubated with AuNP. λ_{ex} = 800 nm and emission filters for GFP signal 505 – 545 nm (green) and AuNP luminescence 618.5 – 675.5 nm (red). Scale bar: 50μm.[127]

The TPL images showed distribution of AuNPs within the 3D spheroids by detecting the two-photon luminescence signal from the AuNPs which could be completely separated from the GFP signal. Being able to detect luminescence signal at these depths is not achievable through single-photon excitation. Interestingly, this work revealed that smaller spherical gold nanoparticles could penetrate deeper into the

spheroid than rod shaped gold nanoparticles. This is invaluable knowledge for researchers designing cancer targeting probes based on gold scaffold, where tumour penetration depth is of high importance. The intrinsic behaviour of gold nanoparticles has shown their importance in *in vivo* imaging using multiphoton excitation. Combining this desirable excitation wavelength with long-luminescence lifetimes can be achieved through conjugation of transition metal complexes to the gold nanoparticle surface. This will not only allow for increased penetration depths for imaging thick tissues but would allow for the mapping of localisation and interactions of these nanoprobes with biomolecules due to the luminescence lifetime of the probe being sensitive to changes in the local microenvironment.

1. 2. 3 Lifetime imaging

Fluorescence lifetime imaging is becoming interestingly popular as a technique used to image nanoparticles. These lifetime based methods detect short-lived fluorescence lifetimes (FLIM) or long-lived phosphorescence lifetimes (PLIM). Lifetime imaging works by using a pulsed laser to induce fluorescence (short) and phosphorescence lifetimes (long) from a sample which are collected simultaneously in two different channels and monitored using a TCSPC (Time-Correlated Single Photon Counting) detector. Detection of the luminescent lifetimes offers more sensitivity in comparison to emission based techniques due to the complete elimination of cellular autofluorescence. This is achieved by gating the short lived background fluorescence (couple of nanoseconds) and only collecting the long-lived fluorescence lifetimes of the nanoparticles. Another advantage of lifetime imaging over emission based methods, is that the detection of luminescence lifetimes is independent of probe concentration,

thus lower concentrations can be used for cellular experiments. These luminescence lifetimes can be sensitive to changes in local environment which is an advantage when studying localisation or interactions with cellular proteins. Most cells and tissues exhibit autofluorescence due to proteins, chemicals and endogenous fluorophores being excited in the UV and visible region. However, their chemical lifetime is usually short, in the picosecond to nanosecond range. Therefore, using nanoparticles which have long fluorescence lifetimes in hundreds of nanoseconds range, would allow for complete elimination of background autofluorescence. This was demonstrated by Shang *et al.* where dihydrolipoic acid (DHLA) capped gold nanoclusters (AuNCs) were synthesised and found to contain attractive properties of bright near-infrared luminescence, high colloidal stability and good biocompatibility in cells. These nanoclusters showed long luminescence lifetimes (>100 ns), which were greater than the lifetime of cellular autofluorescence, allowing them to be used as fluorescence lifetime imaging (FLIM) probes.[128] The results showed that upon internalisation of DHLA-AuNCs in live HeLa cells the average lifetimes increased from 442 $\pm$ 13 ns to 656 $\pm$ 10 ns, showing the sensitivity of lifetime based techniques in detecting changes of the AuNC probes microenvironment. The localisation of these gold nanoparticles could be investigated through analysis of the fluorescence lifetimes. It was found AuNCs around the cell membrane were longer than those fully internalised by the cell (Figure 1.22).

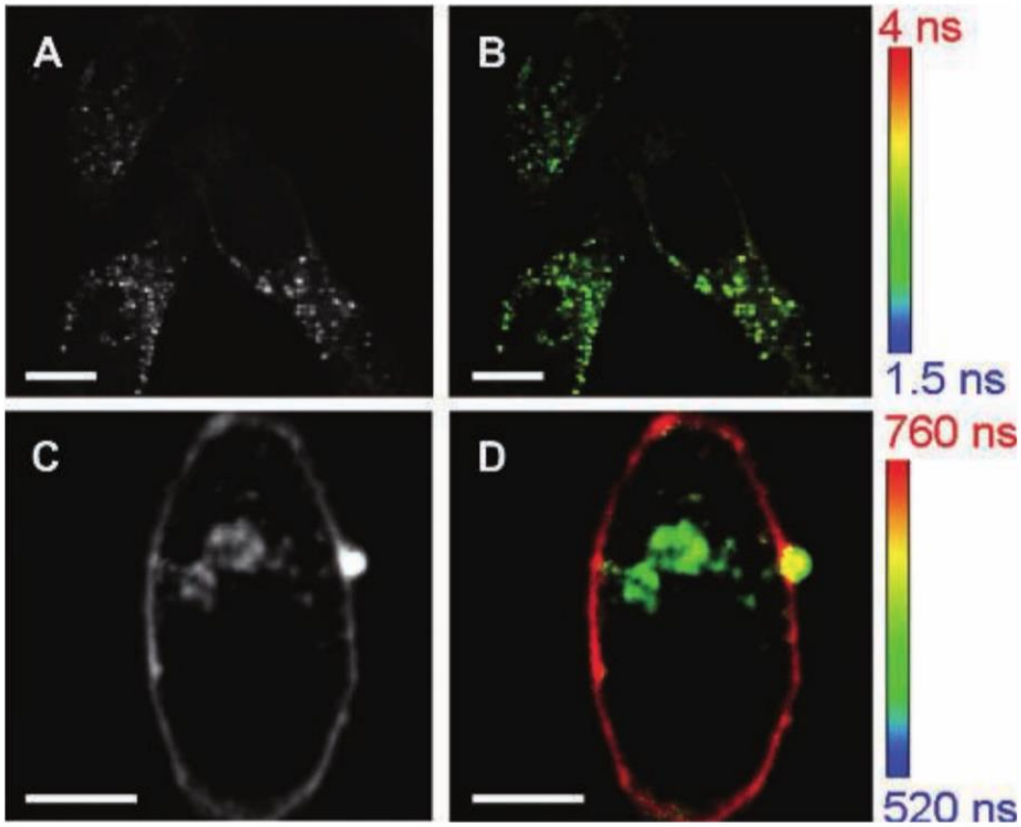

Figure 1.22. Intensity (A,C) and FLIM (B,D) images of cells only (A,B) and cells incubated with 100 μg/ML DHLA-AuNCs for 1 h (C,D). Scale bar: 10 μm.[128]

This showed that FLIM could be used to provide information on the localisation of these particles and identify change in the local environment. Since lifetime based imaging has shown to be extremely sensitive to changes in the local environment, Shang *et al.* developed lipoic acid capped AuNCs to identify temperature changes in HeLa cells, through detection of the gold fluorescence lifetime.[129] The results showed that an increase in temperature significantly reduced the fluorescence lifetime from 970 ns at 14 °C to 670 ns at 43 °C, showing the sensitivity of using lifetime based imaging techniques for probing the local environment (Figure 1.22).

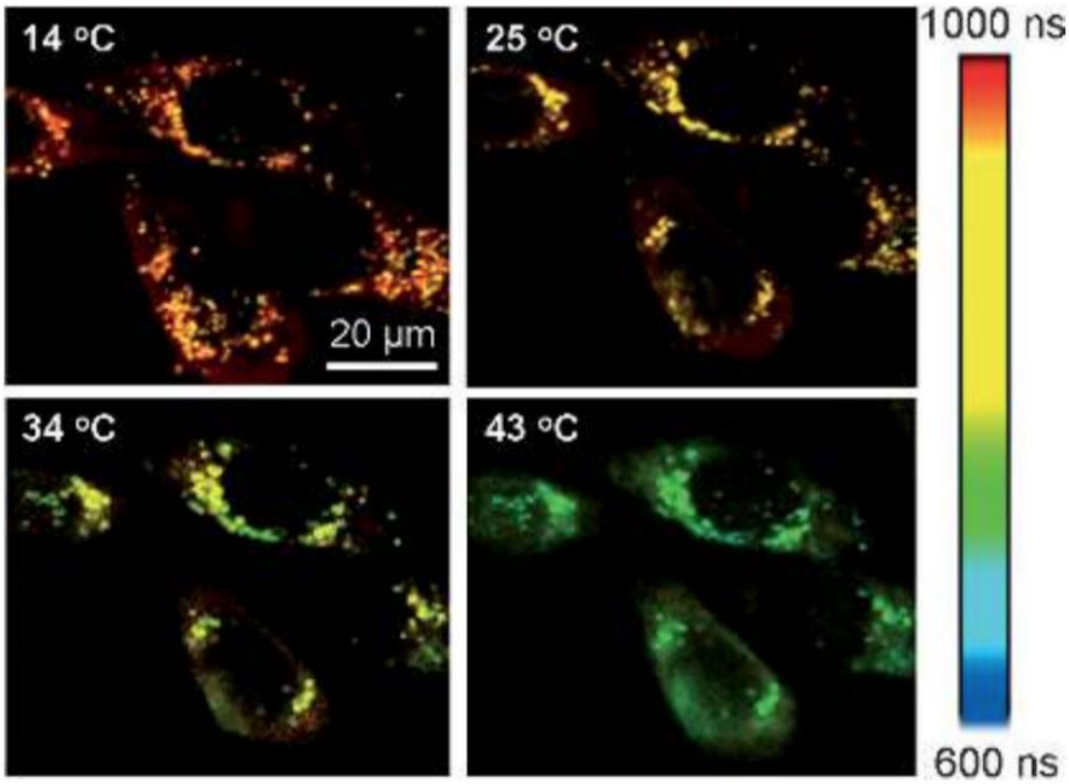

Figure 1.22. Typical FLIM image of HeLa cells with internalised AuNCs at four different temperatures.[129]

1. 3 Functionalised nanoprobes for lifetime imaging applications

As previously discussed, advantages of lifetime imaging over emission based methods include elimination of background autofluorescence, less photobleaching and reduced phototoxicity. Detecting the short lived lifetimes through FLIM still has its limitations as lifetime changes are often small and can overlap with cellular autofluorescence. Therefore, research has shifted onto looking at using phosphorescence lifetime probes which typically have long-lived lifetimes in the hundreds of nanoseconds to the microsecond range. These phosphorescent probes can be detected with complete elimination of background autofluorescence which typically has lifetimes ranging from picoseconds to nanoseconds. Transition metal complexes have often been employed

as lifetime imaging probes due to their favourable photophysical properties. They have long-lived lifetimes phosphorescence lifetimes ranging from microseconds to milliseconds making them ideal candidates for phosphorescence lifetime imaging (PLIM). Transition metals have desirable properties for imaging probes as they have shown to have tuneable emissions from the visible to near-infrared range, high luminescence quantum yields and are photostable. Additionally, their long phosphorescence lifetime can be sensitive to local environment, meaning these probes can be used for mapping, localisation and detection of biological molecules and systems (oxygens, H_2S, pH). Functionalising nanoprobes with transition metal complexes would allow for detection using phosphorescence lifetime imaging. Currently in the literature there are no examples of transition metal complexes being conjugated onto the surface of gold nanoparticles for phosphorescence lifetime imaging applications. There are examples of other types of nanoparticles utilising the long-lived phosphorescence lifetimes of iridium(III) complexes. These examples are present below. Yu *et al.* developed a dual emissive nanohybrid for ratiometric and luminescence lifetime imaging of intracellular hydrogen sulphide. The design consisted of a mesoporous silica nanoparticle (MSN) which was embedded with an iridium(III) complex and a specific merocyanine derivative which showed a unique dual emission (Figure 1.23).[130] This was the first example of lifetime-based imaging of H_2S in live cells using a functionalised nanoprobe.

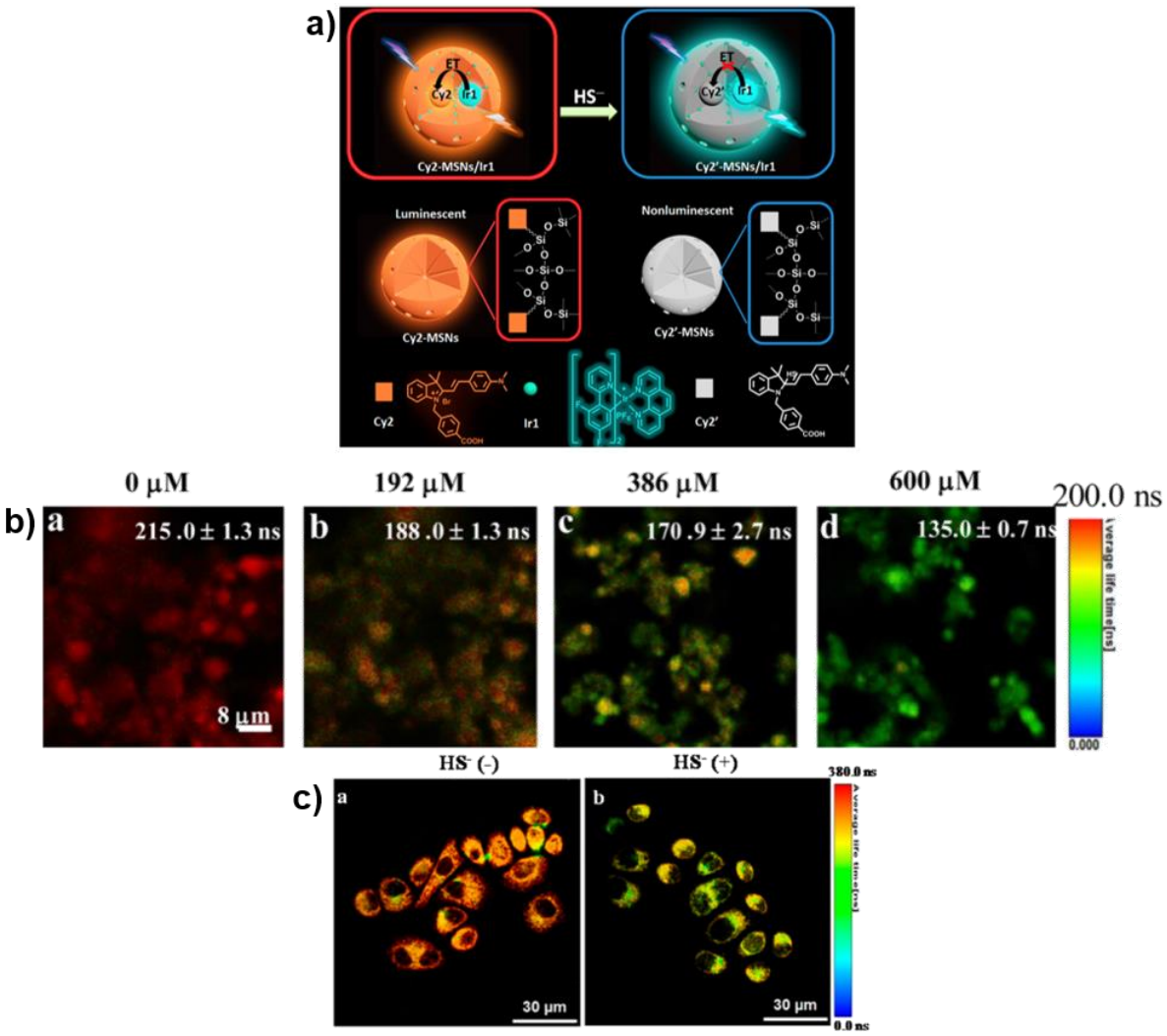

Figure 1.23. (a) Design and architecture of the nanohybrid for the detection of H_2S. (b) PLIM images (a – d) of 1 μg mL^{-1} Cy$_2$-MSNs/Ir1 in PBS (pH = 7.4) upon addition of different concentrations of HS$^-$. (c) PLIM images in live HepG2 cells co-stained by 10 μg mL^{-1} Cy$_2$-MSNs/Ir1 (a) and cells pre-treated with 10 μg mL^{-1} Cy$_2$-MSNs/Ir1 followed by incubation with HS$^-$ (600 μM) for 8 min (b). [130]

It was found that upon addition of HS$^-$ the lifetime of **Cy$_2$**-MSNs/**Ir1** decreased from 105 to 70 ns, whilst the phosphorescence lifetime of **Ir1** remained the same (307 ns). The average lifetime of **Cy$_2$**-MSNs/**Ir1** was found to be 215 ns and upon addition of NaHS the lifetime was reduced from 215 ± 1.3 ns to 135 ± 0.7 ns (Figure 1.23, b, a – d). Further analysis was carried out in live HepG2 cells to identify lifetime changes of the functionalised nanoprobe. It was found that the luminescence lifetime of **Cy$_2$**-

MSNs/**Ir1** detected within the cells was 414 ns, which was longer than in aqueous solution. Addition of HS^- (600 μM) was added to the media causing a decrease in luminescence lifetime to 366 ns, making this an ideal candidate for sensing and mapping HS^- concentrations *in vivo* (Figure 1.23, c).

Subsequently after this work, more research was carried out on developing nanoparticles which could be used for lifetime imaging with various applications. Zhang *et al.* developed a core-shell structured silica nanoparticle which contained two phosphorescent iridium(III) complexes which were immobilised in the inner solid core and the outer mesoporous layer of the nanoparticles respectively for the detection of exogenous and endogenous hypochlorite in live cells using ratiometric imaging and photoluminescence lifetime imaging microscopy.[131] The first iridium complex was prepared as a reference compound that was unreactive towards ClO^-, whereas the second iridium(III) complex was designed as the responsive compound as it was reactive towards ClO^-. The photophysical properties of the core-shell structured nanoparticles SiO_2@mSiO_2-**2** in aqueous solution showed strong phosphorescence for both complexes **1** and **2** and displayed phosphorescence lifetimes of 83 ns and 171 ns, respectively. It was found that the lifetime of complex **2** increased from 171 ns to 406 ns upon addition of ClO^-, and not surprisingly the luminescence lifetime of the unreactive compound **1** remained unchanged. This elongation of the luminescence lifetime shows high potential for the SiO_2@mSiO_2-**2** nanoprobe to be used as an intercellular sensing agent using PLIM microscopy. This was investigated in RAW 264.7 cells treated with SiO_2@mSiO_2-**2** for 2 hours at 37 °C and the detected luminescence lifetimes were recorded at around 31 ns (Figure 1.24, b).

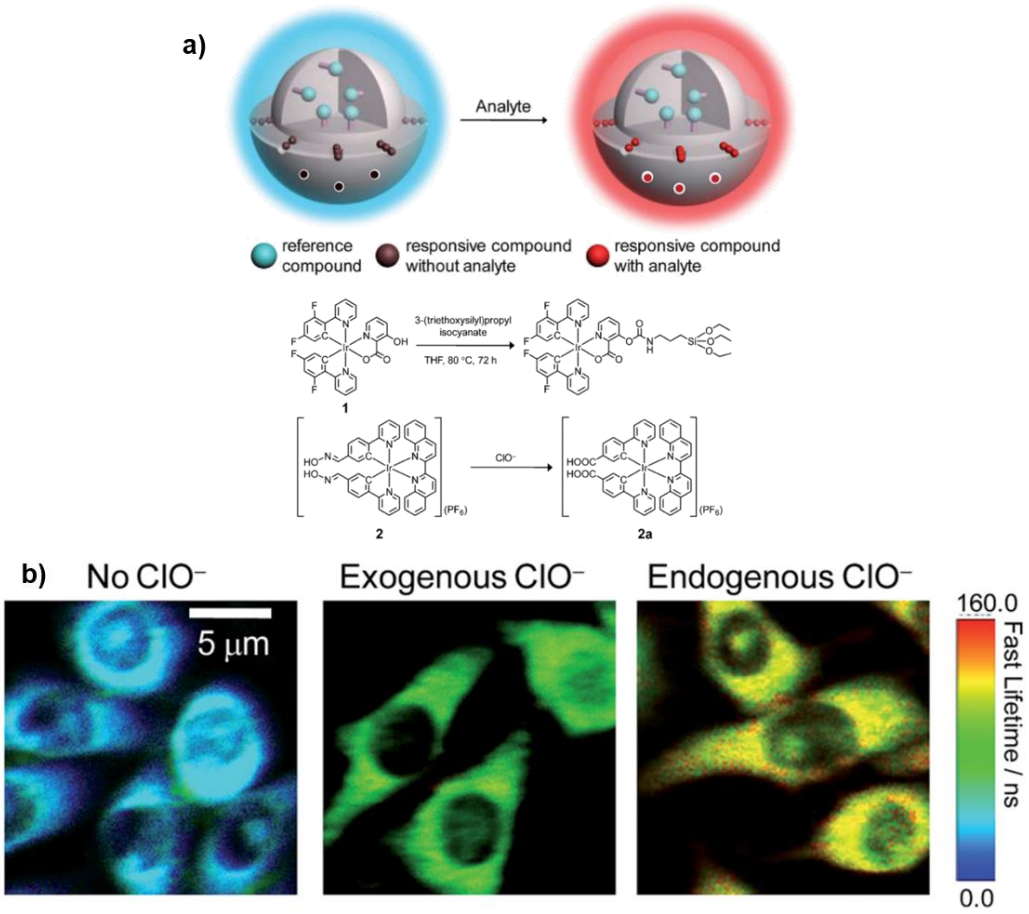

Figure 1.24. (a) (Top) Design concept of a ratiometric probe based on core-shell structured nanoparticles. (Bottom) Preparation of iridium(III) silane analogue from complex 1 and recognition mechanism of complex 2 towards ClO^-.). (b) PLIM images of RAW 264.7 cells treated with SiO_2@mSiO_2-2 (120 μg mL^{-1}) for 2 h at 37 °C (Left), followed by treatment with NaClO (50 μM) for 1 h (Middle), and RAW 264.7 cells stimulated with Lipopolysaccharide (LPS) and Phorbol 12-myristate 12-acetate (PMA) and incubated with SiO_2@mSiO_2-2 (120 μg mL^{-1}) for 2 h at 37 °C (right).[131]

Addition of NaClO (50 μM) for 1 hour caused an extension in luminescence lifetime from 31 ns to roughly 91 ns. The cells were then stimulated to cause activation of RAW 264.7 cells which saw a further extension in the luminescence of SiO_2@mSiO_2-**2** to 160 ns without any treatment with NaClO. This showed that endogenous ClO^- led to more conversion of complex **2** to **2a** compared to exogenous ClO^-. These results all showed that this novel core-shell structure nanoparticle can be used for the sensitive

detection of endogenous and exogenous ClO^- using phosphorescence lifetime imaging. Other nanoprobes based on mesoporous silica-coated core-shell upconverting nanoparticles (UCNPs) covalently have been functionalised with phosphorescent iridium(III) complex for applications in oxygen sensing. These nanoprobes showed sensitive luminescence lifetimes which increased when the environment changed from hypoxia into normoxia.[131] These examples show the power of using iridium(III) coated nanoparticles for lifetime imaging applications, through detection of long-lived luminescence lifetimes which can be used to probe the cellular microenvironment. Combining the advantages of nanotechnology with the desirable photophysical properties of transition metal complexes not only allows for detection through multiple imaging techniques, but these sensitive lifetimes can be used to map localisation of these nanoprobes, understanding their interactions with biomolecules or sensing chemical changes within cells.

1.4 Thesis outline

This thesis outlines the design of luminescent iridium(III) complexes for the attachment onto 13 nm, 25 nm and 100 nm gold nanoparticles to create novel multiphoton lifetime imaging probes. Chapter three describes the modification of a previously synthesised iridium(III) complex with a hexyl chain to enhance the multiphoton properties. The attachment of these iridium(III) complexes onto the surface of gold nanoparticles was optimised and characterised to investigate the multiphoton excitation and lifetime properties of these functionalised nanoprobes. Due to the success in designing an iridium(III) functionalised nanoprobes with long-lived luminescence lifetimes and high two-photon absorption cross-sections, Chapter four details the cellular applications of

these luminescent nanoprobes. Multiphoton lifetime imaging was used to map the localisation of these functionalised nanoprobes in cancer cells by detecting short-lived signal from the gold nanoparticles and the long-lived luminescence lifetimes if the iridium(III) complex. This novel research was done in collaboration with Professor Stanley Botchway and Dr Andy Ward (Rutherford Appleton Laboratory). Chapter 5 looks at further functionalising these iridium(III) coated nanoparticles with biomolecules for targeted delivery into cancer cells. This was achieved through the attachment of a monoclonal antibodies which selectively targets the tumour endothelial marker, CLEC14A as well as SiRNA complexes for gene silencing applications. Preliminary investigations were carried out to show uptake of these targeted nanoprobes into cancer cells which was detected by both fluorescence and phosphorescence lifetime imaging methods.

1. 5 References

1 M. J. Schnermann, *Nature* **2017**, *551*, 176-177.

2 F. L. Thorp-Greenwood, R. G. Balasingham and M. P. Coogan, *J. of. Organomet. Chem.* **2012**, *714*, 12-21.

3 T. Kowada, H. Maeda and K. Kikuchi, *Chem. Soc. Rev.* **2015**, *44*, 4953-72.

4 H. Zhu, J. Fan, J. Du and X. Peng, *Acc. Chem. Res.* **2016**, *49*, 2115-2126.

5 U. Resch-Genger, M. Grabolle, S. Cavaliere-Jaricot, R. Nitschke and T. Nann, *Nat. Methods.* **2008**, *5*, 763-75.

6 V. Fernandez-Moreira, F. L. Thorp-Greenwood and M. P. Coogan, *Chem. Commun.* **2010**, *46*, 186-202.

7 V. Fernandez-Moreira, F. L. Thorp-Greenwood and M. P. Coogan, *Chem. Commun. (Camb).* **2010**, *46*, 186-202.

8 A. Juris, V. Balzani, F. Barigelletti, S. Campagna, P. Belser and A. Von Zelewsky, *Coordin. Chem. Rev.* **1988**, *84*, 85-277.

9 C. Yang, F. Mehmood, T. L. Lam, S. L. Chan, Y. Wu, C. S. Yeung, X. Guan, K. Li, C. Y. Chung, C. Y. Zhou, T. Zou and C. M. Che, *Chem. Sci.* **2016**, *7*, 3123-3136.

10 K. K. W. Lo and K. Y. Zhang, *RSC. Adv.* **2012**, *2*, 12069-12083.

11 K. K. Lo, W. K. Hui, C. K. Chung, K. H. Tsang, D. C. M. Ng, N. Zhu and K. K. Cheung, *Coordin. Chem. Rev.* **2005**, *249*, 1434-1450.

12 K. C. Tang, K. L. Liu and I. C. Chen, *Chem. Phys. Lett.* **2004**, *386*, 437-441.

13 E. Baggaley, S. W. Botchway, J. W. Haycock, H. Morris, I. V. Sazanovich, J. A. G. Williams and J. A. Weinstein, *Chem. Sci.* **2014**, *5*, 879-886.

14 P. Sarder, D. Maji and S. Achilefu, *Bioconjugate. Chem.* **2015**, *26*, 963-974.

15 E. Baggaley, J. A. Weinstein and J. A. G. Williams, *Coordin. Chem. Rev.* **2012**, *256*, 1762-1785.

16 H. Szmacinski and J. R. Lakowicz, *Sensor. Actuat. B-Chem.* **1995**, *29*, 16-24.

17 V. Venkatesh, R. Berrocal-Martin, C. J. Wedge, I. Romero-Canelon, C. Sanchez-Cano, J. I. Song, J. P. C. Coverdale, P. Y. Zhang, G. J. Clarkson, A. Habtemariam, S. W. Magennis, R. J. Deeth and P. J. Sadler, *Chem. Sci* **2017**, *8*, 8271-8278.

18 J. Q. Wang, X. J. Hou, C. Z. Jin and H. Chao, *Chinese. J.Chem.* **2016**, *34*, 583-588.

19 S. Lin, L. H. Lu, J. B. Liu, C. F. Liu, T. S. Kang, C. Yang, C. H. Leung and D. L. Ma, *Bba-Gen. Subjects.* **2017**, *1861*, 1448-1454.

20 M. R. Gill and J. A. Thomas, *Chem. Soc. Rev.* **2012**, *41*, 3179-92.

21 Q. Zhao, C. H. Huang and F. Y. Li, *Chem. Soc. Rev.* **2011**, *40*, 2508-2524.

22 K. K. Lo, *Acc. Chem. Res.* **2015**, *48*, 2985-95.

23 T. Hofbeck and H. Yersin, *Inorg. Chem.* **2010**, *49*, 9290-9299.

24 A. F. Henwood and E. Zysman-Colman, *Chem. Commun.* **2017**, *53*, 807-826.

25 K. K. W. Lo and K. K. S. Tso, *Inorg. Chem. Front* **2015**, *2*, 510-524.

26 K.-W. K. Lo and K. Y. Zhang, *RSC. Advances.* **2012**, *2*, 12069-12083.

27 F. O. Garces, K. A. King and R. J. Watts, *Inorg. Chem.* **1988**, *27*, 3465-3471.

28 F. Neve, A. Crispini, S. Serroni, F. Loiseau and S. Campagna, *Inorg. Chem.* **2001**, *40*, 1093-101.

29 M. G. Colombo and H. U. Gudel, *Inorg. Chem.* **1993**, *32*, 3081-3087.

30 N. P. Ayala, C. M. Flynn, L. Sacksteder, J. N. Demas and B. A. DeGraff, *J. Am. Chem. Soc.* **1990**, *112*, 3837-3844.

31 M. Yu, Q. Zhao, L. Shi, F. Li, Z. Zhou, H. Yang, T. Yi and C. Huang, *Chem. Commun. (Camb)* **2008**, 2115-7.

32 J. S-Y. Lau, P-K. Lee, K. H-K. Tsang, C. H-C. Ng, Y-W. Lam, S-H. Chen and K. K. W. Lo, *Inorg. Chem.* **2009**, *48 (2)*, 708-718.

33 C. P. Leamon and P. S. Low, *Proc. Natl. Acad. Sci. U. S. A.* **1991**, *88*, 5572-6.

34 R. D. Klausner, J. Van Renswoude, G. Ashwell, C. Kempf, A. N. Schechter, A. Dean and K. R. Bridges, *J. Biol. Chem.* **1983**, *258*, 4715-24.

35 K. K-S Tso, K-K. Leung, H-W Liu, and K. K. Lo, *Chem. Comm.* **2012**, *0*, 1-3.

36 Y. Chen, L. Qiao, L. Ji and H. Chao, *Biomaterials.* **2014**, *35*, 2-13.

37 C. Jin, J. Liu, Y. Chen, G. Li, R. Guan, P. Zhang, L. Ji and H. Chao, *Dalton. Trans.* **2015**, *44*, 7538-47.

38 C. Li, M. Yu, Y. Sun, Y. Wu, C. Huang and F. Li, *J. Am. Chem. Soc.* **2011**, *133*, 11231-9.

39 W. R. Zipfel, R. M. Williams and W. W. Webb, *Nat. Biotechnol.* **2003**, *21*, 1368-1376.

40 S. S. Howard, A. Straub, N. G. Horton, D. Kobat and C. Xu, *Nat. Photonics.* **2013**, *7*, 33-37.

41 A. Ustione and D. W. Piston, *J. Microsc-Oxford.* **2011**, *243*, 221-226.

42 S. P. Chong, C. H. Wong, C. J. Sheppard and N. Chen, *Opt. Lett.* **2010**, *35*, 1804-6.

43 H. J. Cho, H. J. Chun, E. S. Kim and B. R. Cho, *World. J. Gastroentero.* **2011**, *17*, 4456-4460.

44 C. Soeller and M. B. Cannell, *Microsc. Res. Tech.* **1999**, *47*, 182-95.

45 T. G. Phan and A. Bullen, *Immunol. Cell. Biol.* **2010**, *88*, 438-44.

46 P. T. C. So, C. Y. Dong, B. R. Masters and K. M. Berland, *Annu. Rev. Biomed. Eng.* **2000**, *2*, 399-429.

47 G. S. He, L. S. Tan, Q. Zheng and P. N. Prasad, *Chem. Rev.* **2008**, *108*, 1245-1330.

48 J. F. Zhang, C. S. Lim, B. R. Cho and J. S. Kim, *Talanta.* **2010**, *83*, 658-62.

49 C. K. Koo, K. L. Wong, C. W. Man, Y. W. Lam, L. K. So, H. L. Tam, S. W. Tsao, K. W. Cheah, K. C. Lau, Y. Y. Yang, J. C. Chen and M. H. Lam, *Inorg. Chem.* **2009**, *48*, 872-8.

50 C. K. Koo, L. K. So, K. L. Wong, Y. M. Ho, Y. W. Lam, M. H. Lam, K. W. Cheah, C. C. Cheng and W. M. Kwok, *Chemistry.* **2010**, *16*, 3942-50.

51 P. Zhang, L. Pei, Y. Chen, W. Xu, Q. Lin, J. Wang, J. Wu, Y. Shen, L. Ji and H. Chao, *Chemistry.* **2013**, *19*, 15494-503.

52 W. Xu, J. Zuo, L. Wang, L. Ji and H. Chao, *Chem. Commun. (Camb)* **2014**, *50*, 2123-5.

53 L. S. Natrajan, A. Toulmin, A. Chew and S. W. Magennis, *Dalton. Trans.* **2010**, *39*, 10837-10846.

54 K. Y. Kim, R. T. Farley and K. S. Schanze, *J. Phys. Chem. B.* **2006**, *110*, 17302-4.

55 L. He, C. P. Tan, R. R. Ye, Y. Z. Zhao, Y. H. Liu, Q. Zhao, L. N. Ji and Z. W. Mao, *Angew. Chem. Int. Edit.* **2014**, *53*, 12137-12141.

56 F. O. Garces, K. A. King, C. A. Craig, P. J. Spellane and R. J. Watts, *Abstr. Pap. Am. Chem. S.* **1987**, *193*, 194-Inor.

57 M. S. Lowry and S. Bernhard, *Chem. Eur. J.* **2006**, *12*, 7970-7977.

58 J. Y. Jiang, C. Q. Zhang, W. P. Lin, Y. H. Liu, S. J. Liu, Y. J. Xu, Q. Zhao and W. Huang, *Macromol. Rapid. Comm.* **2015**, *36*, 640-646.

59 Y. P. Fan, D. C. Ding and D. H. Zhao, *Chem. Commun.* **2015**, *51*, 3446-3449.

60 R. M. Edkins, S. L. Bettington, A. E. Goeta and A. Beeby, *Dalton. Trans.* **2011**, *40*, 12765-12770.

61 C. Xu and W. W. Webb, *J. Opt. Soc. Am. B.* **1996**, *13*, 481-491.

62 C. L. Ho, K. L. Wong, H. K. Kong, Y. M. Ho, C. T. L. Chan, W. M. Kwok, K. S. Y. Leung, H. L. Tam, M. H. W. Lam, X. F. Ren, A. M. Ren, J. K. Feng and W. Y. Wong, *Chem. Commun.* **2012**, *48*, 2525-2527.

63 G. Y. Li, Q. Lin, L. L. Sun, C. S. Feng, P. Y. Zhang, B. L. Yu, Y. Chen, Y. Wen, H. Wang, L. N. Ji and H. Chao, *Biomaterials.* **2015**, *53*, 285-295.

64 J. T. Hou, K. Li, J. Yang, K. K. Yu, Y. X. Liao, Y. Z. Ran, Y. H. Liu, X. D. Zhou and X. Q. Yu, *Chem. Commun. (Camb).* **2015**, *51*, 6781-4.

65 P. Ning, J. Jiang, L. Li, S. Wang, H. Yu, Y. Feng, M. Zhu, B. Zhang, H. Yin, Q. Guo and X. Meng, *Biosens. Bioelectron.* **2016**, *77*, 921-7.

66 D. P. Li, Z. Y. Wang, X. J. Cao, J. Cui, X. Wang, H. Z. Cui, J. Y. Miao and B. X. Zhao, *Chem. Commun. (Camb).* **2016**, *52*, 2760-3.

67 C. Jin, J. Liu, Y. Chen, L. Zeng, R. Guan, C. Ouyang, L. Ji and H. Chao, *Chemistry.* **2015**, *21*, 12000-10.

68 J. Kuil, P. Steunenberg, P. T. Chin, J. Oldenburg, K. Jalink, A. H. Velders and F. W. van Leeuwen, *Chembiochem.* **2011**, *12*, 1897-903.

69 E. B. van Munster and T. W. J. Gadella, *Adv. Biochem. Eng. Biot.* **2005**, *95*, 143-175.

70 R. Ebrecht, C. D. Paul and F. S. Wouters, *Protoplasma.* **2014**, *251*, 293-305.

71 A. Byrne, C. S. Burke and T. E. Keyes, *Chem. Sci.* **2016**, *7*, 6551-6562.

72 S. W. Botchway, M. Charnley, J. W. Haycock, A. W. Parker, D. L. Rochester, J. A. Weinstein and J. A. G. Williams, *Proc. Natl. Acad. Sci. U.S.A* **2008**, *105*, 16071-16076.

73 L. Hao, Z. W. Li, D. Y. Zhang, L. He, W. Liu, J. Yang, C. P. Tan, L. N. Ji and Z. W. Mao, *Chem. Sci.* **2019**, *10*, 1285-1293.

74 A. V. Kuznetsov and R. Margreiter, *Int. J. Mol. Sci.* **2009**, *10*, 1911-29.

75 S. Salvioli, J. Dobrucki, L. Moretti, L. Troiano, M. G. Fernandez, M. Pinti, J. Pedrazzi, C. Franceschi and A. Cossarizza, *Cytometry.* **2000**, *40*, 189-97.

76 X. Zheng, H. Tang, C. Xie, J. Zhang, W. Wu and X. Jiang, *Angew. Chem. Int. Ed. Engl.* **2015**, *54*, 8094-9.

77 S. J. Zhang, M. Hosaka, T. Yoshihara, K. Negishi, Y. Iida, S. Tobita and T. Takeuchi, *Cancer. Res.* **2010**, *70*, 4490-4498.

78 C. Z. Jin, R. L. Guan, J. H. Wu, B. Yuan, L. L. Wang, J. J. Huang, H. Wang, L. N. Ji and H. Chao, *Chem. Commun.* **2017**, *53*, 10374-10377.

79 N. Erathodiyil and J. Y. Ying, *Acc. Chem. Res.* **2011**, *44*, 925-35.

80 D. E. Lee, H. Koo, I. C. Sun, J. H. Ryu, K. Kim and I. C. Kwon, *Chem. Soc. Rev.* **2012**, *41*, 2656-2672.

81 X. H. Huang and M. A. El-Sayed, *J. Adv. Res.* **2010**, *1*, 13-28.

82 M. Hu, J. Y. Chen, Z. Y. Li, L. Au, G. V. Hartland, X. D. Li, M. Marquez and Y. N. Xia, *Chem. Soc. Rev.* **2006**, *35*, 1084-1094.

83 E. C. Dreaden, A. M. Alkilany, X. H. Huang, C. J. Murphy and M. A. El-Sayed, *Chem. Soc. Rev.* **2012**, *41*, 2740-2779.

84 O. S. Wolfbeis, *Chem. Soc. Rev.* **2015**, *44*, 4743-4768.

85 A. M. Alkilany and C. J. Murphy, *J. Nanopart. Res.* **2010**, *12*, 2313-2333.

86 A. Albanese, P. S. Tang and W. C. W. Chan, *Annu. Rev. Biomed. Eng. Vol 14* **2012**, *14*, 1-16.

87 X. Huang, X. Teng, D. Chen, F. Tang and J. He, *Biomaterials.* **2010**, *31*, 438-48.

88 L. W. Zhang and N. A. Monteiro-Riviere, *Toxicol. Sci.* **2009**, *110*, 138-55.

89 S. Santra, D. Dutta, G. A. Walter and B. M. Moudgil, *Technol. Cancer. Res. Treat.* **2005**, *4*, 593-602.

90 X. He, K. Wang and Z. Cheng, *Wiley Interdiscip. Rev. Nanomed. Nanobiotechnol.* **2010**, *2*, 349-66.

91 N. Dinauer, S. Balthasar, C. Weber, J. Kreuter, K. Langer and H. von Briesen, *Biomaterials.* **2005**, *26*, 5898-906.

92 M. Arruebo, M. Valladares and A. Gonzalez-Fernandez, *J. Nanomater.* **2009**.

93 K. Cho, X. Wang, S. Nie, Z. G. Chen and D. M. Shin, *Clin. Cancer. Res.* **2008**, *14*, 1310-6.

94 S. A. A. Rizvi and A. M. Saleh, *Saudi. Pharm. J.* **2018**, *26*, 64-70.

95 Z. Alhalili, J. Shapter, D. Figueroa and B. Sanderson, *Drug. Deliv. Lett.* **2018**, *8*, 217-225.

96 L. Brannon-Peppas and J. O. Blanchette, *Adv. Drug. Deliv. Rev.* **2004**, *56*, 1649-59.

97 H. Gong, R. Peng and Z. Liu, *Adv. Drug. Deliv. Rev.* **2013**, *65*, 1951-63.

98 Z. Liu, S. Tabakman, K. Welsher and H. Dai, *Nano. Res.* **2009**, *2*, 85-120.

99 M. Martincic and G. Tobias, *Expert. Opin. Drug. Deliv.* **2015**, *12*, 563-81.

100 X. Y. Cheng, E. Hinde, D. M. Owen, S. B. Lowe, P. J. Reece, K. Gaus and J. J. Gooding, *Adv. Mater.* **2015**, *27*, 6144-6150.

101 X. Gao, Y. Cui, R. M. Levenson, L. W. Chung and S. Nie, *Nat. Biotechnol.* **2004**, *22*, 969-76.

102 N. A. Frey, S. Peng, K. Cheng and S. Sun, *Chem. Soc. Rev.* **2009**, *38*, 2532-42.

103 A. K. Gupta, C. Berry, M. Gupta and A. Curtis, *IEEE. Trans. Nanobioscience.* **2003**, *2*, 255-61.

104 N. J. Rogers in *The development of Gold Nanoparticles labelled with Transition Metal Complexes for Imaging Applications*, *Vol.* University of Birmingham, **2014**.

105 N. J. Rogers in *Development of Gold Nanoparticles labelled with Transition Metal Complexes for Imaging Applications*, *Vol. PhD* University of Birmingham, **2015**, p. 314.

106 C. R. Patra, R. Bhattacharya, D. Mukhopadhyay and P. Mukherjee, *Adv. Drug. Deliv. Rev.* **2010**, *62*, 346-361.

107 Y. Ding, Z. Jiang, K. Saha, C. S. Kim, S. T. Kim, R. F. Landis and V. M. Rotello, *Mol. Ther.* **2014**, *22*, 1075-1083.

108 Y. I. Park, K. T. Lee, Y. D. Suh and T. Hyeon, *Chem. Soc. Rev.* **2015**, *44*, 1302-1317.

109 H. Dong, L. D. Sun, W. Feng, Y. Y. Gu, F. Y. Li and C. H. Yan, *ACS. Nano.* **2017**, *11*, 3289-3297.

110 C. Molinaro, Y. El Harfouch, E. Palleau, F. Eloi, S. Marguet, L. Douillard, F. Charra and C. Fiorini-Debuisschertt, *J. Phys. Chem. C.* **2016**, *120*, 23136-23143.

111 K. L. Kelly, E. Coronado, L. L. Zhao and G. C. Schatz, *J. Phys. Chem. B.* **2003**, *107*, 668-677.

112 H. He, C. Xie and J. Ren, *Anal. Chem.* **2008**, *80*, 5951-7.

113 S. A. M. Osborne and Z. Pikramenou, *Faraday. Discuss.* **2015**, *185*, 219-231.

114 Z. Pikramenou, A. Davies, D. J. Lewis, S. Claire, N. J. Rogers, R. M. Harris, S. Farabi, I. B. Styles, S. P. Watson, S. G. Thomas and N. J. Hodges, *J. Biol. Inorg. Chem.* **2014**, *19*, S717-S718.

115 N. J. Rogers, S. Claire, R. M. Harris, S. Farabi, G. Zikeli, I. B. Styles, N. J. Hodges and Z. Pikramenou, *Chem. Commun.* **2014**, *50*, 617-619.

116 D. A. N in *Uptake, cellular fate and toxicity of engineered gold nanoparticles in A549 cells*, *Vol. PhD* University of Birmingham, University of Birmingham, **2017**, p. 203.

117 N. J. Rogers, H. C. Jeffery, S. Claire, D. J. Lewis, G. Zikeli, N. J. Hodges, S. Egginton, G. B. Nash and Z. Pikramenou, *Nanomedicine.* **2017**, *12*, 2725-2740.

118 M. B. Mohamed, V. Volkov, S. Link and M. A. El-Sayed, *Chem. Phys. Lett.* **2000**, *317*, 517-523.

119 S. W. Wang, W. Xi, F. H. Cai, X. Y. Zhao, Z. P. Xu, J. Qian and S. L. He, *Theranostics* **2015**, *5*, 251-266.

120 N. J. Durr, B. A. Holfeld, T. Larson, D. K. Smith, B. A. Korgel, K. Sokolova and A. Ben-Yakar, *Confocal, Multiphoton, and Nonlinear Microscopic Imaging Iii* **2007**, *6630*.

121 Y. Z. Shen, A. J. Shuhendler, D. J. Ye, J. J. Xu and H. Y. Chen, *Chem. Soc. Rev.* **2016**, *45*, 6725-6741.

122 Y. Chen, R. L. Guan, C. Zhang, J. J. Huang, L. N. Ji and H. Chao, *Coordin. Chem. Rev.* **2016**, *310*, 16-40.

123 N. J. Durr, B. A. Holfeld, T. Larson, D. K. Smith, B. A. Korgel, K. Sokolova and A. Ben-Yakar, *Plasmonics: Metallic Nanostructures and Their Optical Properties V* **2007**, *6641*.

124 H. F. Wang, T. B. Huff, D. A. Zweifel, W. He, P. S. Low, A. Wei and J. X. Cheng, *Proc. Natl. Acad. Sci. U.S.A* **2005**, *102*, 15752-15756.

125 C. M. Lemon, E. Karnas, X. X. Han, O. T. Bruns, T. J. Kempa, D. Fukumura, M. G. Bawendi, R. K. Jain, D. G. Duda and D. G. Nocera, *J. Am. Chem. Soc.* **2015**, *137*, 9832-9842.

126 Q. Liu, B. D. Guo, Z. Y. Rao, B. H. Zhang and J. R. Gong, *Nano. Lett.* **2013**, *13*, 2436-2441.

127 T. D. Rane and A. M. Armani, *PLoS. One.* **2016**, *11*, e0167548.

128 L. Shang, N. Azadfar, F. Stockmar, W. Send, V. Trouillet, M. Bruns, D. Gerthsen and G. U. Nienhaus, *Small.* **2011**, *7*, 2614-2620.

129 L. Shang, F. Stockmar, N. Azadfar and G. U. Nienhaus, *Angew. Chem. Int. Edit.* **2013**, *52*, 11154-11157.

130 Q. Yu, K. Y. Zhang, H. Liang, Q. Zhao, T. S. Yang, S. J. Liu, C. Q. Zhang, Z. J. Shi, W. J. Xu and W. Huang, *ACS. Appl. Mater. Interfaces* **2015**, *7*, 5462-5470.

131 K. Y. Zhang, J. Zhang, Y. H. Liu, S. J. Liu, P. L. Zhang, Q. Zhao, Y. Tang and W. Huang, *Chem. Sci.* **2015**, *6*, 301-307.

CHAPTER 2. GENERAL METHODS

2. 1 Materials

All chemicals, solvents and deuterated NMR solvents were purchased from Sigma Aldrich or Fisher unless stated otherwise. All reactions were done under a nitrogen atmosphere using a Schlenk line. Solvents were dried using 3Å molecular sieves under nitrogen.

2. 2 Techniques for Characterisation

2. 2. 1 NMR and Mass Spectrometry

^{1}H and ^{13}C NMR spectra were recorded on a Brüker AVIII300 and AVIII400 respectively. NMR spectra were processed using MestReNova. Electrospray mass spectroscopy was carried out on a Waters Micromass LCT- TOF mass spectrometer in a electrospray positive mode, using a nitrogen laser.

2. 2. 2 UV/Vis absorption spectroscopy

UV/Vis spectra were carried out on either a Varian Cary 50 or Cary 5000 spectrometer. UV-Vis spectra were collected at a 600 nm min^{-1} scan rate using a 1 cm path length quartz cuvette at room temperature. Baseline correction was carried out using a matching solvent in reference to the sample being analysed. Extinction coefficients were calculated using beer-lamberts law.

2. 2. 3 Steady-state and Time-resolved Spectroscopy

Emission and excitation spectra were recorded on Edinburgh Instruments FLS920 spectrometer fitted with a 450 W Xenon arc lamp as the illumination source. The detection source was an R928 visible Hamamatsu photomultiplier tube. The emission monochromator is fitted with a grating at 500 nm. 355 or 395 nm emission cut-off filters were used for all appropriate experiments. Edinburgh F900 software was used to record all data. 1 cm path length Quartz cuvettes were used for all experiments.

Quantum yield (ϕ) experiments were carried out using an integrated sphere attachment on Edinburgh Instruments FLS920 spectrometer. This method uses a reference standard measured against the sample (Equation 2.1) For the molecular probe in solution the reference standard was water (1% MeOH) measured against the sample, **IrbpySS** or **IrC_6** in water (1% MeOH). A different method is employed for the iridium functionalised gold nanoparticles. The reference standard was Z **•AuNPs** measured against the sample, IrbpySS **•AuNP** or IrC_6 **•AuNP**. The reference standard (Z **•AuNPs**) was at a higher concentration than the sample and was diluted to the same concentration. This was monitored by UV/Vis and was completed when the SPR peaks of both the reference standard and sample overlapped completely. (Figure 2.1).

$$\eta = \frac{E_s - E_r}{S_r - S_s}$$

Equation 2.1. Calculation for Quantum Yield (ϕ) experiments.

Spectral scans of the emission region (E), recorded from 450 – 700 nm and excitation scatter region (S), recorded from 365 – 385 nm of the sample (s) and reference standard or solvent (r).

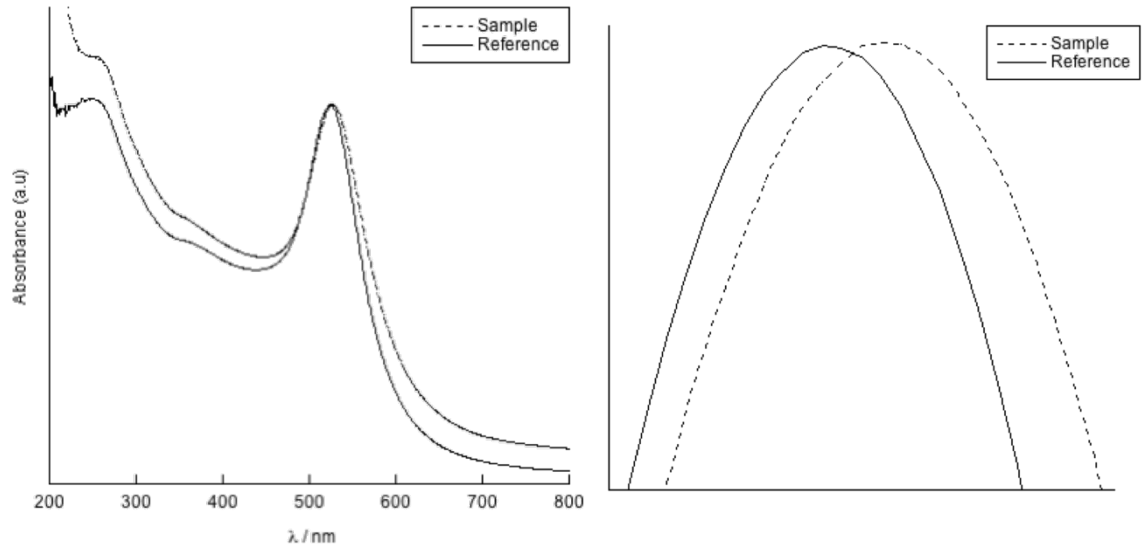

Figure 2.1. Absorption spectra of (left) sample, IrC_6 •AuNP25 (dotted line) and reference, Z •AuNP25 (solid line). (Right) Expanded region showing SPR overlap of sample and reference.

Luminescence lifetime (τ) experiments were carried out using an Edinburgh instruments EPL-376 nm picosecond pulsed diode laser as the excitation source. A time-correlated single-photon counting module on Edinburgh instruments was used to record data along with the R928 visible Hamamatsu photomultiplier tube. Lifetimes were fitted using Edinburgh Instruments FAST software. Luminescence lifetimes were fitted to three components unless stated otherwise with an error of $\pm$ 10 %. The luminescence lifetimes were fitted with a chi-squared (χ^2) value between 1 – 1.3.

2. 2. 4 Dynamic Light Scattering and Zeta Potentials

Dynamic light scattering (DLS) and Zeta potential measurements were acquired using a Malvern Zetasizer nano ZSP. Samples were recorded using a 1 cm disposable cuvette for size analysis and a folded capillary cell for zeta potential measurements. Samples were run using a standard operating procedure (SOP). For the SOP,

refractive index: 1.33, Absorption: 1.00, dispersant: water, temperature: 25 °C, cell: DTS0012 disposable cuvette (DLS) and folded capillary cell (Zeta Potentials). Instrument was left to equilibrate at 25 °C for 180 seconds before measurements were recorded. For DLS samples, 3 measurements were recorded containing 15 runs each, the average was then presented. For Zeta potential samples, 10 runs were recorded containing runs between 10 - 100, the average was then presented. Data was recorded and processed on the Malvern Zetasizer software. Polydispersity index is calculated from the equation below, where the standard deviation (σ) of the particle diameter is divided by the mean particle diameter.

$$PDI = \left(\frac{\sigma}{2a}\right)^2$$

2. 2. 5 Inductively Coupled Plasma Mass Spectrometry (ICP-MS)

ICP-MS was carried out at the chemistry department in the University of Warwick. ICP-MS data was recorded on a 7500cx ICPMS with an integrated auto-sampler (Agilent). For all samples the metal concentrations were determined using PlasmaCal calibration standards (QMX laboratories), with R^2 values >0.999 linear calibration curves. For all nanoparticle samples the solutions are digested in ultrapure aqua regia. Preparation of AuNPs for ICP-MS can be found in Chapter 3, Section **3.4.5.**

2. 3. Microscopy Techniques

2. 3. 1 Transmission Electron Microscopy (TEM)

TEM images were acquired on a JOEL 1200 EX transmission electron microscope, using a Gatan camera, at Materials and Metallurgy department at the University of

Birmingham. Samples were prepared on a 200-mesh formvar-coated copper grid (Agar Scientific). Images were acquired using Gatan software, but converted to TIFF files for analysis on ImageJ, Software version 1.49. Preparations of AuNPs for TEM can be found in Chapter 3, Section **3.4.4.**

2. 3. 2 Total Internal Reflectance Fluorescence Microscopy (TIRF)

Total internal reflection microscopy (TIRF) was constructed around an inverted Nikon Ti-U microscope. Fluorescence excitation was obtained from an Omicron laser hub containing a 405 nm, 488 nm and 561 nm continuous wave lasers and fibre coupled to the TIRF-M unit. The laser light was focused and collimated at the back aperture of a x100 oil immersion, NA 1.49 objective. Fluorescence emission was detected using an electron multiplying charged-coupled device (EMCCD, iXon, Andor) camera. Images were analysed as TIFF files in ImageJ software, version 1.49.

2. 3. 3 Fluorescence and Phosphorescence Lifetime Microscopy (FLIM/ PLIM)

Multiphoton excitation at 760 nm was used to acquire all images. The lifetime signals were detected by an adapted Becker & Hickl DCS120 laser scanning system coupled to a SPC150 time correlated single photon counting PCI card and a PMC-100 detector. The same card was also used to correlate the x,y pixel positions for the FLIM acquisition. The multichannel lifetime collection set up in the two windows was constructed around a Nikon Ti-E microscope. The multiphoton used a pulse modulated Titanium: Sapphire laser (Mira F-900, Coherent, UK) with 76 MHz repetition rate and 200 fs pulse. This was used to image live HeLa cells stained with IrC_6 •**AuNP**s. An water immersion x60 objective was used for all samples. Emission light was collected using a bandpass (BG39) filter. PLIM and FLIM data collected were analysed in

SPCImage (Becker & Hickl software, version 5.0). The data was fitted to an exponential decay model.

2. 3. 4 Confocal microscopy

Confocal microscopy was performed using a Leica TCS SP8 upright confocal laser scanning system using a 40x water immersion objective lens. Solid-state laser 405 nm with 26 % laser intensity was used. An AOBS spectral detector and gateable hybrid (Hy-D) PMT detector was used with the following ex/em ranges: λ_{exc} = 405 nm, λ_{em} = 550 - 800 nm for Iridium luminescence and λ_{exc} = 405 nm, λ_{em} = 425 - 475 nm for Hoechst acquisition. Z-stacks slice widths were performed as stated in the Iridium and Hoechst channel images. Processing and visualization of 3D images was performed by the image processing software FIJI (ImageJ Version 1.52b).

CHAPTER 3. DESIGN OF IRIDIUM(III) COMPLEXES FOR LABELLING GOLD NANOPARTICLES

3. 1 Introduction

Luminescent iridium(III) complexes are highly researched due to their rich photophysical properties such as intense emission in the visible range, long-lived luminescence lifetimes and high photostability.[1-3] The desirable photophysical properties of iridium(III) complexes not only makes them excellent candidates for cellular imaging but for uses in organic light-emitting diodes (OLEDs)[4, 5], dye-sensitised solar cells,[6, 7] and biosensing probes.[8, 9] These iridium(III) complexes can be functionalised with a range of ligands which can enhance their physical and chemical properties. These ligands can be synthesised to interact with biomolecules within cells, target specific cellular organelles or contain anticancer properties.[10-12] An increasing amount of iridium(III) complexes which are cationic or lipophilic have been designed for cellular imaging applications and have shown to be readily taken up into the cell and even localisation in specific regions of the cell.[11, 13-15] Kenneth Lo's group was the first to look at using cyclometalated iridium(III) complexes for luminescence imaging of biological substrates back in early 2000s.[16] Since then his group have developed a vast range of iridium(III) complexes for various biological imaging applications.[9, 17]

The lipophilicity of iridium(III) complexes is closely related to the efficient cellular uptake into cells.[18] Huang *et al.* increased the lipophilicity of iridium(III) complexes through fluorination of the C^N ligand and found this increased the uptake of these iridium(III) complexes into the cytoplasm of cells in comparison to their chloro counterparts (Figure 3.1).[19] Zwitterionic iridium(III) complexes [(Ir(N^C)$_2$(Hdcbpy)]

have also been studied for cellular uptake experiments and have shown to selectively stain the cytoplasm of KB cells. It was also found that the emission intensity detected within the cytoplasm increases as the lipophilicity of the iridium(III) complexes increases.[20]

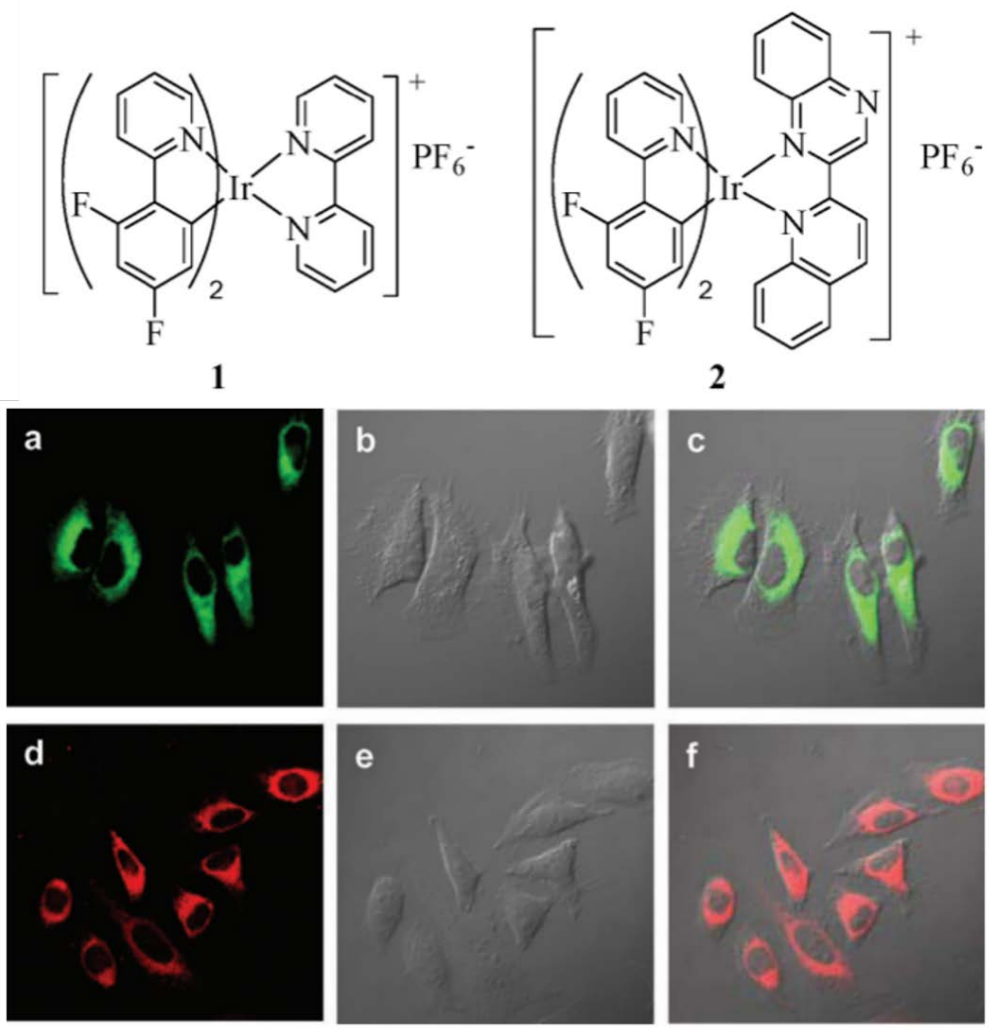

Figure 3.1. (Top) Chemical structure of iridium(III) complexes 1 and 2. (Bottom)(a and d) Confocal luminescence and (b and e) brightfield images of living HeLa cells incubated with 20 mM (a, b, c) 1 or (d, e, f) 2 in DMSO/PBS (pH 7, 1 : 49, v/v) for 10 min at 25 1C. Overlays of luminescence and brightfield images are shown in (c) and (f) for 1 or 2, respectively (λex = 405 nm).[20]

The lipophilicity of iridium(III) complexes has been investigated through functionalisation of different lengths alkyl chains onto the N^N ligand of iridium(III)

complexes.[21] The lipophilicity of the complexes is referred to as log $P_{o/w}$ ($P_{o/w}$ = n-octan-1-ol/water partition coefficient) which is determined by reverse-phase HPLC. The lipophilicity of iridium(III) complexes $[[Ir(N^C)2(Me\text{-}bpy\text{-}CONH\text{-}C_nH_{2n+1})]^+$ where n = 18, 10, 2, was found to be 8.79, 4.42 and 0.44 respectively. For the most part there was an increase in uptake as the iridium(III) complexes increased in lipophilicity, however the most lipophilic compound $[Ir(N^C)_2(Me\text{-}bpy\text{-}CONH\text{-}C_{18}H_{37})]^+$ showed the lowest amount of uptake into cancer cells, which was not expected. It was proposed that the higher molecular weight could hinder the probes ability to penetrate the cell membrane for uptake into cells. Secondly, the large alkyl chain on the ligand could cause the iridium(III) complex to undergo self-aggregation in cell media. Since this iridium(III) complex contained a very hydrophobic octadecyl chain, its interactions with serum binding proteins was examined and found to increase upon binding to human serum albumin (HSA). This means that these iridium(III) complexes not only display high uptake into cells and desirable photophysical properties, but the attachment of an alkyl chain opens up the possibility for these probes to be used as luminescent sensors for probing hydrophobic biological interactions within cells. This shows how important it is to carefully design these metal complexes for the appropriate biomedical application.

Over the past decade there has been increasing interest in using gold nanoparticles (AuNPs) for biomedical applications such as bioimaging, therapeutics, diagnostics and drug delivery due to their unique photophysical and chemical properties.[22, 23] Research has shown that the size, shape, morphology and surface profile can be easily modified to enhance biocompatibility and targeting abilities of these gold nanoparticles *in vitro* and *in vivo*.[24, 25] In addition, these gold nanoparticles have shown to be inert in a cellular environment and their high surface area allows for modification with various

ligands for targeting (antibodies, peptides and DNA) and drug delivery (doxorubicin[26, 27], siRNA). This was demonstrated by Firer *et al.* who showed that a peptide-drug conjugate could be attached to the surface of gold nanoparticles to enhance their chemotherapeutic efficiency within cells.[28] Since gold has a high electron density, imaging techniques such as electron microscopy can be used to visualise these functionalised nanoparticles in cells.[29, 30] However, these electron microscopy methods are often limited to fixed imaging over live cell imaging studies . Therefore, researchers have looked at attaching luminescent probes onto the surface of gold nanoparticles which further extends their uses in biomedical applications.

As previously discussed, these iridium(III) complexes have shown to be suitable for imaging applications with their desirable photophysical properties. The ligands can be functionalised to interact with targeting ligands Furthermore, the ligands can be modified for attachment onto the surface of gold nanoparticles. Conjugation of these luminescent iridium(III) complexes onto the surface of gold nanoparticles has shown to add desirable biological properties such as increased uptake efficiency, cellular distribution and aqueous solubility, making these nanoprobes extremely powerful for biomedical imaging applications. Furthermore, utilizing the chemical and photophysical properties gold nanoparticles and iridium(III) complexes together allows for multimodal detection of these nanoprobes within cells. Despite all the advantages of functionalising gold nanoparticles with iridium(III) complexes, there are very limited examples in the literature. Apart from our group, the only examples of iridium functionalised gold nanoparticles have been carried out by Mayer *et al.* Their first paper showed that bifunctional heteroleptic iridium(III) complexes could be used as a

reducing agent for tetrachloroauric acid and a capping agent for small sized gold nanoparticles (2 – 3 nm) (Figure 3.2).[31]

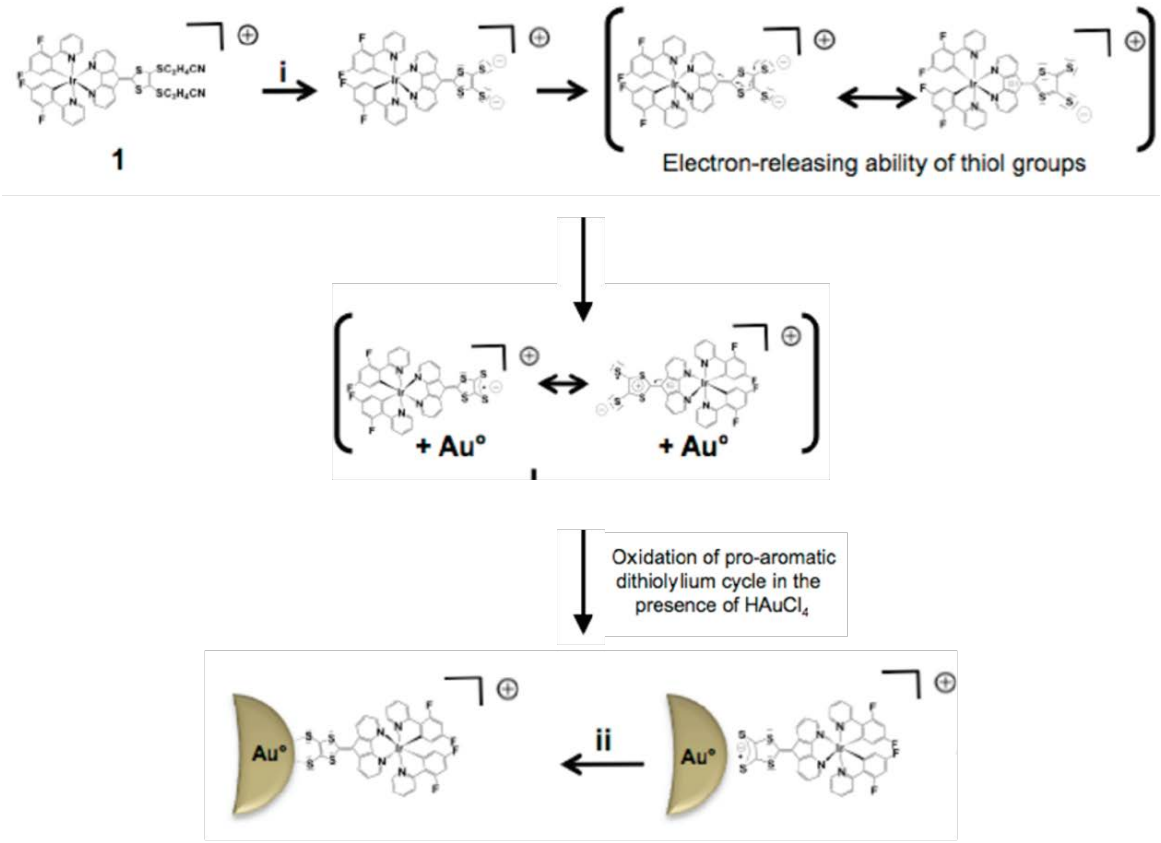

Figure 3.2. Mechanism of the reduction and capping process: (i) Deprotection in a basic medium; (ii) reduction by the reaction media.[31]

They found that the iridium(III) complex displayed strong luminescence with a λ_{max} at 537 nm, however no luminescence was observed upon conjugation of these complexes to the gold nanoparticle surface. It was proposed that the short distance between the iridium(III) complex and the gold surface caused quenching of the luminescence signal. Similar effects from quenching of gold has previously been observed on ruthenium functionalised gold nanoparticles.[32, 33] Since these nanoprobes displayed no luminescence, their applications as bioimaging probes were not explored. More recently, Mayer *et al.* synthesised iridium(III) complexes for functionalisation onto

gold and silver nanoparticles.[34] The iridium(III) complex was synthesised containing a modified 1,10-phenanthroline ligand with a pyridine end which is already known as a capping agent to stabilise metal nanoparticles (Figure 3.3).

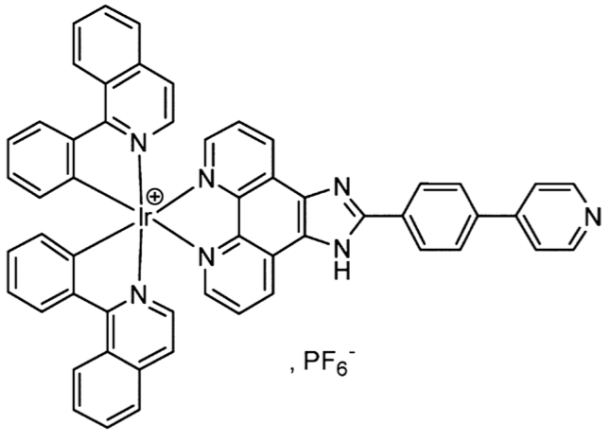

Figure 3.3. Structure of iridium(III) complex containing an anchoring group for conjugation onto gold nanoparticles.[34]

The iridium(III) complex was conjugated onto the surface of 5 – 6 nm gold nanoparticles by a ligand exchange reaction, at low concentrations to avoid particle aggregation. The results showed the first example of functionalising gold nanoparticles with iridium(III) complexes without loss of luminescence signal upon conjugation. This was shown through photophysical characterisations of both the iridium(III) complex in solution and iridium functionalised gold nanoparticles. It was found that upon excitation at 340 nm both **Ir2** and **NPAu-Ir2** were luminescent with an emission λ_{max} of 630 nm. However, there was a significant reduction in signal intensity upon conjugation of **Ir2** onto the gold surface. It was proposed that the spectral overlap between the SPR band of the gold (516 nm) and the luminescence of **Ir2** (λ_{max} =633 nm) was the cause of this substantial quenching of the luminescence signal.[34] Previous work from the Pikramenou group has shown iridium(III) complexes being synthesised for conjugation

onto larger, 100 nm sized particles and their applications for *in vivo* monitoring of blood flow explored (Figure 3.4).[35]

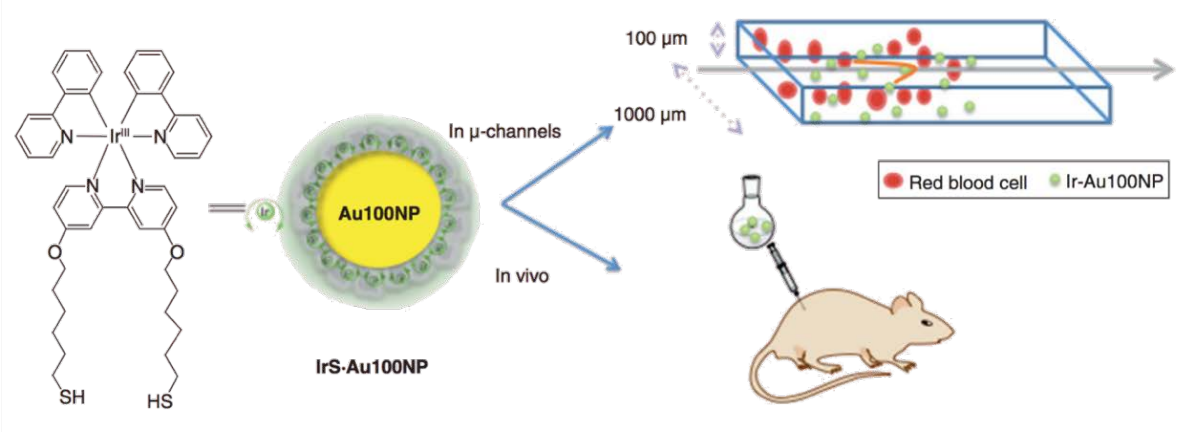

Figure 3.4. Luminescent iridium-coated gold nanoparticles for imaging blood flow in murine tissues.[35]

The results showed that luminescence signal from the iridium could be detected within vessels without any interference from cellular autofluorescence. Development of iridium(III) functionalised gold nanoparticles for bioimaging applications is still an emerging field. The aim of this thesis is to develop iridium(III) complexes that can be functionalised onto the surface of gold nanoparticles for their uses as multichannel luminescence lifetime imaging probes. Furthermore, a biorecognition molecule will be conjugated to gold nanoparticles alongside the iridium(III) complex allowing for both imaging and therapeutic applications.

3. 1. 1 Chapter Summary

This chapter will talk about the synthesis and photophysical characterisations of two iridium complexes and iridium functionalised nanoprobes. These iridium functionalised nanoprobes need to be fully characterised to identify their potential as two-photon lifetime imaging agents. Two iridium probes were synthesised for this work, the first

has previously been defined in the Pikramenou group and contains a bipyridine ligand with leg longs for attachment onto gold nanoparticles, **IrBpySS**. The second probe sees the modification of **IrBpySS** with a hexyl chain on the phenyl pyridine ligands, **IrC_6** (Figure 3.5). The incorporation of the hexyl chain was designed to increase hydrophobicity of the iridium complex which would increase the permeability across the cell membrane. These iridium probes were conjugated onto AuNPs and their single and two photon properties investigated for their use as bioimaging probes.

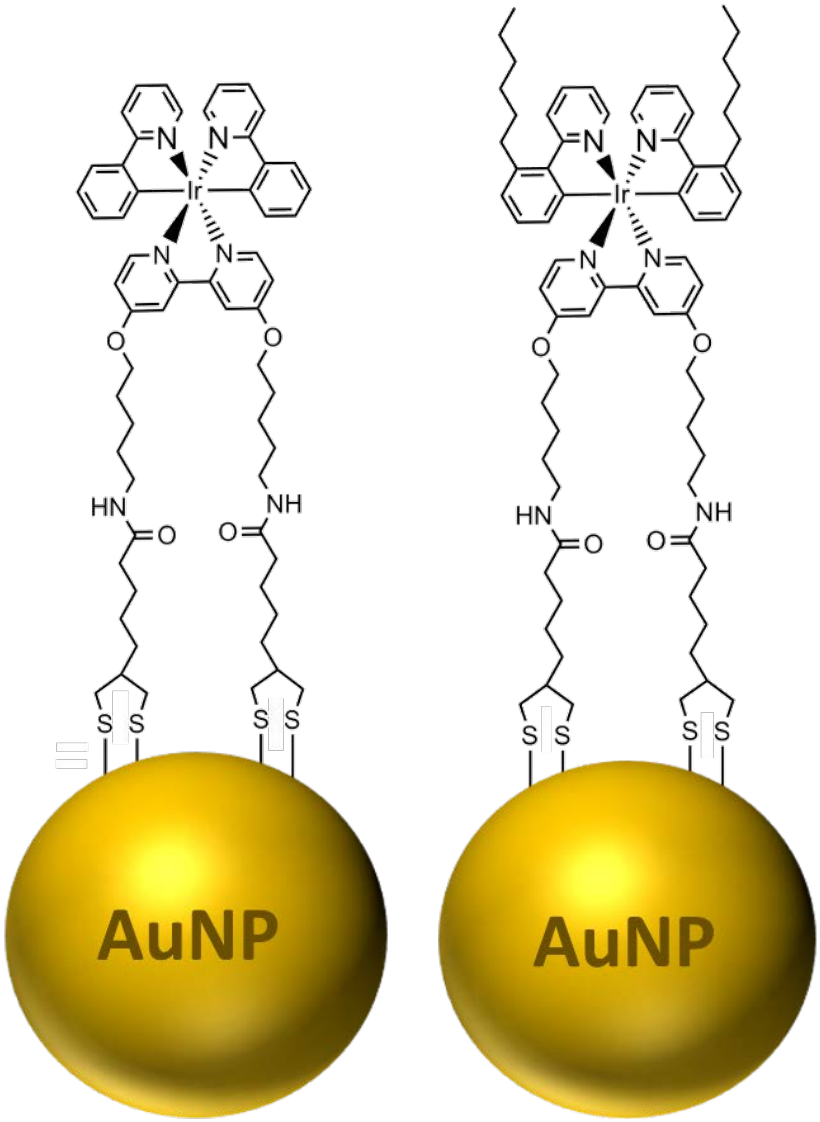

Figure 3.5. Schematic for the conjugation of IrBpySS (Left) and IrC_6 (Right) onto AuNPs.

3. 2 Results and Discussion

3. 2. 1 Cyclometalated iridium(III) complexes

3. 2. 1. 1 Synthesis

Two iridium complexes were synthesised for this work. The iridium complex, **IrBpySS** and the modified **IrC_6** were synthesised and fully characterised. Both the iridium complexes were conjugated onto AuNPs by methods previously established in the Pikramenou group[36, 37], these were then characterised and investigated as imaging probes. Both complexes contain the surface active bipyridine ligand with thiol active groups for the attachment onto gold nanoparticles. **IrC_6** contains a phenyl pyridine ligand which has been modified with a hexyl chain to increase the hydrophobicity of the complex. The iridium dimers, $[Ir(ppy)_2(\mu\text{-}Cl)]_2$ and $[Ir(ppy\text{-}C_6)_2(\mu\text{-}Cl)]_2$ were synthesised according to a method developed by Watts *et al.*[38] For **IrbpySS**, A mixture of iridium trichloride hydrate and 2-phenyl pyridine was refluxed in 2-ethoxyethanol and water, the precipitation was collected and fully characterised (Scheme 3.1). For **IrC_6**, the 2-phenylpyridine ligand was modified with a hexyl chain based on the method developed by Ackermann *et al.*[39] This involves the direct alkylation of 1-bromohexane onto the *ortho* C-H position on the 2-phenylpyridine. This ligand was then refluxed with Iridium trichloride hydrate in 2-ethoxyethanol and water. The precipitate was collected and fully characterised (Scheme 3.2).

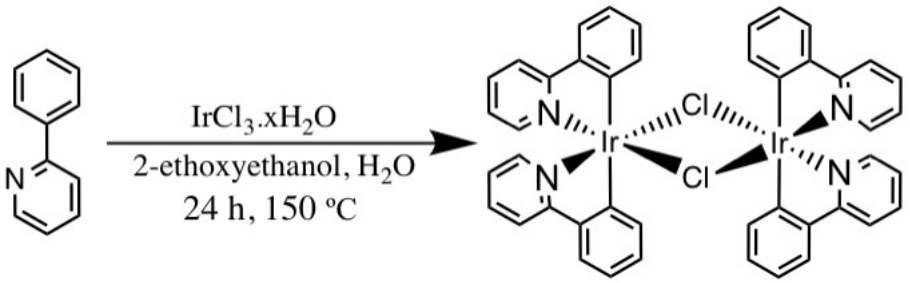

Scheme 3.1. Synthesis of $[Ir(ppy)_2(\mu\text{-}Cl)]_2$

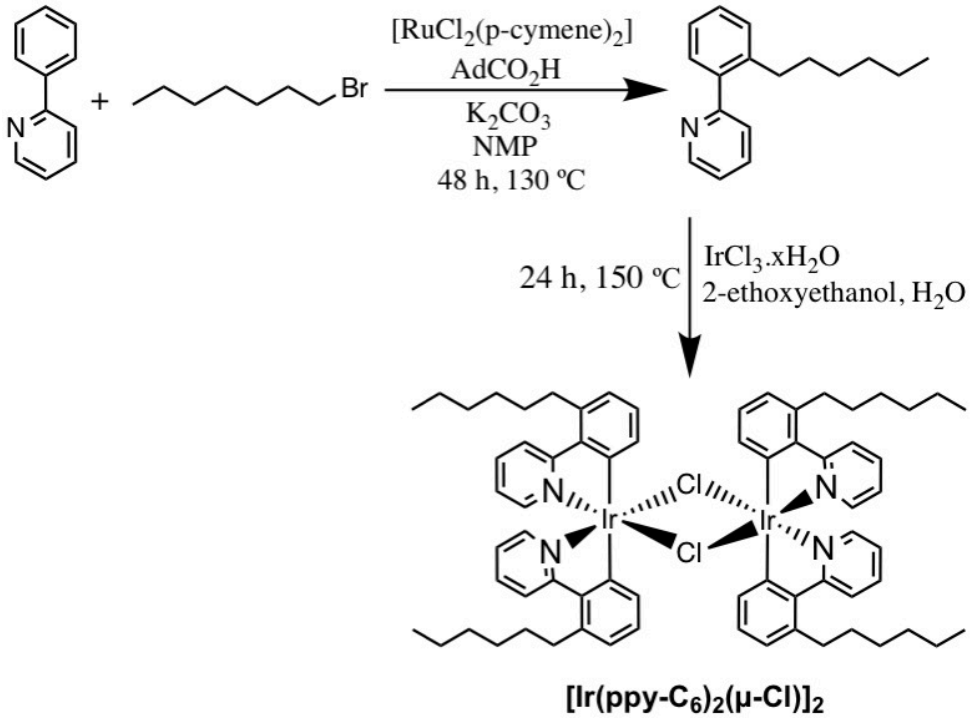

Scheme 3.2. Synthesis of $[Ir(ppy\text{-}C_6)_2(\mu\text{-}Cl)]_2$

The final iridium(III) complexes were synthesised by refluxing the iridium dimer with the bipyridine ligand in 2-ethoxyethanol and then precipitating the hexafluorophosphate salt out in water. The synthesis for **IrbpySS** and **IrC_6** can be seen in scheme 3.3 and 3.4 respectively, the synthesis for the bipyridine ligand can be found in the experimental section for this chapter. These iridium probes were fully characterised by ^{1}H and ^{13}C NMR and ESI^{+} MS (Appendix) and agree with previously

published work.[40].An ion exchange mechanism was carried out to convert the PF_6 counter ion to the chloride ion for increased solubility in water which is required for attachment onto nanoparticles.

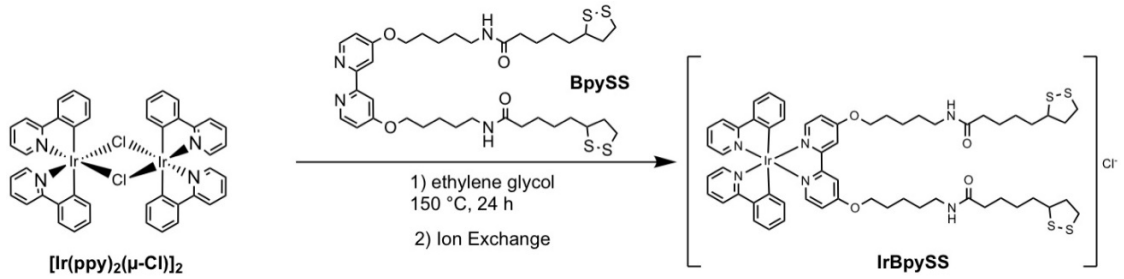

Scheme 3.3. Synthesis of IrBpySS

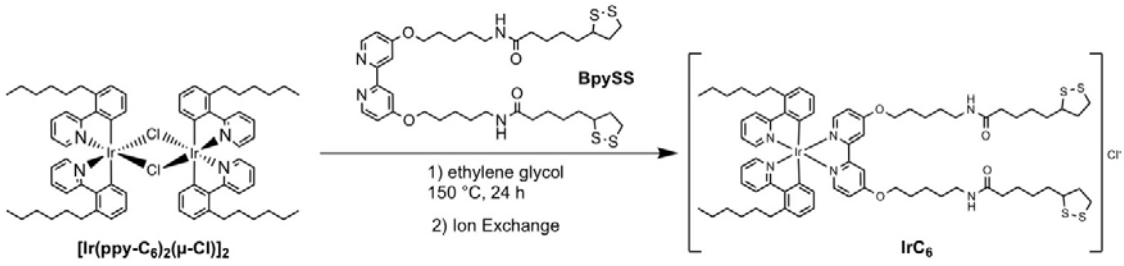

Scheme 3.4. Synthesis of IrC_6

3. 2. 1. 2 Photophysical Characterisation

The photophysical properties of the two iridium complexes have been studied in 1% MeOH in water and degassed MeOH for comparison. These probes have been designed for conjugation onto gold nanoparticles for their use as biological cellular imaging probes. Therefore, it is important to study the photophysical properties of these iridium complexes in conditions which are closely related to this application. After being converted to the chloride ion, the Iridium probes are made up to a concentration of 1 mM in Methanol. The absorption, steady state emission and excitation spectra of **IrC_6 and IrbpySS** was recorded in water (1% MeOH), at a concentration of 30 μM. Both the iridium complexes display similar photophysical

characteristics. The **IrC$_6$** complex absorbs in the UV-Vis region and exhibits intense bands at 230 nm and 260 nm arising from the spin allowed ^{1}LC (π-π*) transition of both the C^N and N^N ligands.[41, 42] The absorption profiles show a tail with shoulders at 300 nm and 350 nm with the profile extending into the visible range (450 nm) (Figure 3.6).

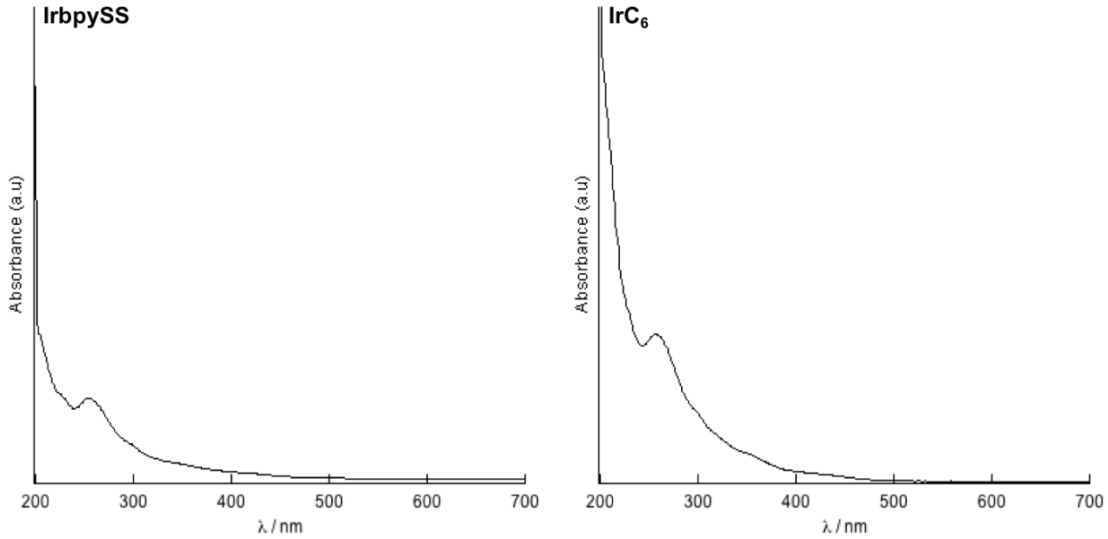

Figure 3.6. Absorbance spectra of 30 μm (left) IrbpySS and (right) IrC$_6$ in water (1% MeOH).

This is attributed to the spin allowed ^{1}MLCT transition state, which corresponds to previous assignments.[2] The absorption profiles for these iridium complexes are similar to the parent compound [Ir(ppy)$_2$bpy]$^+$ which has been extensively studied.[1, 43] Excitation of a solution of **IrbpySS** and **IrC$_6$** in water at 375 nm produced a broad peak emission spectra in the visible range of 400 – 750 nm. The luminescence spectra have a λ_{max} at 570 nm and 580 nm for **IrbpySS** and **IrC$_6$** respectively (Figure 3.7). This is attributed to the triplet charge transfer state which usually has contributions from ^{3}MLCT and ^{3}LMCT.[44-46] The iridium(III) complexes were found to display strong luminescence signal upon excitation at 375 nm and 405 nm (Appendix).

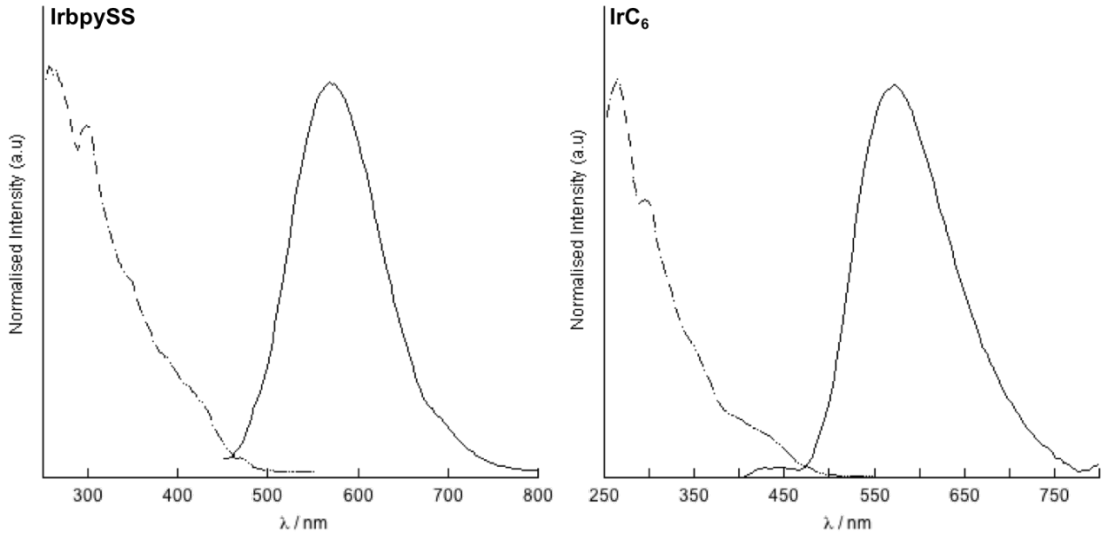

Figure 3.7. Photophysical characterisations of Iridium complexes in water. Excitation spectra (dotted line) λ_{em} = 570 nm and 580 nm for IrbpySS and IrC_6 respectively and luminescence spectra (solid line) of 30 μM (left) IrbpySS and (right) IrC_6 in water (1% MeOH). λ_{exc} = 375 nm. Spectra have been corrected for PMT and instrument response.

The excitation spectrum showed characteristics of the absorption spectra, revealing that excitation in the visible range up to 450 nm is possible to provide emission. This makes these iridium complexes suitable candidates for conventional light microscopy. The photophysical properties upon addition of a Zonyl FSA surfactant was investigated and it was found that a 5 nm and 10 nm bathochromic shift was observed in emission for **IrbpySS** and **IrC_6**, respectively (Figure 3.8). This differs from the effect of the Zonyl FSA surfactant on previously studied ruthenium complex (**RuS12**), where no significant shift was observed upon addition of the surfactant.[33] The shift is indicative of an interaction of the iridium probe with the Zonyl FSA surfactant, changing the environment around the iridium complex and affecting the charge transfer transitions. This is more predominant for **IrC_6** because the hydrophobic chain on the complex causes a greater interaction with the surfactant.

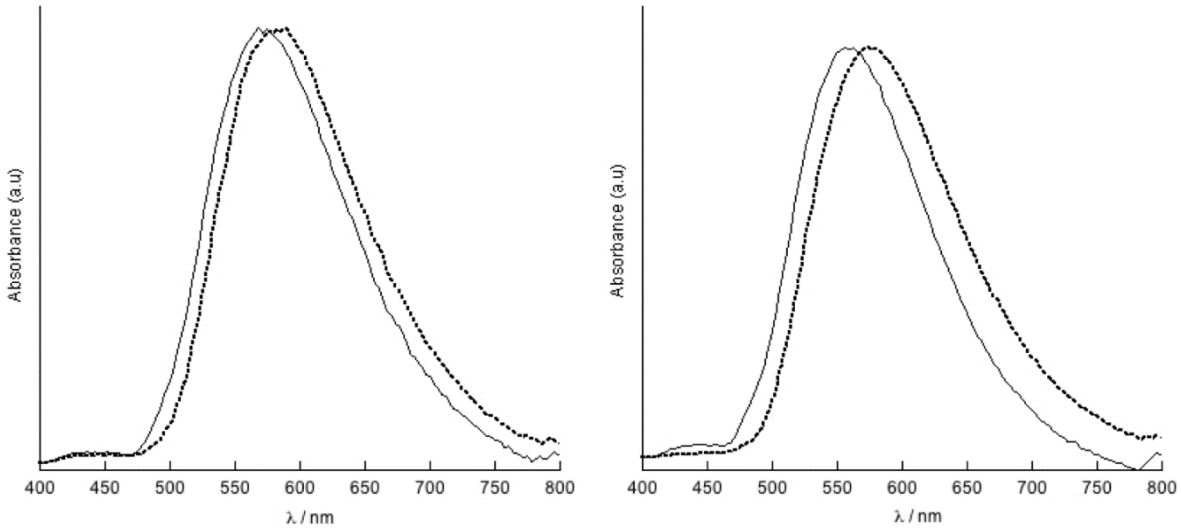

Figure 3.8. Luminescence spectra of (left) 30 μM IrbpySS (Right) 30 μM IrC_6 in water. The solid line represents the iridium complex in water and the dotted line is with 10 μL 10% Zonyl FSA. λ_{exc} = 350 nm. Spectra have been corrected for PMT and instrument response and normalised.

To further understand the effects of the Zonyl FSA surfactant on the photophysical properties of the iridium complexes, the luminescence lifetimes were analysed and both complexes were found to have 3 components in the lifetime fitting. The luminescence lifetimes for **IrbpySS** and **IrC_6** in water and with the addition of 10% Zonyl FSA can be found in Table 3.1.

Table 3.1. Lifetimes recorded for IrbpySS and IrC_6 in water and with the addition of Zonyl FSA surfactant (10% in water). Lifetimes were recorded using a 376 nm laser and were fitted with a χ^2 between 1 and 1.1.

	Lifetimes under different conditions (ns)	
	Water (1% MeOH)	10% Zonyl FSA
IrbpySS	30 (8%) 100 (33%) 310 (59%)	35 (1%) 140 (56%) 530 (44%)
IrC_6	40 (6%) 170 (45%) 430 (49%)	40 (3%) 150 (35%) 320 (62%)

Both Iridium complexes show a multi-exponential decay in the observed luminescence lifetime. The iridium complexes in water display long luminescence lifetimes in the nanosecond range. The data agrees with phenyl-pyridine iridium(III) complexes previously studied.[3, 47] **IrbpySS** has a lifetime of 310 ns and a luminescence quantum yield of 3 %. **IrC$_6$** showed a slightly longer luminescence lifetime of 430 ns and a luminescence quantum yield of 4 %. Upon addition of Zonyl surfactant (10% in water), **IrbpySS** shows an increase in luminescence lifetime by 71 % in comparison to the complex in water. This agrees with the results seen for **RuS12** where the luminescence lifetime increased from 280 ns to 350 ns, resulting in an increase of 25%. This increase was attributed to the surfactant interacting with the ruthenium complex and protecting it from ^{3}O quenching.[48] A similar effect is happening with **IrbpySS** where the iridium complex is being protected from the environment, increasing the luminescence lifetime. This affect is not seen for **IrC$_6$**, where the luminescence lifetime decreased by 26 % when compared to the free metal complex in water. Previous studies have shown that the luminescence properties of iridium complexes containing different length hydrophobic alkyl chains, were affected in the presence of different surfactants. It was found that the iridium complexes, based on the phenylpyridine ligand, containing hydrocarbon chain lengths of 18 and 10 (**IrC18** and **IrC10**, respectively) had long luminescence lifetimes of 390 ns (**IrC18**) and 210 ns (**IrC10**) in 1 % aqueous methanol, which agrees with the results for **IrC$_6$**. This is attributed to the polar medium causing the hydrocarbon chains to “wrap” around the complex cores resulting in a hydrophobic local environment. When these complexes were placed in the presence of a neutral surfactant, a red-shift in emission was seen along with a decrease in luminescence lifetime by 84 % for **IrC18** and 71 % for **IrC10**. It was reasoned that the surfactant then

caused “unwrapping” of the hydrophobic chains around the core, therefore reducing the hydrophobic local environment.[21]

To summarise, excitation of these iridium complexes at 375 nm leads to broad emission peak within the visible range. The emission comes from the triplet charge transfer state which usually has contributions from ^{3}MLCT and ^{3}LMCT. The luminescence lifetime recorded in 1 % aqueous methanol leads to long luminescence lifetimes of 310 ns and 430 ns for **IrbpySS** and **IrC$_6$**, respectively. When studying the effects of the Zonyl surfactant on the luminescence properties of these iridium complexes, it was found that the luminescence lifetime increased by 71 % for **IrbpySS** and decrease by 26 % for **IrC$_6$** in comparison to the metal complex in water. The quantum yields recorded were 3 % for **IrbpySS** and 4 % for **IrC$_6$**.

3. 2. 2 Gold Nanoparticles (AuNPs)

3. 2. 2. 1 Synthesis

Monodisperse 13 nm AuNPs (**AuNP13**) were synthesised following a previously published method, in which modifications were made.[49] This method synthesises colloidal gold nanoparticles following the reduction of tetrachloroauric acid ($HAuCl_4$) with trisodium citrate (Na_3Ct), a well-documented method which was first reported by Turkevich et al in 1951[50] and later refined by Frens in 1973[51]. This protocol has been extensively used over the past six decades and became known as the “Turkevich Synthesis”, which yields 15 nm spherical gold nanoparticles with a narrow size distribution. This method has been modified and optimised by numerous groups to create AuNPs in a wide range of sizes from 5 – 150 nm.[52, 53] Grabar *et al.*[54] modified the method to produce a large range of AuNP sizes which have showed to be stable

and non-toxic in water. The method shows the reduction of Au^{3+} → Au^{0} in water by adding sodium citrate to form 13 nm AuNP seeds at a high concentration (9 nM), labelled direct synthesis of AuNPs. This method was previously used in the Pikramenou group[55]; however, it was found that the AuNPs produced had a large size distribution and a low reproducibility. Therefore, a new method of gold nanoparticle synthesis was followed, known as the inverse Turkevich method, which has shown to drastically improve the size distribution and PDI in solution. In this method Au^{3+} salt is reduced by Na_3Ct, and the size of the nanoparticles is determined by the ratio of these reactants. The Au^{3+} salt is added into a mixture of citric acid and sodium citrate, which is the reverse order in comparison to the original Turkevich method[56]. It is identified that Na_3Ct has three important roles in the synthesis, (1) the reduction of Au(III) → Au(0), (2) citrate capping of the AuNPs (stabilising the AuNPs) and (3) pH mediator (modifies the reactivity of Au species in solution).[57] During the reaction sodium citrate oxidises to acetonedicarboxylate (ADC) which was found to be a kinetically faster reducing agent for $HAuCl_4$ than sodium citrate. ADC organises the gold ions into polymolecular complexes delivering a large local concentration of gold precursor which facilitates the reduction of Au^{3+} → Au^{0}. The formation of the ADC-Au^{+} complex selectively facilitates the disproportionation of AuCl → Au^{0} which accelerates the nucleation and growth to AuNPs[58] (Figure 3.9). This accelerated rate of reaction means a faster nucleation rate which in turn gives us the narrow size distribution.

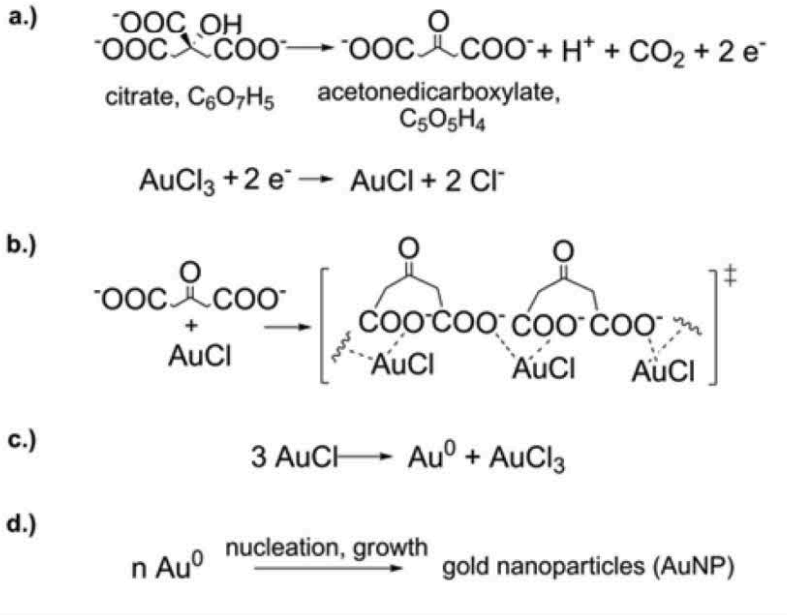

Figure 3.9. Mechanism of the Turkevich Synthesis showing (a) Redox reaction of citrate and the Au(III) precursor to yield Au(I) ions and acetonedicarboxylate (ADC). (b) Organisation of Au(I) ions in polymolecular complexes, (c) Disproportionation of Au(I) to Au(0) and Au(III) and (d) nucleation and growth of Au(0) to AuNPs.[49]

The actual growth mechanism of the gold nanoparticle synthesis is still poorly understood, with many different papers hypothesising different theories as to what is occurring. The reasoning being that there is limited *in situ* techniques that are able to follow the reactions that are occurring.[59] The summary of the growth mechanism proposed in the Turkevich method can be found below (Figure 3.10)

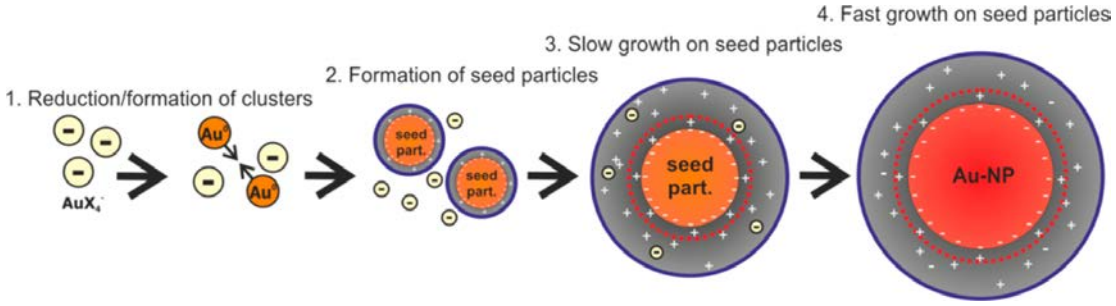

Figure 3.10. Summary of the growth mechanism used in the Turkevich method.[60]

There are four steps in the formation of AuNPs from the initial gold precursor. As discussed, the first step is the reduction of the gold salt from Au(III) → Au(0) which forms small clusters of the gold monomer. These clusters go on to form small seed particles (r <1.5 nm). The remaining gold ions are attracted to these seed particles and attach in the electronic double layer (EDL) causing further reduction. These then grow forming monodisperse, stable AuNPs in solution. Since this reaction is highly dependent of pH control, the rate of reaction was increased by lowering the pH, which increases the reactivity of Au^{3+}. This is done by creating a buffer solution of citric acid and sodium citrate.[60]

For this work, AuNPs were synthesised using the inversed Turkevich method producing monodisperse 1.53 nM **AuNP13**. EDTA was added to the reaction mixture and found to significantly improve the shape uniformity of the AuNPs.[49] Through this method, the produced AuNPs showed improved size distributions, better reproducibility and consistently low polydispersity indexes (PDI) of <0.15 in comparison to the previous method of synthesis. These **AuNP13** are then grown to produce **AuNP25** (0.65 nM), **AuNP50** (73 pM) and **AuNP100** (37 pM) stabilised with citrate anions, following a previously published protocol.[61] This seeded growth method allows for growth to larger sized gold nanoparticles whilst retaining their spherical shape (Figure 3.11). This method allows for high reproducibly with narrow size distributions and low PDIs of <0.1, forming mono-stable AuNPs in water.

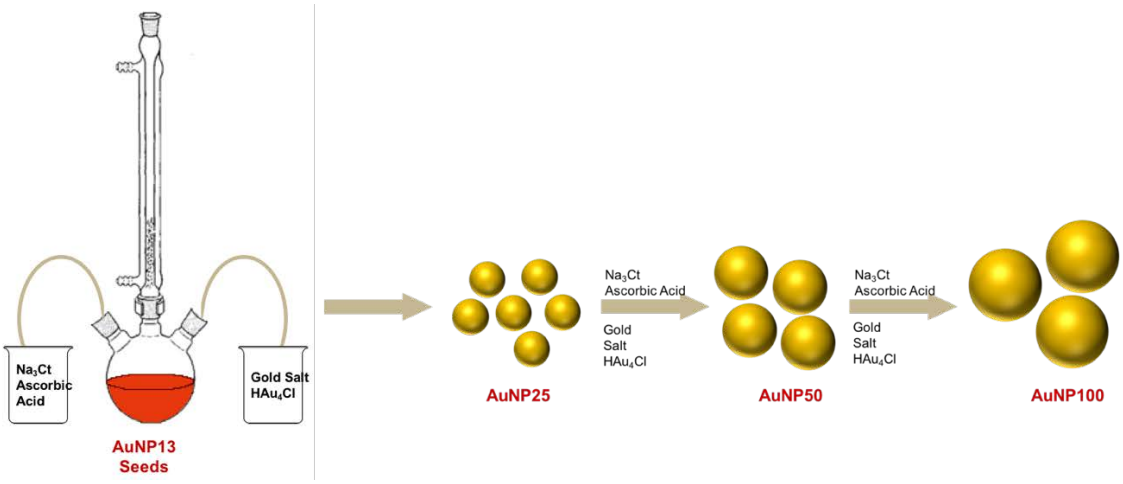

Figure 3.11. Seed mediated growth mechanism for AuNPs producing AuNP25 (0.65 nM), AuNP50 (73 pM) and AuNP100 (37 pM).

The **AuNPs** were then fully characterised by UV/Vis spectroscopy, dynamic light scattering (DLS), Zeta potential measurements and transmission electron microscopy (TEM).

3. 2. 2. 2 Nanoparticle characterisations

UV/Vis spectroscopy was used to measure the characteristic surface plasmon resonance (SPR) band of **AuNP13**, **AuNP25** and **AuNP100** in water which was found to have a λ_{max} (H_2O) at 517, 519 and 556 nm respectively (Figure 3.12). The SPR band is characteristic to the shape, size and morphology of gold nanoparticles and indicates particle aggregation and surface modification.[22, 62]

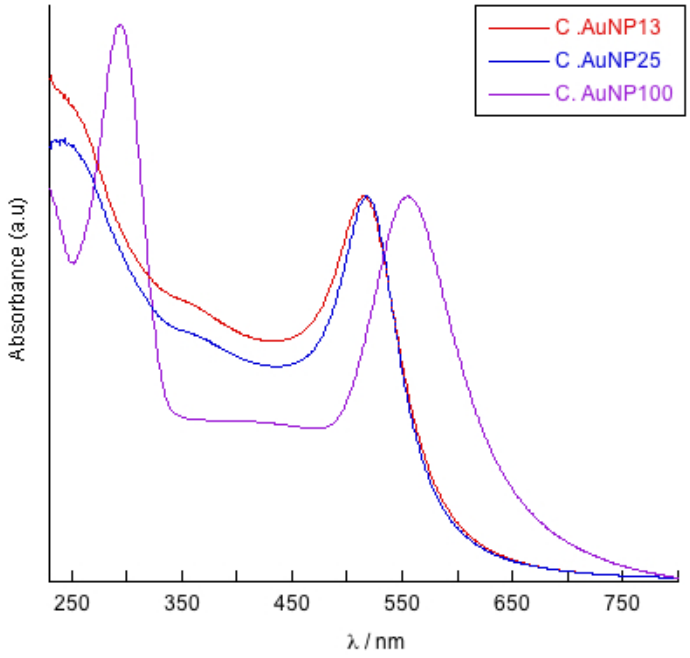

Figure 3.12. UV/Vis spectra of citrate stabilised nanoparticles in water.

AuNP13, **AuNP25** and **AuNP100** were sized by DLS and their number and intensity distributions reported (Table 3.2 and Figure 3.13). The intensity distribution measures the amount of scattered light from the particles, whereas number distribution is derived from the intensity distribution using Mie theory.[63] The particle scattering intensity is proportional to the square of the molecular weight, this means that any larger particles and aggregates present in the sample will dominate the distribution, causing the results to be weighted towards measuring larger particles. The number distribution is proportional to the intensity distribution, meaning that the presence of larger particles and aggregates in the sample will not be displayed in the number distribution, which provides a more accurate representation of particle size.[64, 65] The polydispersity Index (PDI) is the measure of the average uniformity of particles in a solution. If the PDI values are large, this indicates a large size distribution and can often be an indication

of particle aggregation. A PDI of less than 0.1 indicates that particles in solution are fully monodisperse.[66] The PDI calculations can be found in Chapter 2, Section 2.2.4.

Table 3.2. Dynamic Light Scattering (DLS) for AuNPs in water. Results displayed are Size by Number Distribution, Size by Intensity Distribution and Polydispersity Index (PDI).

	Number Distribution (nm)	Intensity Distribution (nm)	PDI
AuNP13	13 ± 3	19 ± 5	0.07
AuNP25	18 ± 5	27 ± 8	0.05
AuNP100	80 ± 20	101 ± 25	0.03

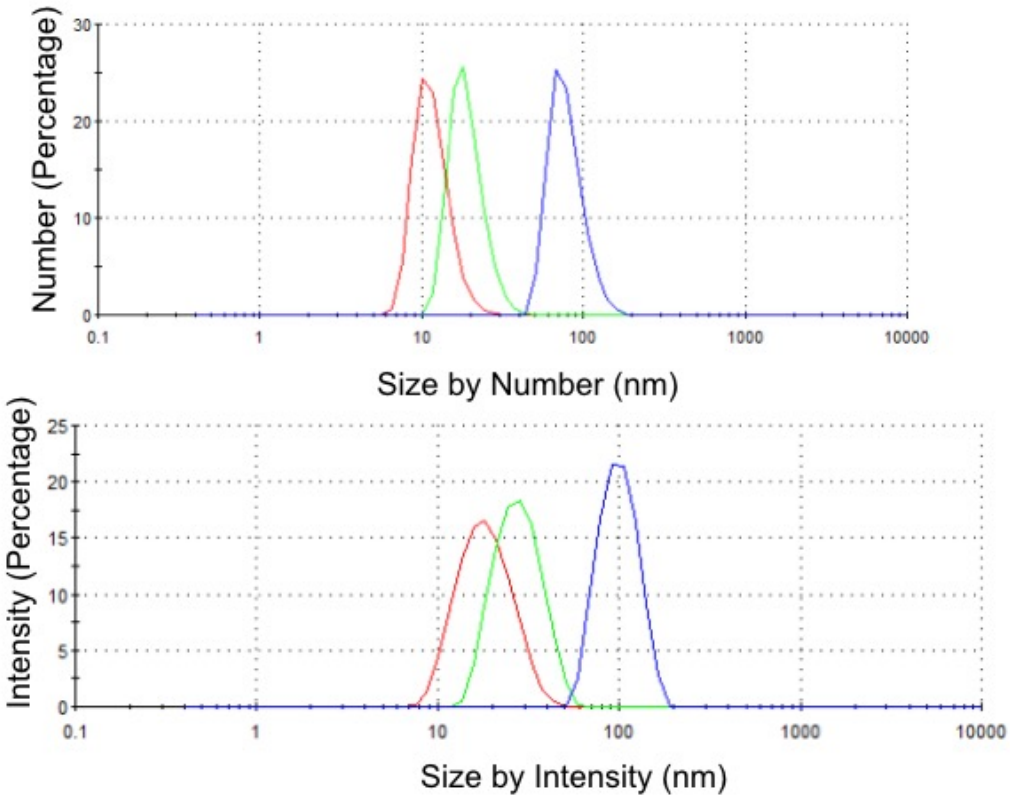

Figure 3.13. Dynamic Light Scattering (DLS) Data showing sizing by (Top) Number Distribution and (Bottom) Intensity Distribution. Results displayed are for AuNP13 (red), AuNP25 (green) and AuNP100 (Blue).

The nanoparticles were sized by Transmission Electron Microscopy (TEM). TEM images show sizes of 15 nm, 25 nm and 95 nm for **AuNP13**, **AuNP25** and **AuNP100** respectively (Figure 3.14). TEM images show highly uniform, spherical particles which is in good agreement with the DLS results, for all three nanoparticle sizes.

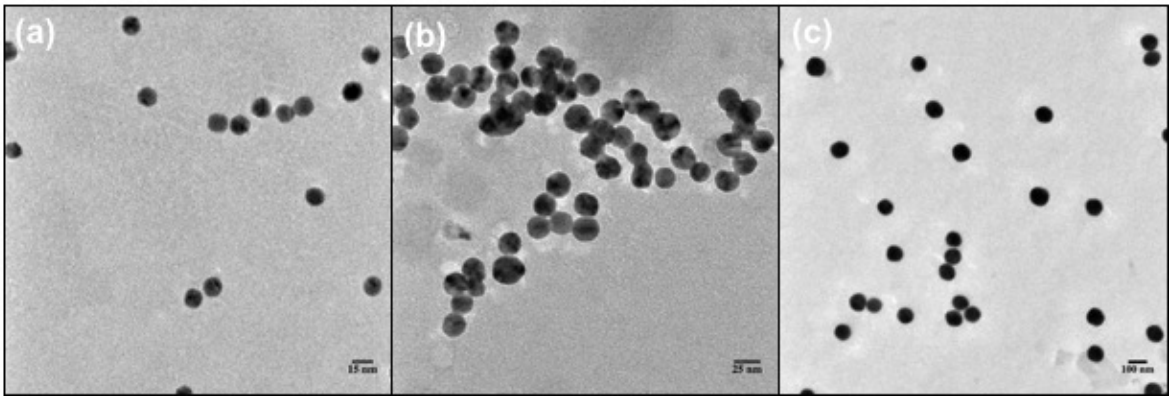

Figure 3.14. Transmission Electron Microscopy (TEM) images of (a) AuNP13, (b) AuNP25 and (c) AuNP100. Images were acquired on Joel 2100 EX TEM. Scale bars are 15 nm, 25 nm and 100 nm respectively.

Zeta-potentials is a measure of the stability of particles in solution. It is measured by sending an electric field through the sample to measure the electrostatic or charge repulsion/attraction between particles, which is the factors that affect stability of particles in solution. For colloidal nanoparticle systems Zeta-potential values of > ± 30 mV are classed as highly stable in solution.[67] The Zeta-potentials of the citrate coated nanoparticles were measured and found to be -33 ± 13 mV, -30 ± 12 mV and -33 ± 12 mV for **AuNP13**, **AuNP25** and **AuNP100** respectively (Figure 3.15). These results show highly stable nanoparticles in solution with an overall similar negative charge for all three sizes, which is to be expected due to the nanoparticles being capped with citrate ions.

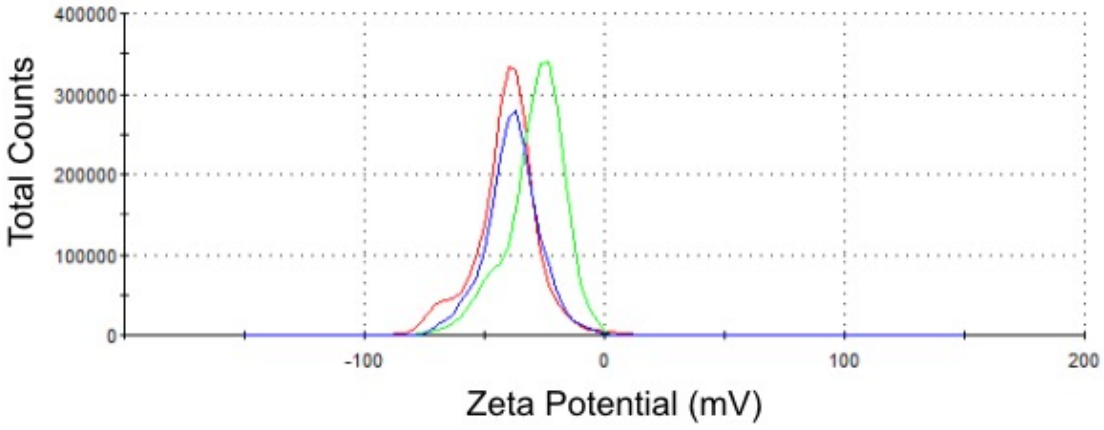

Figure 3.15. DLS data showing the absolute Zeta-Potential measurements for AuNP13 (red), AuNP25 (green) and AuNP100 (green) in water.

3. 2. 3 Iridium(III) functionalised gold nanoparticles

3. 2. 3.1 Synthesis and nanoparticle characterisations

The iridium complexes (**IrbpySS** and **IrC$_6$**) were conjugated onto gold nanoparticles by attachment of the thiol group on the bipyridine ligand onto the surface of the gold.[68-70] However, because the solution of citrate coated gold nanoparticles is negatively charged, addition of the iridium complexes which carry a positive charge of +2, would cause complete aggregation of the nanoparticles due to the loss of electrostatic repulsions which would destabilise the solution (Appendix). Therefore, prior to coating with the **IrbpySS** and **IrC$_6$** complexes, the nanoparticles were pre-coated with a fluorinated surfactant, Zonyl FSA (Scheme 3.5). The surfactant directly replaces the negative citrate ions on the gold surface which prevents the particles from aggregating. The Zonyl FSA surfactant has been shown to increase the stability and lipophilicity of gold nanoparticles in solution.[71, 72]

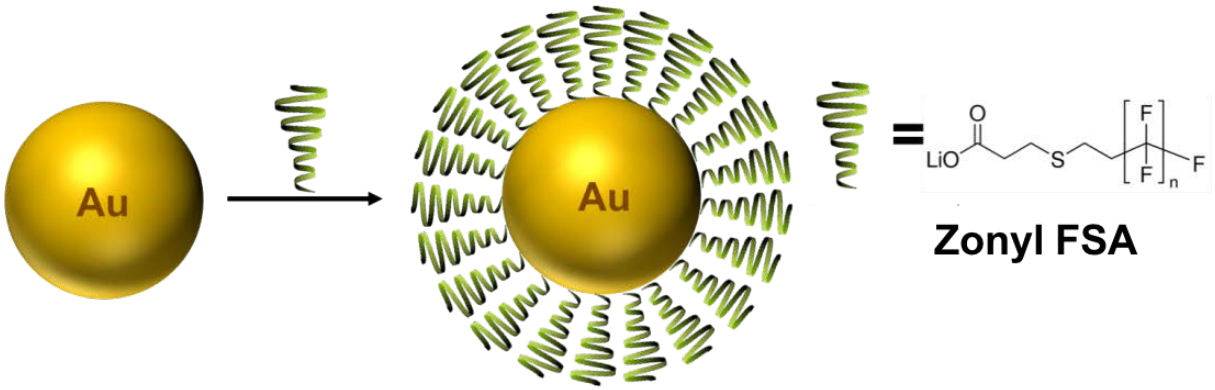

Scheme 3.5. Schematic for the procedure of coating AuNPs with the fluorinated surfactant (Zonyl FSA).

A change in the SPR provides information on changes to the surface, shape and size of the nanoparticles. When coating with surfactants and metal complexes the λ_{max} shift in absorption is monitored. This shift represents a change to the gold surface, which means that there been attachment onto the gold. Molecules which chemically bond to the surface of gold can be detected by the observed change they induce in electron density on the surface, which results in a shift in SPR λ_{max}.[73] Addition of Zonyl FSA (10 % in water) causes a shift in the surface plasmon resonance (SPR) by 2 nm, 3 nm and 1 nm making the recorded value 519 nm, 521 nm and 557 nm for **AuNP13**, **AuNP25** and **AuNP100** respectively. These particles are then isolated by centrifugation to give Z •**AuNP13**, Z •**AuNP25** and Z •**AuNP100**. These particles were sized to ensure no aggregation had occurred upon addition of the surfactant, the results can be seen below (Table 3.3, Figure 3.16). The results show an increase in size and PDI in comparison to citrate **AuNPs**, which confirms the presence of Zonyl FSA to the surface of the nanoparticles.

Table 3.3. Dynamic Light Scattering (DLS) for AuNPs in water. Results displayed are Size by Number Distribution, Size by Intensity Distribution and Polydispersity Index (PDI).

	Number Distribution (nm)	Intensity Distribution (nm)	PDI
Z •**AuNP13**	17 ± 4	26 ± 8	0.24
Z •**AuNP25**	22 ± 6	38 ± 18	0.14
Z •**AuNP100**	87 ± 21	107 ± 24	0.02

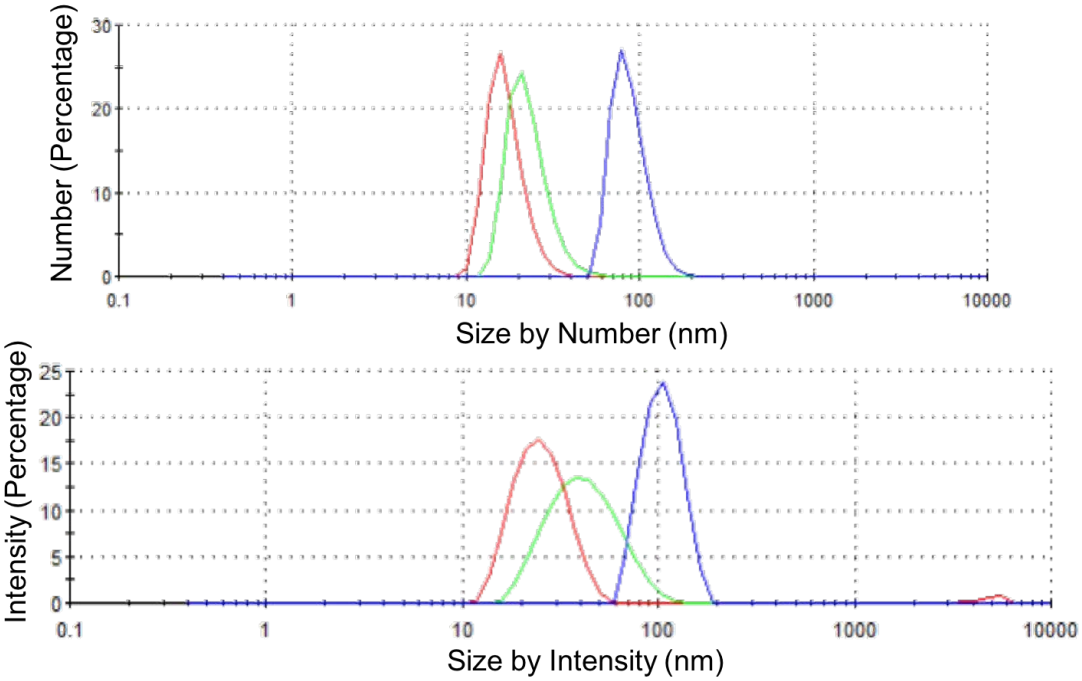

Figure 3.16. Dynamic Light Scattering (DLS) data showing sizing by (Top) Number Distribution and (Bottom) Intensity Distribution. Results displayed are for Z •AuNP13 (red), Z •AuNP25 (green) and Z •AuNP100 (Blue).

Zeta-potentials were measured and found to be -66 ± 21 mV, -56 ± 13 mV and -68 ±16 mV for Z •**AuNP13**, Z •**AuNP25** and Z •**AuNP100** respectively (Figure 3.17). The results show an increase in negative potential compared to the citrate stabilised nanoparticles, increasing the stability of the nanoparticles in solution.

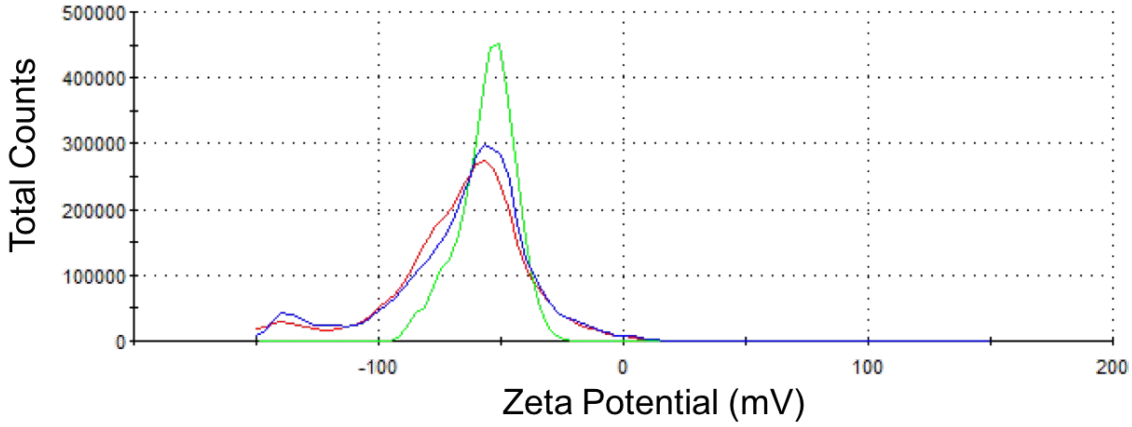

Figure 3.17. DLS data showing the absolute Zeta-Potential measurements for Z •AuNP13 (red), Z •AuNP25 (green) and Z •AuNP100 (Blue).

The iridium complexes (**IrbpySS** and **IrC$_6$**) were then added to the colloid suspension of gold nanoparticles (Scheme 3.6). Gold nanoparticles were concentrated from their stock solutions to the concentrations stated below for the coating protocol.

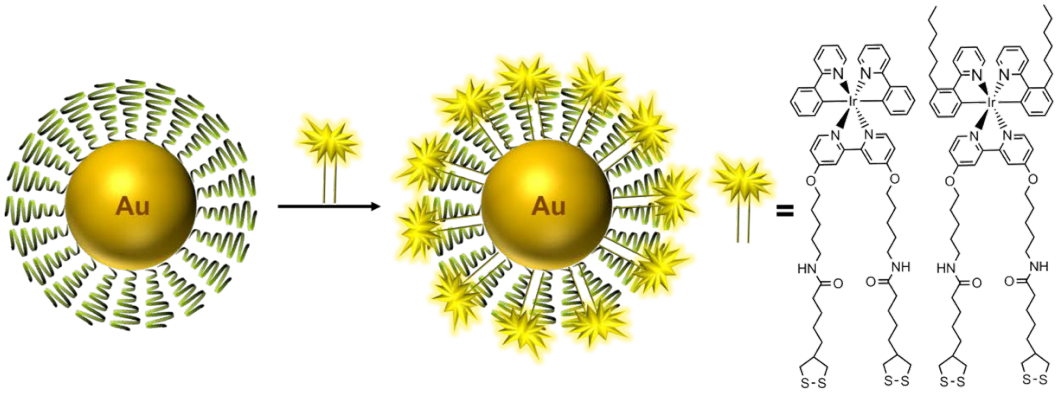

Scheme 3.6. Schematic for the procedure of coating Z •AuNPs with Iridium complexes.

A solution of **IrbpySS** and **IrC$_6$** in MeOH (1 mM) was titrated in 5 μL and 2.5 μL aliquots, for **IrbpySS** and **IrC$_6$** respectively, into an aqueous solution of 4.5 nM for Z **•AuNP13** (1 mL) and the SPR shift monitored within the visible region (Figure 3.18). The shift in SPR shows a modification on the gold surfaces and allows us to identify the full saturation of the gold surface with the iridium complexes.

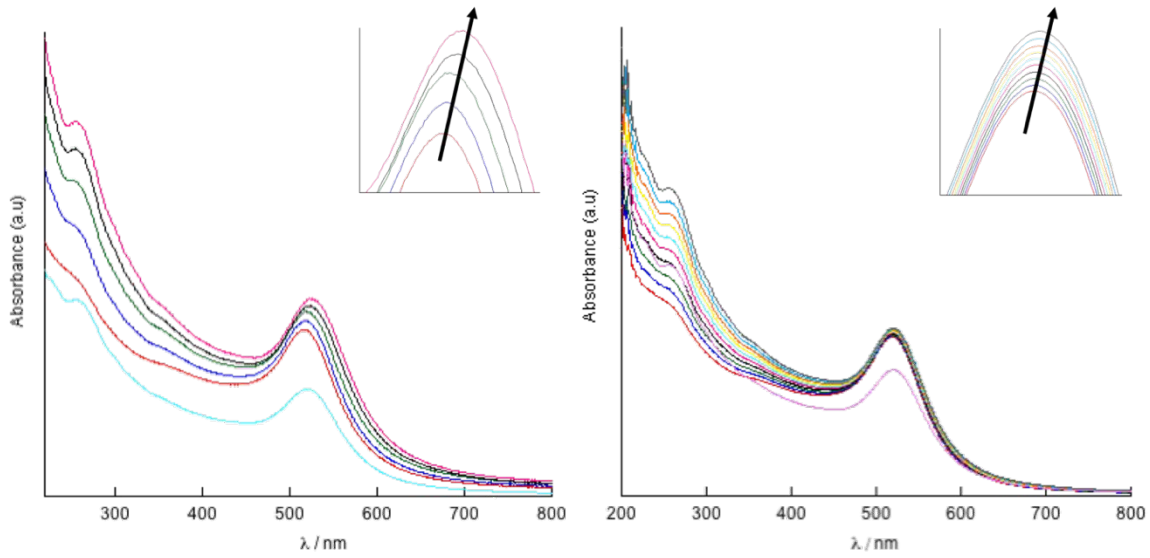

Figure 3.18. UV/Vis titration of Iridium complexes into 4.5 nM Z •AuNP13 in water (1 mL). (Left) 1 mM IrbpySS titrated in 5 μL aliquots and (right) 1 mM IrC_6 titrated in 2.5 μL aliquots.

As the complex is titrated into a solution of gold a red shift is seen, this shift stops as the surface is fully saturated with the iridium complex. Addition of 20 μL, 1mM **IrbpySS** and 22.5 μL, 1mM **IrC_6** into 4.5 nM Z **•AuNP13** resulted in an 8 nm (525 nm) and 5 nm (522 nm) shift in λ_{max} (H_2O), respectively. A similar coating was seen for the addition for iridium complexes into Z **•AuNP25** and Z **•AuNP100**. Addition of 20 μL, 1mM **IrbpySS** and 40 μL, 1mM **IrC_6** into 1.6 nM Z **•AuNP25** resulted in a 6 nm (525 nm) shift in λ_{max} (H_2O) for both complexes (Figure 3.19).

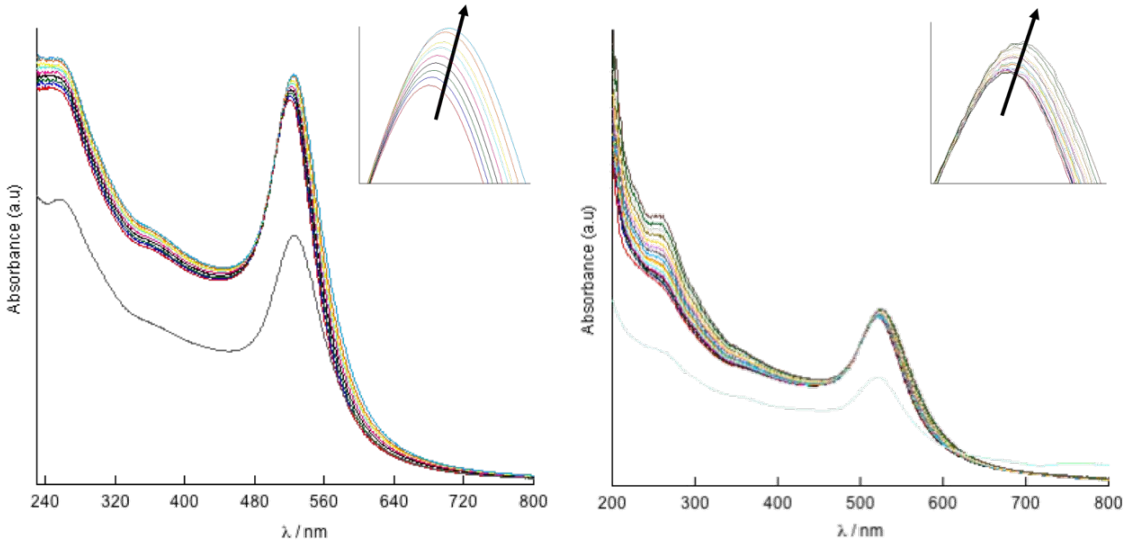

Figure 3.19. UV/Vis titration of Iridium complexes into 1.6 nM Z •AuNP25 in water. (Left) 1 mM IrbpySS and (right) 1 mM IrC_6 titrated in 2.5 μL aliquots for both.

Addition of 20 μL, 1mM **IrbpySS** and 30 μL, 1mM **IrC_6** into 30 pM Z **•AuNP100** resulted in a 6 nm (562 nm) and 2 nm (558 nm) shift in λ_{max} (H_2O) respectively (Figure 3.20).

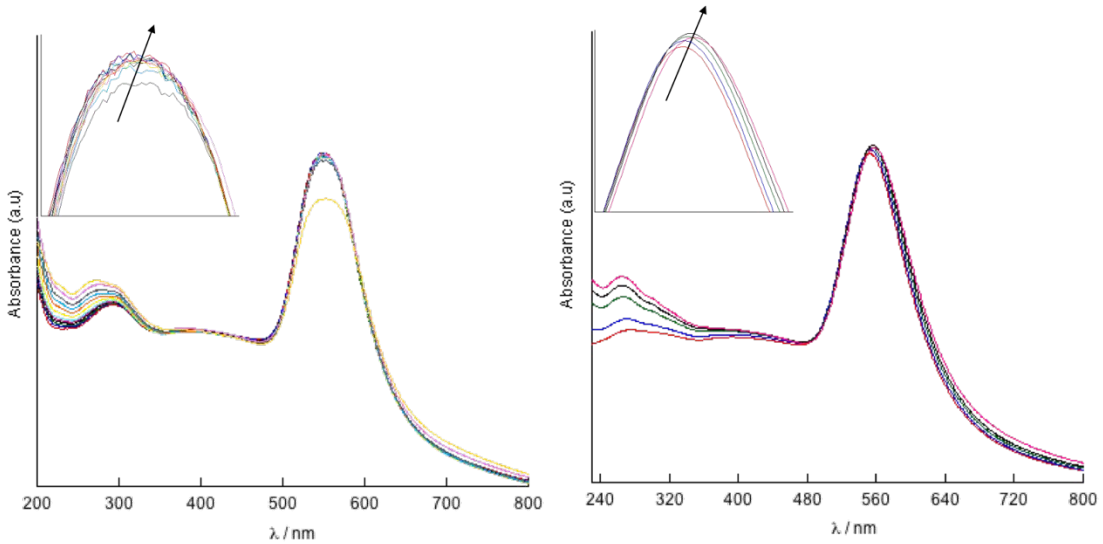

Figure 3.20. UV/Vis titration of Iridium complexes into 30 pM Z •AuNP100 in water. (Left) 1 mM IrbpySS and (right) 1 mM IrC_6 titrated in 2.5 μL aliquots for both.

The iridium coated nanoparticles were isolated by size exclusion chromatography to produce IrbpySS **•AuNP13**, IrC_6 **•AuNP13**, IrbpySS **•AuNP25**, IrC_6 **•AuNP25**, IrbpySS

•AuNP100 and IrC_6 **•AuNP100**. Upon isolation of these nanoparticles the SPR λ_{max} (H_2O) maximum remains unchanged showing that the surface coating remains the same upon removal of excess metal complex, and no aggregation has occurred for all three sizes of nanoparticles. DLS shows that the size of the AuNPs does not significantly change when coated with **IrbpySS** and **IrC_6** (Table 3.4 and Figure 3.21). The slight increase in size and PDI is indicative of the iridium complex being present on the nanoparticles, which would increase the hydrodynamic size.

Table 3.4. Dynamic light scattering data for IrC_6•AuNP in water, showing polydispersity index (PDI), size by number (nm) and size by intensity (nm).

	PDI	Size by number (nm)	Size by intensity (nm)
IrbpySS **•AuNP13**	0.24	14 ± 4	25 ± 8
IrC_6 **•AuNP13**	0.27	17 ± 4	28 ± 10
IrbpySS **•AuNP25**	0.21	26 ± 10	32 ± 17
IrC_6 **•AuNP25**	0.18	22 ± 6	30 ± 16
IrbpySS **•AuNP100**	0.02	95 ± 30	123 ± 34
IrC_6 **•AuNP100**	0.02	89 ± 22	109 ± 25

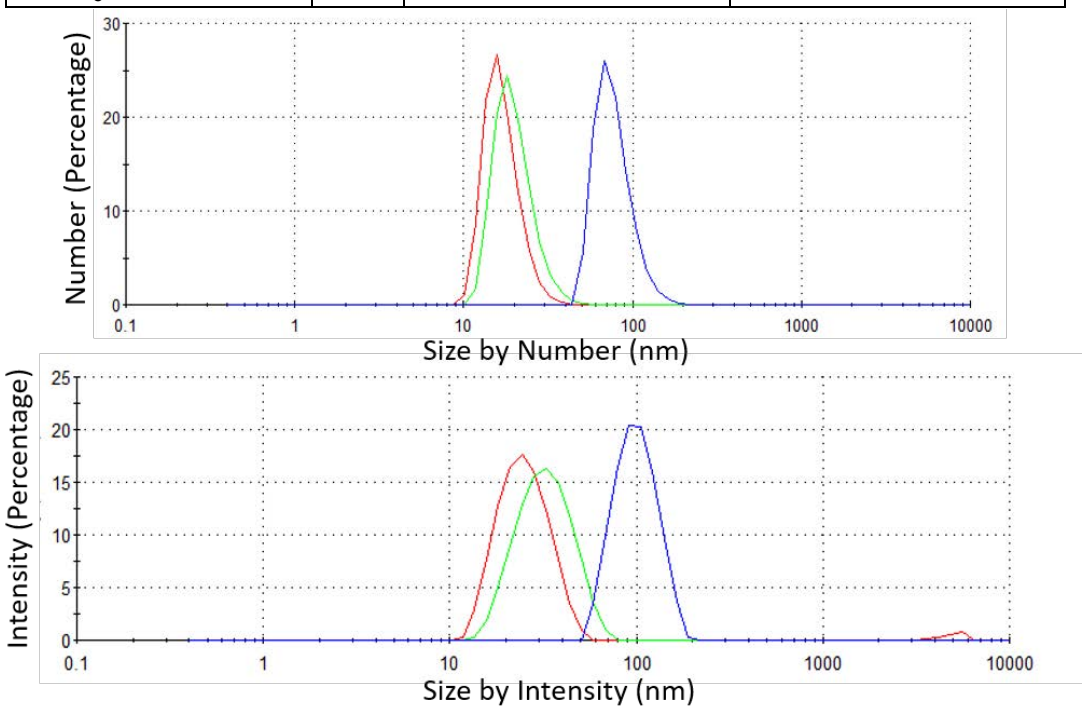

Figure 3.21. Dynamic Light Scattering (DLS) data showing sizing by (Top) Number Distribution and (Bottom) Intensity Distribution. Results displayed are for IrC_6 •AuNP13 (red), IrC_6 •AuNP25 (green) and IrC_6 •AuNP100 (Blue).

Zeta-potentials were measured and found to be -32 ± 15 mV, -35 ± 20 mV and -42 ± 24 mV for IrC_6 •**AuNP13**, IrC_6 •**AuNP25** and IrC_6 •**AuNP100** respectively (Figure 3.22). The results showed a decrease in negative potential in comparison to the Z • **AuNPs**, which had a zeta-potential of -66 ± 21 mV, -56 ± 13 mV and -68 ±16 mV for Z •**AuNP13**, Z •**AuNP25** and Z •**AuNP100** respectively. This was to be expected as the iridium complex holds an overall positive charge. The iridium(III) complex could cause displacement of the Zonyl FSA surfactant since the disulphide bond on the iridium complexes have a higher affinity for binding to the gold nanoparticles. Therefore, upon addition of **IrC_6**, this would decrease the overall negative potential of the solution.

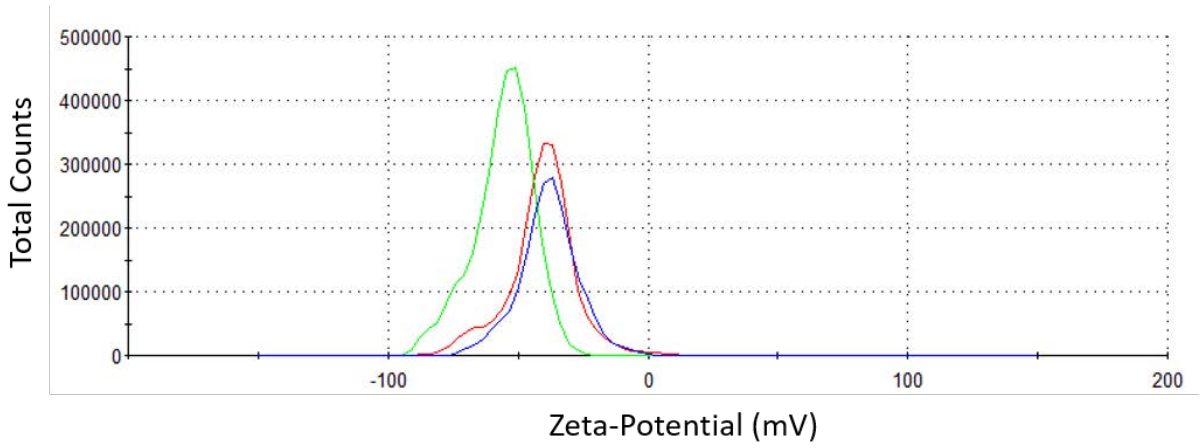

Figure 3.22. DLS data showing the absolute Zeta-Potential measurements for IrC_6 •AuNP13 (red), IrC_6 •AuNP25 (green) and IrC_6 •AuNP100 (Blue).

TEM show spherical particles with estimated diameters of 15 nm for IrC_6 •**AuNP13**, 25 nm for IrC_6 •**AuNP25**, and 95 nm for IrC_6 •**AuNP100** respectively. IrbpySS coated particles were sized and found to be 19 nm for IrC_6 •**AuNP13**, 30 nm for IrC_6 •**AuNP25**, and 102 nm for IrC_6 •**AuNP100** respectively (Figure 3.23).

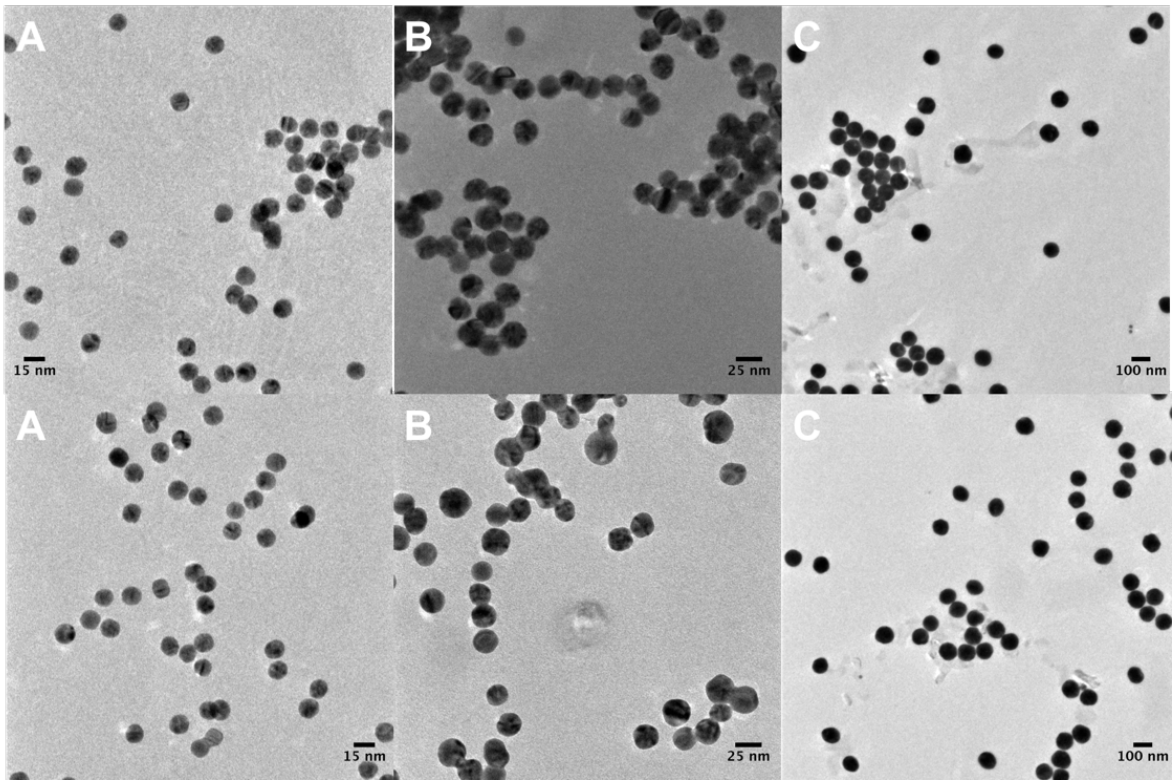

Figure 3.23. Transmission Electron Microscopy (TEM) images of (top) IrbpySS •AuNPs and (bottom) IrC_6 •AuNPs. (A) 13 nm AuNPs, (B) 25 nm AuNPs (C) 100 nm AuNPs. Images were acquired on Joel 2100 EX TEM. Scale bars are 15nm, 25 nm and 100 nm respectively.

Elemental composition of the nanoparticles by inductively coupled plasma mass spectroscopy (ICP-MS) was carried out to calculate the number of iridium complexes per nanoparticle (Table 3.5), in which the calculation can be found in the Appendix. The results show a high coating of iridium complexes onto Z •**AuNPs**, with thousands of iridium complexes per **AuNPs**. There is a higher number of **IrC_6** complexes per nanoparticle compared to **IrbpySS** for all three nanoparticle sizes.

Table 3.5. Elemental composition of nanoparticles by ICP-MS, showing number of iridium complexes per AuNPs.

Sample	Number of Iridium complexes per AuNPs
IrbpySS •**AuNP13**	1200
IrC_6 •**AuNP13**	1400
IrbpySS •**AuNP25**	2300
IrC_6 •**AuNP25**	3200
IrbpySS •**AuNP100**	15000
IrC_6 •**AuNP100**	22000

3. 2. 2. 2 Photophysical characterisations

The photophysical properties of these functionalised nanoparticles were investigated to identify any changes in behaviour of the iridium complexes when conjugated to the surface of gold nanoparticles. The luminescence properties were characterised by steady state and time resolved spectroscopy. The luminescence spectra of IrbpySS •**AuNPs** and IrC_6 •**AuNPs** were recorded and compared to that of the metal complex in solution (Figure 3.24).

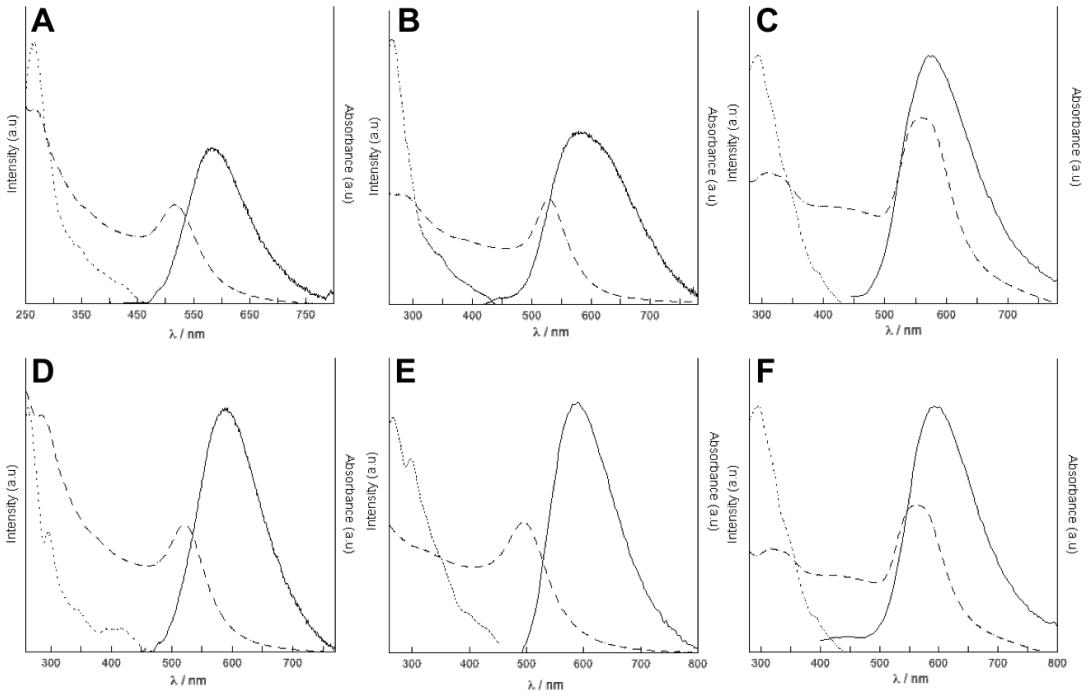

Figure 3.24. Steady-state emission spectrum λ_{exc} = 375 nm (solid line), UV/Vis absorption spectra (dashed line) and excitation spectra, λ_{em} = 580 nm for IrbpySS •AuNPs and λ_{em} = 590 nm IrC_6 •AuNPs (dotted line) of (A) 4.5 nM IrbpySS •AuNP13, (B) 1.6 nM IrbpySS •AuNP25, (C) 30 μM IrbpySS •AuNP100, (D) 4.5 nM IrC_6 •AuNP13, (E) 1.6 nM IrC_6 •AuNP25 and (F) 30 pM IrC_6 •AuNP100. Spectra corrected for PMT and instrument response.

These nanoprobes are highly emissive upon excitation at 350, 375 and 405 nm, with a λ_{max} at 580 nm for IrbpySS •**AuNPs** and a λ_{max} at 590 nm for IrC_6 •**AuNPs**. The emission has red shifted by 10 nm for both iridium functionalised nanoparticles in comparison to the free complex in water, which has an emission λ_{max} at 570 nm for **IrbpySS** and λ_{max} at 580 nm for **IrC_6**. This effect was seen when the surfactant was added to the iridium complexes in aqueous solution where a 5 nm and 10 nm shift was seen for **IrbpySS** and **IrC_6** respectively. The shift is even more enhanced for IrbpySS •**AuNPs**, this could be due to an increased interaction of the complex with Zonyl FSA when they are both locked onto the surface of the nanoparticle, leading to a greater shielding effect in comparison the complex free in solution. The excitation spectra

displayed the iridium characteristic bands which are responsible for the observed emission and are similar for all three sizes of nanoparticles with both iridium complexes. The luminescent lifetimes of the functionalised **AuNPs** are summarised in Table 3.6.

Table 3.6. Luminescent lifetimes of iridium functionalised gold nanoparticles in comparison to the complexes free in solution. Luminescent lifetimes were fitted with a χ^2 between 1 and 1.1.

	Probe in H_2O	AuNP13 (τ ns)	AuNP25 (τ ns)	AuNP100 (τ ns)
IrbpySS	30 (8%) 100 (33%) 310 (59%)	40 (4%) 110 (57%) 480 (39%)	40 (3%) 110 (52%) 490 (45%)	40 (3%) 100 (40%) 430 (57%)
IrC_6	40 (6%) 170 (52%) 430 (42%)	50 (5%) 180 (48%) 340 (47%)	40 (5%) 160 (42%) 330 (53%)	25 (3%) 140 (43%) 340 (54%)

The luminescent lifetime of IrC_6 •**AuNPs** and IrbpySS •**AuNPs** are similar for all three sizes. The luminescence lifetime were analysed with three components for both IrC_6 •**AuNPs**, IrbpySS •**AuNPs** and the free metal complex in solution. A short component of 25 – 50 ns was observed at a small percentage of 1 – 5 % for all sets of nanoparticles and the metal complexes in water. The long component of the IrC_6 •**AuNPs** (~ 335 ns) decreases by 22 % when compared to the **IrC_6** in solution, whereas the opposite effect is seen for IrbpySS •**AuNPs** which showed an increase of 38% - 58 % in comparison to **IrbpySS** in solution. These results follow the same trend that was seen from the addition of Zonyl® FSA to the metal complexes in solution (3.2.1.2). The luminescence lifetimes of the IrbpySS •**AuNPs** reflect the same increase in lifetimes as was seen from the addition of Zonyl® FSA to **IrbpySS** in water, where an increase of 71 % was seen. This same effect has been seen in previously published methods, in which the lifetime of IrbpySS.Au increased from 130 ns (83 %) to 245 ns (86 %) upon addition of

Zonyl® FSA, Zonyl® FS-300 and PEG.[74] The luminescence lifetimes of the IrC_6 •**AuNPs** follows the same trend for the increase in lifetimes that was seen from the addition of Zonyl® FSA to **IrC_6** in solution, where a decrease of 22 % was seen (3.2.1.2). This shows that the decrease in lifetime is from the Zonyl surfactant environment rather than any quenching from the gold nanoparticles. This is also evident in the observed λ_{max} shift in the emission spectra of the nanoparticles in comparison with the **IrC_6** molecular probe. The quantum yields were measured using an integrated sphere with Zonyl coated gold nanoparticles being the reference sample, in which the SPR peak was diluted to match the SPR peak of IrC_6 coated nanoparticles. The quantum yields for IrC_6 •**AuNP13** and IrC_6 •**AuNP25** were found to be 5 %. This was a small increase in quantum yield in comparison to the metal complexes in solution which were found to be 4%.

3. 3 Conclusions

Modification of previously designed iridium(III) complexes (**IrbpySS**) with a hexyl chain on the phenyl pyridine ligands led to the successful synthesis of **IrC_6** molecular probe. The incorporation of the hexyl chain was designed to increase hydrophobicity of the iridium complex which would increase the permeability across the cell membrane, and therefore it was important to have the optimal photophysical properties for imaging applications. These were measured for **IrC_6** and compared to **IrbpySS**, and the results showed desirable properties for bioimaging applications with intense emission in the visible range and long-lived luminescent lifetimes. These luminescent iridium complexes were successfully conjugated to gold nanoparticles of different sizes and found to retain their long-lived luminescence lifetimes and emission profiles. The

fluorinated surfactant used to stabilise the gold nanoparticles led to a reduction in the luminescence lifetime of **IrC$_6$** in water, but no further decrease was seen upon conjugation to the different sized nanoparticles. The opposite affect was seen for **IrbpySS** functionalised gold nanoparticles. The long-lived luminescence lifetimes recorded make these iridium functionalised nanoparticles suitable for two-photon lifetime imaging probes, which will be investigated in Chapter 4. Going forward, only the **IrC$_6$** probe is investigated for lifetime imaging studies. This is due to the inefficient excitation of **IrbpySS** under multiphoton excitation. Furthermore, design of these nanoprobes for both imaging and selective targeting will be explored through conjugation of biomolecules to the surface of different sized gold nanoparticles (Chapter 5).

3. 4 Experimental section

3. 4. 1 Synthesis of iridium(III) complexes

3. 4. 1. 1 Synthesis of IrbpySS

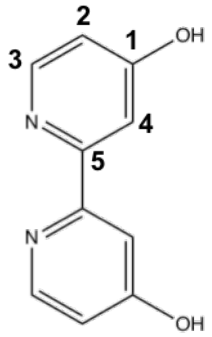

4,4'-dihydroxy-2,2'-bipyridine

The synthesis is from the method developed by Hong *et al.* A solution of 4,4'-dimethoxy-2,2'-bipyridine (5.12 g, 23.7 mmol) in glacial acetic acid (295 mL) was

added to a hydrobromic acid (48 % w/v, 41 mL, 362.5 mmol) dropwise and refluxed for 24 hours under N_2. The solution was cooled to room temperature and the solvent removed *in vacuo*, affording an off-white solid. The solid was dissolved in H_2O (250 mL) and neutralised with aqueous ammonia solution (31% by weight) dropwise. The precipitate was filtered, washed with H_2O (50 mL) and ice cold acetone (4 x 10 mL) and dried at 60 °C for 1 hour to give a white solid (2.06 g, 73.9% yield). δH(300 MHz; D_2O/NaOH) 4.75 (2H, br s, OH), 6.37 (2H, dd, J = 5.7, 2.5, H-2), 6.84 (2H, d, J = 2.5, H-4), 7.84 (2H, d, J = 5.8, H-3). δC(100 MHz; D_2O/NaOH) 115.75 (C-2), 114.52 (C-4), 146.48 (C-3), 159.24 (C-1), 174.92 (C-5). MS (ESI+) m/z: 187.06 $(M-H)^+$.

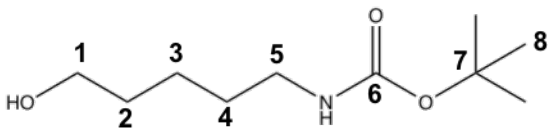

N-(Boc)-5-amino-1-pentanol

Potassium bicarbonate (14.12 g, 141.1 mmol) was suspended in a solution of 5-amino-1-pentanol (5.04 g, 48.8 mmol) in H_2O: THF (70 mL, 1:1). The white suspension was cooled in an ice bath to 0-10 °C, to which di-*tert*-butyl dicarbonate (11.12 g, 51.0 mmol) dissolved in H_2O:THF (80 mL, 1:1) was added dropwise over 15 minutes, maintaining the temperature between 0-10 °C. The solution was then heated to 50 °C and stirred for 24 hours under N_2. The organic phase was separated and concentrated *in vacuo* forming a white microsuspension. The suspension was dissolved in H_2O:Et_2O (150 mL, 2:1) and the organic layer separated. The aqueous layer was washed with Et_2O (50 mL), and the combined aqueous layers were dried (Na_2SO_4), filtered, and the solvent removed *in vacuo* to give a clear oil N-Boc-5-amino-1-pentanol (7.73 g, 90%); δ_H(300 MHz; $CDCl_3$) 1.28-1.58 (6 H, m, H-2,3,4), 1.37 (9 H, s, H-8), 1.72 (1 H, s, OH),

3.11 (2 H, q, H-5), 3.63 (2 H, t, H-1) and 4.59 (1 H, s, NH); δ_C(100 MHz; $CDCl_3$) 22.9 (C-2), 28.3 (C-8), 29.7 (C-3), 32.1 (C-4), 40.3 (C-1), 62.1 (C-5), 79.0 (C-7) and 156.2 (C-6). M/z 226.2 ($[M+Na]^+$)

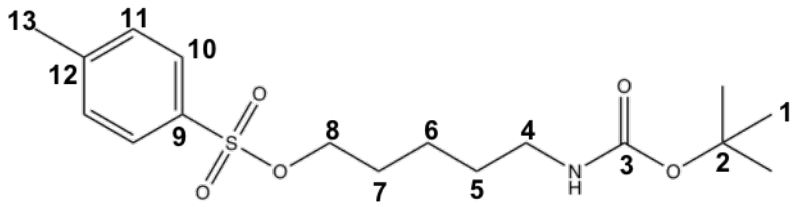

N-(Boc)-5-amino-1-tosylpentane

N-(Boc)-5-amino-pentanol (7.80 g, 38.4 mmol) and para-toluene sulfonyl chloride (8.97 g 47.1 mmol) were dissolved in anhydrous CH_2Cl_2 (50 mL) under an atmosphere of N_2 and cooled to 0-5 °C. Anhydrous Pyridine (11 mL, 149.0 mmol) was added dropwise over 5 minutes, maintaining the temperature between 0-5 °C. The solution was heated to room temperature and stirred for 24 hours. The mixture was concentrated *in vacuo* until it yielded a white suspension. The suspension was added to H_2O:Et_2O (100 mL 1:1) and separated, followed by washing the organic layer with aqueous $NaHCO_3$ (50 mL) and brine (50 mL). The solution was dried (Na_2SO_4), filtered, and the solvent was removed *in vacuo* to give a clear oil (9.75 g), which was triturated in hexane (50 mL). The solid was filtered and washed with cold hexane (2 x 30 mL) to afford a white solid N-Boc-5-amino-1-tosylpentane (5.61 g, 45%); δ_H(300 MHz, $CDCl_3$) 1.32-1.43 (4 H, m, H-6,7), 1.45 (9 H, s, H-1), 1.68 (2 H, dd, H-5), 2.47 (3 H, s, H-13), 3.04-3.12 (2 H, m, H-4), 4.04 (2 H, t, H-8), 4.51 (1 H, s, NH), 7.37 (2 H, d, H-11) and 7.81 (2 H, d, H-10); δ_c(300 MHz, $CDCl_3$) 21.6 (C-13), 22.6 (C-7), 28.4 (C-1), 28.5 (C-6), 29.4 (C-5), 40.2 (C-8), 70.4 (C-4), 79.1 (C-2), 127.89 (C-11), 129.9 (C-10), 133.1 (C-12), 144.8 (C-9) and 156.0 (C-3); MS (ESI+) m/z: 380.2 $(M+Na)^+$.

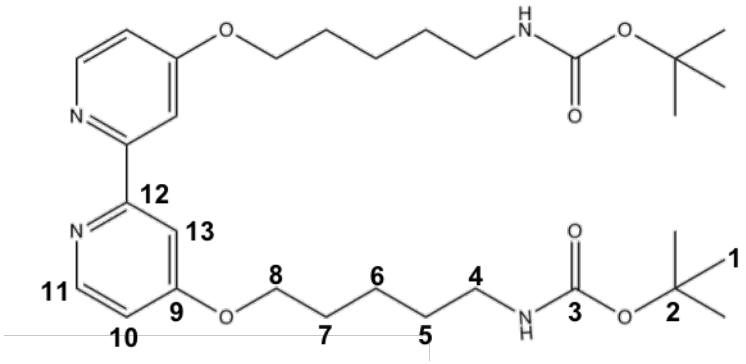

4,4'-di-(N-(Boc)-5-amino-1-pentoxy)-2,2'-bipyridine

N-(Boc)-5-amino-1-tosylpentane (6.67 g, 15.7 mmol), 4,4'-dihydroxy-2,2'-bipyridine (0.94 g, 4.9 mmol) and Potassium carbonate (2.22 g, 15.8 mmol) was suspended in acetone (210 mL) with a catalytic amount of 18-crown-6 and heated to 60 °C and stirred for 36 hours. The reaction mixture was hot filtered and cooled to 0 -5°C to afford a white precipitate which was washed with cold acetone (2x 20 mL) to yield a yellow solid (1 g, 1.45 mmol, 35%); δ_H(300 MHz; $CDCl_3$) 1.47 (18 H, s, H-1), 1.52-1.63 (8 H, m, H-6,7), 1.84-1.87 (4 H, m, H-5), 3.10-3.25 (4 H, m, H-4), 4.15 (4 H, t, H-8), 4.58 (2 H, s, NH), 6.84 (2 H, dd, H-10), 7.96 (2 H, d, H-13) and 8.48 (2 H, d, H-11); δ_c(300 MHz; $CDCl_3$) 23.3 (C-7), 28.4 (C-1), 28.6 (C-6), 29.8 (C-5), 40.4 (C-8), 67.8 (C-4), 77.3 (C-2) 106.6 (C13), 111.3 (C-10), 150.1 (C-11), 157.9 (C-12) and 166.1 (C-9); m/z (ES) 581.3 ($[M+Na]^+$).

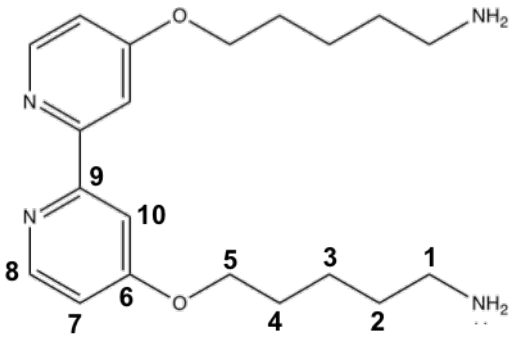

4,4'-di-(5-amino-1-pentoxy)-2,2'-bipyridine

4,4'-di-(N-(Boc)-5-amino-1-pentoxy)-2,2'-bipyridine (0.97 g, 1.7 mmol) was dissolved in trifluoroacetic acid (14.9 mL) was stirred under N_2 for 1 hour. The solvent was removed *in vacuo*, before separation (20 mL NaOH (1M)/ 20 mL chloroform). The aqueous layer was washed with chloroform (6 x 10 mL), and the combined organic extracts were dried (Na_2SO_4) and filtered. The solvent was removed *in vacuo* to give a white solid (0.26 g, 86%); δ_H (300 MHz; $CDCl_3$) 1.48 (4 H, s, NH_2), 1.37-1.55 (8 H, m, H-3,4), 1.72-1.81 (4 H, m, H-2), 2.73 (4 H, t, H-1), 4.07 (4 H, t, *J* = 6.4, H-5), 6.86 (2 H, dd, H-7), 7.87 (2 H, d, *J* = 2.6, H-10) and 8.50 (2 H, d, H-8); m/z (ES) 359.2 ($[M+Na]^+$, 100 %)

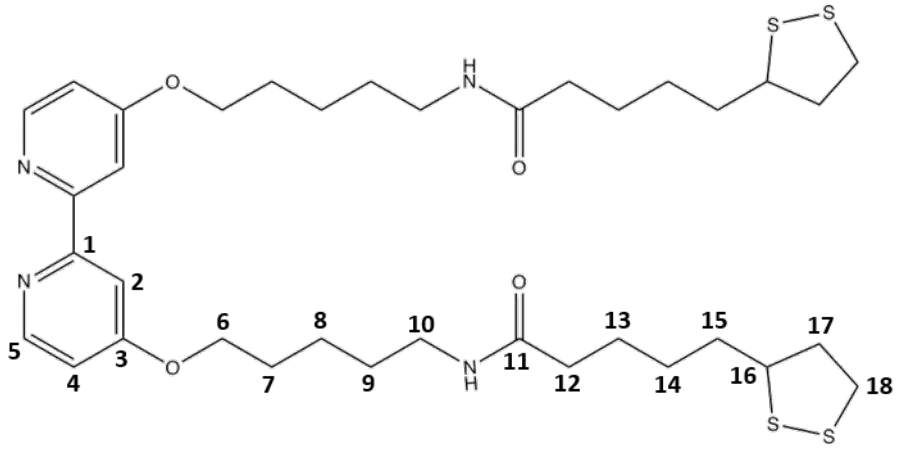

4,4'-di-(5-lipoamido-1-pentoxy)-2,2'-bipyridine (bpySS)

α-lipoic acid (0.48 g, 2.3 mmol) and 1-hydroxybenzotriazole hydrate (0.36 g, 2.7 mmol) in anhydrous DMF (8.8 mL) was cooled to 0-5 °C, upon which 1-Ethyl-3-(3-dimethylaminopropyl)carbodiimide (EDC) (0.41 g, 2.6 mmol) was added and stirred for 1 hour, maintaining this temperature. After EDC had dissolved the solution was warmed to room temperature and stirred for a further 1 hour. A solution of N-ethylmorpholine (N-EM) (0.27 g, 2.4 mmol), and 4,4'-di-(5-amino-1-pentoxy)-2,2'-bipyridine (0.35 g, 9.8 mmol) in anhydrous DMF (12.3 mL) was added to the reaction mixture and stirred for 14 hours. The crude product was slurried in $CHCl_3$ (50 mL) and

filtered again, before washing with $CHCl_3$ (4 x 10 mL) to give a pale yellow powder **bpySS** (0.215 g, 20%); (δ_H (300 MHz; $CDCl_3$) 1.30-1.58 (12 H, m, H-7,8,13), 1.54-1.68 (8 H, m, H-14,15), 1.74-1.90 (6 H, m, H-9, H-17'), 2.10 (4 H, t, H-12), 2.38-2.50 (2 H, m, H-17), 2.98-3.16 (4 H, m, H-18, 18'), 3.22 (4 H, dd, H-10), 3.44-3.53 (2 H, m, H-16), 4.06 (4 H, t, H-6), 5.48 (2 H, s, NH), 6.75 (2 H, dd, H-4), 7.87 (2 H, d, H-2) and 8.38 (2 H, d, H-5); δ_C (100 MHz; $CDCl_3$) 23.4 (C-8), 25.4 (C-13), 28.6 (C-14), 28.9 (C-7), 29.4 (C-9), 34.7 (C-15), 36.6 (C-12), 38.5 (C-18), 39.3 (C-10), 40.3 (C-17), 56.5 (C-16), 67.7 (C-6), 106.7 (C-2), 111.3 (C-4), 150.2 (C-5), 157.8 (C-1), 166.1 (C-3), and 172.7 (C-11); m/z (ES) 757.2 ([M+Na]$^+$, 100 %).

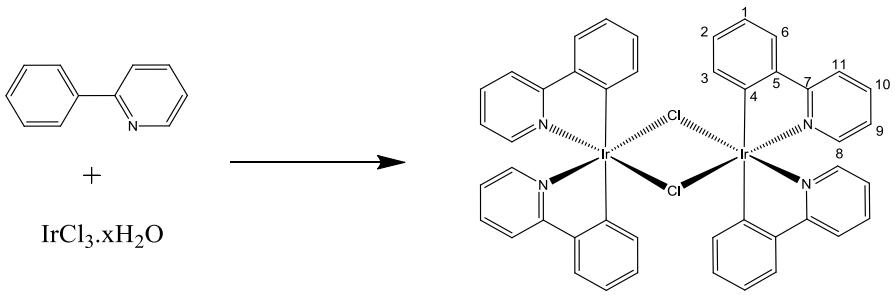

Tetrakis(2-phenylpyridine-*C2,N'*)(μ-dichloro)diiridium

The synthesis was based on the method of Watts *et. al*.[38] Iridium trichloride hydrate (0.340g) and 2-phenylpyridine (0.79g) and dissolved in a mixture of 2-ethoxyethanol (30 mL) and water (10 mL) and refluxed for 24 h. The solution was cooled to room temperature affording a white precipitate. The precipitate was washed with 95% ethanol (60 mL) and acetone (60 mL) and dissolved in anhydrous DCM (75 mL) and filtered producing $[Ir(ppy)_2Cl]_2$ (0.428 g, 72%). δH (300 MHz; $CDCl_3$) 5.96 (1H, d J = 7.8), 6.59 (1H, t J = 7.4), 6.78 (2H, dd, J = 16.2, 7.0), 7.51 (1H, d J = 7.8), 7.76 (1H, dd J = 11.8, 5.2), 7.90 (1H, d J = 7.7) and 9.27 (1H, d, J = 5.8); MS (ESI+) m/z: 1077.7 $[M-Cl]^+$.

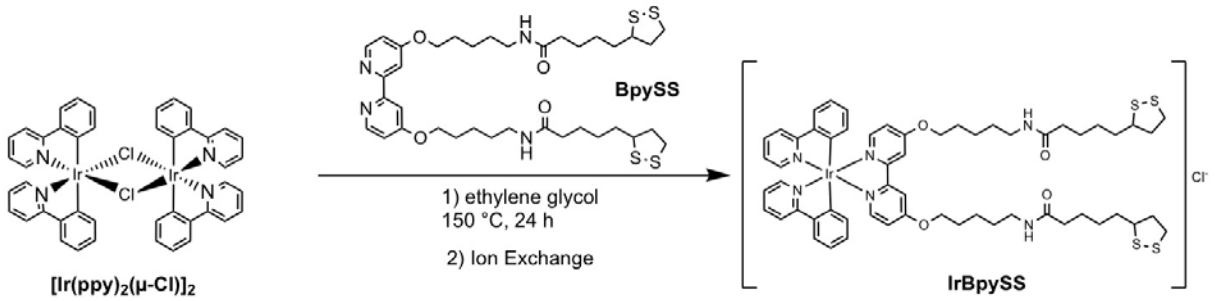

[Ir(ppy)$_2$bpySS]PF$_6$

IrbpySS was synthesised via a modified method outlined by Slinker *et al.* Briefly, [Ir(ppy)$_2$Cl]$_2$ (66.6 mg, 0.06 mmol) and **bpySS** (100.8 mg, 0.14 mmol) was suspended in ethylene glycol (6.5 mL) and heated to 150 °C for 19 hours. The yellow mixture was cooled to room temperature, upon which H_2O (150 mL) was added, and the mixture heated to 60-70 °C. Saturated aqueous ammonium hexafluorophosphate (1 g in 2.5 mL H_2O) was added, immediately forming a yellow precipitate, which was cooled on ice, filtered and washed with H_2O. The solid was dissolved in minimal acetone and the solvent removed *in vacuo* to give [Ir(ppy)bpySS]PF$_6$ (103.8 mg, 61%); δ_H (300 MHz; d^6-acetone) 1.24-1.61 (20 H, m, H-8,9,10,14,16), 1.64-1.83 (6 H, m, H-15,18'), 2.0 (4 H, t, H-13), 2.22-2.39 (2 H, m, H-18), 2.92-3.17 (8 H, m, H-11,19), 3.35-3.49 (2 H, m, H-17), 4.2 (4 H, t, *J* = 6.4, H-7), 6.22 (2 H, dd, H-k), 6.76 (2 H, td, H-j), 6.9 (2 H, td, H-i), 6.97 (2 H, s, NH), 7.01-7.10 (4 H, m, H-5,d), 7.67 (2 H, d, H-6), 7.70-7.75 (4 H, m, H-e,h), 7.80 (2 H, dd, H-c), 8.10 (2 H, d, H-b) and 8.3 (2 H, d, H-3); m/z (ES+) 1235.4 ([M-Cl]$^+$).

The pH of a suspension of two spatulas of Dowex 1x8 50-100 Mesh in deionised water (30mL) was lowered to 1 using HCl (10%) and stirred for 1 hour. The Dowex was filtered in vacuum and washed with deionised water (20mL) and methanol (50mL). The Dowex was resuspended in MeOH (~30mL). A solution of [Ir(ppy)$_2$bpySS]PF$_6$ (~0.005g, in 5mL of MeOH) was added and the mixture is stirred for 2 hours. The

Dowex was filtered off, and the resin was washed with MeOH until colourless. The solution was dried and made to a concentration of 1mM with MeOH to give a solution of [Ir(ppy)$_2$bpySS]Cl. λ_{max} (H_2O)/nm (ε/dm^3.mol^{-1}cm^{-1}); [Ir(C$_6$-ppy)$_2$bpySS]Cl: 229sh (24472), 258 (23568), 298sh (12216), and 354sh (4722). Emission λ_{max} = 570 nm, τ = 30 ns (8%), 100 ns (33%), 430 ns (49%), ϕ = 4 %. Upon addition of 10% Zonyl FSA. Emission λ_{max} = 580 nm, τ = 35 ns (1 %), 140 ns (56 %), 530 ns (44 %), ϕ = 3 %.

3. 4. 1. 2 Synthesis of IrC$_6$

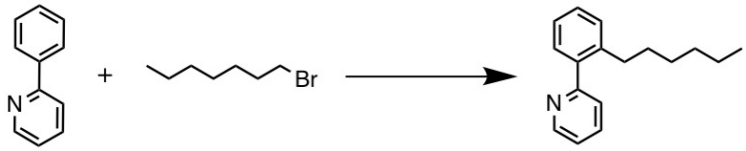

2-(hexylphenyl)-pyridine

The synthesis was based on the method of Ackermann et. al.[39] A suspension of [RuCl$_2$(p-cymene)$_2$] (15.4 mg, 0.025 mmol, 2.5 mol%), 1-AdCO$_2$H (54.1 mg, 0.30 mmol, 30 mol%), K$_2$CO$_3$ (276 mg, 2.00 mmol), 2-phenylpyridine (155 mg, 1.00 mmol), and 1-bromo-n-hexane (495mg, 3.00mmol) in NMP (4mL) was stirred for 48h at 130 ºC under N$_2$. EtOAc (100 mL) and H_2O (100 mL) were added to the cold reaction mixture. The aqueous phase was extracted with EtOAc (4 x 50 mL). The combined organic layers were washed with H_2O (2 x 50 mL) and brine (2 x 50 mL), dried over Na_2SO_4, and concentrated in vacuum. The remaining residue was purified by column chromatography on silica gel (n-hexane/EtOAc 3:1) to yield 2-(hexylphenyl)-pyridine (163 mg, 68%) as a light yellow oil. δH(300 MHz; $CDCl_3$) 0.73 (t, *J* = 6.8 Hz, 3H, H-18), 1.16 – 1.03 (m, 6H, H-15,16,17), 1.36 (dt, *J* = 15.3, 7.7 Hz, 2H, H-14), 2.74 – 2.50 (m, 2H, H-13), 7.37 – 6.99 (m, 6H, H-1,2,5,6,8,10), 7.64 (td, *J* = 7.7, 1.8 Hz, 1H, H-9), 8.60 (d, *J* = 5.7 Hz, 1H, H-11); δC (100 MHz; $CDCl_3$) 14.1 (C-18), 22.5 (C-17), 29.1 (C-

15), 31.3 (C-14), 31.5 (C-16), 32.9 (C-13), 121.6 (C-8), 124.11 (C-2), 125.7 (C-10), 128.3 (C-5), 129.7 (C-6,1), 136.1 (C-9), 140.4 (C-4), 140.8 (C-3), 149.1 (C-11), 160.4 (C-7); MS (ESI+) m/z: 239.2 (M^+).

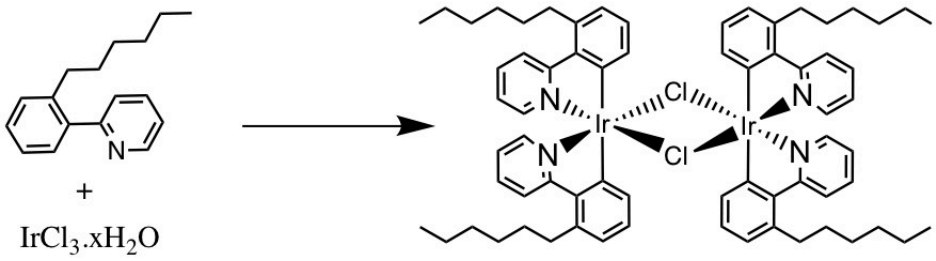

Tetrakis(hexyl-phenylpyridine-*C2,N'*)(μ-dichloro)diiridium.

The synthesis was based on the method of Watts et. al.[38] Iridium trichloride hydrate (0.235 g, 0.79 mmol) and 2-(2'-hexylphenyl)pyridine (0.71 g, 2.92 mmol) was dissolved in a mixture of 2-ethoxyethanol (20 mL) and water (10 mL) and refluxed for 24 h. The solution was cooled to room temperature affording a yellow precipitate. The precipitate was washed with 95% ethanol (25 mL) and methanol (50 mL) to give yellow crystals of $[Ir(C_6\text{-}ppy)_2Cl]_2$ (0.290 g, 0.205 mmol, 53%). δH (300 MHz; $CDCl_3$) 0.84 (H1, t, *J* = 6.9 Hz, 12H), 1.28 (H2-3, dd, *J* = 8.8, 5.0 Hz, 16H), 1.39 (H4, dd, *J* = 12.9, 6.6 Hz, 8H), 1.71 – 1.51 (H5, m, 8H), 3.09 – 2.60 (H6, m, 8H), 5.58 (H10, dd, *J* = 7.7, 1.0 Hz, 4H), 6.33 (H9, t, *J* = 7.6 Hz, 4H), 6.47 (H8, d, *J* = 7.3 Hz, 4H), 6.65 (H16, t, *J* = 6.3 Hz, 4H), 7.65 (H15, t, *J* = 7.1 Hz, 4H), 7.89 (H14, d, *J* = 8.4 Hz, 4H), and 9.26 (H17, dd, *J* = 5.8, 1.4 Hz, 4H). δC (100 MHz; $CDCl_3$) 14.2 (C1), 22.7 (C2), 29.6 (C4), 30.4 (C5), 31.8 (C3), 35.6 (C6), 121.5 (C16), 122.1 (C15), 124.8 (C8), 128.0 (C9), 128.5 (C10), 135.7 (C14), 140.5 (C12), 141.8 (C7), 148.3 (C11), 152.7 (C17) and 168.4 (C13). NMR assignments were confirmed by COSY, HSQC, and HMBC.

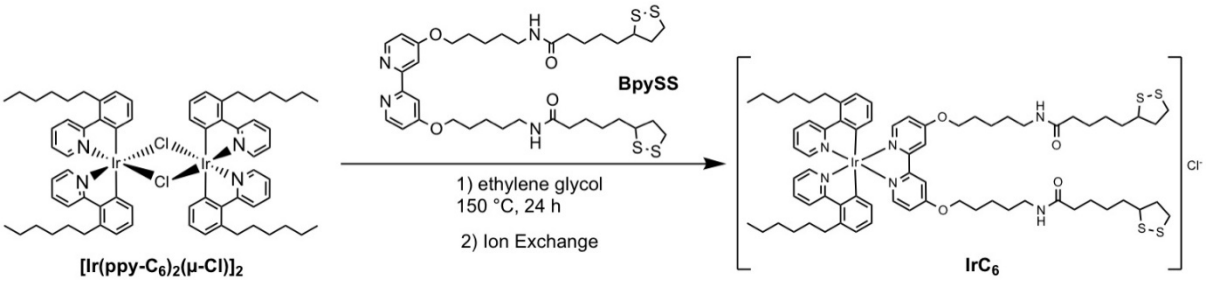

[Ir(C_6-ppy)$_2$bpySS]PF_6

[Ir(C_6-ppy)$_2$bpySS]PF_6 was also synthesized via a modified method outlined by Slinker et al. [Ir(C_6-ppy)$_2$Cl]$_2$ (0.040 g, 0.028 mmol) and bpySS (0.053 g, 0.057 mmol) was suspended in ethylene glycol (10 mL) and heated to 150 °C for 24h. The yellow mixture cooled to room temperature, upon which H_2O (50 mL) was added, and the mixture heated to 60−70 °C. Saturated aqueous ammonium hexafluorophosphate (1 g in 2.5 mL H_2O) was added, forming an orange precipitate that was left on agitation for 1 hour. The solution was cooled on ice, filtered, and washed with H_2O. The solid was dissolved in minimal acetone and the solvent removed in vacuum. The residual solid was triturate in n-hexane and vacuum filtered to give [Ir(C_6-ppy)bpySS]PF_6 (0.0944 g). λ_{max} (MeCN)/nm (ε/dm3.mol^{-1}cm^{-1}) 223 (46961), 258 (40567), 297sh (19366) 322sh (12850) and 353sh (7493); δH (300MHz; $CDCl_3$) 0.92 (t, *J* = 6.2 Hz, 6H), 1.42 – 1.27 (m, 12H), 1.52 – 1.42 (m, 8H), 1.66 – 1.52 (m, 12H), 1.77 – 1.67 (m, 8H), 1.87 (d, *J* = 3.1 Hz, 8H), 2.31 – 2.20 (m, 4H), 2.73 (d, *J* = 4.2 Hz, 4H), 3.03 (t, *J* = 7.2 Hz, 4H), 3.28 (d, *J* = 4.0 Hz, 4H), 3.90 (s, 2H), 4.02 (s, 2H), 4.27 (t, 4H), 6.06 (d, *J* = 7.4 Hz, 2H), 6.76 (t, *J* = 7.4 Hz, 2H), 6.90 – 6.78 (m, 4H), 7.02 (d, *J* = 3.9 Hz, 2H), 7.53 (d, *J* = 5.8 Hz, 2H), 7.69 (d, *J* = 4.6 Hz, 2H), 7.77 (t, *J* = 7.6 Hz, 2H), 8.00-8.05 (m, 4H); δC (100 MHz; $CDCl_3$) 14.1 (C-q), 22.7 (C-p) 22.9 (C-3), 23.6 (C-9), 28.2 (C-10) 28.7 (C-n), 29.4 (C-m), 30.2 (C-4), 31.7 (C-o), 35.9 (C-5,7), 39.2 (C-l), 63.8 (C-13), 65.3 (C-11), 69.4 (C-1), 110.6 (C-18), 115.2 (C-j), 122.6 (C-c), 123.2 (C-d), 126.0 (C-16), 129.7.8 (C-h/i),

137.4 (C-b), 141.4 (C-f), 141.9 (C-k), 149.1 (C-a), 150.3 (C-15), 153.6 (C-19), 157.5 (C-e), 167.4 (C-17), 167.9 (C-9), and 216.2 (C-6); NMR assignments were confirmed by COSY, HSQC, and HMBC.

The pH of a suspension of two spatulas of Dowex 1x8 50-100 Mesh in deionised water (30mL) was lowered to 1 using HCl (10%) and stirred for 1 hour. The Dowex was filtered in vacuum and washed with deionised water (20mL) and methanol (50mL). The Dowex was resuspended in MeOH (~30mL). A solution of $[Ir(C_6\text{-ppy})_2bpySS]PF_6$ (~0.005g, in 5mL of MeOH) was added and the mixture is stirred for 2 hours. The Dowex was filtered off, and the resin was washed with MeOH until colourless. The solution was dried and made to a concentration of 1mM with MeOH to give a solution of $[Ir(C_6\text{-ppy})_2bpySS]Cl$. λ_{max} (H_2O)/nm (ε/$dm^3.mol^{-1}cm^{-1}$); $[Ir(C_6\text{-ppy})_2bpySS]Cl$: 229sh (24472), 258 (23568), 298sh (12216), and 354sh (4722). Emission λ_{max} = 580 nm, τ = 40 ns (6%), 170 ns (45%), 430 ns (49%), ϕ = 4%. Upon addition of 10% Zonyl FSA. Emission λ_{max} = 590 nm, τ = 40 ns (6%), 150 ns (35%), 320 ns (62%), ϕ = 4%.

3. 4. 2 Synthesis of gold nanoparticles (AuNPs)

AuNP13. The protocol for synthesizing 13 nm AuNPs was based on the published method Turkevich *et al.*[49] in which glassware used was washed with aqua regia ($HCl:HNO_3$, 3:1) and dried in the oven. A solution of trisodium citrate dihydrate (60.6mg, 0.21 mmol), citric acid (13.6 mg, 0.07 mmol) and ethylenediaminetetraacetic acid (EDTA) (1.6 mg, 0.004 mmol) in 100 mL ultrapure water was vigorously stirred and brought to reflux. This was left to reflux for 15 minutes, before rapid addition of a solution of gold(III)chloride trihydrate ($HAuCl_4.3H_2O$) (8.6 mg, 0.020 mmol) in 25 mL of ultrapure water. After refluxing for a further 15 minutes, the heat was turned off and the

solution left to cool to room temperature, forming 1.53 nM **AuNP13**. $\lambda_{max}(H_2O)$: 517 nm (SPR). Diameter 13 ± 3 nm (DLS number distribution), PDI = 0.07, ζ-potential = -33 ± 13 mV. The final concentration of **AuNP13** was changed by centrifuged at 10, 000 *g* for 30 minutes. The supernatant was decanted and the pellet was redispersed in ultrapure water to form a 4.5 nM solution of **AuNP13**.

AuNP25 and **AuNP100**. The protocol for the formation of **AuNP25** and **AuNP100** was modified using a previously published method.[61] Three stock solutions were prepared; 5 mM $HAuCl_4.3H_2O$, 57 mM ascorbic acid and 34 mM trisodium citrate dihydrate in water. **AuNP13** (34 mL, 1.53 nM) were diluted to 40 mL with ultrapure water and vigorously stirred. The three solutions were diluted to 1 mM, 2.85 mM and 0.85 mM in ultrapure water for $HAuCl_4.3H_2O$, ascorbic acid and trisodium citrate dehydrate respectively. The three solutions ($HAuCl_4.3H_2O$ and ascorbic acid, trisodium citrate dehydrate) were added simultaneously to the vortex of the solution via a peristaltic pump over 25 minutes. The solution was refluxed for 30 minutes forming 0.65 nM **AuNP25**. $\lambda_{max}(H_2O)$: 519 nm (SPR). Diameter 18 ± 5 nm (DLS number distribution), PDI = 0.05. ζ-potential = -30 ± 12 mV. The **AuNP25** were then centrifuged at 10, 000*g* for 30 minutes and redispersed in ultrapure water to remove excess ascorbic acid and concentrated to give 1.6 nM **AuNP25**. **AuNP25** (9 mL, 0.65 nM) were diluted to 40 mL with ultrapure water and vigorously stirred. The three solutions were diluted to 1 mM, 2.85 nM and 0.85 nM in ultrapure water for $HAuCl_4.3H_2O$, ascorbic acid and trisodium citrate dehydrate respectively. The two solutions ($HAuCl_4.3H_2O$ and ascorbic acid, trisodium citrate dehydrate) were added simultaneously to the vortex of the solution via a peristaltic pump over 25 minutes. The solution was refluxed for 30 minutes forming 70 pM **AuNP50**. $\lambda_{max}(H_2O)$: 527 nm (SPR). Diameter 46 ± 10 nm (DLS number

distribution), PDI = 0.03. ζ-potential = -33 ± 17 mV. The **AuNP50** (40 mL, 70 pM) was left to vigorously stir. The three solutions were diluted to 4 mM, 12 nM and 3.4 nM in ultrapure water for $HAuCl_4.3H_2O$, ascorbic acid and trisodium citrate dehydrate respectively. The two solutions ($HAuCl_4.3H_2O$ and ascorbic acid, trisodium citrate dehydrate) were added simultaneously to the vortex of the solution via a peristaltic pump over 25 minutes. The solution was refluxed for 30 minutes forming 35 ρM **AuNP100**. $\lambda_{max}(H_2O)$: 556 nm (SPR). Diameter 80 ± 20 nm (DLS number distribution), PDI = 0.03. ζ-potential = -33 ± 12 mV. The **AuNP100** were taken and centrifuged at 10, 000 *g* for 90 s. The supernatant was decanted and the pellet was redispersed in ultrapure water.

3. 4. 3 Attachment of iridium(III) complexes to AuNPs

Z •**AuNP13**. 10% Zonyl FSA solution in ultrapure water (3 μL) was added to 4.5 nM **AuNP13** (1 mL) and sonicated for 10 minutes. This was centrifuged at 10, 000*g* for 30 minutes, the supernatant was decanted and the pellet was resuspended in ultrapure water (1 mL) to form Z •**AuNP13**. $\lambda_{max}(H_2O)$: 519 nm (SPR). Diameter 17 ± 4 nm (DLS number distribution), PDI = 0.24. ζ-potential = - 66 ± 21 mV.

IrbpySS •**AuNP13**. IrC_6 (20 μL, 1 mM) was titrated into 4.5 nM solution of Z •**AuNP13** (1 mL) with sonication in between. A Sephadex G-10 size exclusion column was performed to give a solution of IrbpySS •**AuNP13**. $\lambda_{max}(H_2O)$: 522 nm (SPR). Diameter 14 ± 4 nm (DLS number distribution), PDI = 0.24. ζ-potential was not recorded. ICP-MS results show 12,00 complexes per **AuNP13**.

IrC_6 •**AuNP13**. IrC_6 (22.5 μL, 1 mM) was titrated into 4.5 nM solution of Z •**AuNP13** (1 mL) with sonication in between. A Sephadex G-10 size exclusion column was performed to give a solution of IrC_6 •**AuNP13**. $\lambda_{max}(H_2O)$: 525 nm (SPR). Diameter 17 ± 4 nm (DLS number distribution), PDI = 0.27. ζ-potential = - 32 ± 15 mV. ICP-MS results show 1,400 complexes per **AuNP13**.

Z •**AuNP25**. 10% Zonyl FSA solution in ultrapure water (3 μL) was added to 1.6 nM **AuNP25** (1 mL) and sonicated for 10 minutes. This was centrifuged at 10, 000*g* for 30 minutes, the supernatant was decanted and the pellet was resuspended in ultrapure water (1 mL) to form Z •**AuNP25**. $\lambda_{max}(H_2O)$: 521 nm (SPR). Diameter 22 ± 6 nm (DLS number distribution), PDI = 0.14. ζ-potential = -56 ± 13 mV.

IrbpySS •**AuNP25**. IrC_6 (20 μL, 1 mM) was titrated into 1.6 nM solution of Z •**AuNP25** (1 mL) with sonication in between. A Sephadex G-10 size exclusion column was performed to give a solution of IrbpySS •**AuNP25**. $\lambda_{max}(H_2O)$: 525 nm (SPR). Diameter 26 ± 10 nm (DLS number distribution), PDI = 0.21. ζ-potential was not recorded. ICP-MS results show 23,00 complexes per **AuNP25**.

IrC_6 •**AuNP25**. IrC_6 (40 μL, 1 mM) was titrated into 1.6 nM solution of Z •**AuNP25** (1 mL) with sonication in between. A Sephadex G-10 size exclusion column was performed to give a solution of IrC_6 •**AuNP25**. $\lambda_{max}(H_2O)$: 525 nm (SPR). Diameter 22 ± 6 nm (DLS number distribution), PDI = 0.18. ζ-potential = -35 ± 20 mV. ICP-MS results show 3,200 complexes per **AuNP25**.

Z •**AuNP100**. 10% Zonyl FSA solution in ultrapure water (3 μL) was added to 30 pM **AuNP100** (1 mL) and sonicated for 10 minutes. This was centrifuged at 10, 000*g* for 90 seconds, the supernatant was decanted and the pellet was resuspended in

ultrapure water (1 mL) to form Z •**AuNP100**. $\lambda_{max}(H_2O)$: 556 nm (SPR). Diameter 87 ± 21 nm (DLS number distribution), PDI = 0.02. ζ-potential = -68 ± 16 mV.

IrbpySS •**AuNP100**. IrC_6 (20 μL, 1 mM) was titrated into 30 pM solution of Z • **AuNP100** (1 mL) with sonication in between. A Sephadex G-10 size exclusion column was performed to give a solution IrbpySS • **AuNP100**. $\lambda_{max}(H_2O)$: 558 nm (SPR). Diameter 95 ± 30 nm (DLS number distribution), PDI = 0.02. ζ-potential not recorded. ICP-MS results show 15,000 complexes per **AuNP100**.

IrC_6 •**AuNP100**. IrC_6 (30 μL, 1 mM) was titrated into 30 pM solution of Z • **AuNP100** (1 mL) with sonication in between. A Sephadex G-10 size exclusion column was performed to give a solution IrC_6 • **AuNP100**. $\lambda_{max}(H_2O)$: 562 nm (SPR). Diameter 89 ± 22 nm (DLS number distribution), PDI = 0.02. ζ-potential = -42 ± 24 mV. ICP-MS results show 22,000 complexes per **AuNP100**.

3. 4. 4 Preparing AuNPs for TEM

TEM imaging was carried out on Citrate •**AuNPs**, IrbpySS •**AuNPs** and IrC_6 •**AuNPs**. For all nanoparticle samples 20 μL was added to a 200-mesh formvar-coated grid TEM grid and left to dry for 1 hour. Excess liquid was removed using filter paper. Samples prepared were 4.5 nM Citrate •**AuNP13**, IrbpySS •**AuNP13** and IrC_6 •**AuNP13**, 1.6 nM Citrate •**AuNP25**, IrbpySS •**AuNP25** and IrC_6 •**AuNP25** and 30 pM Citrate •**AuNP100**, IrbpySS •**AuNP100** and IrC_6 •**AuNP100**.

3. 4. 5 Preparing AuNPs for ICP-MS

Standard solutions were prepared containing the metals which were to be detected through ICP-MS (Gold and Iridium) in a series of concentrations from 0, 10, 25, 50,

100, 250, 500, 1000 ppb. These were used to calibrate the system and to calculate the metal content for each iridium functionalised AuNPs.

IrbpySS •**AuNPs** and IrC_6 •**AuNPs** were prepared as outlined in Section **3.4.3**. The AuNP samples were dissolved in minimal ultrapure Aqua Regia (3 HCl: 1 HNO_3), which was added in small aliquots until samples were fully digested. These samples were left to stir overnight at room temperature to ensure that the gold nanoparticles had fully digested. These samples were analysed at the University of Warwick to determine the number of iridium complexes per gold nanoparticle. In order to determine the gold concentration, a 1:200 dilution was done into 4% ultrapure Nitric Acid.

3.5 References

1 F. O. Garces, K. A. King, C. A. Craig, P. J. Spellane and R. J. Watts, *Abstr. Pap. Am. Chem. S.* **1987**, *193*, 194-Inor.

2 S. Lamansky, P. Djurovich, D. Murphy, F. Abdel-Razzaq, R. Kwong, I. Tsyba, M. Bortz, B. Mui, R. Bau and M. E. Thompson, *Inorg. Chem.* **2001**, *40*, 1704-1711.

3 M. S. Lowry and S. Bernhard, *Chem. Eur. J.* **2006**, *12*, 7970-7977.

4 A. Tsuboyama, H. Iwawaki, M. Furugori, T. Mukaide, J. Kamatani, S. Igawa, T. Moriyama, S. Miura, T. Takiguchi, S. Okada, M. Hoshino and K. Ueno, *J. Am. Chem. Soc.* **2003**, *125*, 12971-12979.

5 C. H. Yang, Y. M. Cheng, Y. Chi, C. J. Hsu, F. C. Fang, K. T. Wong, P. T. Chou, C. H. Chang, M. H. Tsai and C. C. Wu, *Angew. Chem. Int. Ed. Engl.* **2007**, *46*, 2418-21.

6 E. I. Mayo, K. Kilsa, T. Tirrell, P. I. Djurovich, A. Tamayo, M. E. Thompson, N. S. Lewis and H. B. Gray, *Photochem. Photobiol. Sci.* **2006**, *5*, 871-3.

7 E. Baranoff, J. H. Yum, I. Jung, R. Vulcano, M. Gratzel and M. K. Nazeeruddin, *Chem. Asian. J.* **2010**, *5*, 496-9.

8 K. Y. Zhang, P. Gao, G. Sun, T. Zhang, X. Li, S. Liu, Q. Zhao, K. K. Lo and W. Huang, *J Am Chem Soc* **2018**, *140*, 7827-7834.

9 K. K. W. Lo, M. W. Louie and K. Y. Zhang, *Coordin. Chem. Rev.* **2010**, *254*, 2603-2622.

10 L. He, Y. Li, C. P. Tan, R. R. Ye, M. H. Chen, J. J. Cao, L. N. Ji and Z. W. Mao, *Chem. Sci.* **2015**, *6*, 5409-5418.

11 K. K. W. Lo and K. K. S. Tso, *Inorg. Chem. Front.* **2015**, *2*, 510-524.

12 V. Venkatesh, R. Berrocal-Martin, C. J. Wedge, I. Romero-Canelon, C. Sanchez-Cano, J. I. Song, J. P. C. Coverdale, P. Y. Zhang, G. J. Clarkson, A. Habtemariam, S. W. Magennis, R. J. Deeth and P. J. Sadler, *Chem. Sci.* **2017**, *8*, 8271-8278.

13 H. F. Shi, H. B. Sun, H. R. Yang, S. J. Liu, G. Jenkins, W. Feng, F. Y. Li, Q. Zhao, B. Liu and W. Huang, *Adv. Funct. Mater.* **2013**, *23*, 3268-3276.

14 J. Y. Jiang, C. Q. Zhang, W. P. Lin, Y. H. Liu, S. J. Liu, Y. J. Xu, Q. Zhao and W. Huang, *Macromol. Rapid. Comm.* **2015**, *36*, 640-646.

15 J. Q. Wang, X. J. Hou, C. Z. Jin and H. Chao, *Chinese. J. Chem.* **2016**, *34*, 583-588.

16 K. K. Lo, W. K. Hui, D. C. Ng and K. K. Cheung, *Inorg. Chem.* **2002**, *41*, 40-6.

17 K. K. Lo, B. T. Chan, H. W. Liu, K. Y. Zhang, S. P. Li and T. S. Tang, *Chem. Commun. (Camb).* **2013**, *49*, 4271-3.

18 K. K. W. Lo and K. Y. Zhang, *RSC. Adv.* **2012**, *2*, 12069-12083.

19 M. Yu, Q. Zhao, L. Shi, F. Li, Z. Zhou, H. Yang, T. Yi and C. Huang, *Chem. Commun. (Camb).* **2008**, 2115-7.

20 W. L. Jiang, Y. Gao, Y. Sun, F. Ding, Y. Xu, Z. Q. Bian, F. Y. Li, J. Bian and C. H. Huang, *Inorg. Chem.* **2010**, *49*, 3252-3260.

21 K. K. W. Lo, P. K. Lee and J. S. Y. Lau, *Organometallics.* **2008**, *27*, 2998-3006.

22 K. L. Kelly, E. Coronado, L. L. Zhao and G. C. Schatz, *J. Phys. Chem. B.* **2003**, *107*, 668-677.

23 M. C. Daniel and D. Astruc, *Chem. Rev.* **2004**, *104*, 293-346.

24 E. Boisselier and D. Astruc, *Chem. Soc. Rev.* **2009**, *38*, 1759-1782.

25 C. R. Patra, R. Bhattacharya, D. Mukhopadhyay and P. Mukherjee, *Adv. Drug. Deliv. Rev.* **2010**, *62*, 346-361.

26 Y. J. Gu, J. Cheng, C. W. Man, W. T. Wong and S. H. Cheng, *Nanomedicine.* **2012**, *8*, 204-11.

27 M. Prabaharan, J. J. Grailer, S. Pilla, D. A. Steeber and S. Gong, *Biomaterials.* **2009**, *30*, 6065-75.

28 K. Kalimuthu, B. C. Lubin, A. Bazylevich, G. Gellerman, O. Shpilberg, G. Luboshits and M. A. Firer, *J. Nanobiotechnology.* **2018**, *16*, 34.

29 C. S. Kim, X. Li, Y. Jiang, B. Yan, G. Y. Tonga, M. Ray, D. J. Solfiell and V. M. Rotello, *Methods.* **2015**, *2*, 306-15.

30 M. Azubel, J. Koivisto, S. Malola, D. Bushnell, G. L. Hura, A. L. Koh, H. Tsunoyama, T. Tsukuda, M. Pettersson, H. Hakkinen and R. D. Kornberg, *Science.* **2014**, *345*, 909-12.

31 G. Nasr, A. Guerlin, F. Dumur, S. A. Baudron, E. Dumas, F. Miomandre, G. Clavier, M. Sliwa and C. R. Mayer, *J. Am. Chem. Soc.* **2011**, *133*, 6501-4.

32 P. Pramod, P. K. Sudeep, K. G. Thomas and P. V. Kamat, *J. Phys. Chem. B.* **2006**, *110*, 20737-41.

33 S. A. M. Osborne and Z. Pikramenou, *Faraday. Discuss.* **2015**, *185*, 219-231.

34 F. Miomandre, S. Stancheva, J. F. Audibert, A. Brosseau, R. B. Pansu, M. Lepeltier and C. R. Mayer, *J. Phys. Chem. C.* **2013**, *117*, 12806-12814.

35 N. J. Rogers, H. C. Jeffery, S. Claire, D. J. Lewis, G. Zikeli, N. J. Hodges, S. Egginton, G. B. Nash and Z. Pikramenou, *Nanomedicine.* **2017**, *12*, 2725-2740.

36 Z. Pikramenou, A. Davies, D. J. Lewis, S. Claire, N. J. Rogers, R. M. Harris, S. Farabi, I. B. Styles, S. P. Watson, S. G. Thomas and N. J. Hodges, *J. Biol. Inorg. Chem.* **2014**, *19*, S717-S718.

37 N. J. Rogers, S. Claire, R. M. Harris, S. Farabi, G. Zikeli, I. B. Styles, N. J. Hodges and Z. Pikramenou, *Chem. Commun.* **2014**, *50*, 617-619.

38 S. Sprouse, K. A. King, P. J. Spellane and R. J. Watts, *J. Am. Chem. Soc.* **1984**, *106*, 6647-6653.

39 L. Ackermann, P. Novak, R. Vicente and N. Hofmann, *Angew. Chem. Int. Edit.* **2009**, *48*, 6045-6048.

40 S. J. Adams, D. J. Lewis, J. A. Preece and Z. Pikramenou, *ACS Appl. Mater. Interfaces.* **2014**, *6*, 11598-11608.

41 S. Ladouceur, D. Fortin and E. Zysman-Colman, *Inorg. Chem.* **2010**, *49*, 5625-5641.

42 B. Schmid, F. O. Garces and R. J. Watts, *Inorg. Chem.* **1994**, *33*, 9-14.

43 S. H. Wu, J. W. Ling, S. H. Lai, M. J. Huang, C. H. Cheng and I. C. Chen, *J. Phys. Chem. A.* **2010**, *114*, 10339-10344.

44 Z. J. Li, P. Cui, C. Z. Wang, S. Kilina and W. F. Sun, *J. Phys. Chem. C.* **2014**, *118*, 28764-28775.

45 J. N. Demas and G. A. Crosby, *J. Am. Chem. Soc.* **1970**, *92*, 7262-&.

46 M. G. Colombo, A. Hauser and H. U. Gudel, *Inorg. Chem.* **1993**, *32*, 3088-3092.

47 D. R. Martir and E. Zysman-Colman, *Coordin. Chem. Rev.* **2018**, *364*, 86-117.

48 S. A. M. Osborne in *Luminescent Ruthenium Nanoprobes for Applications in Dye Sensitized Solar Cells*, *Vol. P.h.D* University of Birmingham, **2017**.

49 F. Schulz, T. Homolka, N. G. Bastus, V. Puntes, H. Weller and T. Vossmeyer, *Langmuir.* **2014**, *30*, 10779-10784.

50 J. Turkevich, P. C. Stevenson and J. Hillier, *Discuss Faraday Soc* **1951**, 55-&.

51 G. Frens, *Nature-Phys. Sci.* **1973**, *241*, 20-22.

52 N. R. Jana, L. Gearheart and C. J. Murphy, *Langmuir.* **2001**, *17*, 6782-6786.

53 J. Kimling, M. Maier, B. Okenve, V. Kotaidis, H. Ballot and A. Plech, *J. Phys. Chem. B.* **2006**, *110*, 15700-15707.

54 K. C. Grabar, R. G. Freeman, M. B. Hommer and M. J. Natan, *Anal. Chem.* **1995**, *67*, 735-743.

55 N. J. Rogers in *The development of Gold Nanoparticles labelled with Transition Metal Complexes for Imaging Applications*, *Vol.* University of Birmingham, **2014**.

56 I. Ojea-Jimenez, N. G. Bastus and V. Puntes, *J. Phys. Chem. C.* **2011**, *115*, 15752-15757.

57 J. Polte, *Crystengcomm.* **2015**, *17*, 6809-6830.

58 I. Ojea-Jimenez, F. M. Romero, N. G. Bastus and V. Puntes, *J. Phys. Chem. C.* **2010**, *114*, 1800-1804.

59 C. Engelbrekt, P. S. Jensen, K. H. Sorensen, J. Ulstrup and J. D. Zhang, *J. Phys. Chem. C.* **2013**, *117*, 11818-11828.

60 M. Wuithschick, A. Birnbaum, S. Witte, M. Sztucki, U. Vainio, N. Pinna, K. Rademann, F. Emmerling, R. Kraehnert and J. Polte, *ACS. Nano.* **2015**, *9*, 7052-7071.

61 C. Ziegler and A. Eychmuller, *J. Phys. Chem. C.* **2011**, *115*, 4502-4506.

62 P. K. Jain, K. S. Lee, I. H. El-Sayed and M. A. El-Sayed, *J. Phys. Chem. B.* **2006**, *110*, 7238-7248.

63 Malvern in *Dynamic Light Scattering: An Introduction in 30 Minutes*, *Vol.* **2019**.

64 M. Panalytical in *Dynamic Light Scattering: Common Terms Defined*, *Vol. 2018* **2018**.

65 M. Panalytical in *Intensity - Volume - Number*, *Vol. 2018* **2018**.

66 K. N. Clayton, J. W. Salameh, S. T. Wereley and T. L. Kinzer-Ursem, *Biomicrofluidics.* **2016**, *10*, 054107.

67 S. Bhattacharjee, *J. Control. Release.* **2016**, *235*, 337-351.

68 H. Hakkinen, *Nat. Chem.* **2012**, *4*, 443-455.

69 D. J. Lavrich, S. M. Wetterer, S. L. Bernasek and G. Scoles, *J. Phys. Chem. B.* **1998**, *102*, 3456-3465.

70 C. D. Bain, E. B. Troughton, Y. T. Tao, J. Evall, G. M. Whitesides and R. G. Nuzzo, *J. Am. Chem. Soc.* **1989**, *111*, 321-335.

71 N. J. Rogers in *Development of Gold Nanoparticles labelled with Transition Metal Complexes for Imaging Applications*, *Vol. PhD* University of Birmingham, **2015**, p. 314.

72 S. Claire in *Development of Nanoparticles for Imaging Applications*, *Vol. PhD* University of Birmingham, **2016**.

73 S. Eustis and M. A. El-Sayed, *Chem. Soc. Rev.* **2006**, *35*, 209-217.

74 S. J. Adams, A. J. Carrod, L. A. Rochford, M. Walker and Z. Pikramenou, *Chemistry. Select.* **2018**, *3*, 3251-3257.

CHAPTER 4. IRIDIUM NANOPARTICLES FOR MULTICHANNEL LUMINESCENCE LIFETIME IMAGING, MAPPING LOCALISATION IN LIVE CANCER CELLS

4. 1 Introduction

The effective sensitivity of single-photon fluorescence microscopy is often limited by out-of-focus light, especially in thick samples such as tissues. Therefore, multiphoton microscopy is often employed and is fast becoming the most widely used optical microscopy for *in vivo* experiments.[1, 2] Multiphoton imaging has led to breakthroughs in medical diagnostics, specifically in quantification of angiogenesis and cancer metastasis, reaching to several millimetres in depth detection, thus providing invaluable information on tumour vasculature and tumour microenvironment.[3-5] A limitation to using intensity based methods is the high concentrations of luminescent probes needed to visualise subcellular structures, which can be toxic and generates a high background signal. Therefore, researchers have started looking at lifetimes based techniques as a more sensitive method of detection in comparison to emission based methods. Utilising the advantages of multiphoton excitation and combining this with lifetime imaging has revealed a wealth of additional information, which is independent of the probe concentration but sensitive to local changes of the environment.[6, 7]

Lifetime based techniques are advantageous over emission based techniques because they allow for complete elimination of background autofluorescence which is only a couple of nanoseconds, by using time-gating methods.[8-10] This means that long phosphorescence and fluorescence lifetimes can be detected separately from background autofluorescence. Luminescence lifetimes are detected independent of

probe concentration,[11] meaning lower concentrations can be used in comparison to emission based techniques, where high loading is needed in cells. There are currently two types of imaging methods that utilize the luminescence lifetimes of chemical and biological imaging probes. Fluorescence lifetime imaging microscopy (FLIM) uses probes that contain short nanosecond fluorescent lifetimes, typical around 1 – 10 ns.[12] These short nanosecond lifetimes are within the range of lifetimes detected from cellular autofluorescence lifetimes, so research has shifted into looking at phosphorescent probes for phosphorescence lifetimes imaging microscopy (PLIM). These probes have long-lived luminescence lifetimes extending into the microsecond range, due the spin-forbidden triplet excited state.[13] Therefore there is a strong interest in developing phosphorescent probes with long excited state lifetimes, which can be gated from short-lived signals associated with autofluorecence, expanding sensitivity in signal detection.[14]

Transition metal complexes are ideal candidates for phosphorescence lifetime imaging as they emit from a long-lived triplet excited state, have high two-photon absorption cross-sections and have previously been found to function effectively as biological imaging probes for fluorescence emission based microscopy due to their desirable photophysical properties. Despite this, there are only a few examples in the literature utilising these desirable properties of transition metal complexes for their use in phosphorescence lifetime imaging. This was seen by using ruthenium(II) complexes as PLIM probes to study nuclear DNA in both fixed and live cells.[11] The results showed that DNA-bound ruthenium(II) complexes exhibited longer luminescence lifetimes of 185 ns in comparison to that of unbound ruthenium(II) complexes present in the cytoplasm which displayed a lifetime of 124 ns (Figure 4.1).

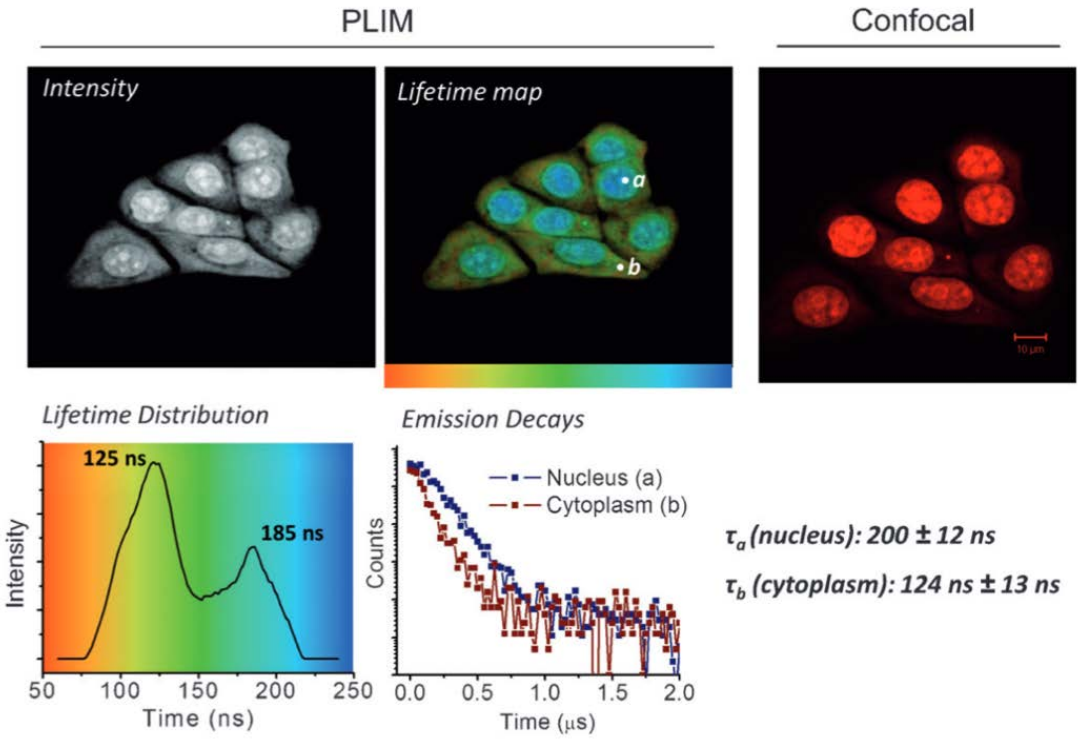

Figure 4.1. (Left) Phosphorescence lifetime images (PLIM) and (Right) confocal images of fixed, permeabilized MCF7 cells treated with complex 1 (100 μm, 45 minutes, PBS buffer).[11]

The cytoplasmic staining appears to show weak emission from the ruthenium(II) complexes in comparison to the nuclear staining which can be seen in the confocal image. However, the corresponding lifetime image shows a lot of detail within the cytoplasm and further analysis was carried out to identify the small changes in lifetimes between the two regions of the cells. This shows how sensitive the detection is for lifetime imaging techniques and highlights the limitations of emission based methods. The ability to detect these differences in the phosphorescent probes luminescence lifetime within cells will lead to more sensitive way of mapping localisation patterns, understanding interactions with biological targets and probing the cellular microenvironment. The latter was demonstrated by Baggaley *et al*. which showed the first example of oxygen sensing in cells using a heteronuclear Ir(III)-Ln(III) luminescent

complex, in which lifetime changes were monitored by PLIM.[15] They showed some very promising results with the Ir(III) luminescence lifetime decreasing upon increasing volumes of O_2 levels within HeLa cells, showing that the probe is sensitive to local changes in environment. The recorded lifetimes were 435, 520, 586 and 664 ns for a relative oxygen concentration of 100 %, 50%, 21 % and 0 % respectively. These changes in lifetimes correspond to the visual change seen in the lifetime images, where the colour shifts from orange to blue in the lifetime images (Figure 4.2).

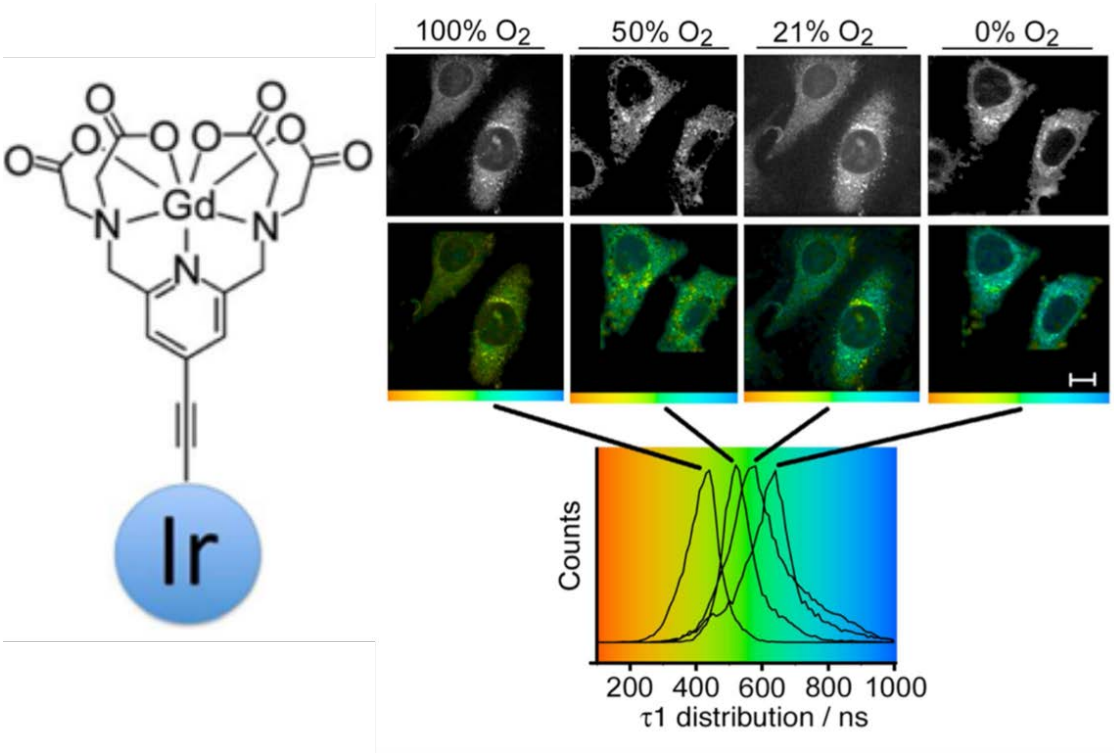

Figure 4.2. (Left) Schematic representation of dyad Ir-Gd phosphorescence complex. (Right) Two-photon phosphorescence lifetime (λ_{ex} = 760 nm) imaging of Ir-Gd stained HeLa cells (50 μm, 18 h, fixed) under varying concentrations of O_2. Scale bar = 10 μm.[15]

Combining both phosphorescence and fluorescence lifetime imaging is highly advantageous for samples containing multiple labels and is made possible through time-gated methods (FLIM/PLIM).[16] The technique has been demonstrated successfully in the literature on cyclometalated platinum(III) complexes which showed

variable lifetimes from the nanosecond range to the millisecond range depending on the probes localisations within cells.[16] Through this technique the short nanosecond lifetimes could be detected by FLIM and the long-lived lifetimes detected by PLIM, with no overlap of the emitting signals. The results showed that discrimination between fluorescent and phosphorescent labels in multiply stained cells and tissues could be achieved using this method (Figure 4.3).

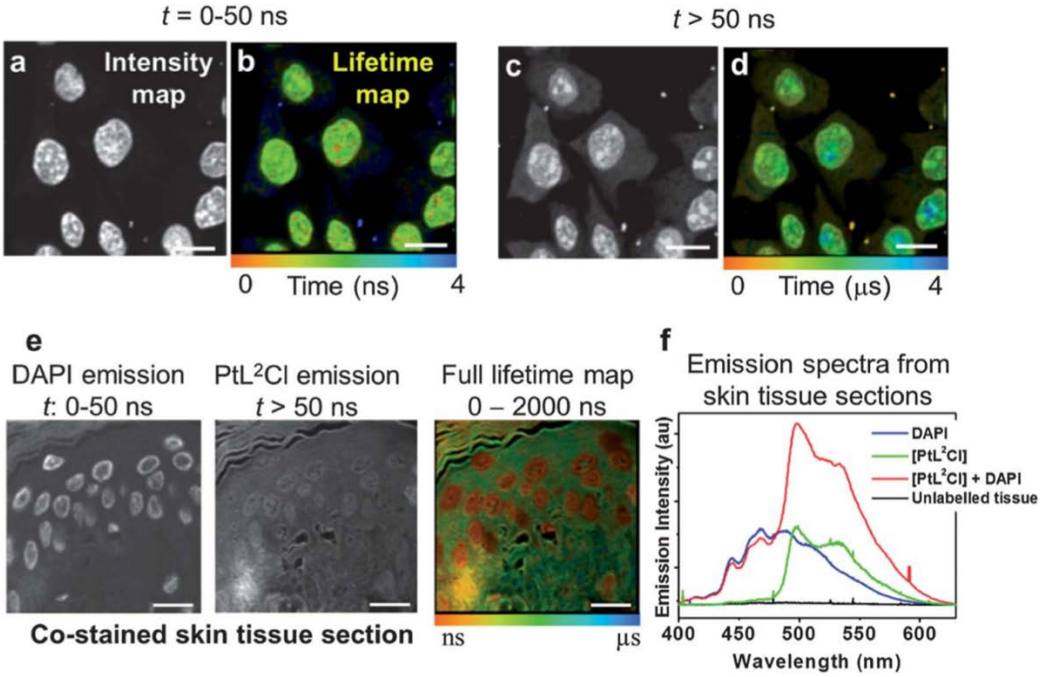

Figure 4.3. (Top) Two-photon images of live CHO-K1 cells co-labelled with PtL1 Cl and Hoechst. (a and c) Intensity images, (b and d) lifetime maps for short nanosecond lifetimes and (c and d) correspond to long-lived emission from PtL1 Cl. (Bottom) Skin epidermis co-labelled with PtL2 Cl and DAPI. (e) Time-gated intensity images demonstrate separation of short-lived emission of DAPI/autofluorescence from PtL2 Cl. (f) Emission spectra from epidermis: unlabelled (black), labelled with DAPI (blue) or PtL2 Cl (green), co-labelled with PtL2 Cl and DAPI (red).[16]

The lifetime images show that short-lived lifetimes from DAPI and cellular autofluorescence can be completely separated from PtL2 long-lived signal which can be seen visually in Figure 4.3, e. This was a novel approach which used the powers of

multiphoton excitation and both lifetime imaging methods on transition metal complexes. To date, there are no examples in the literature for using multiphoton excitation and FLIM/PLIM imaging on transition metal complexes coated on gold nanoparticles.

Gold nanoparticles have unique optical properties and can easily incorporate more than one type of imaging or targeting agent, which allows them to be used as multifunctional nanoplatforms for both imaging and cancer therapies.[17-19] The gold nanoparticle scaffold is ideal as a multimodal probe which can be detected by electron microscopy techniques as well as reflectance microscopy, which is highly advantageous for 100 nm gold nanoparticles to be detected as single, non-aggregated particles within the microscope diffraction limit.[20, 21] Even though the characteristic surface plasmon resonance of the gold nanospheres has been used extensively as signal detection,[22] there is little investigation in monitoring gold nanoparticles by lifetime imaging.[23] We have been interested in the development of nanosized probes based on gold scaffold and luminescent transition metal complexes in order to translate the attractive luminescent properties of the metal complexes to the nanosized probe.[24-26]

4. 2 Chapter Summary

This chapter looks at the synthesis of iridium(III) coated nanoparticles for multichannel lifetime imaging using multiphoton excitation and the design of novel nanoprobe based on a luminescent iridium complex with long legs for attachment to gold. The previous chapter discussed the synthesis and photophysical characterisations of two iridium functionalised nanoparticles (Scheme 4.1). It was previously shown that the distance

of the luminescent centre from the gold nanoparticle enhances the lifetime properties of the ruthenium probes.[25] Incorporating the hexyl chain on the phenyl pyridine was designed to increase hydrophobicity of the iridium complex and stabilization onto gold, increasing signal and therefore proposing better permeability across the cell membrane.[27, 28]

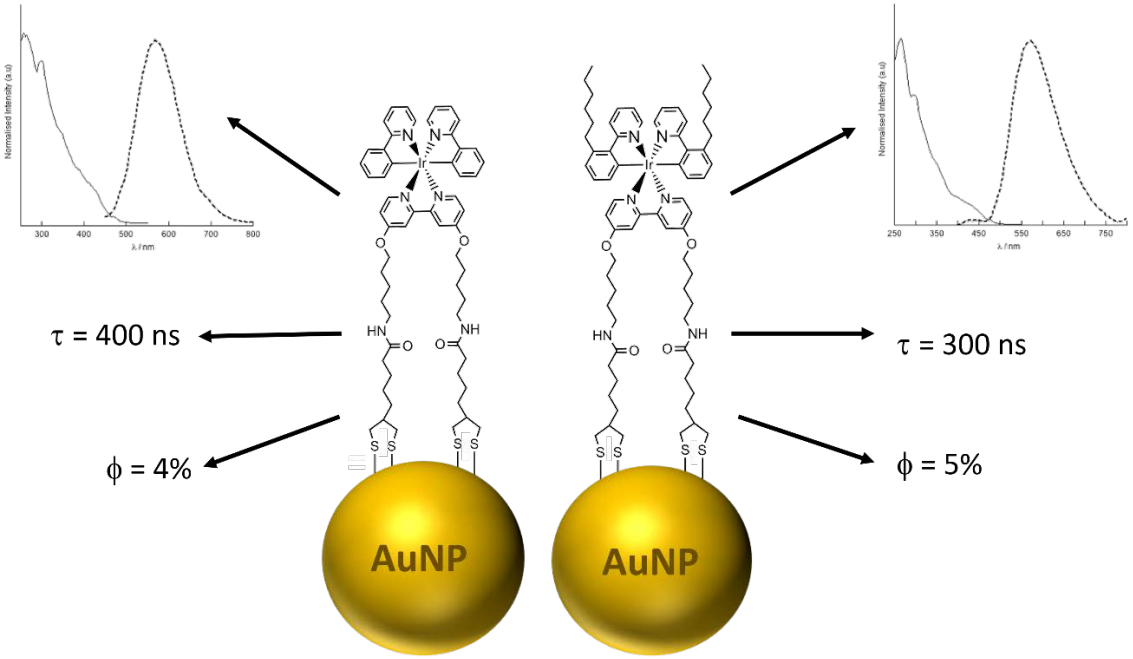

Scheme 4.1. Summary of the photophysical properties of IrbpySS •AuNPs and IrC_6 •AuNPs

Detection of the characteristic long luminescence lifetime of the iridium complex and the short-lived lifetime detected from the gold resonance signal was monitored by lifetime imaging microscopy. Different sizes of gold nanoparticles (13 nm, 25 nm and 100 nm) were functionalised with the iridium(III) probe and their uptake in live HeLa cells was analysed using lifetime imaging, optical microscopy and electron based techniques. The results of nanoparticle localisation in cells are also supported by Total Internal Reflection Fluorescence Microscopy (TIRF), electron microscopy as well as Inductively Coupled Plasma Mass Spectrometry (ICP-MS) analysis.

4. 3 Results and Discussion

4. 3. 1 Iridium functionalised AuNPs as multiphoton lifetime imaging probes

4. 3. 1.1 Multiphoton properties

The photophysical properties of these iridium functionalised nanoprobes were characterised to assess their ability to undergo multiphoton excitation for multiphoton lifetime imaging applications. The multiphoton absorption cross-sections and power dependence analysis of the luminescence upon excitation at 760 nm was examined. The two-photon luminescence spectra of **IrC_6** in MeOH and IrC_6 **•AuNP25** were successfully recorded and compared to their corresponding single-photon luminescence spectra. The results showed that two-photon excitation at 760 nm produced a nearly identical emission spectra as produced by single-photon excitation (Figure 4.4).

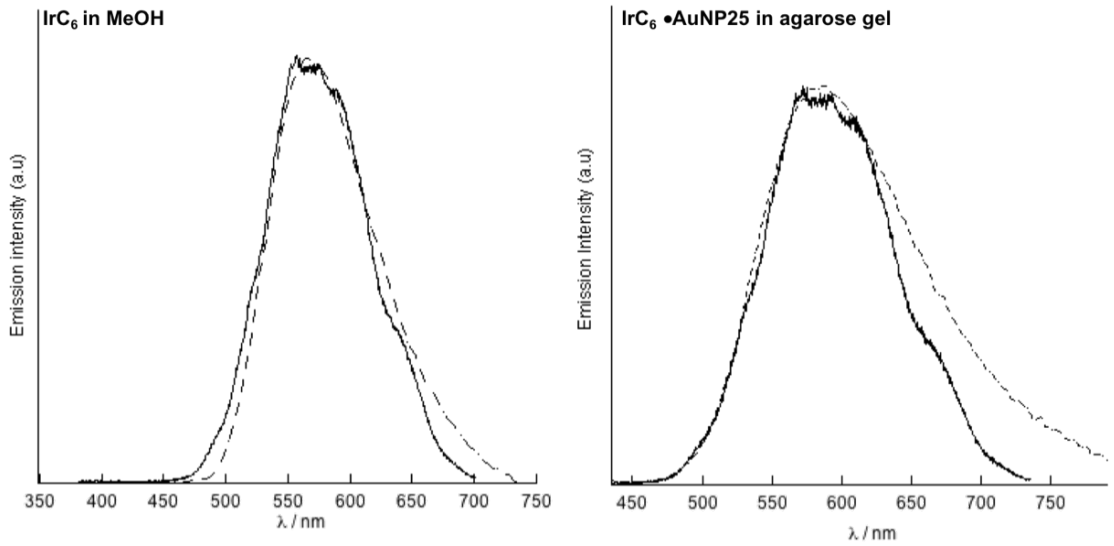

Figure 4.4. Emission spectra produced from one photon excitation λ_{exc} = 375 nm (dotted line) and two-photon excitation λ_{exc} = 760 nm (solid line) for (Left) IrC_6 and (Right) IrC_6 •AuNP25 in agarose gel. Spectra have been normalized.

Whilst trying to obtain the two-photon luminescence spectra for IrC_6 •**AuNP25** in water, some issues arose. Two-photon excitation was attempted in solution, however it appeared nanoparticles were moving in and out of focus due to Brownian motion in solution which meant an emission spectra could not be recorded using this method. Therefore, an immobilisation technique was carried out to record the two-photon luminescence spectra, which allowed us to calculate the two-photon absorption cross-sections and power dependence. The IrC_6 •**AuNP25** (1.6 nM, 1 mL) were immobilised in 0.1% agarose gel, and a luminescence spectra was generated using multiphoton excitation. This meant that the two-photon luminescence spectra for IrC_6 •**AuNP25** had to be recorded in agarose gel. A solution of 0.1 % agarose gel containing no iridium functionalised nanoparticles was excited at 760 nm and found to produce no luminescence. Power dependence studies determines the ability for the compound to undergo two-photon excitation by measuring the luminescence intensity at increasing laser powers. For IrC_6 •**AuNP25** immobilised in 0.1 % agarose gel, the laser dependence studies were carried out on four different areas and the average presented (Figure 4.5).

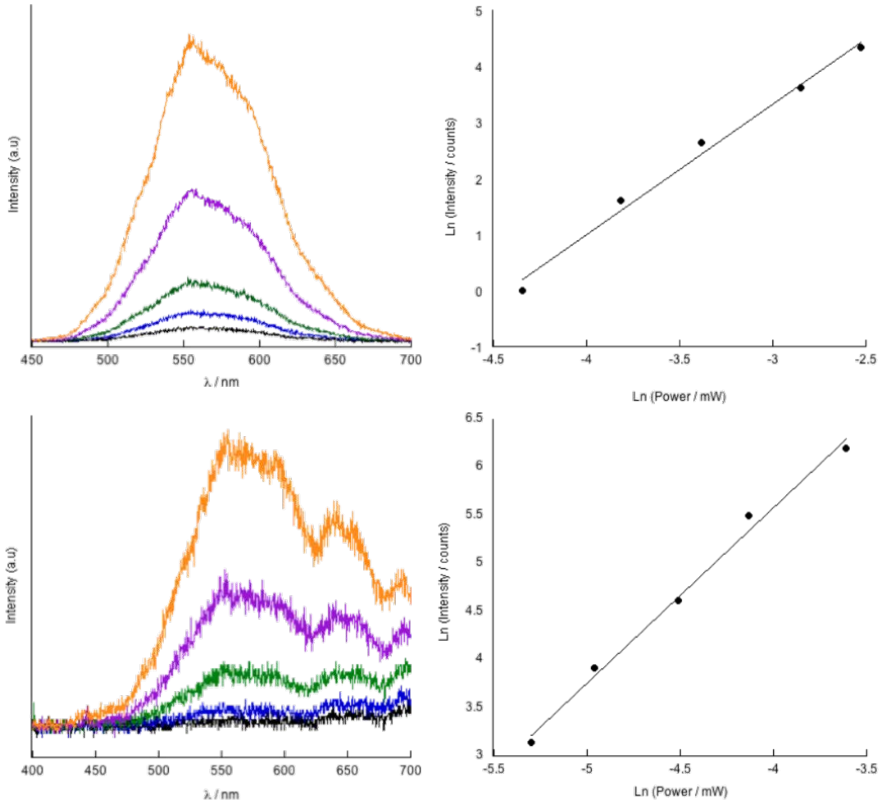

Figure 4.5. (Left) Two-photon luminescence spectra taken at increasing laser power for (Top) IrC_6 and (Bottom) IrC_6 •AuNP25 using 760 nm excitation. (Right) Power dependence studies showing log-log plot of integrated emission intensity versus laser power. Slope calculated as 2.30, R = 0.9959 for (Top) IrC_6 and 2.06, R = 0.9944 for (Bottom) IrC_6 •AuNP25.

A log-log plot of the integrated emission intensity versus laser power shows quadratic dependence for both the **IrC_6** probe and IrC_6 **•AuNP25**. The slope was calculated and found to be 2.30 and 2.06 for **IrC_6** and IrC_6 **•AuNP25** respectively, indicating strongly that a two-photon process is occurring.[29] The two-photon absorption cross-sections ($\sigma 2$) were calculated using the results from the highest laser power (0.069 mW for both **IrC_6** (MeOH) and IrC_6 **•AuNP25** (0.1% agarose gel). The two-photon absorption cross-section were calculated using the equation below, where r and s stand for the reference standard and sample respectively, $\sigma 2$ for two-photon absorption cross-section, c for concentration, $I\lambda$ and $\Phi I\lambda$ are the fluorescence intensity at the wavelength λ for two-

photon and one-photon, respectively. ∑FL describes the integrated intensity of the one-photon fluorescence spectra and ϕ is the one-photon fluorescence quantum yield, which is assumed to be the same under two-photon conditions.[30]

$$\sigma_{2s} = \frac{C_r}{C_s} * \frac{I_{\lambda s}}{I_{\lambda r}} * \frac{(FI_{\lambda r}/(\sum FI_r))}{(FI_{\lambda s}/(\sum FI_s))} * \frac{\phi_r}{\phi_s} * \sigma_{2r}$$

This equation compares the luminescence intensity of the samples to a reference standard, Rhodamine B in Methanol[31]. The recorded cross-sections are in units of Goeppert-Mayer (GM) where 1 GM = 10^{-50} cm^4 s $photon^{-1}$. The results showed an absorption cross-section of 38 GM for the IrC_6 in methanol and 2 x 10^3 GM per particle for IrC_6 •**AuNP25**. The absorption cross-section calculated for **IrC_6** agrees with similar iridium compounds.[32, 33] The absorption cross-section calculated for IrC_6 •**AuNP25**, is unusually high for any iridium-based luminescence signal and is therefore attributed to the enhancement by the gold nanoparticles surface plasmon resonance. Jiang *et al.* investigated the two-photon absorption properties of non-aggregated gold nanoparticles (40 nm) and aggregated gold nanoparticles. They found that the two-photon absorption cross-section increased from 4 x 10^2 GM to 5 x 10^3 GM when the particles aggregated. The increase was attributed to the enhanced plasmon coupling in the aggregated particles, which lead to an increase in two-photon absorption.[34] It is evident from our results that upon immobilisation of IrC_6 •**AuNP25** in 0.1% agarose gel, the nanoparticles have come together to form clusters or 'aggregates' of nanoparticles. The nanoparticles are in close spatial proximity to each which causes an enhancement in the plasmon resonance band, which is reflected in the high two-photon absorption cross-section.[35] These studies have shown the potential for these nanoprobes to be used as multiphoton lifetime imaging probes. This will be explored

in the following section, where uptake into HeLa cells will be investigated using two-photon lifetime microscopy and characterisation of the lifetimes detected will be used to map localisation in cells.

4. 3. 2 Multichannel luminescence lifetime imaging

Two-photon lifetime imaging works by detecting the characteristic long-lived lifetimes and short lifetimes in two separate channels. A pulsed Titanium: Sapphire (Ti: Sa) laser is used to induce fluorescence lifetimes (short) and phosphorescence lifetimes (long) from a sample which are collected simultaneously in two different channels. During the on-time the laser excites fluorescence and allows phosphorescence to be built up, when the laser is switched off the true phosphorescence is obtained, all within the same pixel dwell time (Figure 4.6).[36]

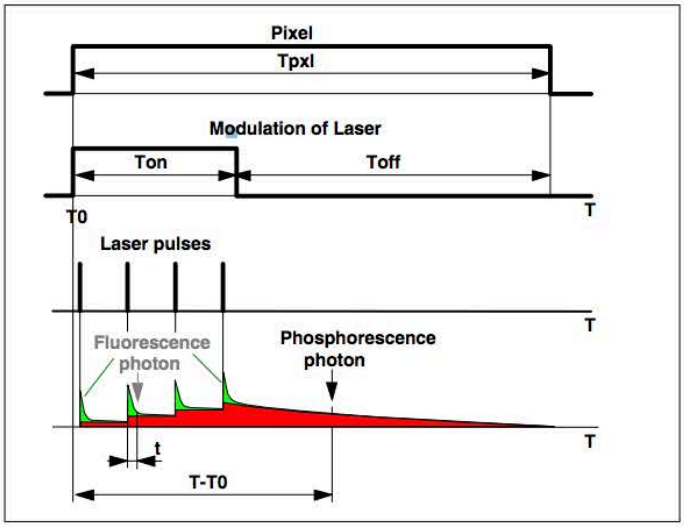

Figure 4.6. Principles of PLIM/ FLIM set up

Therefore, the PLIM channel detected the long-lived signal from the iridium complex and the FLIM channel identified the presence of AuNPs within the cell by detecting the characteristic SPR band of the gold. The co-localisation of these two signals revealed

uptake of these iridium functionalised nanoparticles with no decomposition of particles when inside the cell.

To investigate the potential of these nanoprobes as lifetime imaging agents, live HeLa cells were treated with IrC_6 •**AuNP13**, IrC_6 •**AuNP25** and IrC_6 •**AuNP100**. HeLa cells were dosed with a final concentration of 0.45 nM, 0.16 nM and 3 pM for IrC_6 •**AuNP13**, IrC_6 •**AuNP25** and IrC_6 •**AuNP100** respectively. Cells dosed with IrC_6 •**AuNP13** and IrC_6 •**AuNP100** were incubated for 5 hours and cells dosed with IrC_6 •**AuNP25** for 3 hours. Two-photon lifetime imaging was carried out at Rutherford Appleton Laboratories (RAL), in which long and short lifetimes were detected in two different channels. One channel was set to detect the long component of the iridium signal in the hundreds of nanoseconds range (PLIM) and the second channel was set to detect a short-lived signal in the tens of picosecond range (FLIM). The lifetimes obtained from the two channels were analysed separately for all three sizes of nanoparticles. The long-lived lifetimes detected in the PLIM channel were fit to three components for all samples and the lifetimes displayed in the PLIM channel are from the τ_3 lifetime component.

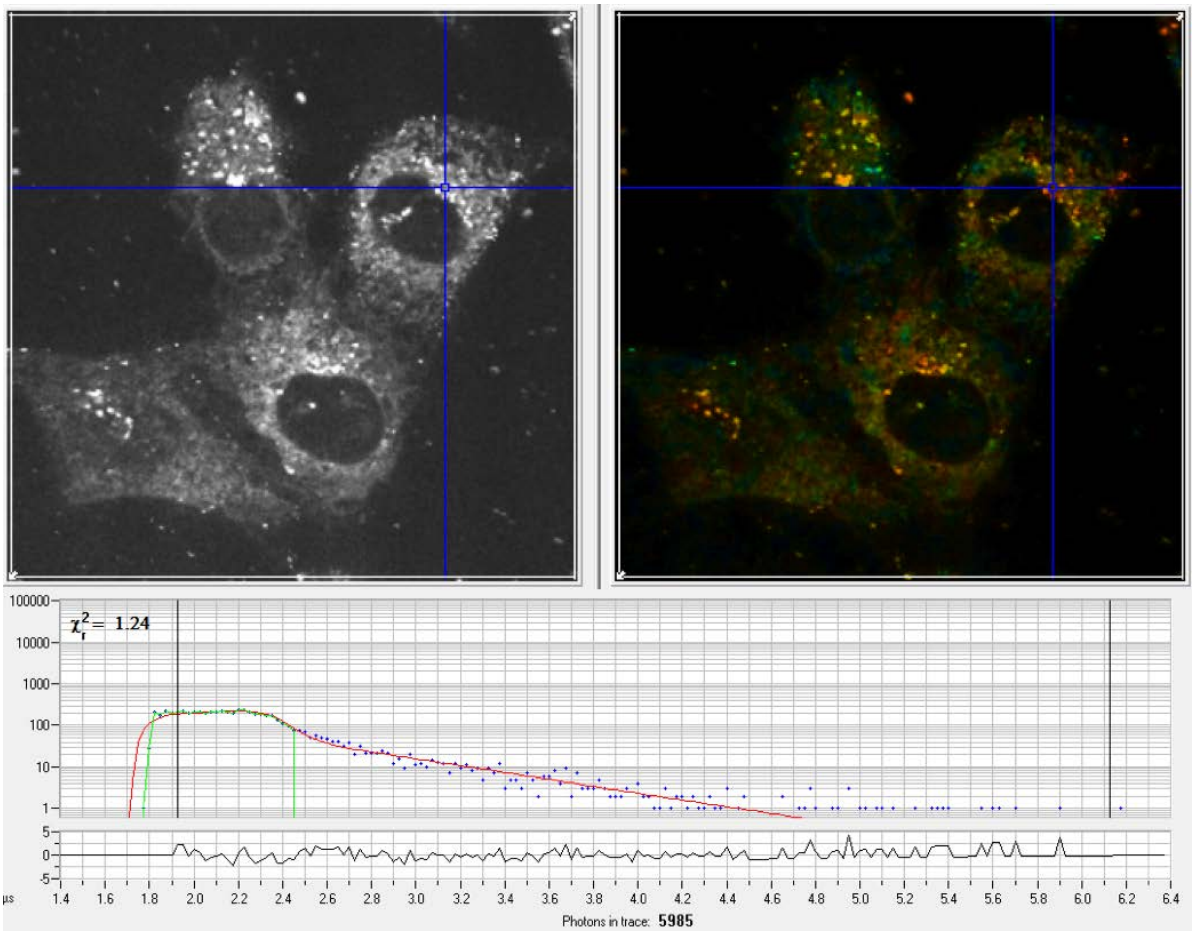

Figure 4.7. Two-photon phosphorescence lifetime analysed on SPCImage (Becker & Hickl software, version 5.0). (Left) Intensity image and (right) TP PLIM lifetime image displaying the τ_3 component coloured in RGB. Blue cross hairs showing iridium gold nanoparticles. Lifetime decay for the long-lived iridium signal, fitted to three components to give a χ^2 of 1.24.

The short-lived lifetimes detected in the FLIM channel were fit to one component. These short-lived picosecond lifetimes have been attributed to the characteristic SPR band of the gold nanoparticles. An example of the PLIM and FLIM lifetime decay plots that are extracted from the lifetime images are shown in Figure 4.7 (PLIM) and 4.8 (FLIM). This is an example dataset to show the lifetime decay plots extracted from a specific coordinate (blue crosshairs) within the images.

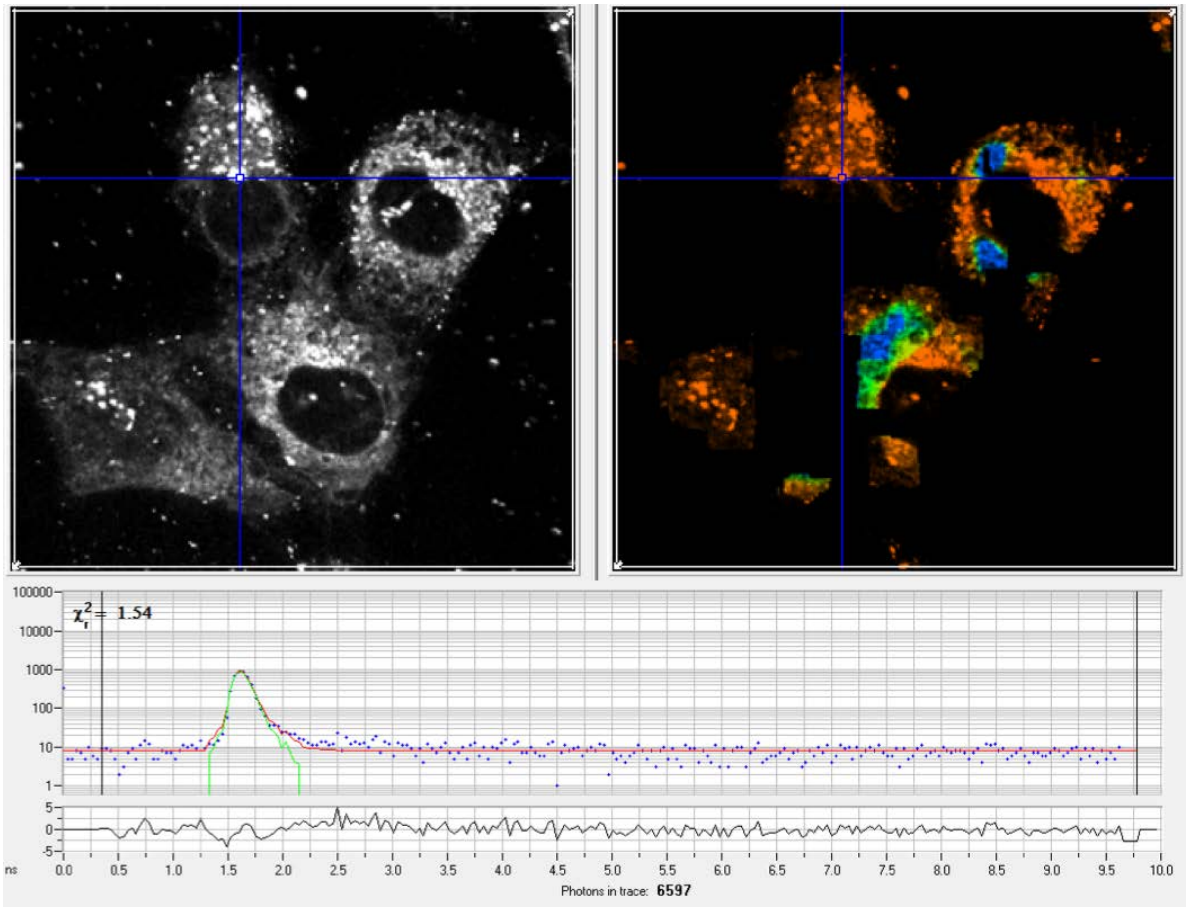

Figure 4.8. Two-photon fluorescence lifetime analysed on SPCImage (Becker & Hickl software, version 5.0). (Left) Intensity image and (Right) TP FLIM image displaying short-lived lifetimes coloured in RGB. Blue cross hairs showing iridium gold nanoparticles. A sharp peak is shown in the lifetime decay plot which is attributed to the short-lived signal from the gold. Lifetime decay is fitted to one component to give a χ^2 of 1.54.

The two-photon PLIM and FLIM images in live HeLa cells are shown below for IrC_6 •**AuNP13** (Figure 4.9), IrC_6 •**AuNP25** (Figure 4.10) and IrC_6 •**AuNP100** (Figure 4.11). The lifetime images from the FLIM channel can be seen on the left-hand side of the intensity image, with its corresponding colour map in picoseconds. The images from the PLIM channel are on the right-hand side of the intensity image and its corresponding colour map is in nanoseconds.

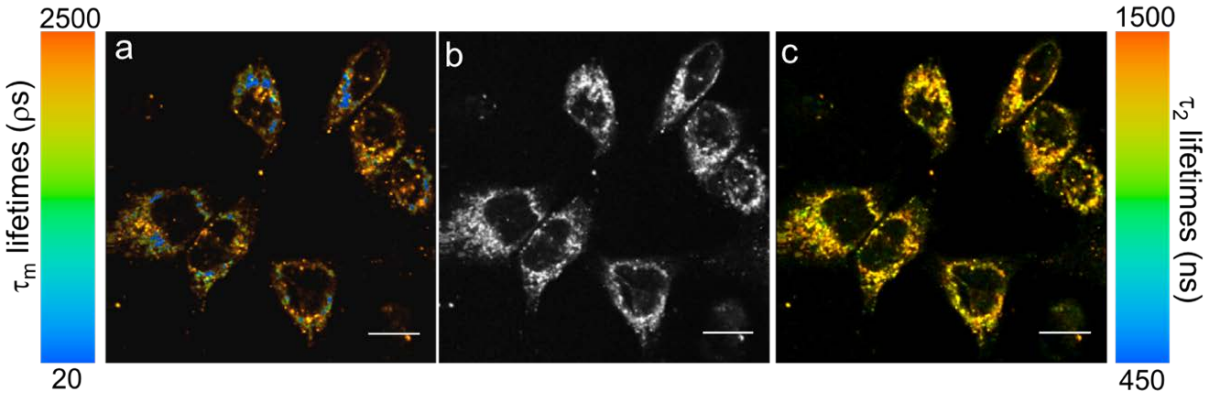

Figure 4.9. Two-photon images showing detection of the long-lived phosphorescence (PLIM) and short lived fluorescence (FLIM) lifetimes for multichannel detection. HeLa cells incubated with 0.45 nM IrC_6 •AuNP13 for 5 hours. (a) FLIM image showing detection of lifetimes in the range 20 – 2500 ps (colour map on the left). (b) Intensity image and (c) PLIM images showing detection of lifetimes in the range of 450 – 1500 ns (colour map on the right). λ_{exc} = 760 nm, scale bar = 10 µm.

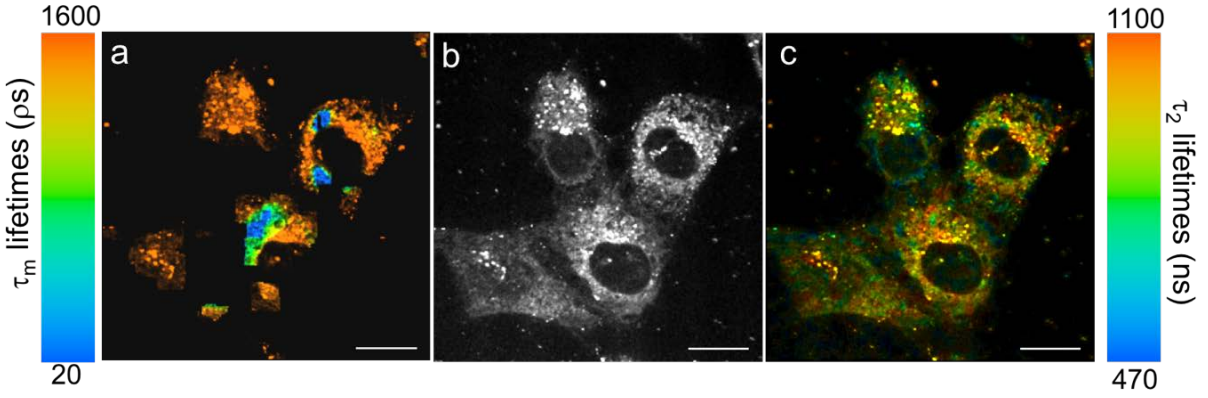

Figure 4.10. Two-photon images showing detection of the long-lived phosphorescence (PLIM) and short lived fluorescence (FLIM) lifetimes for multichannel detection. HeLa cells incubated with 0.16 nM IrC_6 •AuNP25 for 3 hours. (a) FLIM image showing detection of lifetimes in the range 20 – 1600 ps (colour map on the left). (b) Intensity image and (c) PLIM images showing detection of lifetimes in the range of 470 – 1100 ns (colour map on the right). λ_{exc} = 760 nm, scale bar = 10 µm.

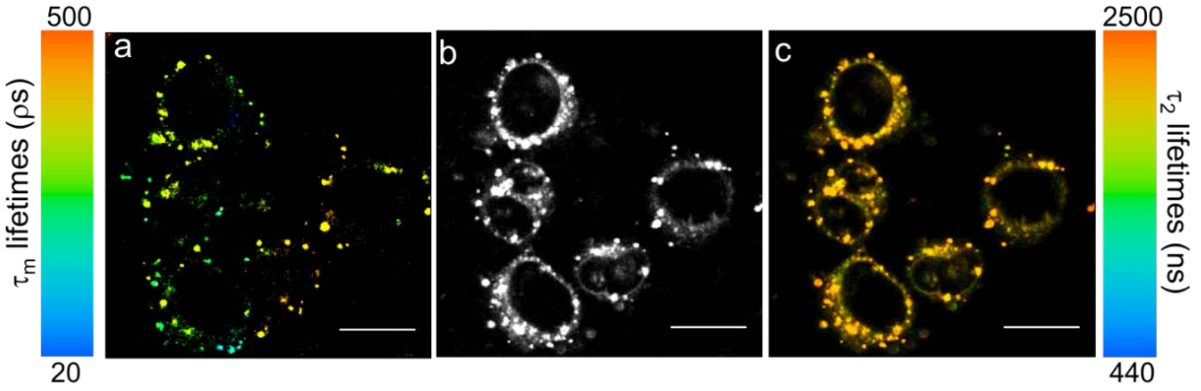

Figure 4.11. Two-photon images showing detection of the long-lived phosphorescence (PLIM) and short lived fluorescence (FLIM) lifetimes for multichannel detection. HeLa cells incubated with 3 pM IrC_6 •AuNP100 for 5 hours. (a) FLIM image showing detection of lifetimes in the range 20 – 500 s (colour map on the left). (b) Intensity image and (c) PLIM images showing detection of lifetimes in the range of 450 – 2500 ns (colour map on the right). λ_{exc} = 760 nm, scale bar = 10 µm.

The PLIM images revealed strong signal from the long-lived luminescence lifetimes within HeLa cells which could be detected using multiphoton lifetime imaging. The lifetimes detected were in the hundreds of nanoseconds range, positively identifying the characteristic lifetime of iridium in HeLa cells. A control of Z •**AuNP13** in HeLa cells was carried out to show no long-lived lifetimes detected in the PLIM channel (Appendix). The colour map shows a range of lifetimes detected from blue (short nanosecond lifetimes) to orange (long nanosecond lifetime). The range of lifetimes detected are similar for IrC_6 •**AuNP13** and IrC_6 •**AuNP25** which show a range between ~450 – 1500 ns. This is different for IrC_6 •**AuNP100** where the lifetime range extends to 2500 ns. The lifetime range present in the PLIM images shows lifetimes detected which are in the same range as the characteristic lifetimes recorded for **IrC_6** in water and the IrC_6 •**AuNPs** in solution (Figure 4.9, 4.10 and 4.11, c). It should be noted that detection in the nanosecond range revealed lifetimes which were longer than the

iridium nanoparticles in solution. This is due to the probe interacting with cellular proteins, causing the lifetimes to extend. This will be discussed in detail later in the chapter. The FLIM images (Figure 4.9, 4.10 and 4.11, a) show detection of short-lived lifetimes in the range of ~20 – 1600 ps for IrC_6 •**AuNP13** and IrC_6 •**AuNP25** and ~20 – 500 ps for IrC_6 •**AuNP100**. The fitting of the lifetime decay suggests this signal is coming from the gold. Interestingly, the short-lived signal detected within HeLa cells is slightly different for each size of nanoparticles as they appear to have different patterns of uptake. In the next figure, the PLIM and FLIM lifetime images have been false coloured yellow and magenta so the signals can be overlaid. This overlap of the short-lived and long-lived lifetime signals can be seen in Figure 4.12, c.

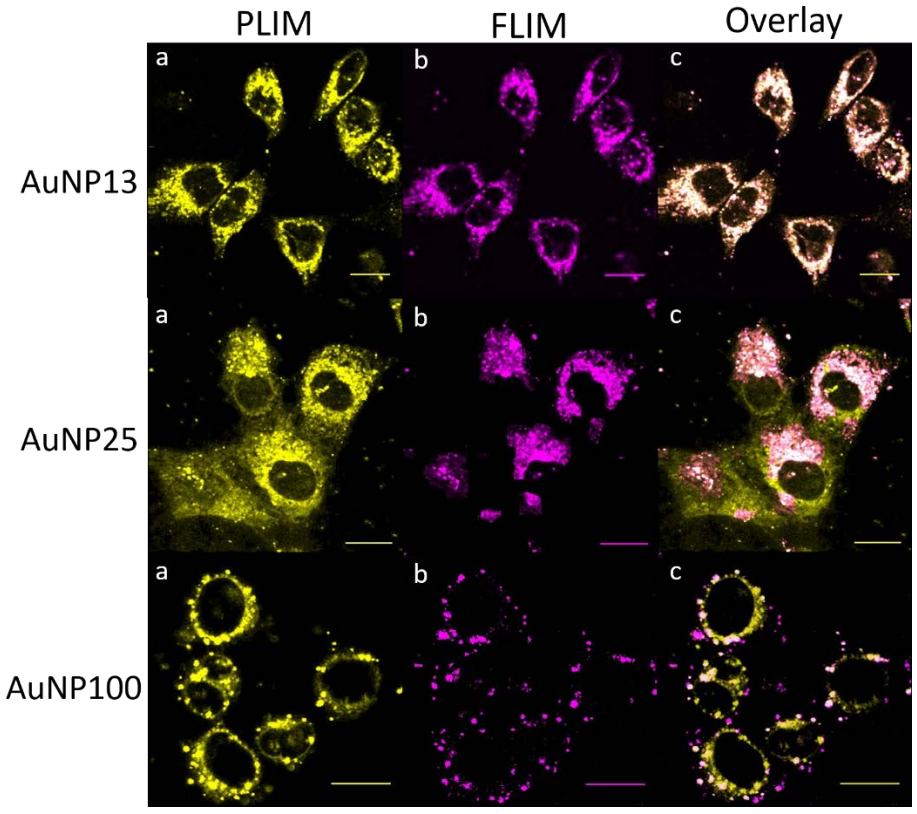

Figure 4.12. Two-photon lifetime microscopy showing multichannel detection of lifetimes present in PLIM and FLIM channels. (a) PLIM image showing long-lived lifetime signal (False coloured yellow), (b) FLIM images showing short-lived lifetime signal (False coloured magenta) and (c) Overlay of the PLIM and FLIM channels. λ_{exc} = 760 nm, scale bar = 10 µm.

The results for IrC_6 •**AuNP13** in HeLa cells show detection of short-lived lifetimes from the gold nanoparticles within the cytoplasm by FLIM and the long-lived lifetimes from the iridium in the PLIM channel. When overlaid the gold and iridium signals detected from the two channels appear to fully co-localise. This differs from the results of IrC_6 •**AuNP25** and IrC_6 •**AuNP100** in HeLa cells, where the gold signal from the FLIM channel has only been detected in certain areas of the cell and does not fully co-localise with the iridium signal detected in the PLIM channel. It is proposed that in areas where strong gold signal has been detected for IrC_6 •**AuNP25**, is where gold nanoparticles have localised together within the cell, giving strong resonance signal which can be detected. The areas where there is iridium signal detected within the cytoplasm, but appears to be no gold signal, could be due to the small sized 25 nm gold nanoparticles not having a strong enough resonance to be detected in the FLIM channel. This is not the case for IrC_6 •**AuNP13** in HeLa cells because the cells were loaded with a much higher concentration of IrC_6 •**AuNP13** (0.45 nM for 5 hours) in comparison to IrC_6 •**AuNP25** (0.16 nM for 3 hours) allowing for more nanoparticles to enter the cells, which in turn provides a stronger resonance signal which can been detected in the FLIM channel. The FLIM images of IrC_6 •**AuNP100** in HeLa cells shows strong signal around the cellular membrane, where the gold nanoparticles have localised.

The results from PLIM and FLIM images shows that uptake of IrC_6 •**AuNP13** and IrC_6 •**AuNP25** into HeLa cells mainly in the cytoplasm of the cell but also shows uptake around the cellular and nuclear membranes. These nanoparticles could be localised within endosomes or lysosomes, but further studies would need to be carried out to confirm uptake into these cellular compartments. The uptake for IrC_6 •**AuNP100** differs

from IrC_6 •**AuNP13** and IrC_6 •**AuNP25** with more clusters forming around the cell membrane, which is evident from the gold signal detected in the FLIM channel. The clustering of gold nanoparticles could be due to the larger size of nanoparticles slowing down uptake and confining the nanoparticles to the cellular membrane, which slows down uptake due to steric hindrance and receptor saturation, where the larger gold nanoparticles block the receptors, stopping their uptake into cells.[37]

4. 3. 1. 3 Mapping the localisation of IrC_6 •AuNPs in cancer cells

Further analysis of the PLIM images was carried out to identify whether localisation of these nanoprobes in cells could be mapped by detecting the changes in iridium τ_3 lifetime signal present in different regions of the HeLa cells. Looking at the lifetime variations of the iridium coated nanoparticles the areas chosen for mapping were the cytoplasm, nucleus and clusters of gold nanoparticles (Table 4.1). The lifetime variations were mapped by taking the average lifetimes in 10 different regions within the cytoplasm, nucleus and clusters of gold nanoparticles.

Table 4.1. Lifetimes detected within different cellular regions for each cell sample. Lifetimes were collected from 4 different coordinates within each cellular region and an average lifetime calculated.

	IrC_6 •**AuNP13**	IrC_6 •**AuNP25**	IrC_6 •**AuNP100**
Cytoplasm	650 ± 80 ns	660 ± 75 ns	660 ± 60 ns
Nucleus	790 ± 90 ns	740 ± 80 ns	750 ± 80 ns
Cluster	590 ± 80 ns	590 ± 75 ns	580 ± 65 ns
In Solution (Long component for comparison)	340 (47%)	330 (53%)	340 (54%)

The results showed that iridium luminescence lifetimes in the cytoplasm of HeLa cells extends to 650 ns, 660 ns and 660 ns with a standard deviation of ± 75 ns for IrC_6 •**AuNP13,** IrC_6 •**AuNP25** and IrC_6 •**AuNP100** respectively. These average lifetimes

observed for the iridium long component show an increase of ~320 ns from the lifetimes recorded for IrC_6 •**AuNPs** in water. The largest increase in lifetimes recorded was in the nucleus of the cell. The luminescence lifetimes recorded in the nucleus were 790 ns, 740 ns and 750 ns with a standard deviation of ± 85 ns. These lifetimes showed an increase of ~420 ns from the IrC_6 •**AuNPs** recorded in water. The clusters of gold nanoparticles have an average lifetime of 590 ns, 590 ns and 580 ns with a standard deviation of ± 75 ns. These lifetimes are longer than IrC_6 •**AuNPs** recorded in water, with an increase of ~250 ns being recorded. This extension in luminescence lifetime proves that aggregation has not occurred upon uptake of IrC_6 •**AuNPs** within HeLa cells. It is known that aggregation of gold nanoparticles causes quenching of the iridium luminescence lifetime, and therefore a decrease would have been seen. This was shown on a solution of IrC_6 •**AuNP25**, forced into aggregation by addition of 50 mM Tris Buffer and the luminescence lifetimes recorded. The aggregation of IrC_6 •**AuNP25** in water was confirmed by a visual colour change from red to purple and broadening of the SPR peak by UV/Vis (Appendix). The lifetimes of aggregated particles in solution were found to be 45 ns (4 %), 170 ns (63 %) and 300 ns (33 %). This showed an increase in the contribution of the shorter component to 170 ns (63 %), in comparison to 160 ns (42 %) for IrC_6 •**AuNP25** in water and a decrease in the long component to 300 ns (33 %), in comparison to 330 ns (53 %) for IrC_6 •**AuNP25** in water. These recorded lifetimes are much shorter than the lifetimes observed for the clustered gold nanoparticles in cells, for all three sizes of nanoparticles, which was recorded at ~590 ns. This data provides evidence to show that these gold nanoparticles within HeLa cells are non-aggregated nanoparticles but most likely gold nanoparticles which have been coated in proteins causing an increase in the

luminescence lifetime. It is therefore concluded that the AuNPs have localised together during uptake to form clustering of nanoparticles within the cell rather than aggregation of nanoparticles. This is supported by electron microscopy which showed a high content of gold nanoparticles being detected within vesicles inside the cells. Notably, the iridium lifetime observed from these clusters of nanoparticles within the cells is longer than that recorded for IrC_6 •**AuNPs** in solution.

To map the localisation of iridium functionalised nanoparticles within HeLa cells, a colour map has been created to highlight the areas of interest based on the average lifetimes recorded from the cytoplasm, nucleus and the clusters of gold nanoparticles. The lifetime range 700 – 1000 ns highlights the longest lifetimes found in the nucleus, which can be seen in red. The lifetime range 600 – 690 ns coloured in green highlights the lifetimes recorded from the cytoplasm and the lifetime range 450 – 590 ns, coloured in blue highlights the lifetimes recorded from the clusters of gold nanoparticles. The results can be seen in Figure 4.13, below.

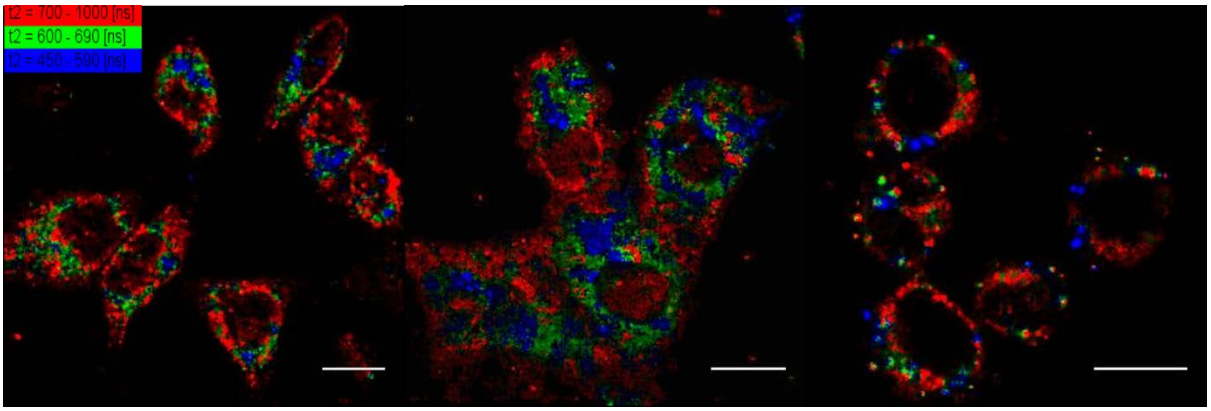

Figure 4.13. Mapping the iridium signal of iridium-coated nanoparticles in live HeLa cells: IrC_6 •AuNP13 (left), IrC_6 •AuNP25(middle) and IrC_6 •AuNP100 (right).; Image of signal with a lifetime range of 700 – 1000 ns (red), 600-690 ns (green) and 450-590 ns (blue). HeLa cells incubated with 0.16 nM IrC_6 •AuNP25 for 3 hours and 0.45 nM IrC_6 •AuNP13 and 3 pm IrC_6 •AuNP100 for 5 hours. λexc = 760 nm, scale bar = 10 µm.

IrC_6 •**AuNP13**, IrC_6 •**AuNP25** and IrC_6 •**AuNP100** show a similar pattern, with uptake mainly being within the cytoplasm of the cells. Uptake appears to be evenly distributed within the cytoplasm, as seen in green. The images show areas of clustering being formed around the cell outer and inner nuclear membranes. This is more predominant for IrC_6 •**AuNP100** which shows more clusters of nanoparticles around the outer cell membrane. The PLIM images show that these cluster of gold nanoparticles seem to be accompanied with lifetimes highlighted in the range of 450 – 590 ns, presented in blue. The lifetime variation at this range shows more clustering of nanoparticles seen for IrC_6 •**AuNP25** in comparison to the clustering detected in IrC_6 •**AuNP13.** Long-lived lifetimes which extend past 700 ns were detected in the nucleus of the cells for both IrC_6 •**AuNP13** and IrC_6 •**AuNP25,** this is coloured red in the PLIM images. These results positively confirm through detection of the long-lived iridium signal, that functionalised gold nanoparticles are localising within the nucleus of cells. Interestingly, the longer lifetimes detected in the range of 700 – 1000 ns seem to be the most predominant lifetimes present in all the PLIM images. It is proposed that the extension of luminescence lifetime for IrC_6 •**AuNPs** within the cell is due to the iridium(III) complex interacting with proteins and biomolecules. Multiphoton lifetime imaging has shown to be extremely sensitive in detecting these changes in iridium lifetimes which has allowed us to successfully map gold nanoparticle localisation within HeLa cells.

4. 3. 1. 4 Lifetime analysis of IrC_6 •AuNPs in cancer cells

To further understand the changes in iridium luminescence lifetimes of these nanoparticles in HeLa cells, the lifetimes of IrC_6 •**AuNPs** were recorded in full cell

culture media (Dulbecco modified Eagle's Medium (DMEM), 10% Fetal Bovine Serum (FBS) and 5% penicillin-streptomycin-glutamine) and FBS serum (90 % v/v) to emulate the conditions in a cell (Table 4.2).

Table 4.2. Lifetimes recorded for samples in water, cell media and FBS serum. Lifetimes were recorded using a 376 nm laser and were fitted with a χ^2 between 1 and 1.1.

	Lifetimes under different conditions (ns)		
	IrC_6 •**AuNP13**	IrC_6 •**AuNP25**	IrC_6 •**AuNP100**
Water	50 (5%) 180 (48%) 340 (47%)	40 (5%) 160 (42%) 330 (53%)	25 (3%) 140 (43%) 340 (54%)
Cell Media	13 (5%) 120 (15%) 450 (80%)	16 (2%) 125 (12%) 475 (86%)	30 (2%) 160 (22%) 440 (76%)
FBS Serum	14 (5%) 121 (17%) 515 (78%)	21 (3%) 161 (13%) 565 (84%)	10 (5%) 110 (20%) 530 (85%)

The results showed a large increase in luminescence lifetimes for iridium nanoparticles when measured in cell media and FBS serum for all sizes of nanoparticles. The largest increase in lifetimes was seen for IrC_6 •**AuNP25** in cell culture media and serum which showed lifetimes of 145 ns and 232 ns respectively. The SPR of IrC_6 •**AuNP25** were checked by UV/Vis to prove no aggregation had occurred when placed in cell media (Figure 4.14).

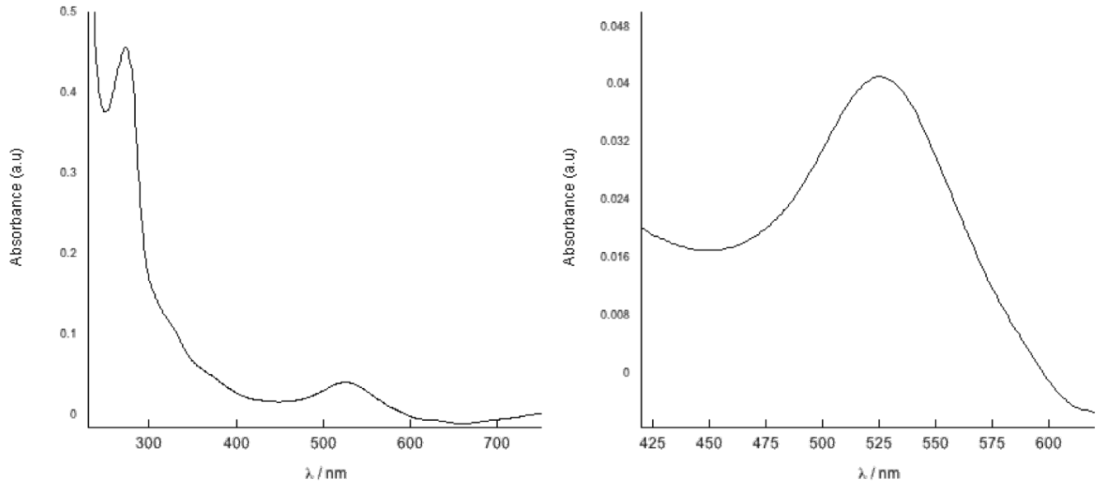

Figure 4.14. Nanoparticle SPR in cell media. Absorption spectra of IrC_6 •AuNP25 in cell media highlighting the SPR peak (right) to show non-aggregated particles in cell media. λ_{max} = 527 nm, indicating a shift of 2 nm from IrC_6 •AuNP25 in water, but showing no aggregation.

We postulate that the long lifetimes of the iridium nanoparticles in cells reflect their interaction with cellular chemicals and proteins. The lifetime of the molecular complex **IrC_6** is also affected by cell culture media and FBS although the increase is not as enhanced as seen on the nanoparticles.

4. 3. 1. 5 Assessing nuclear uptake of IrC_6 •AuNPs in cancer cells

To positively identify uptake of IrC_6 •**AuNPs** into the nucleus of HeLa cells, Z-stacks were acquired in both fluorescence and phosphorescence lifetime channels. For these experiments, HeLa cells were dosed with 0.16 nM IrC_6 •**AuNP25** for 3 hours and images were acquired every 2.5 microns in depth, obtaining four slices through the nucleus. The intensity images show the HeLa cells in the whole field of view, with a red box highlighting the nuclear region of the cell analysed (Figure 4.15).

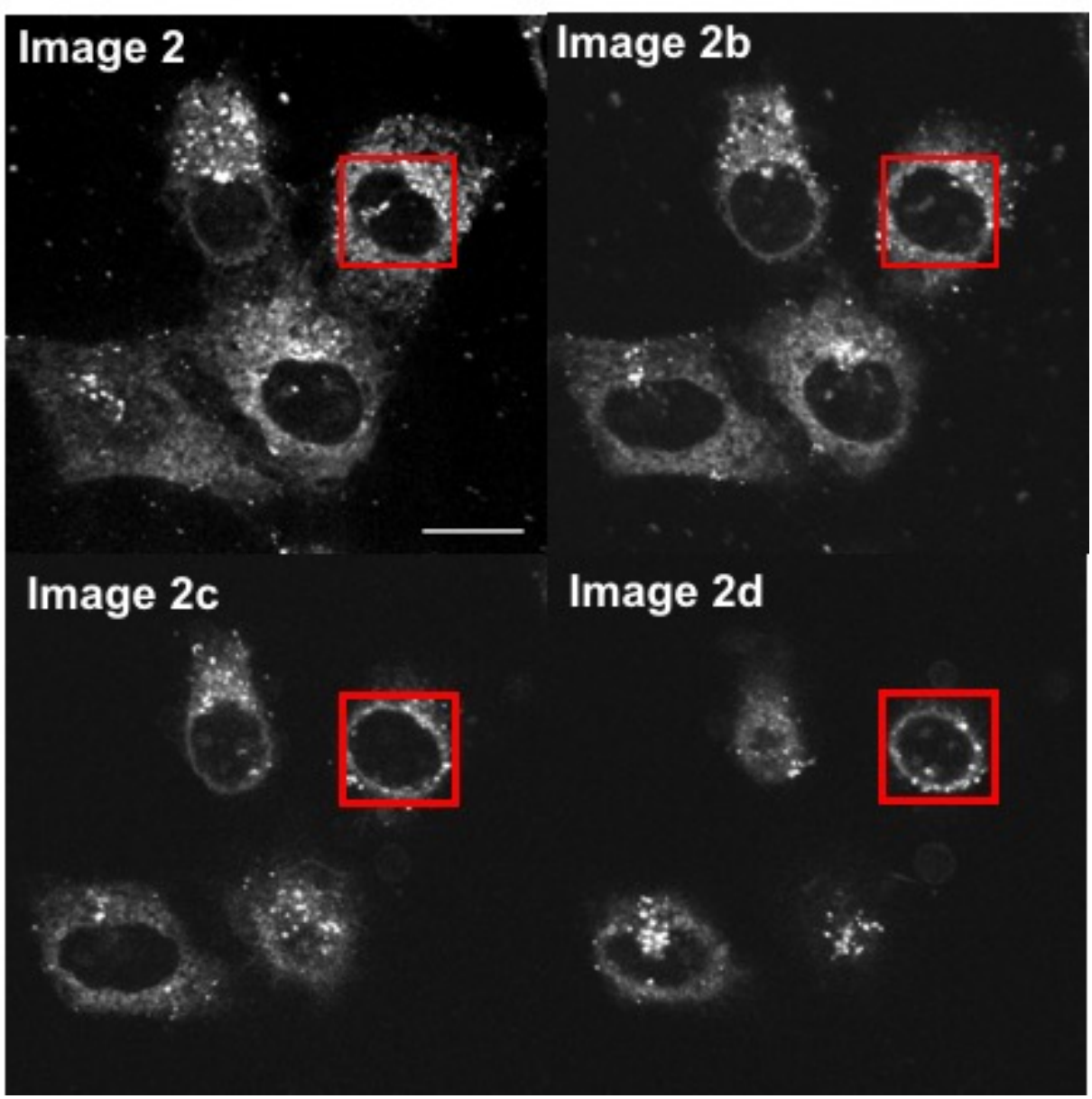

Figure 4.15. (Top) Intensity images of live HeLa cells dosed with IrC_6 •AuNP25 for 3 hours. Images increase by 2.5 μm up the cell from Image 2. (Bottom) Nuclear stacks of HeLa highlighting the nucleus as marked by a red box in top image.

Further lifetime analysis was carried out on the nuclear region highlighted by the red box in the intensity images. The corresponding phosphorescence and fluorescence lifetime images in this nuclear region can be seen in Figure 4.16.

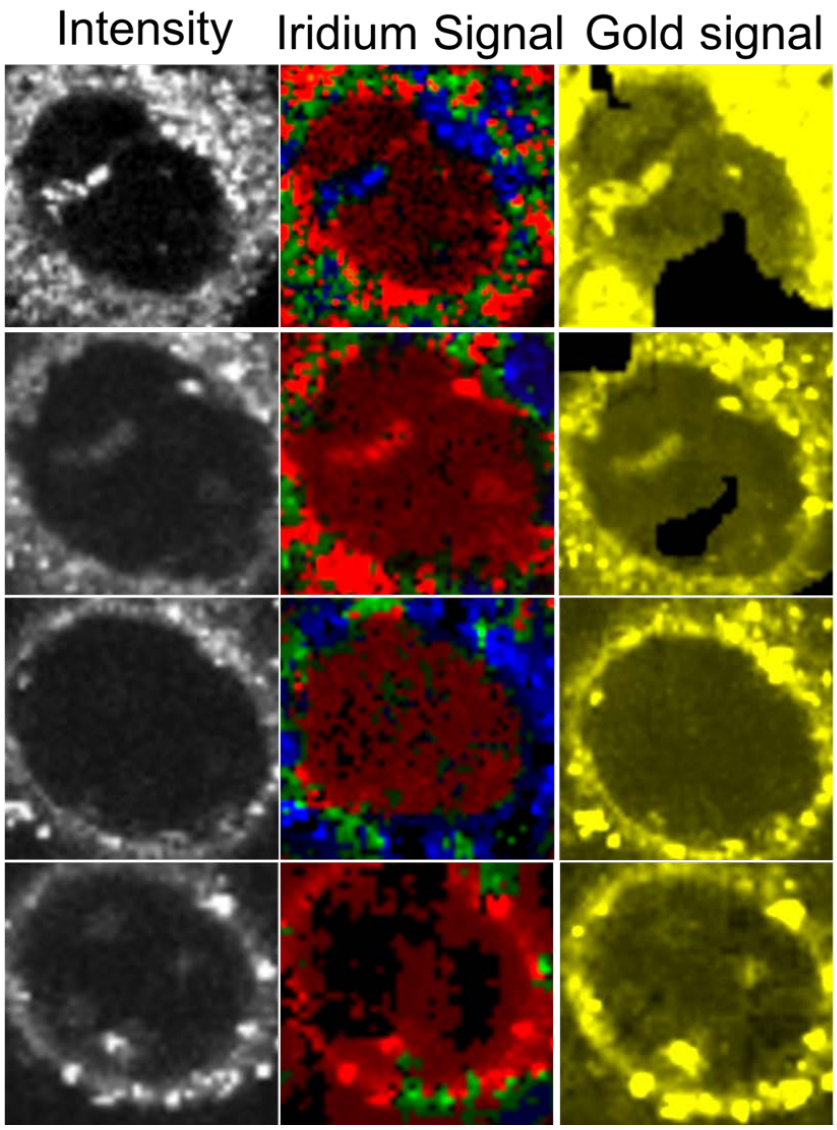

Figure 4.16. (Left) Intensity image, (middle) Long-lived lifetimes showing Iridium signal in nucleus, colour coded lifetimes showing blue: 450 – 590 nm, green: 600 – 690 nm and red: 700 – 1000 nm. (Right) Short-lived lifetimes showing gold detection in the nucleus, t_m: 20 – 120 ps. Top to bottom corresponds to Image 2, 2b, 2c and 2d, which corresponds to the intensity images in Figure X. λexc = 760 nm, scale bar = 20 µm.

It should be noted that normally for a Z-Stack more than four steps would be taken, however since the microscope was not set up for Z-stack acquisitions during this visit only four steps were manually taken. Nonetheless, this was enough to show that the lifetimes detected for iridium and gold are present within the nucleus. The PLIM images show long-lived signal from the iridium within the nucleus of the cell in all four images,

which can be seen in red. The shorter lifetimes in blue can be seen around the cell nuclear membrane as the steps go through the cell, which are identified as the clusters of gold nanoparticles. The long-lived lifetimes appear strongly in the nucleus, but these start to fade as you get to the top of the cell. To show that the signal is coming from fully coated iridium nanoparticles, the corresponding FLIM images have been shown. This has positively identified short-lived picosecond lifetimes coming from the gold nanoparticles, by detecting the sharp peak decay. Detection of the short-lived signal from the gold in the FLIM channel alongside detection of long-lived signal from the iridium in the PLIM channel, positively identifies iridium functionalised gold nanoparticles within the nucleus. This is the first time this technique has been used for dual channel imaging showing localisation of gold nanoparticles within the nucleus of cancer cells. It should be noted that the previous lifetime images (Figure 4.12), showed no FLIM signal in the nucleus. This is because the weak signal detected in the nucleus meant that the binning had to be increased to get a good fitting, which was done when an ROI (region of interest) was created over the nucleus. To prove this was true FLIM/PLIM signal coming from the gold nanoparticles within the nucleus, the decay plots of a coordinate within the nucleus have been shown in Figure 4.17.

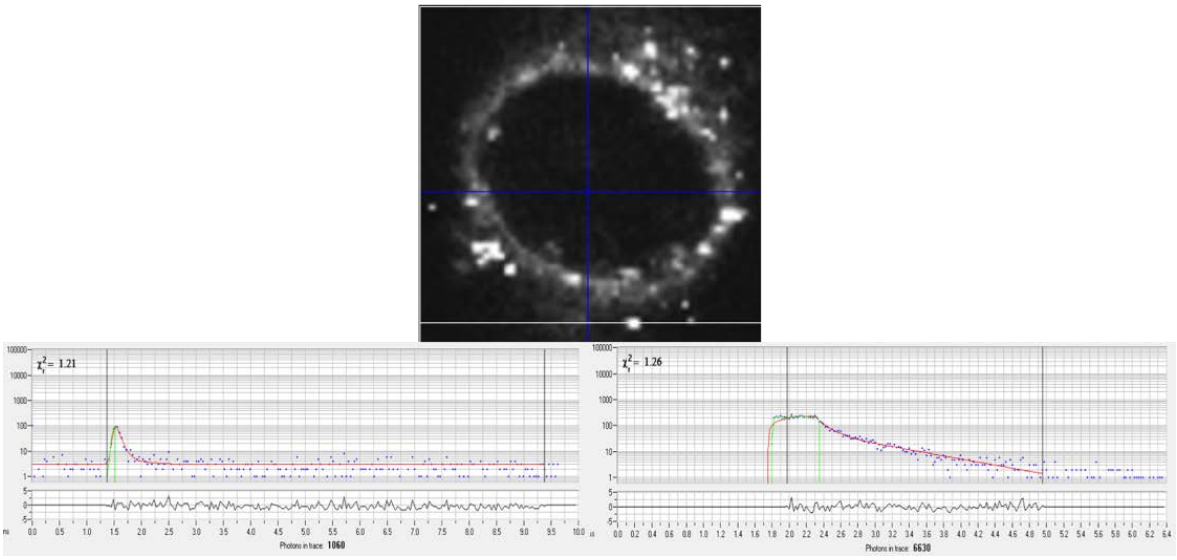

Figure 4.17. Two-photon fluorescence lifetime analysed on SPCImage (Becker & Hickl software, version 5.0). Blue cross hairs are placed on a spot where there are iridium gold nanoparticles. Lifetime decays are shown for (left) a sharp peak decay which can be seen in the lifetime plot which is attributed to the short-lived signal from the gold. (Right) The long-lived characteristic lifetime from the iridium signal. The short-lived and long-lived lifetime signals are detected in two separate channels, allowing for multichannel detection of these nanoparticles in cells.

Analysis of the FLIM and PLIM for the IrC_6 •**AuNP100** in HeLa cells showed very weak signal detected in the nucleus for both the gold and iridium. This is because these larger particles have shown to localise around the cell membrane and cytoplasm and therefore it is expected that there would be less signal in the nucleus for these sized particles. This technique has shown to be sensitive to the detection of the smaller sized gold nanoparticles in the nucleus. This is a great achievement over emission based techniques where detecting localisation in the nucleus can be challenging as it requires higher concentrations and longer accumulation times to detect the nanoparticles. Detecting short-lived picosecond lifetime signal and long-lived nanosecond lifetime signals simultaneously in two separate channels has allowed us to positively identify the uptake of iridium coated gold nanoparticles into cancer cells. This is novel work

which has for the first time has used this multichannel detection for iridium functionalised gold nanoparticles. Uptake into the nucleus was investigated further using confocal microscopy and inductively coupled plasma mass spectroscopy (ICP-MS). Confocal microscopy was carried out to provide further evidence of nanoparticle localisation within the nucleus (Figure 4.18).

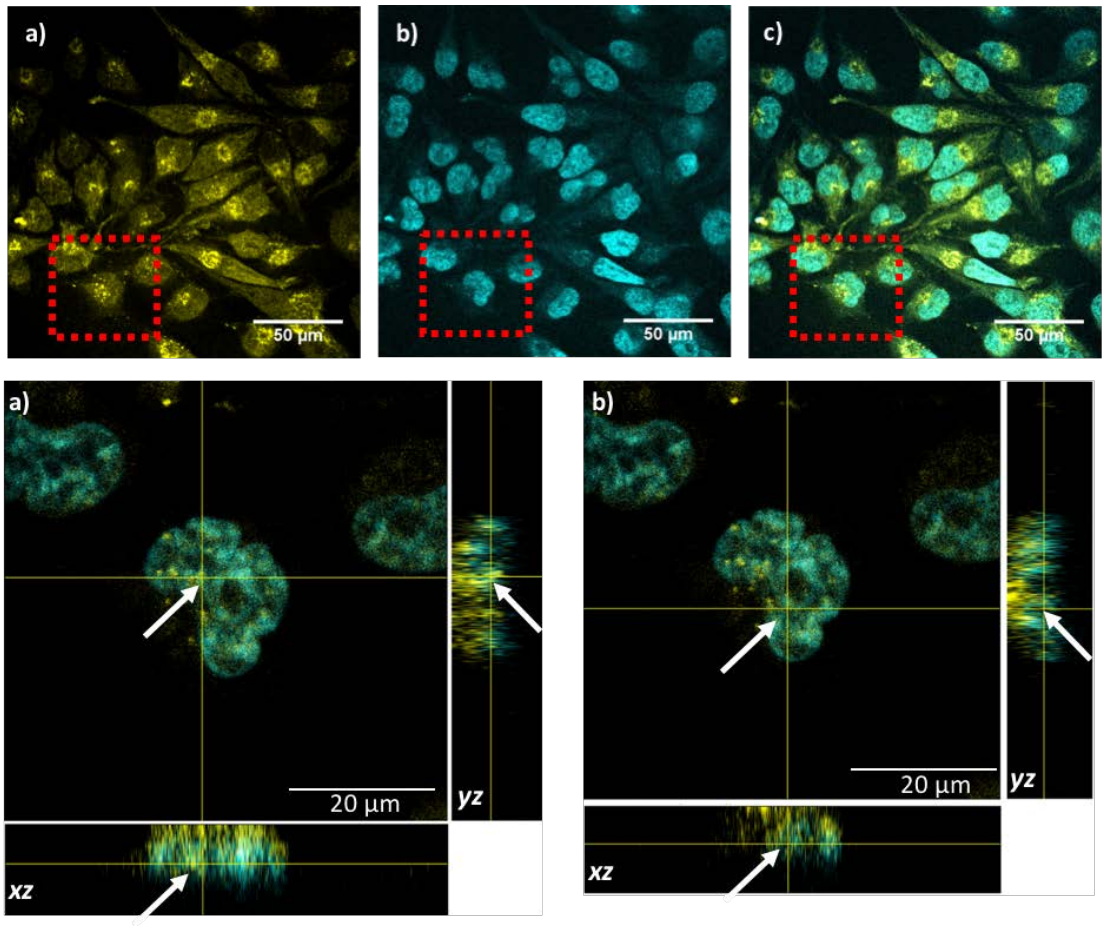

Figure 4.18. (Top) Widefield confocal luminescence images of IrC_6 •AuNP25 in HeLa cells (3 h incubation). (a) Iridium-based luminescence image λ_{exc} = 405 nm, λ_{em} = 550 - 800 nm, (b) Hoechst based luminescence image (nucleus) λ_{exc} = 405 nm, λ_{em} = 425 - 475 nm and (c) overlay of iridium and Hoechst luminescence images. Scale bar 50 µm. (Bottom) Orthogonal view Z-stacks of the red-dashed inset box. (a) and (b) correspond to orthogonal views of nanoparticle clusters at two locations. Main image shows central *z*-stack slice, with *xz* plane below and *yz* plane-right. Images show nuclear localised iridium luminescence from clusters of nanoparticles within the central *z*-planes containing the nuclear Hoechst stain (white arrows). Z-stack is 10.4 µm thick, comprising 14 slices, slice width 0.7 µm. Scale bar 20 µm. This work was carried out by Dr Sunil Claire.

Hela cells were treated with 0.16 nM IrC_6 •**AuNP25** for 3 hours. Prior to imaging the HeLa cells were treated with Hoechst 33258, a dye which binds to double stranded DNA and emits a blue fluorescence when excited at 405 nm. Z-stacks were acquired throughout the cells revealing iridium and Hoechst signals in the nucleus. The iridium signal is collected in the yellow channel, in which the IrC_6 •**AuNP25** are excited using a 405 nm laser and the emission collected from 550 – 800 nm. The Hoechst dye is collected in the blue channel upon excitation with the 405 nm laser, collecting the emission from 425 – 475 nm. The images show the iridium luminescence localising within the whole cell, evenly distributed throughout the cytoplasm. There are areas within the cytoplasm where brighter spots can be seen in the iridium channel (Figure 4.18, top, a). This “spot” like pattern is evidence of nanoparticle accumulation within the cytoplasm. The images appear to show nanoparticle accumulation within the nucleus of some HeLa cells. To investigate this an orthogonal Z-stack of a HeLa cell marked with a red box was acquired. The Z-stack shows nuclear localised iridium luminescence from clusters of nanoparticles within the central *z*-planes containing the nuclear Hoechst stain (Figure 4.18, bottom, white arrows). This was carried out on two different nanoparticle clusters in that region and both showed localisation within the nucleus of the cell from the Z-stack.

To further evidence the accumulation of nanoparticles in the nucleus, ICPMS was carried out on HeLa cells in which the organelles were separated for analysis. This method consists of treating HeLa cells with 0.16 nM IrC_6 •**AuNP25** for 6 and 24 hours. HeLa cells were pelleted by centrifugation and cell fractions were isolated using a Mitochondrial isolation kit. The cell fractions isolated for analysis were cytoplasm, vesicles, mitochondria and nucleus. The samples were analysed by ICP-MS to identify

the concentration of gold (ppb) within the cell organelles, the results can be seen in Figure 4.19. The samples were done in triplicate and the average gold content presented.

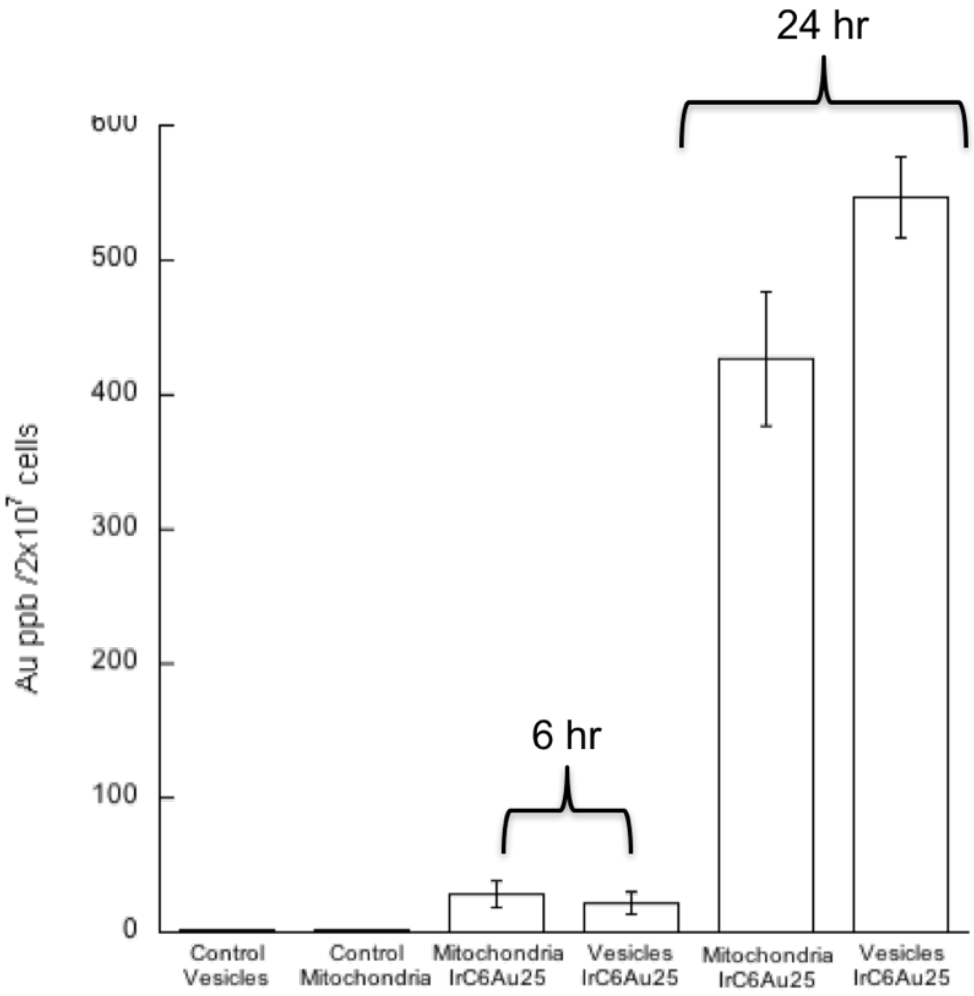

Figure 4.19. ICPMS results of Au content in isolated mitochondria and vesicles following fractionation of HeLa cells loaded with IrC_6 •AuNP25 for 6 and 24 hours as indicated. Cell dosing and digestion carried out by Sunil Claire.

The results show a low concentration of gold nanoparticles detected in mitochondria and vesicles after 6 hours of incubation with IrC_6 •**AuNP25**, which is to be expected. The concentration of gold (ppb) detected increases after 24 hours, due to more particles accumulating within the cell, with the highest concentration being found in

vesicles. This is supported by data acquired using electron microscopy, where nanoparticles could be seen localising within the vesicles of cells and is a known occurrence of nanoparticle uptake from literature.[38-40] After 24 hours, high accumulation of nanoparticles was seen in the mitochondria of the cells. There are examples of iridium(III) complexes in the literature that have been designed with specific targeting for accumulation within the mitochondria.[41-43] So, it is interesting that IrC_6 •**AuNP25** shows high accumulation within the mitochondria with no targeting ligand present on the complex. This could be due to the high 2+ charge of the iridium(III) complex, which explains the accumulation in the mitochondria. During the cell fractionation it was found that the nucleus couldn't be extracted by itself and instead contained mostly cytoplasm within the fraction, therefore the results obtained from this were invalid and not presented. Since this was a preliminary study, future work would be carried out to repeat the nucleus fractionation to identify whether particles were accumulating in the nucleus. Further characterisation would need to be carried out on the nanoparticle location within the mitochondria and vesicles, to fully understand the pattern of uptake.

4. 3. 2 Optical and electron microscopy of IrC_6 •AuNPs in cancer cells

To further analyse the internalisation of the IrC_6 •**AuNP25** we used total internal reflectance fluorescence (TIRF) microscopy and transmission electron microscopy (TEM). TIRF provides high-resolution imaging of the cell surface[44, 45], which allowed us to determine localisation of these nanoparticles throughout the cell as TIRF angle is varied (Figure 4.20).

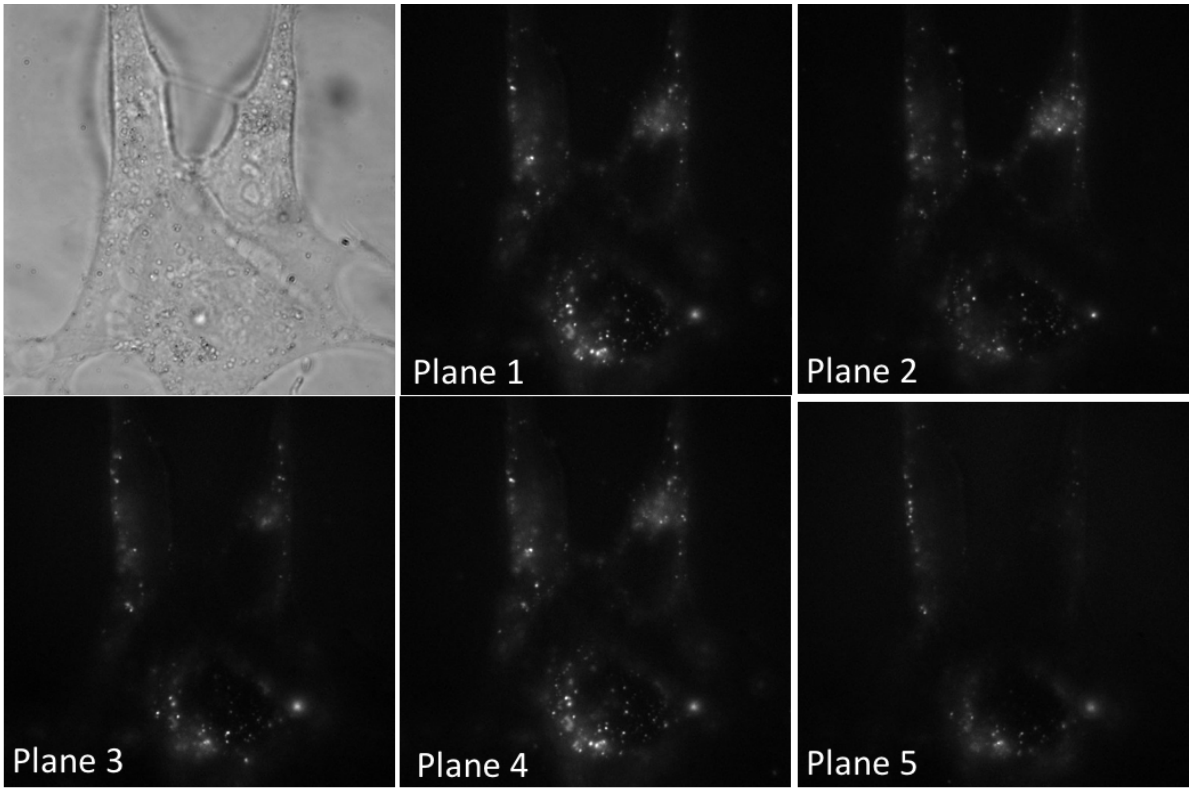

Figure 4.20. Total internal reflectance fluorescence (TIRF) microscopy of 0.16 nM IrC_6 •AuNP25 in HeLa cells after incubation of 3 hours. a) Bright field, (b-f) TIRF images. λ_{exc} = 405 nm. Plane increase from 1-5 is going upwards through the cell and away from the cover glass

Clear bright white spots in the luminescence image (planes 1-5) are attributed to iridium luminescence from the non-clustered gold nanoparticles on planes moving upwards from the imaging dish. This shows nanoparticle localisation within the cell more specifically in the cytoplasm and around the cell membrane, which is in good agreement with the lifetime imaging studies and confocal microscopy. Most importantly the images show clearly non-aggregated nanoparticles with good resolution. TIRF microscopy is governed by the evanescent wave with the resolution restricted to 200 nm depth, providing information inside the cell membrane only and not within the whole cell. TIRF clearly shows non-clustered, single nanoparticles in each plane, which is in good agreement with the other imaging data collected.

Electron microscopy shows IrC_6 •**AuNP25** appear as dark spheres located throughout the cytoplasm of the cell (Figure 4.21). They appear to be individual spheres suggesting that no aggregation occurs upon uptake. The nanoparticles are localised into vesicles suggesting the mechanism of uptake is endocytosis, this is also supported by the ICPMS data which showed high gold accumulation of nanoparticles in vesicles as well as mitochondria and cytoplasm. This data agrees with previous studies looking at uptake of ruthenium(II) functionalised nanoparticles in cancer cells.[46] A high loading of iridium(III) functionalised gold nanoparticles can be seen within the vesicles, confirming that the nanoparticles are taken up together and accumulated in the same space as single particles. Since these nanoparticles have localised in one place, at lower magnifications they appear to have formed clusters of nanoparticles within the cell. This supports the two-photon lifetime images where clusters of nanoparticles could be seen within the cytoplasm of the cell that still retained long luminescence lifetimes of the functional nanoprobes. Long luminescent lifetimes were also seen within the nucleus of the cell, however the TEM images revealed no nanoparticles uptake within the nucleus. This could be because electron microscopy requires thin sections of the cell to be imaged, and with short incubation times, it makes it harder to identify nuclear uptake using TEM.

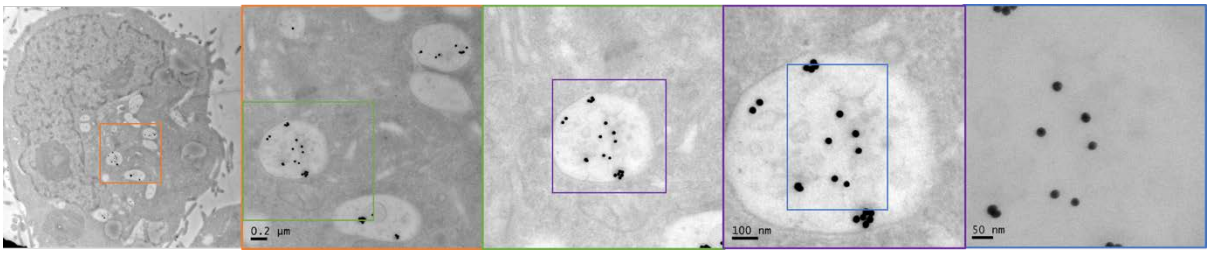

Figure 4.21. TEM images of sectioned HeLa cells which were incubated with 0.16 nM IrC_6 •AuNP25 for 3 hours. Zoomed in images (b-d).

4. 4 Conclusions

We have shown that iridium(III) functionalised gold nanoparticles displayed two-photon luminescence in agreement with the single-photon luminescence spectra. The power dependence studies revealed strongly that a two-photon absorption process was occurring for the **IrC_6** probe in solution and IrC_6 •**AuNPs** in agarose gel. The two-photon absorption cross-section of IrC_6 •**AuNP25** was measured and found to be much higher than the molecular probe in solution, which was attributed to enhancement from the gold nanoparticles. Two-photon lifetime imaging of IrC_6 •**AuNP25** in cancer cells demonstrated that detection can be performed in two channels, one for the long luminescence lifetime signal of the iridium complex in hundreds of nanoseconds and the other for the short lifetime signal from the gold in tens of picoseconds. The two channel detection showed clearly the iridium and gold signal for all nanoparticle sizes investigated, with uptake being seen in the cytoplasm and cell membrane. The lifetime images allowed us to visualise the pattern of uptake for the different sized nanoparticles. It was found that IrC_6 •**AuNP25** and IrC_6 •**AuNP13** showed a similar pattern in uptake, whereas IrC_6 •**AuNP100** located mainly around the cell plasma membrane. The lifetime images revealed that upon uptake these gold nanoparticles were localising in clusters within some areas of the cytoplasm, which could be seen for all three sizes of nanoparticles. It is unclear from the lifetime images whether the iridium(III) functionalised gold nanoparticles were localising within vesicles in the cytoplasm of the cells, but this pattern of uptake was identified from the TEM images. Investigation into the luminescence lifetimes within the cell revealed detection of long and short lifetimes within the cytoplasm and nucleus of the cells, which identified

nanoparticle uptake in these regions. Further investigations revealed remarkably long lifetimes detected within the nucleus showing an average of 740 ns, which was an increase of 410 ns in comparison to IrC_6•**AuNP25** in solution. The lifetime of the cluster of nanoparticles were recorded and found to be ~450 – 590 ns, which showed that these were non-aggregated particles as this is an enhancement from the IrC_6•**AuNPs** in solution. This "clustering" seen from the nanoparticles was also confirmed by electron microscopy, which showed a high accumulation of single gold nanoparticles within vesicles in the cytoplasm. Nuclear localisation of small non-aggregated nanoparticles is challenging but the sensitivity of the luminescence lifetime signal demonstrated nuclear localisation by detecting the long-lived lifetimes, which was more dominant for the IrC_6 •**AuNP13** and IrC_6 •**AuNP25**. There was no signal detected in the nucleus for IrC_6 •**AuNP100**, which is to be expected since the size restricted the localisation to the cell membrane. The cells were also dosed with a much lower concentration of IrC_6 •**AuNP100** which had a final concentration of 3 pM within the cells. The lifetimes of IrC_6 •**AuNPs** in cell media, serum and FBS were independently examined, the luminescent lifetimes elongated in comparison to nanoparticles in water, this effect was attributed to interactions of the nanoparticles with biomolecules. Confocal microscopy showed nanoparticle accumulation within the cytoplasm and confirm nanoparticle uptake into the nucleus. The results from ICPMS showed that gold was accumulating within vesicles in the cytoplasm, which agrees with the electron microscopy data. This technique also showed that after 24 hours a high gold content was detected within mitochondria. Unfortunately, this technique could not be used to confirm nuclear uptake, this method would be improved for future investigations.

Overall, the iridium-coated nanoparticles are introduced as novel nanoprobes for multiphoton lifetime imaging providing multichannel detection for independent monitoring of the gold scaffold and the iridium signal. The long-lived lifetime signal is sensitive to the cell environment, providing local information which can be used for gating specific biomolecular interactions and tracking nanoparticles in *in vivo* models.

4. 5 Experimental section

4. 5. 1 Cell culture and Nanoparticle dosing

4. 5. 1. 1 Live cell imaging

Human cervical epithelioid cancer cells (HeLa cells) obtained from Public Health England (catalogue number 93021013) were used in all experiments. HeLa cells were maintained and grown in complete Dulbecco's Modified Eagle Medium (DMEM) without phenol red supplemented with 10% Fetal Bovine Serum (FBS), 2 mM glutamine, 100 units/mL penicillin and 0.4 mg/mL streptomycin. Cells were grown as monolayer in vented cap T75 flasks at 37 °C in a humidified atmosphere of 5 % CO_2 incubator. A day prior to dosing with nanoparticles, HeLa cells were counted with Biorad automated cell counter and viability determined by trypan blue exclusion. Cells were seeded at a density of 100,000 cells per 35 mm MaTek glass dishes and allowed to attach overnight in a humidified 5 % CO_2 atmosphere. For nanoparticle dosing, cell media was removed and the dishes washed twice with phosphate buffered saline (PBS) at pH 7. HeLa cells were dosed for 5 hours for IrC_6 • **AuNP13** (0.45 nM) and IrC_6 • **AuNP100** (3 pM) and 3 hours for IrC_6 • **AuNP25** (0.16 nM)**.** At the end of each

time point, cells were rinsed three times with PBS and imaging was carried out in imaging buffer (HEPES, pH 7).

4. 5. 1. 2 Fixed cell imaging

Coverslips (35 mm x 35 mm) were sterilised in EtOH and washed twice with PBS before use. Cells were seeded at a density of 100,000 cells per 35 mm coverslip, placed in complete DMEM and allowed to attach overnight in a humidified environment. For nanoparticle dosing, cell media was removed and the coverslips washed twice with PBS. Hela cells were dosed for 5 hours for IrC_6 •**AuNP13** (0.45 nM) and IrC_6 •**AuNP100** (3 pM) and 3 hours for IrC_6 •**AuNP25** (0.16 nM)**.** At the end of each time point, cells were rinsed three times with PBS. The coverslips were immersed in 4% paraformaldehyde (PFA) for 1 hour. The coverslips were then washed three times with PBS. Microscopy slides were sterilised in EtOH and air dried before use. Non-Fluorescent hydromount was used to adhere coverslips to the microscope slide which were left at 4 ºC overnight. Covergrip® was used to seal the edges of the coverslip and left to dry for 1 hour prior to imaging.

4. 5. 2 Microscopy techniques

4. 5. 2. 1 Multiphoton FLIM and PLIM

Multiphoton excitation at 760 nm was used to acquire all images. The lifetime signals were detected by an adapted Becker & Hickl DCS120 laser scanning system coupled to a SPC150 time correlated single photon counting PCI card and a PMC-100 detector. The same card was also used to correlate the x,y pixel positions for the FLIM acquisition. The multichannel lifetime collection set up in the two windows was

constructed around a Nikon Ti-E microscope. The multiphoton used a pulse modulated Titanium: Sapphire laser (Mira F-900, Coherent, UK) with 76 MHz repetition rate and 200 fs pulse. This was used to image live HeLa cells stained with IrC_6•**AuNP**s. A water immersion x60 objective was used for all samples. Emission light was collected using a bandpass (BG39) filter. PLIM and FLIM data collected were analysed in SPCImage (Becker & Hickl software, version 5.0). The data was fitted to an exponential decay model.

4. 5. 2. 2 Confocal Microscopy

Confocal microscopy was performed using a Leica TCS SP8 upright confocal laser scanning system using a x40 water immersion objective lens. Solid-state laser 405 nm with 26 % laser intensity was used. An AOBS spectral detector and gateable hybrid (Hy-D) PMT detector was used with the following ex/em ranges: λ_{exc} = 405 nm, λ_{em} = 550 - 800 nm for Iridium luminescence and λ_{exc} = 405 nm, λ_{em} = 425 - 475 nm for Hoechst acquisition. Z-stacks slice widths were performed as stated in the iridium and Hoechst channel images. Processing and visualization of 3D images was performed by the image processing software FIJI (ImageJ Version 1.52b).

4. 5. 2. 3 Total Internal Reflectance Fluorescence (TIRF) Microscopy

Total internal reflectance fluorescence (TIRF) microscopy was constructed around an inverted Nikon Ti-U microscope. Fluorescence excitation was obtained from an Omicron laser hub containing a 405 nm, 488 nm and 561 nm continuous wave lasers and fibre coupled to the TIRF-M unit. The laser light was focused and collimated at the back aperture of a x100 oil immersion, NA 1.49 objective. Fluorescence emission was

detected using an electron multiplying charged-coupled device (EMCCD, iXon, Andor) camera. Images were analysed as TIFF files in ImageJ software, version 1.49.

4. 5 .2. 4 Transmission Electron Microscopy (TEM)

Coverslips (12 mm x 13 mm) were sterilised in EtOH and washed twice with PBS before use. Cells were seeded at a density of 50,000 cells per 12 mm coverslip, placed in complete DMEM and allowed to attach overnight in a humidified environment. For nanoparticle dosing, cell media was removed and the coverslips washed twice with PBS. HeLa cells were dosed for 5 hours for IrC_6 •**AuNP13** (0.45 nM) and IrC_6 •**AuNP100** (3 pM) and 3 hours for IrC_6 •**AuNP25** (0.16 nM)**.** At the end of each time point, cells were rinsed three times with PBS. The coverslips were immersed in 2.5 % glutaraldehyde fixative in 100 nM phosphate buffer, wrapped in foil and left overnight in the fridge prior to TEM imaging.

4. 5. 2. 5 Sample preparations for TEM

TEM imaging was carried out on Citrate •**AuNPs** and IrC_6 •**AuNPs**. For all nanoparticle samples 20 μL was added to a 200-mesh formvar-coated grid TEM grid and left overnight to dry. Samples were carried out on 4.6 nM IrC_6 •**AuNP13**, 4.5 nM Citrate• **AuNP13**, 1.6 nM IrC_6 •**AuNP25**, 1.6 nM Citrate •**AuNP25**, 30 pM IrC_6 •**AuNP100** and 30 pM Citrate •**AuNP100**. Cells dosed with nanoparticles were grown onto cover slips (see cell culture and nanoparticle dosing protocol). Samples were prepared for electron microscopy in Materials and Metallurgy department. Samples were stained with 1% osmium tetroxide solution. The cells were placed in a resin, sectioned and mounted on a 200-mesh formvar-coated TEM grids for imaging.

4. 5. 3 ICP-MS sample preparations

4. 5. 3. 1 Nanoparticle solutions

Iridium functionalised gold nanoparticles were dissolved in 300 μL ultrapure aqua regia (~70% HNO_3) and left to digest overnight at 80 °C. To aid digestion, these solutions were left to stir overnight. The following day ultrapure water was added to the samples until a final dilution of HNO_3 to 5%. Sonication was used to aid digestion of the gold nanoparticles.

4. 5 .3 .2 Cell Fractionation

HeLa cells were cultured in T_{165} flasks and treated with nanoparticles (final concentration of 0.9 nM) for 6 and 24 hours. After treatment, the cells were washed three times with phosphate buffered saline (PBS, 20mL) to remove membrane bound nanoparticles, detached from the flask by trypsinization and resuspended in 15 mL of media. Cell density was calculated using a haemocytometer and each sample adjusted to a total of $2x10^7$ cells. Cells were pelleted by centrifugation and cell fractionation was undertaken using a Mitochondrial Isolation Kit with the reagent-based method (Thermo Scientific) according to manufacturer's instructions. Briefly, the cell pellet was resuspended in 800 μL of isolation reagent A, mixed by vortexing and incubated on ice for 2 minutes. Next 10 μL of reagent B was added, the sample vortexed for 5 seconds and incubated on ice for 5 minutes with vortexing every minute. Reagent C (800 L) was then added and the sample mixed by gentle inversion and centrifuged for 10 minutes (700 g, 4°C) to pellet the cell nuclei along with any free nanoparticles not associated with other cellular compartments that remained in suspension after this first

centrifugation step. The supernatant containing the mitochondria was carefully transferred to a clean tube and centrifuged for 15 minutes (3000 g, 4°C), the supernatant removed and the mitochondrial pellet resuspended in 500 μL of reagent C and centrifuged at 12 000g for 5 minutes at 4°C and the pellet retained as the mitochondrial fraction. Finally, the supernatant from the second (mitochondrial) centrifugation step was centrifuged at 12 000g for 15 minutes at 4°C. The supernatant removed and the residual pellet retained as the vesicular fraction (containing endosomes, lysosomes and peroxisomes).

4. 5 .3 .3 Cell digestion for ICP-MS

Cell fractions were dissolved in 300 μL ultrapure aqua regia (~70% HNO_3) and left to digest overnight at 80 °C. The following day ultrapure water was added to the samples until a final dilution of HNO_3 to 5%. Samples were transferred to ICP-MS grade tubes for analysis.

4. 5 References

1 I. M. Schiessl and H. Castrop, *Pflug. Arch. Eur. J. Phy.* **2016**, *468*, 1505-1516.

2 F. Helmchen and W. Denk, *Nat. Methods.* **2005**, *2*, 932-940.

3 E. B. Brown, R. B. Campbell, Y. Tsuzuki, L. Xu, P. Carmeliet, D. Fukumura and R. K. Jain, *Nat. Med.* **2001**, *7*, 1069-1069.

4 D. M. McDonald and P. L. Choyke, *Nat. Med.* **2003**, *9*, 713-725.

5 W. R. Zipfel, R. M. Williams and W. W. Webb, *Nat. Biotechnol.* **2003**, *21*, 1368-1376.

6 J. C. G. Bunzli, *Chem. Rev.* **2010**, *110*, 2729-2755.

7 M. Y. Berezin and S. Achilefu, *Chem. Rev.* **2010**, *110*, 2641-2684.

8 Z. W. Wang, Y. P. Zheng, D. Q. Zhao, Z. W. Zhao, L. X. Liu, A. Pliss, F. Q. Zhu, J. Liu, J. L. Qu and P. Luan, *J. Innov. Opt. Heal. Sci.* **2018**, *11*.

9 R. Ebrecht, C. D. Paul and F. S. Wouters, *Protoplasma.* **2014**, *251*, 293-305.

10 S. S. Howard, A. Straub, N. G. Horton, D. Kobat and C. Xu, *Nat. Photonics.* **2013**, *7*, 33-37.

11 E. Baggaley, M. R. Gill, N. H. Green, D. Turton, I. V. Sazanovich, S. W. Botchway, C. Smythe, J. W. Haycock, J. A. Weinstein and J. A. Thomas, *Angew. Chem. Int. Edit.* **2014**, *53*, 3367-3371.

12 E. B. van Munster and T. W. J. Gadella, *Adv. Biochem. Eng. Biot.* **2005**, *95*, 143-175.

13 A. Raza, H. E. Colley, E. Baggaley, I. V. Sazanovich, N. H. Green, J. A. Weinstein, S. W. Botchway, S. MacNeil and J. W. Haycock, *Sci. Rep-UK.* **2017**, *7*.

14 A. Byrne, C. S. Burke and T. E. Keyes, *Chem. Sci.* **2016**, *7*, 6551-6562.

15 A. Jana, B. J. Crowston, J. R. Shewring, L. K. McKenzie, H. E. Bryant, S. W. Botchway, A. D. Ward, A. J. Amoroso, E. Baggaley and M. D. Ward, *Inorg. Chem.* **2016**, *55*, 5623-5633.

16 E. Baggaley, S. W. Botchway, J. W. Haycock, H. Morris, I. V. Sazanovich, J. A. G. Williams and J. A. Weinstein, *Chem. Sci.* **2014**, *5*, 879-886.

17 E. Boisselier and D. Astruc, *Chem. Soc. Rev.* **2009**, *38*, 1759-1782.

18 E. C. Dreaden, A. M. Alkilany, X. H. Huang, C. J. Murphy and M. A. El-Sayed, *Chem. Soc. Rev.* **2012**, *41*, 2740-2779.

19 R. A. Sperling, P. Rivera gil, F. Zhang, M. Zanella and W. J. Parak, *Chem. Soc. Rev.* **2008**, *37*, 1896-1908.

20 A. Davies, D. J. Lewis, S. P. Watson, S. G. Thomas and Z. Pikramenou, *Proc. Natl. Acad. Sci. U. S. A.* **2012**, *109*, 1862-7.

21 N. J. Rogers, S. Claire, R. M. Harris, S. Farabi, G. Zikeli, I. B. Styles, N. J. Hodges and Z. Pikramenou, *Chem. Commun.* **2014**, *50*, 617-619.

22 O. P. Varnavski, M. B. Mohamed, M. A. El-Sayed and T. Goodson, *J. Phys. Chem. B.* **2003**, *107*, 3101-3104.

23 L. Shang, N. Azadfar, F. Stockmar, W. Send, V. Trouillet, M. Bruns, D. Gerthsen and G. U. Nienhaus, *Small.* **2011**, *7*, 2614-2620.

24 N. J. Rogers, H. C. Jeffery, S. Claire, D. J. Lewis, G. Zikeli, N. J. Hodges, S. Egginton, G. B. Nash and Z. Pikramenou, *Nanomedicine.* **2017**, *12*, 2725-2740.

25 S. A. M. Osborne and Z. Pikramenou, *Faraday. Discuss.* **2015**, *185*, 219-231.

26 C. R. Maldonado, L. Salassa, N. Gomez-Blanco and J. C. Mareque-Rivas, *Coordin. Chem. Rev.* **2013**, *257*, 2668-2688.

27 H. Komatsu, K. Yoshihara, H. Yamada, Y. Kimura, A. Son, S. Nishimoto and K. Tanabe, *Chem-Eur. J.* **2013**, *19*, 1971-1977.

28 W. L. Jiang, Y. Gao, Y. Sun, F. Ding, Y. Xu, Z. Q. Bian, F. Y. Li, J. Bian and C. H. Huang, *Inorg. Chem.* **2010**, *49*, 3252-3260.

29 G. H. Patterson and D. W. Piston, *Biophys. J.* **2000**, *78*, 2159-2162.

30 S. Mathai, D. K. Bird, S. S. Stylli, T. A. Smith and K. P. Ghiggino, *Photoch. Photobio. Sci.* **2007**, *6*, 1019-1026.

31 C. Xu and W. W. Webb, *J. Opt. Soc. Am. B.* **1996**, *13*, 481-491.

32 R. M. Edkins, S. L. Bettington, A. E. Goeta and A. Beeby, *Dalton. Trans.* **2011**, *40*, 12765-12770.

33 C. L. Ho, K. L. Wong, H. K. Kong, Y. M. Ho, C. T. L. Chan, W. M. Kwok, K. S. Y. Leung, H. L. Tam, M. H. W. Lam, X. F. Ren, A. M. Ren, J. K. Feng and W. Y. Wong, *Chem. Commun.* **2012**, *48*, 2525-2527.

34 C. F. Jiang, T. T. Zhao, P. Y. Yuan, N. Y. Gao, Y. L. Pan, Z. P. Guan, N. Zhou and Q. H. Xu, *ACS Appl. Mater. Interfaces* **2013**, *5*, 4972-4977.

35 J. Borglin, R. Selegard, D. Aili and M. B. Ericson, *Nano. Lett.* **2017**, *17*, 2102-2108.

36 Becker-Hickl in *Combined Fluorescence and Phosphorescence Lifetime Imaging (FLIM / PLIM) with the Zeiss LSM 710 NLO Microscopes Vol.* **2018**.

37 N. Hoshyar, S. Gray, H. B. Han and G. Bao, *Nanomedicine.* **2016**, *11*, 673-692.

38 N. Oh and J. H. Park, *Int. J. Nanomedicine.* **2014**, *9 Suppl 1*, 51-63.

39 A. Albanese, P. S. Tang and W. C. W. Chan, *Annu. Rev. Biomed. Eng. Vol 14* **2012**, *14*, 1-16.

40 B. D. Chithrani, A. A. Ghazani and W. C. W. Chan, *Nano. Lett.* **2006**, *6*, 662-668.

41 V. Venkatesh, R. Berrocal-Martin, C. J. Wedge, I. Romero-Canelon, C. Sanchez-Cano, J. I. Song, J. P. C. Coverdale, P. Y. Zhang, G. J. Clarkson, A. Habtemariam, S. W. Magennis, R. J. Deeth and P. J. Sadler, *Chem. Sci.* **2017**, *8*, 8271-8278.

42 G. Y. Li, Q. Lin, L. L. Sun, C. S. Feng, P. Y. Zhang, B. L. Yu, Y. Chen, Y. Wen, H. Wang, L. N. Ji and H. Chao, *Biomaterials.* **2015**, *53*, 285-295.

43 K. Q. Qiu, H. Y. Huang, B. Y. Liu, Y. K. Liu, P. Y. Zhang, Y. Chen, L. N. Ji and H. Chao, *J. Mater. Chem. B.* **2015**, *3*, 6690-6697.

44 E. Betzig, G. H. Patterson, R. Sougrat, O. W. Lindwasser, S. Olenych, J. S. Bonifacino, M. W. Davidson, J. Lippincott-Schwartz and H. F. Hess, *Science.* **2006**, *313*, 1642-1645.

45 A. L. Mattheyses, S. M. Simon and J. Z. Rappoport, *J. Cell. Sci.* **2010**, *123*, 3621-3628.

46 D. A. N in *Uptake, cellular fate and toxicity of engineered gold nanoparticles in A549 cells*, *Vol. PhD* University of Birmingham, University of Birmingham, **2017**, p. 203.

CHAPTER 5: SELECTIVE TARGETING OF CANCER CELLS USING ANTIBODY FUNCTIONALISED GOLD NANOPARTICLES

5.1 Introduction

5. 1. 1 Angiogenesis and cancer therapies

Angiogenesis is the formation of blood vessels from pre-existing blood vessels in the body. Angiogenesis starts by breaking into the wall of the pre-existing blood vessel which causes hypoxia.[1-3] Endothelial cells are then activated by angiogenic factors which cause them to proliferate and migrate.[4] Angiogenesis that happens in the body is a controlled process which is monitored by strict regulation of signalling factors that only occur during specific events such as wound healing in adults. However, tumour angiogenesis is a known process of cancer which help provide oxygen and nutrients to tumour cells causing the tumour to grow rapidly (Figure 5.1).

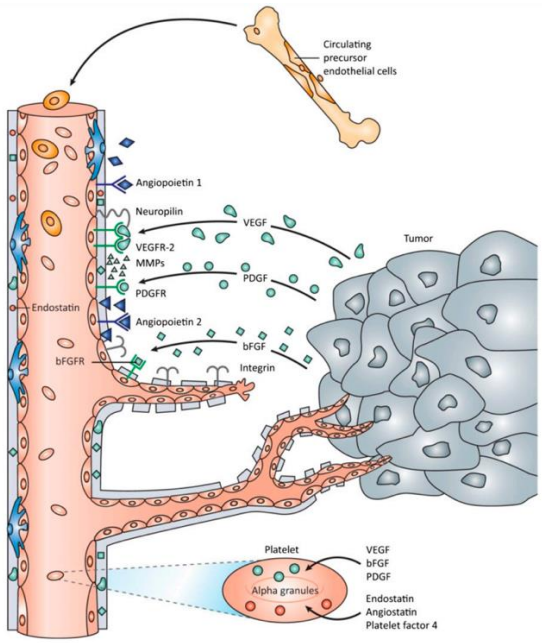

Figure 5.1. Mechanism of tumour angiogenesis showing soluble angiogenic factors (VEGF, PDGF and FGF) which are secreted from the tumour and surrounding cells to induce and regulate key steps in angiogenesis.[2]

The main difference between tumour angiogenesis and physiological angiogenesis is the rapid and uncontrolled rate at which the former progresses. This can then lead to leaky and twisted vessels that are highly inflamed.[5] It has been found that tumours grown in an environment where angiogenesis cannot occur, the tumour does not grow beyond 1-2 mm. This is because the lack of vascular support causes the tumours to become apoptotic. These are the factors which compromise the delivery of chemotherapeutics, and therefore research has looked at targeting angiogenesis for cancer therapeutics since inhibiting these angiogenic factors and molecules can halt angiogenesis and consequently the progression of tumours. Most commonly the vascular endothelial cell growth factor (VEGF) and angiopoietin (Ang) are targeted due to their role in upregulating angiogenesis. In 2008, the FDA approved Bevacizumab (Avastin) which targets VEGF proteins overexpressed on colorectal cancer vasculature as the first anti-angiogenic therapeutic agent using a monoclonal antibody. Another approach is to target tumour endothelial cells which have unique markers on their surface in comparison to normal endothelial cells. These are known as tumour endothelial markers (TEMs) which are highly expressed in human tumour vasculature and minimally expressed in healthy vasculature, making them attractive candidates for targeted cancer therapies.[6] CLEC14A has been identified as a novel tumour endothelial marker (TEM) which has shown to be expressed strongly on tumour associated vessels in contrast to healthy tissue where nearly no expression is seen.[7] CLEC14A is an endothelial transmembrane glycoprotein that has shown to regulate endothelial cell migration and sprouting of blood vessels. CLEC14A is part of the C-type lectin domain (CTLD) group 14 family known to mediate cellular functions such as angiogenesis and inflammation (Figure 5.2).[8]

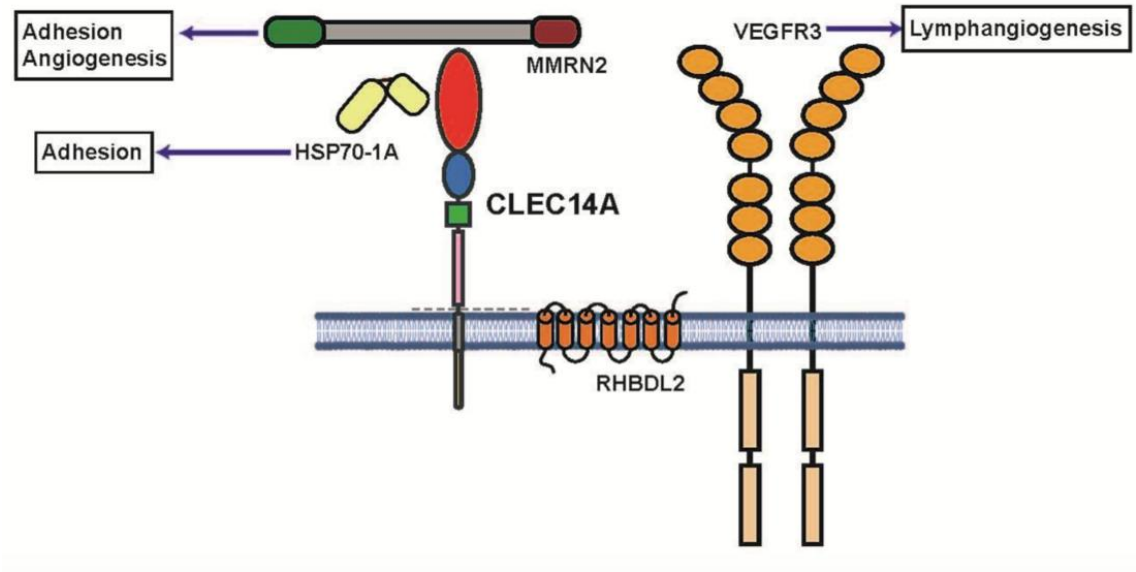

Figure 5.2. Schematic of CLEC14A protein with ligand binding sites.[6]

The ability to selectively target CLEC14A and block it's angiogenic functions could lead to novel anti-cancer approaches. Targeting these markers can be achieved with monoclonal antibodies, peptides or vaccines. Monoclonal antibodies have been developed as therapeutic agents for many biological applications such as cancer therapies, infection and inflammation.[9] The ability to specifically target a cancerous cell over a normal cell presents a lot of challenges, and one where antibody targeting strategies could be beneficial. Monoclonal antibodies have a Y shaped structure consisting of antigen recognition sites known as Fab fragments, which can specifically target tumour antigens which are only present on cancerous cells (Figure 5.3). The antigen binding site is highly specific and varies between different types of antibodies, making them desirable for therapeutics.[10] In 1997 Rituximab became the first FDA approved monoclonal antibody for the treatment of lymphoma. Since then several more monoclonal antibodies have been approved by the FDA for the treatment of many different types of cancers and solid tumours.[11]

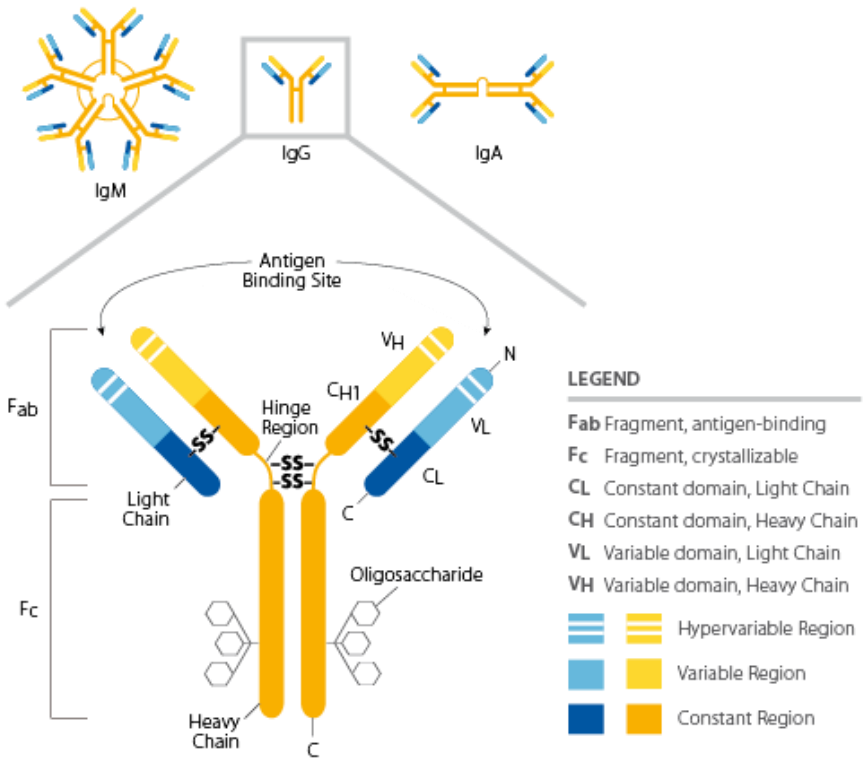

Figure 5.3. Antibody structure[12]

There are many advantages of using monoclonal antibodies as anti-angiogenic agents in comparison to conventional chemotherapy drugs. Firstly, there is selective targeting of tumour endothelial cells present in the tumour vasculature instead of just targeting tumour cells alone. Secondly, tumour endothelial cells are more accessible to anti-angiogenic therapeutic agents as they are in direct contact with blood circulating the body, whereas tumour cells residing inside tumour tissues are less accessible to administered chemotherapeutic drugs. Lastly, there is less toxicity for anti-angiogenic therapy agents due to the lower doses administered.[13] While using monoclonal antibodies for cancer therapies is attractive, it comes with some limitations. Monoclonal antibodies have a high molecular weight and slow distribution kinetics which increases the chances of the antibody degrading before reaching the target tumour vessels, thus resulting in poor biodistribution followed by adverse side-effects and low efficiency of

delivery.[14,15] In recent years researchers have started looking at conjugating these monoclonal antibodies onto nanoparticles as delivery carriers that can target the tumour microenvironment. Harnessing the power of nanotechnology has allowed researchers to develop a more efficient way of selectively targeting tumour-associated vasculature.

5. 1. 2 Methods for Conjugating Antibodies onto AuNPs

To date, there have been many methods published for the conjugation of biomolecules such as antibodies onto the surface of gold nanoparticles for applications such as biosensing, immunoassays and targeted delivery. An important consideration for these applications is to immobilise the antibody in the correct orientation to maintain the antibodies biological activity. This means having the antigen binding site free and not directly conjugated or close to the gold surface.[16] The binding orientation of monoclonal antibodies is key for maintaining the functionality of the antibody for targeting applications. Schematic 5.1 shows the strategies that have been used to conjugate antibodies onto the surface of gold nanoparticles which include i) passive adsorption (hydrophobic attractions and electrostatic interactions), ii) covalent attachment (amino groups), iii) chemisorption (thiol linkers) or iiii) non-covalent attachment (protein intermediate).[17]

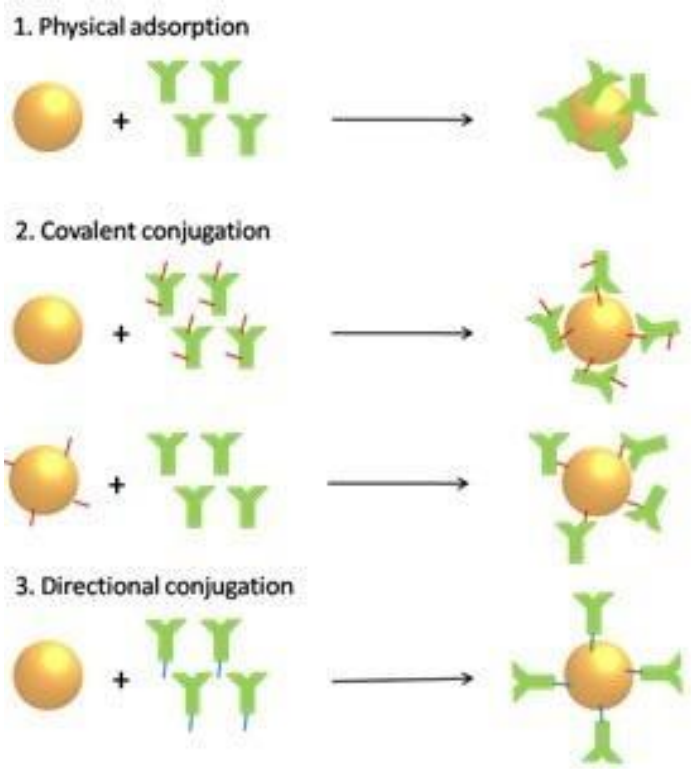

Scheme 5.1. Schematic showing methods for attaching antibodies on the surface of gold nanoparticles.[18]

Passive absorption is the simplest way of conjugating antibodies onto the surface of gold nanoparticles. This method relies on weak hydrophobic or electrostatic interactions of the antibody and the gold surface.[19] For instances, positively charged amino groups from a monoclonal antibody have shown to attach to the surface of negatively charged citrate-capped gold nanoparticles, through electrostatic and hydrophobic interactions.[20, 21] There are many limitations with these adsorption methods which included random orientation of antibodies on the gold surface which significantly reduced the amount of biologically active antibodies; binding is highly dependent on pH and small changes will affect the attachment on the surface; other biomolecules can replace the antibody on the gold surface since binding is done through weak interactions.[22] Another approach which uses non-covalent attachment

of antibodies onto gold nanoparticles is through specific receptor-ligand interactions. For example, using biotin-streptavidin system to immobilize antibodies by using highly specific interactions between the biomolecules.[23, 24]

Research shifted to using covalent methods for attaching antibodies onto the gold nanoparticle surface. The most commonly used covalent method is EDC/NHS coupling reaction which uses the reaction between amino groups present on the antibody and carboxyl groups present on the gold surface. In comparison to physical adsorption, these covalent methods provide strong bonding of the antibody to the gold surface which prevents displacement of other biomolecules, and controls the orientation of the antibody on the gold surface. To increase the binding and biological activity of the antibody (free antigen binding site), spacers have often been used. This type of covenant method increases the stability of the antibody and gives control of the antigen binding site.[25] Predominately thiolated ligands are used due to their high affinity and strong bonding to the gold surface. These ligands have terminal carboxylic groups which react with the terminus amino groups present on the antibody.

5. 1. 3 Targeting angiogenesis with nanoparticles

5. 1. 3. 1 Passive targeting

Nanoparticles have often been used for application within cancer research due to their attractive chemical and structural properties. There have been many types of nanoparticles studied for biological applications, however inorganic nanoparticles such as gold nanoparticles offer many additional benefits for imaging and cancer therapy. Gold nanoparticles have desirable properties such as large surface area, tuneable size and shape and their surface can be easily functionalised for selective targeting of

cancer. There are two methods in which these gold nanoparticles have been used to target tumour cells, passive and active targeting. Passive targeting allows nanoparticles to accumulate into the tumour microenvironment through the tumour's leaky vessels and is heavily reliant on the nanoparticles' size and shape. Active targeting uses nanoparticles functionalised with biorecognition molecules to selectively target tumour cells for uptake into tumours (Figure 5.4).[26] These methods will be discussed and compared to understand more about the desirable properties of nanoparticles and why they are good candidates for cancer therapies.

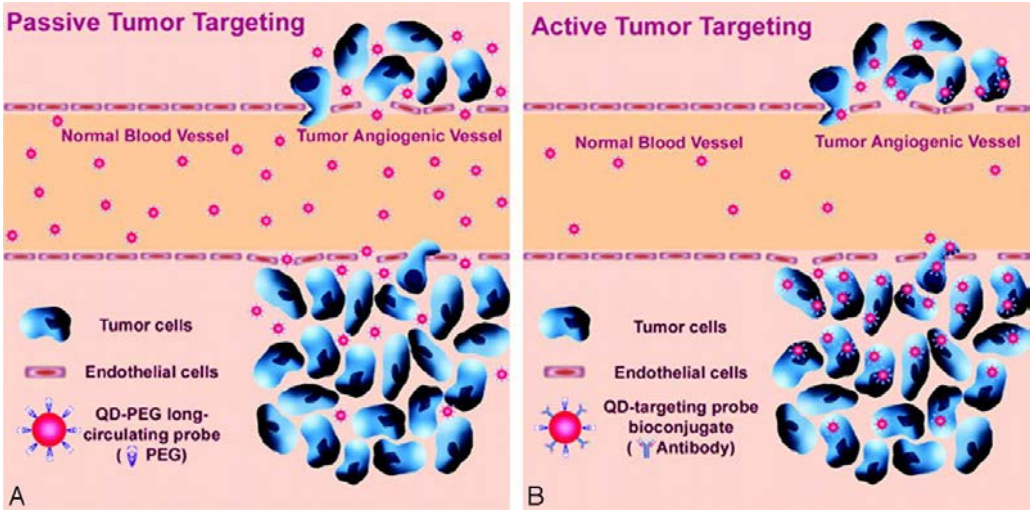

Figure 5.4. Example of passive and active targeting of tumour vasculature using Quantum Dots (QD). A) Permeation and retention of QD probes via leaky tumour vasculatures (passive targeting) and B) High affinity binding of QD-antibody conjugates to tumour antigens (active targeting).[26]

Most types of nanoparticles have shown to accumulate directly into the tumour microenvironment which is dictated by the enhanced permeability and retention effect (EPR). The EPR effect allows for the accumulation of nanoparticles within the tumour microenvironment because of the tumour's leaky vasculature and poor lymphatic drainage system. This makes it possible for nanoparticles to passively target tumour vessels during this period of increased permeability due to the leaky nature of the

vessels. It has been shown that nanoparticles in the size range of 40-200 nm have optimal for passive uptake because of longer circulation times and therefore increase accumulation into the tumour microenvironment through EPR effect.[27] Studies have also shown that larger pores can be found on tumour vessels which allows for penetration of larger nanoparticles such as liposomes up to the size of 400 nm.[28]

Li *et al.* showed the passive targeting of gold nanoparticles into the tumour microenvironment.[29] The gold nanoparticles acted as a drug carrier to deliver recombinant human endostatin (rhES) which could passively target the tumour site. rhES is a well-known vascular angiogenesis-disrupting agent that has been used to treat non-small lung cancer (NSCLC) in the clinic.[30] These anti-angiogenic treatments are known to “starve” tumours and induce tumour cell death by blocking specific angiogenesis signal pathways. Improvements to the *in vivo* efficiency of rhES and reduction of the dosing frequency was done by using gold nanoparticles (AuNPs) as a drug-delivery system. AuNPs can accumulate in the tumour microenvironment and be retained at high concentrations by passive uptake. This research successfully showed an enhanced concentration of rhES being delivered to the tumour site through conjugation onto the nanoparticle carriers. This then promoted the decrease in hypoxia and leaking which showed the improvements in therapeutic efficiency that these nanocarriers have achieved. Further studies showed that AuNPs without any modifications could decrease the expression of VEGF in tumours. This led to the normalisation of tumour vasculature through the decrease of hypoxia and the strengthening of the tumour vascular wall (Figure 5.5).[31]

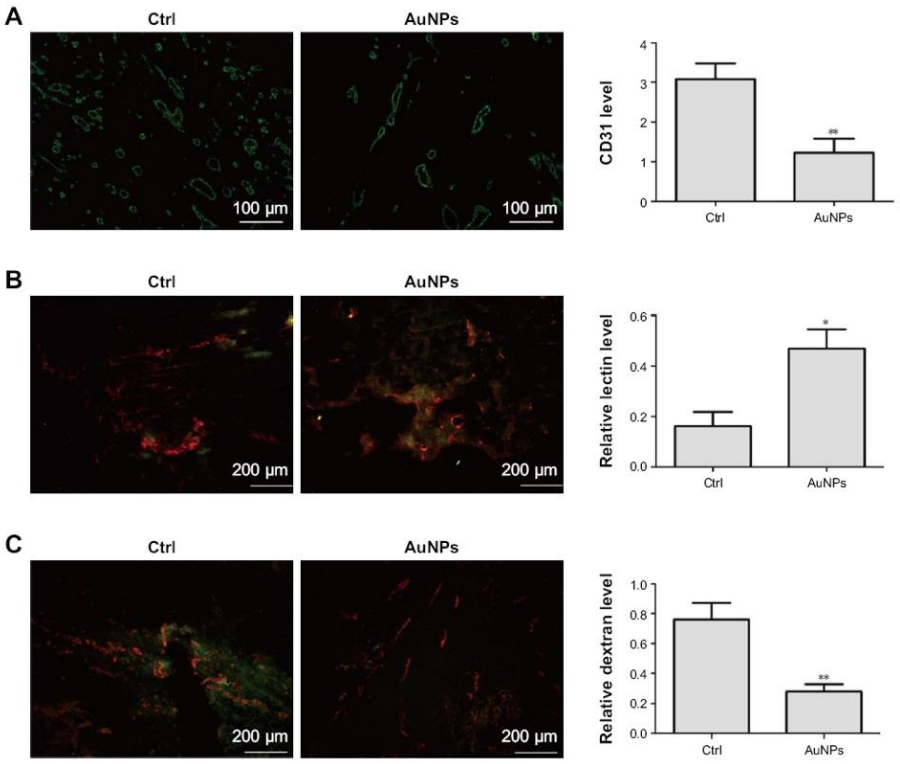

Figure 5.5. Gold nanoparticles as potential candidates for normalising tumour vasculature. A) CD31 staining showed the tumour vessels decreased after treatment with AuNPs, scale bar 100 μm. B) FITC-conjugated lectins (green) and CD61 (red) staining indicated improved perfusion in tumours after treatment with AuNPs, scale bar 200 μm. C) FITC-dextran (green) and CD31 (red) shows decreased number of sites of vascular leakage after treatment with AuNPs, scale bar 200 μm.[31]

Another group showed that small 5 nm AuNPs could interact selectively with heparin-binding glycoproteins such as VEGF165 and BFGF to inhibit their activity. AuNPs could directly bind heparin-growth factors through cysteine residues in the heparin-binding domain, creating a strong bond between gold and thiol/amine groups present. This lead to inhibition of VEGF-induced angiogenesis which was shown in endothelial and fibroblast cells.[32] The fact that these AuNPs could be used to inhibit signalling events and growth factors known to promote angiogenesis is a significant step forward in developing effective therapeutic delivery agents through nanotechnology.

5. 1. 3. 2 Active targeting

Targeting strategies have been further developed over the past few years to enhance the selective uptake of nanoparticles into the tumour cells.[33] Nanoparticles can be easily modified to selectively target tumour cells by the attachment of biorecognition molecules such as antibodies to the surface which can target specific markers overexpressed by cancer cells. This type of targeting is known as active targeting which increases the specificity and efficiency in targeting tumours in comparison to passive targeting. Nanoparticles functionalised with antibodies could potentially function as targeted vessels as these biomolecules can interact with receptors on the cell membrane allowing for selective uptake of these nanoparticles into cells. El-Sayed *et al.* studied spherical AuNPs conjugated with EFGR antibodies and observed differences in binding patterns between non-cancerous and cancerous cell types. They showed that conjugated nanoparticles bound specifically to the surface receptors present on the cancerous cells whereas the binding in the noncancerous cells appeared to be non-specific and random. The ability to distinguish between cancerous and noncancerous cells shows the power of using these targeted gold nanoparticles for cancer diagnostic applications.[34]

Additionally, the surface of the gold can be modified with drugs or small molecules such as DNA, siRNA or peptides for targeted delivery inside the tumour cells. Bartczak *et al.* demonstrated this by conjugating peptides to the surface of AuNPs to selectively activate or inhibit angiogenesis. The results showed that for the AuNPs functionalised with the activation peptide showed capillary formation after 2 hours of incubation. This showed an increased amount of angiogenesis in comparison to untreated cells.

However, the gold nanoparticles functionalised with the inhibitor peptide showed no angiogenesis occurring at any of the time points studied (Figure 5.6).[35]

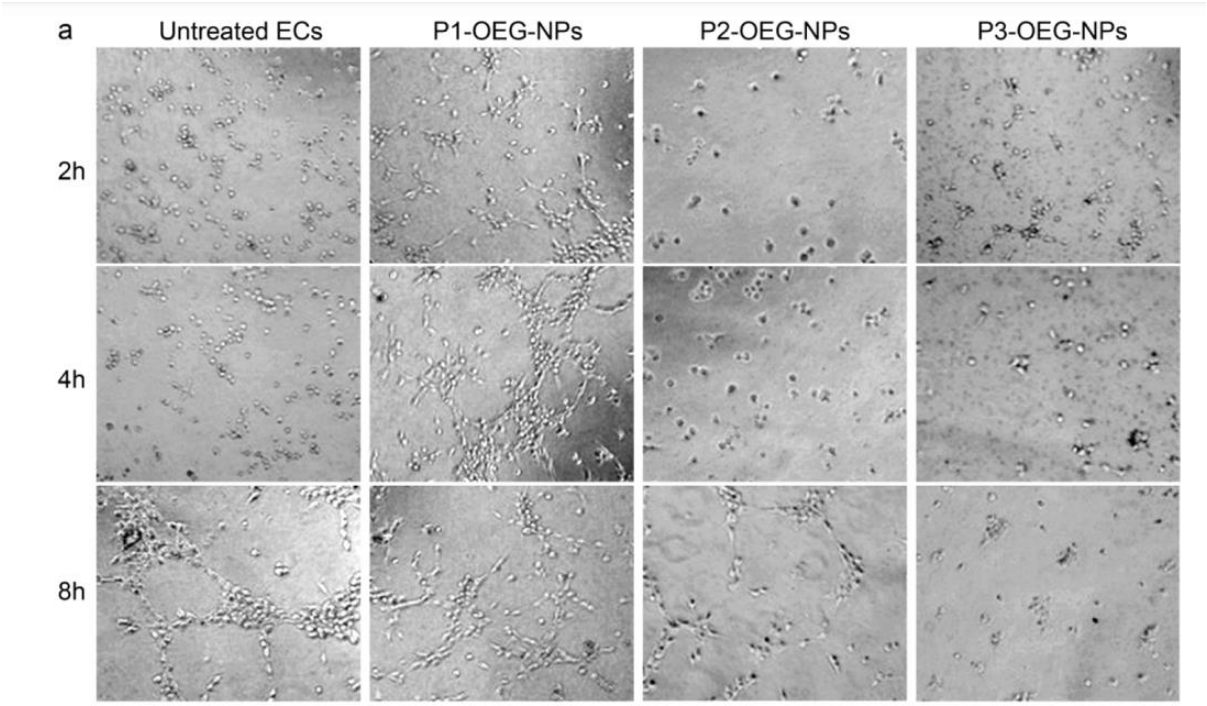

Figure 5.6. Peptide-coated gold nanoparticles for activation and inhibition of angiogenesis. a) Phase-contract images show endothelial cells grown on reduced serum matrix gel after treatment with P1-OEG-NPs (activators), P2-OEG-NPs (mutants) and P3-OEG-NPs (inhibitors) compared with untreated endothelial cells (ECs) for 2, 4 and 8 hours after incubation. [35]

Furthermore, luminescent probes can be conjugated onto the nanoparticle surface to allow for visualisation of tumour vessels whilst also being able to target the microenvironment.[36] Nanoparticles are advantageous to use as delivery carriers as they often have low cytotoxicity and do not provoke an immune response, allowing for a higher density of therapeutic agents to be functionalised onto the gold's surface before administration.

5. 1. 4 SiRNA delivery strategies

Short interfering RNAs (SiRNA) are small double stranded RNAs which are about 21 – 22 nucleotides long and have 2-base 3' overhangs that are known to regulate gene expression.[37] Since this fundamental area of research started over a couple of decades ago, the basic principles of RNA interference and gene silencing are now well understood.[38] The mechanism sees double-stranded RNA interacting with a protein complex known as Dicer to generate short interfering RNAs (SiRNA). These SiRNA complexes then bind with proteins to form an RNA-induced silencing complex (RISC). This SiRNA/RISC complex binds the complementary sequence of the target mRNA and unwinds the double strand into single stranded fragments. These mRNA fragments are then degraded within the cell (Figure 5.7).[39] The ability to silence genes makes these excellent candidates for targeted cancer therapies.

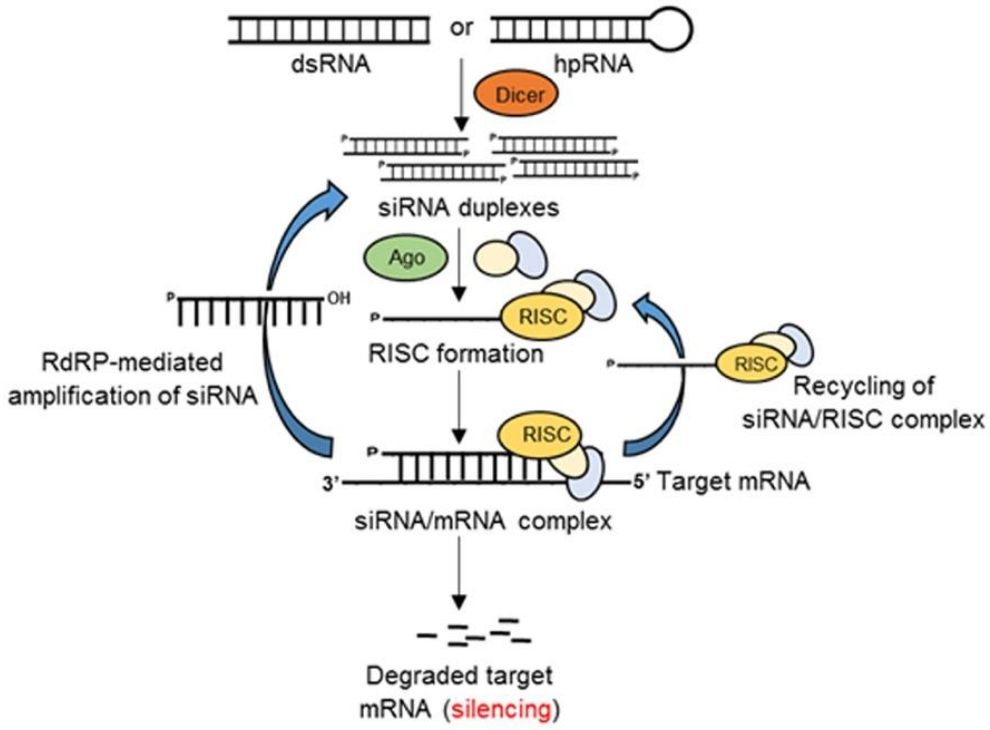

Figure 5.7. Schematic for RNA-mediated gene silencing in Eukaryotes.[39]

Despite the advantages of using SiRNA complexes as potential cancer therapeutic agents, the delivery into cells is hard enough since SiRNA complexes are degraded upon entry into the cell. SiRNA suffers from poor intracellular uptake and degradation *in vivo,* which has made this form of cancer therapeutics very challenging. [40] Therefore, for effective pharmacological use of SiRNA in cells "carriers" that can efficiently delivery SiRNA to the intended site are needed.[41] Nanoparticles are advantageous as "carriers" because their size and surface charge can be easily modified to overcome the cell membrane barrier for efficient uptake. Nanoparticles have shown to remain in circulation for longer periods of time, via the EPR effect, making delivery to tumour cells more efficient. The surface of the nanoparticle can be functionalised with target-specific ligands, which allows for targeted delivery of SiRNA. There have been many types of nanoparticles investigated for SiRNA delivery into cells. There are two mechanisms for delivering SiRNA into cells using nanotechnology, 1) SiRNA complexes are contained within the nanoparticles or 2) SiRNA complexes are conjugated to the surface of the nanoparticle (Figure 5.8).[42]

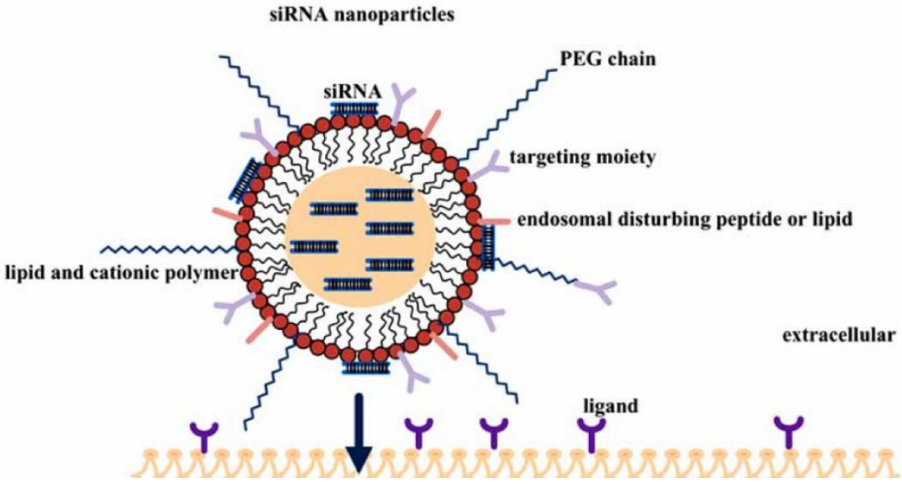

Figure 5.8. Functionalising nanoparticles with SiRNA can be achieved through conjugation to the surface of the nanoparticles or containment within the nanoparticle. Both methods are effective ways of delivering SiRNA into cells with degradation.[42]

To date, extensive studies have been carried out using both organic and inorganic nanoparticles for the delivery of SiRNA into cells. Organic based nanomaterial such as liposomes and chitosan nanoparticles can be synthesised to entrap SiRNA within the core, thus protecting the SiRNA from enzymatic degradation.[43-45] Inorganic nanoparticles made from gold has been explored for delivery SiRNA into cells because the gold surface can be further functionalised with imaging probes which allows for both targeting and imaging. Gold nanoparticles have shown to be biocompatible and easily taken up by both cancer cells. Mirkin *et al*. functionalised the surface of gold nanoparticles with SiRNA molecules and thiol-modified oligonucleotides. It was found that the additional coverage of the gold surface with the oligonucleotides protected the SiRNA molecules from degradation within cells. They showed these SiRNA functionalised gold nanoparticles were taken up readily into cancer cells, despite the high overall negative charge of the particles which was expected to prevent their uptake into cells.[46] Mirkin *et al.* then went on to look at improving the delivery of nucleic acid functionalised gold nanoparticles by adding a targeting antibody (HER2 mAb) onto the surface of the gold. This work showed impressive results with HER2 mAb functionalised gold nanoparticles showing higher selectively, faster uptake and more efficient gene knockdown in comparison to gold nanoparticles without the targeting antibody (Figure 5.9).[47] It was also shown that in cells that did not express HER2, no selectively was seen from the targeting gold nanoparticles.

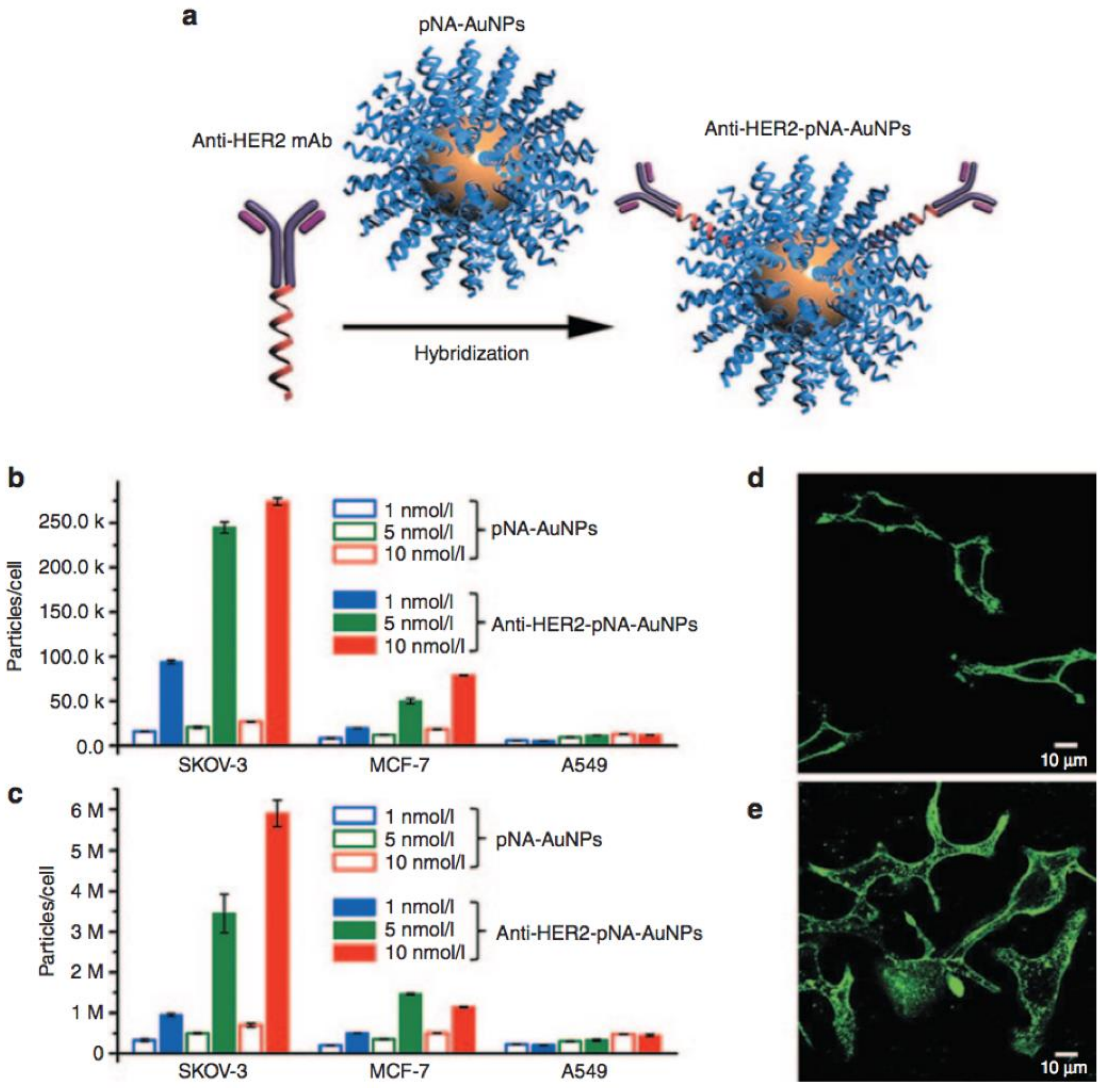

Figure 5.9. Antibody functionalised gold nanoparticles for the delivery of nucleic acids for cellular targeting. (a) anti-HER2-pNA-AuNPs. The number of AuNPs per cell for (b) 4 °C and (c) 37 °C after 4 hours of incubation. Confocal images of SKOV3 cells after incubation for 4 hours with 5 nmol/ L anti-HER2-pNA-AuNPs at (d) 4 °C and (e) 37 °C.[48]

The ability to easily functionalise the surface of gold nanoparticles with targeting vectors and imaging probes is a significant step forwards in developing novel constructs for efficiently targeting diseases such as cancer whilst being able to visualise the effect.

5. 2 Chapter summary

Iridium(III) coated gold nanoparticles of various sizes were found to be suitable multiphoton lifetime imaging probes, due to their desirable long-luminescence lifetime which could be detected in cancer cells. The results showed that the iridium lifetimes were sensitive to changes in the local environment which was used to map localisation patterns. It was found that fluorescence lifetime imaging could be used to detect the unique SPR signal from the gold nanoparticles separately from the long-lived iridium signal, allowing for multichannel detection using lifetime microscopy. This chapter will explore the iridium(III) functionalised gold nanoparticles ability to selectively target cancer cells which will be monitored by multiphoton lifetime imaging. An anti-CLEC14A antibody (**AbH**) will be chemically modified for the attachment onto gold nanoparticles and the anti-angiogenic properties and selective targeting abilities assessed through changes in the probe's luminescence lifetime. Thiolated SiRNA will be conjugated onto the gold nanoparticle surface and the delivery into cancer cells will be assessed for gene silencing applications. The ability to deliver SiRNA selectively into cancer cells will be explored through attachment of both AbH and SiRNA onto the gold surface. These functionalized nanoparticles have been shown in Scheme 5.2. These functionalised nanoprobes have clear potential as cancer therapeutic agents and the ability to monitor uptake and targeting patterns *in vitro* by multiphoton lifetime imaging shows the design and synthesis of novel cancer targeting nanoprobes.

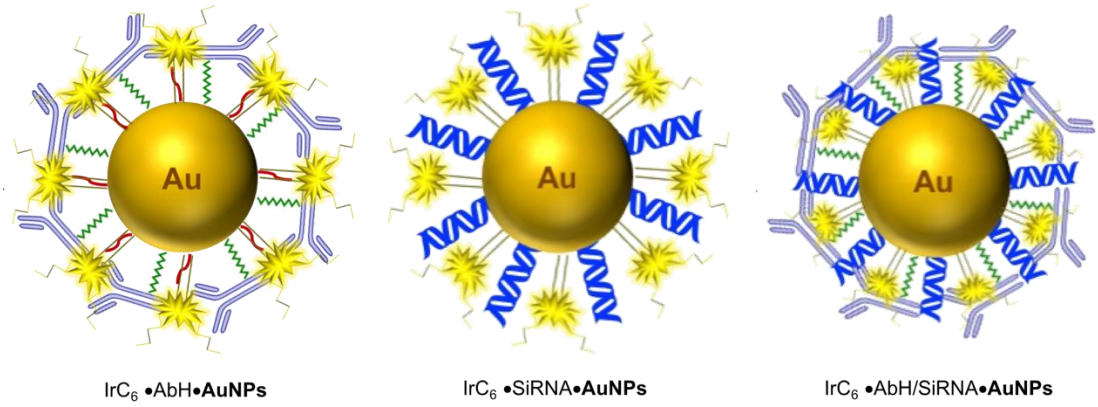

Scheme 5.2. Schematic showing gold nanoparticles functionalised with AbH, SiRNA and both which will be discussed in detail within this chapter.

5. 3 Results and discussion

The method for conjugating **AbH**, **SiRNA** and both **AbH**/**SiRNA** will be discussed in each sub chapter. The gold nanoparticles used for these experiments, unless stated otherwise, are monodisperse 13, 25 and 100 nm citrate stabilised AuNPs (**AuNP13, AuNP25** and **AuNP100** respectively). These particles were synthesised and characterised according to the methods described in Chapter 4. For these experiments the citrate coated **AuNP25** were concentrated up to 8 nM before the addition of **AbH** or **SiRNA**, unless stated otherwise. The purification of these functionalised nanoparticles requires 3 washing steps to remove any excess biomolecules in solution, therefore it was found that the stock concentration of **AuNP25** (1.6 nM) was reduced too much after purification that it was not suitable for cell dosing experiments.

5. 3. 1 Synthesis of IrC_6 •AbH •AuNPs

5. 3. 1. 1 Chemical Modification of Antibody for attachment onto AuNPs

For attachment onto gold nanoparticles the monoclonal antibodies were functionalised with a hydrazide linker containing a thiol group for conjugation onto the gold surface.

The high affinity between the thiol group and the gold surface creates a strong attachment of the antibody to the gold surface. The hydrazide linker provides enough distance from the gold surface to stop the antibody adsorbing onto the gold surface. The synthesis of the antibody-hydrazide conjugate (**AbH)** was followed using a method by Kumar *et al.* in Nature Protocols.[49] The carbohydrates on the base of the antibody were oxidised using sodium periodate (Scheme 5.3, Top). To confirm the oxidation reaction was successful a Purpald test was conducted, in which the colour turned purple after 5 minutes. The Purpald test verifies the oxidation of carbohydrates to aldehydes which is indicated by a change in colour from colourless to purple, confirming oxidation of the antibody. The Purpald reagent will only react with the oxidised antibody (aldehyde) present in the solution causing the colour to change. After successful oxidation of the antibody, the hydrazide linker was conjugated to the aldehyde on the antibody, via a hydrazide click reaction (Scheme 5.3, bottom).

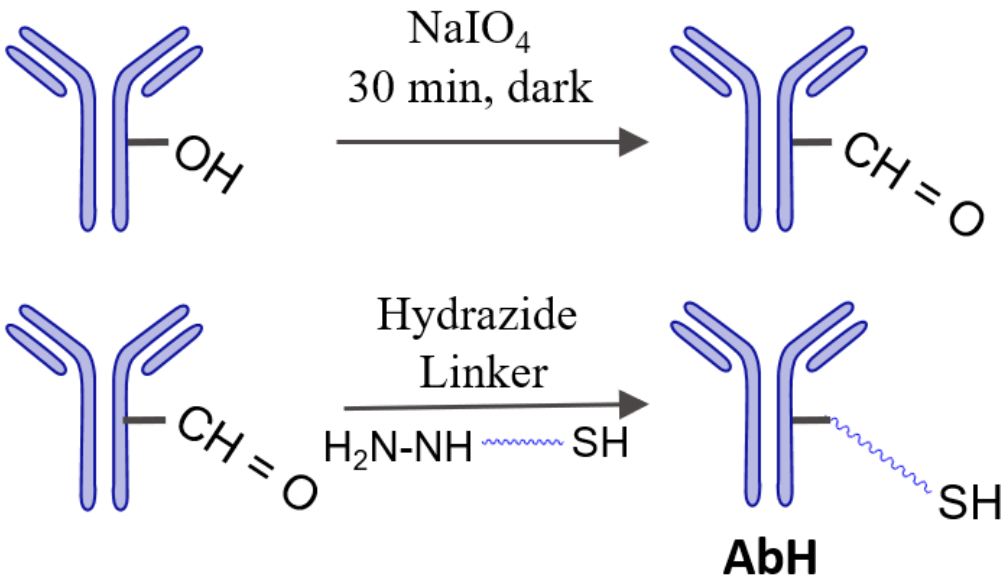

Scheme 5.3. Modifying monoclonal antibodies with a hydrazide linker to produce antibody-hydrazide (AbH). (Top) Oxidation of the carbohydrate on monoclonal antibody to produce an aldehyde. (Bottom) Chemical modification of the aldehyde with a hydrazide linker to produce AbH.

The antibody was characterised by UV/Vis absorption, showing a peak at 280 nm (Figure 5.10). This absorption peak is characteristic of an antibody which contains amino acids that absorb in this region.

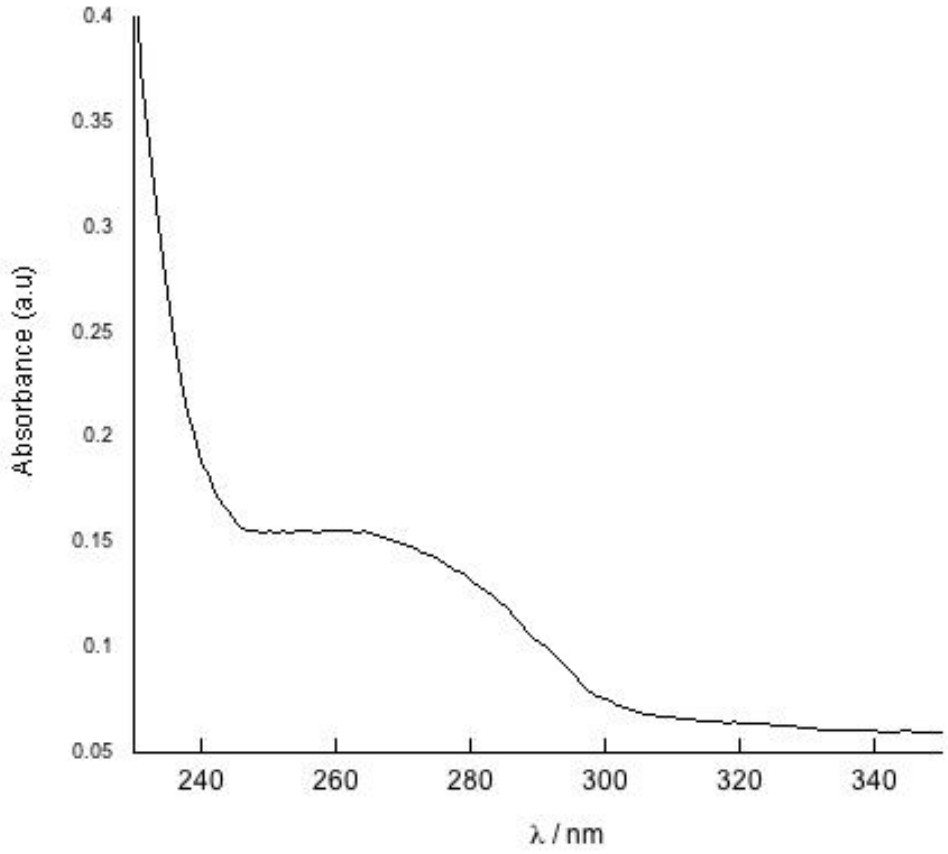

Figure 5.10. Absorption spectrum of 100 μg mL^{-1} AbH in HEPES buffer (pH 7.5).

5. 3. 1 .2 Attachment of AbH onto AuNPs

The Nature Protocol[49] which described the chemical modification of the antibody was followed for the conjugation of **AbH** onto **AuNPs.** The **AuNPs** were synthesised at 13 nm, 25 nm and 100 nm following previously described methods in Chapter 3[50]. The protocol outlines the addition of 100 μL **AbH** into a solution of 1 mL **AuNPs** in water, giving a final antibody concentration of 100 μg/ mL^{-1}. However, after following these steps visible aggregation occurred upon addition of **AbH** into **AuNPs**. To move forward

with this protocol, the point of aggregation had to be determined. This was done by titrating the **AbH** into a solution of **AuNP25**. The spectra showed the characteristic antibody peak at 280 nm, which proved the presence of **AbH** in the solution of gold nanoparticles (Figure 5.11, arrow). However, the results also showed complete aggregation of gold particles after the addition of only 10 μL **AbH**. This was identified by the broadening of the SPR peak seen through UV/Vis spectroscopy. The broadened SPR peak was compared to the citrate coated **AuNP25**, where clear deviations could be seen (Figure 5.11, blue line). There was also a shift in SPR and a visual change in colour from red to purple.

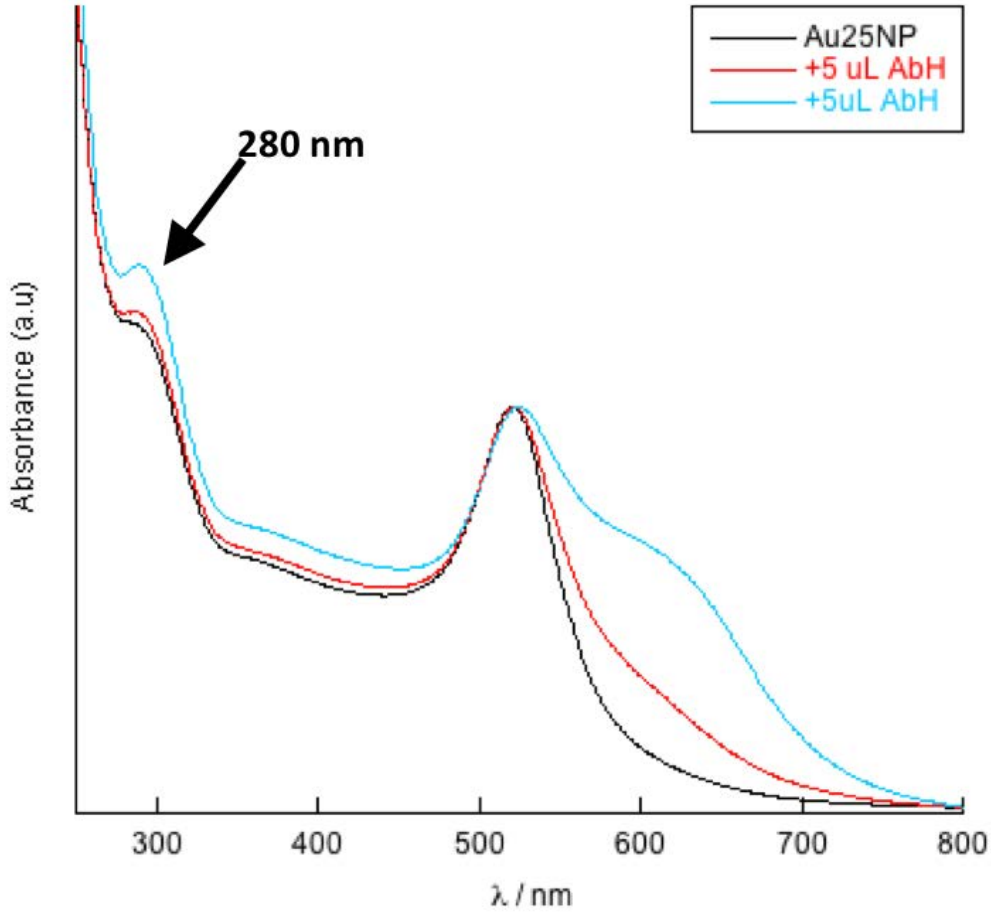

Figure 5.11. Absorbance spectrum of 2 nM AuNP25 in water (black), addition of 5 μL AbH (red) and addition of 10 μL AbH (blue), showing aggregation of particles.

The only deviation from the nature protocol was the method of synthesis for gold nanoparticles. Therefore, gold nanoparticles were synthesised according to the nature protocol to yield 18 nm AuNPs, using Frens' method of synthesis.[51] Upon addition of **AbH** into a solution of 18 nm AuNPs complete aggregation could be seen, therefore yielding the same outcome as the previous method. The method was then optimised for conjugation of the antibody onto our previously synthesised gold nanoparticles (**AuNP25**). Since aggregation was occurring upon addition of **AbH** into citrate coated **AuNP25**, it was decided to first partially coat the gold surface with PEG-SH (230 MW) before addition of the antibody (Scheme 5.4). The partial coating of the gold nanoparticles with PEG-SH was determined by a UV/Vis titration (Figure 5.12).

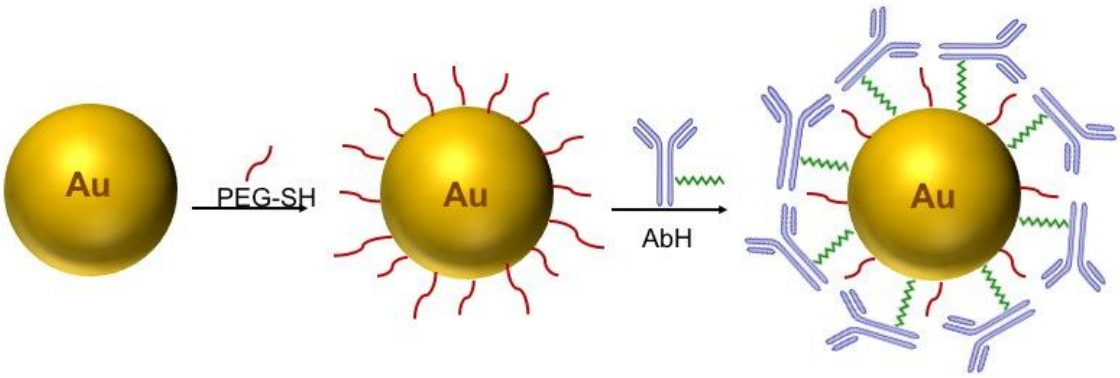

Scheme 5.4. Schematic for the procedure of coating AuNPs with PEG-SH and modified monoclonal antibodies (AbH).

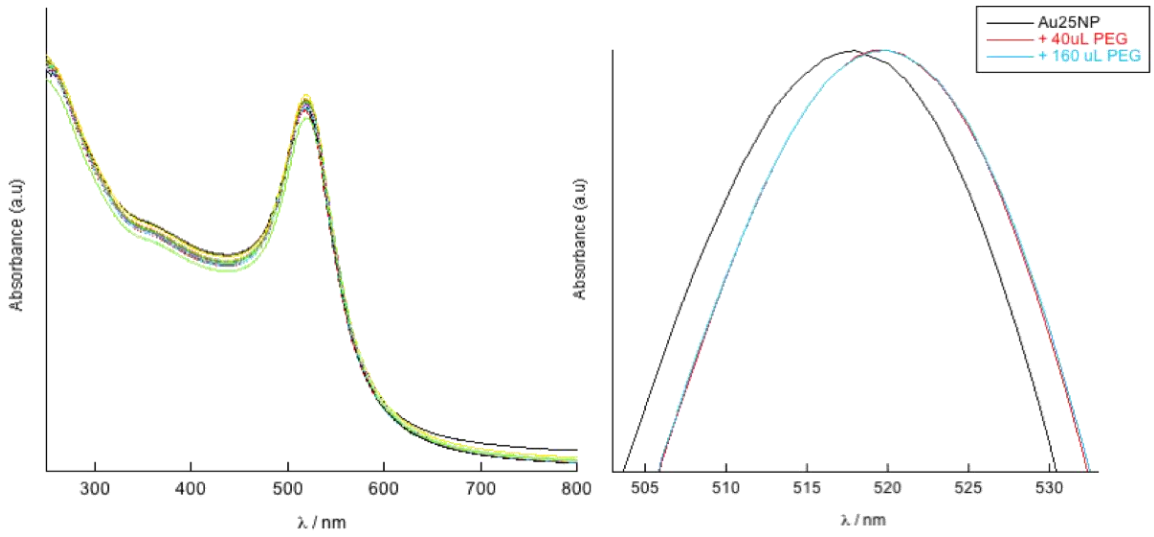

Figure 5.12. (Left) UV/Vis titration of 28 μM PEG-SH into 2 mM AuNP25 (2 mL) in water and (Right) highlighting SPR shifts of AuNP25, 0.5 μM PEGSH and 2 μM PEGSH.

A solution of PEG-SH in water was titrated in 2 μL, 5 μL and 10 μL aliquots into an aqueous solution of **AuNP25** (2 mL) and the SPR shift was monitored. The shift in SPR indicated that a modification had occurred on the gold surface, and this shift would stop once the surface has been saturated with PEG-SH. The SPR shifted from 517 nm to 520 nm upon addition of 0.01 μM to 0.5 μM PEG-SH into **AuNP25.** PEG-SH was added up to a concentration of 2 μM, but no further shift was seen. This identified a concentration of 0.5 μM PEG-SH was needed to fully saturate the gold surface. Therefore, partial coating of **AuNPs** (13 nm, 25 nm and 100 nm) with 0.25 μM PEG-SH was carried out for these experiments. The PEG coated gold nanoparticles were centrifuged for 30 minutes at 13.3 RPM to remove any excess PEG-SH in solution. This produced 4.5 nM PEG •**AuNP13**, 1.6 nM PEG •**AuNP25** and 30 pM PEG •**AuNP100** in water. Next a titration of **AbH** was carried out in 5 – 20 μL aliquots into the aqueous solution of PEG •**AuNP13**, PEG •**AuNP25** and PEG •**AuNP100**

respectively up to a final volume of 100 μL **AbH** or a final concentration of 100 μg/ mL^{-1} in accordance to the Nature Protocol. The shift was monitored to identify the conjugation of antibody onto the gold surface and to observe any changes which could be indicative of particle aggregation. Addition of 100 μL **AbH** into PEG •**AuNP13**, PEG •**AuNP25** and PEG •**AuNP100** resulted in a 4 nm (524 nm), 2 nm (521 nm) and 2 nm (556 nm) shift in λ_{max} (H_2O), respectively (Figure 5.13).

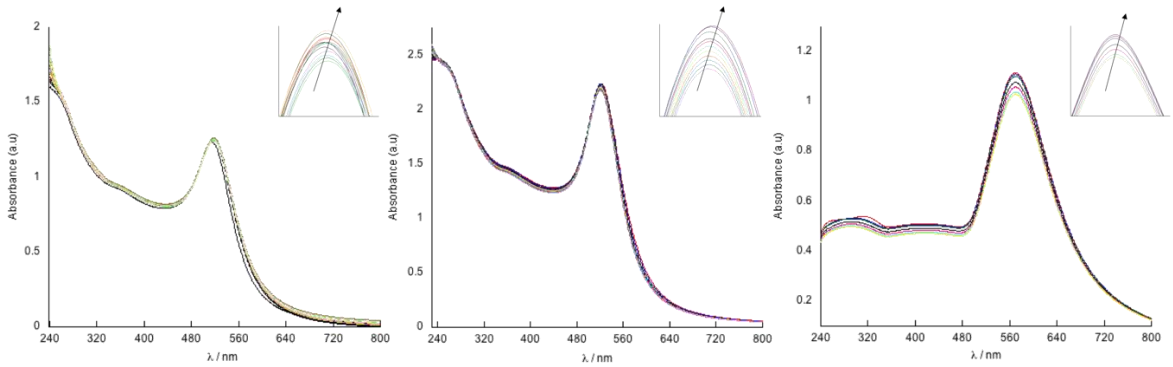

Figure 5.13. UV/Vis titration of AbH (1 mg/ mL^{-1}) into (Left) 4.5 nM PEG •AuNP13, (Middle) 1.6 nM PEG •AuNP25 and (Right) 30 pm PEG •AuNP100 in water giving a final AbH concentration of 100 μg/ mL. The SPR region is shown in the inset to highlight the shift in SPR.

The antibody coated gold particles were purified using Millipore filters (300 kDa MWCO) to produce 3.5 nM AbH •**AuNP13**, 1.3 nM AbH •**AuNP25** and 25 pM AbH •**AuNP100**. Upon isolation of these nanoparticles the SPR λ_{max} (H_2O) maximum remained unchanged confirming that no aggregation occurred after coating with the monoclonal antibody (Appendix). The particles were sized by DLS to further show that no aggregation had occurred during coating with **AbH**. The results can be seen in Table 5.1 and Figure 5.14. The attachment of the antibody onto the gold nanoparticles was confirmed by the increase in size both by number and intensity distribution. Further

evidence was the increase in PDI, which is sensitive to the antibody being present on the gold surface.

Table 5.1. Dynamic Light Scattering (DLS) for AbH • AuNP13, AbH • AuNP25 and AbH • AuNP100 in water. Results displayed are Size by Number Distribution, Size by Intensity Distribution and Polydispersity Index (PDI).

	Number Distribution (nm)	Intensity Distribution (nm)	PDI
AbH •**AuNP13**	22 ± 7	41 ± 15	0.26
AbH •**AuNP25**	28 ± 8	60 ± 25	0.21
AbH •**AuNP100**	115 ± 28	143 ± 32	0.04

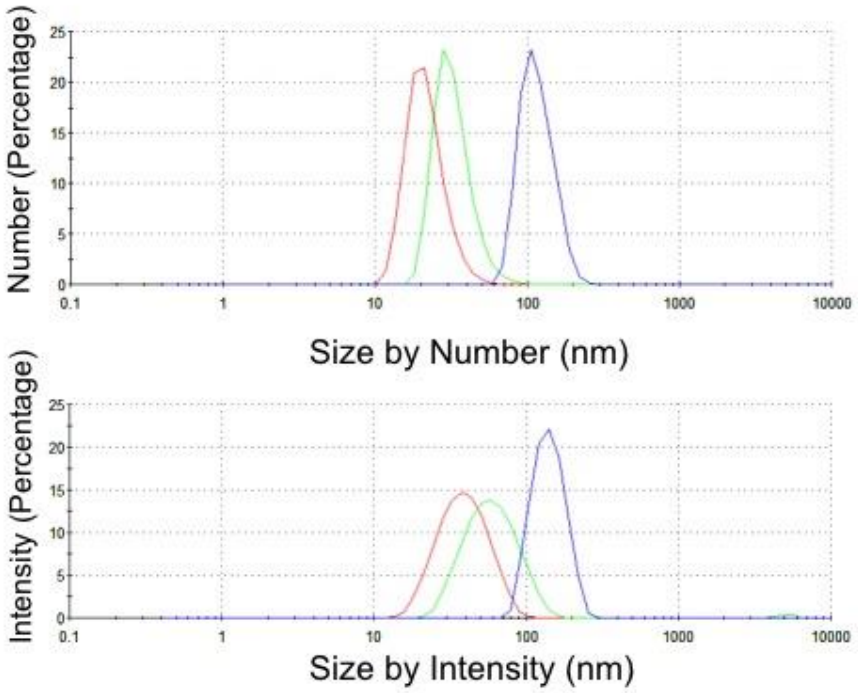

Figure 5.14. Dynamic Light Scattering (DLS) Data showing sizing by Number Distribution (top) and Intensity Distribution (bottom). Results displayed are for AbH •AuNP13 (red), AbH •AuNP25 (green) and AbH •AuNP100 (Blue).

Zeta-potentials (ζ-potential) were measured and found be -39 ± 21 mV, -36 ± 23 mV and -40 ± 26 mV for AbH •**AuNP13**, AbH •**AuNP25** and AbH •**AuNP100** respectively (Figure 5.15). The results showed a negligible decrease in negative potential in comparison to the PEG stabilised nanoparticles which were found to be -43 ± 21 mV, -44 ± 19 mV and -41 ± 27 mV for PEG •**AuNP13**, PEG •**AuNP25** and PEG •**AuNP100**

respectively. This is to be expected as both the PEG complexes and the antibody have an overall negative charge, therefore upon displacement of the PEG complexes the overall negative charge is not expected to change.

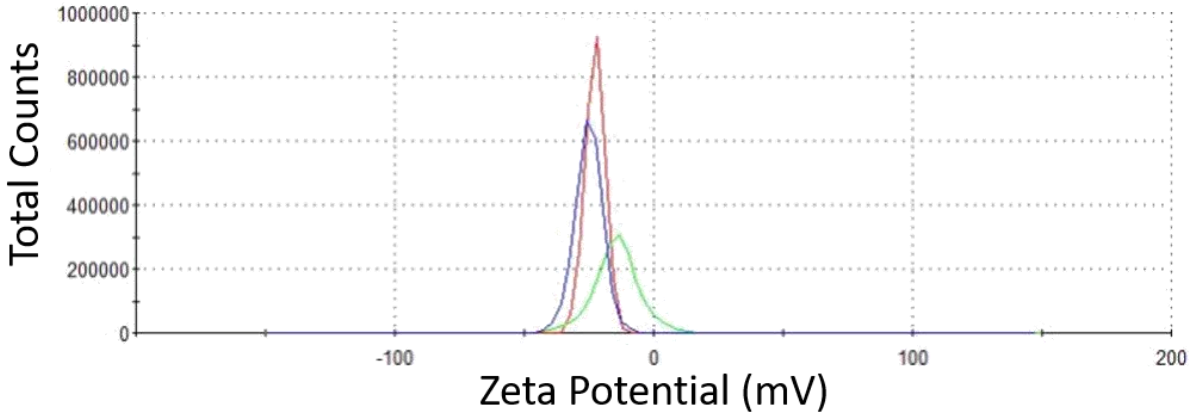

Figure 5.15. DLS data showing the absolute Zeta-Potential measurements for AbH • AuNP13 (red), AbH • AuNP25 (green) and AbH • AuNP100 (blue) in water.

5. 3 .1. 3 Attachment of IrC_6 onto AbH •AuNPs

A solution of **IrC_6** in MeOH (1 mM) was titrated into AbH •**AuNP13**, AbH •**AuNP25** and AbH •**AuNP100** in 1 – 2 μL aliquots (Scheme 5.5).

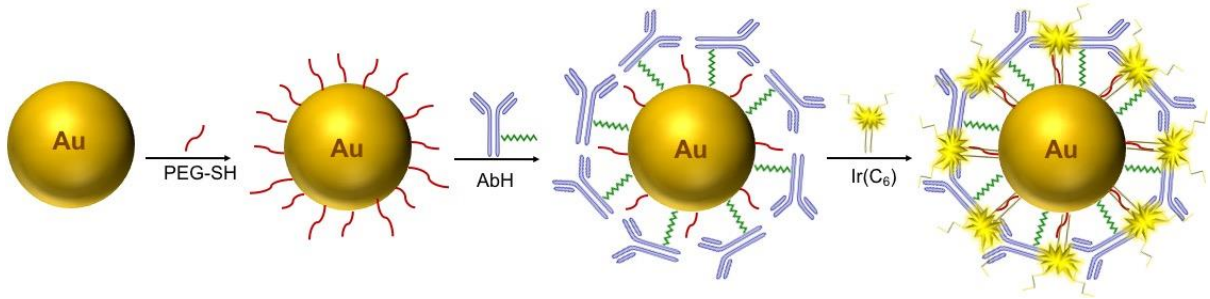

Scheme 5.5. Schematic showing coating of AbH •AuNPs with IrC_6 to produce IrC_6 •AbH •AuNP25.

The **IrC_6** probe was added to a final concentration of 5 μM, 7 μM and 5 μM for AbH •**AuNP13**, AbH •**AuNP25** and AbH •**AuNP100** respectively (Figure 5.16). This addition of 1mM **IrC_6** into the colloidal solution of gold resulted in a 4 nm (528 nm), 4 nm (527

nm) and 1 nm (558 nm) shift in λ_{max} (H_2O) for AbH • **AuNP13**, AbH • **AuNP25** and AbH • **AuNP100** respectively.

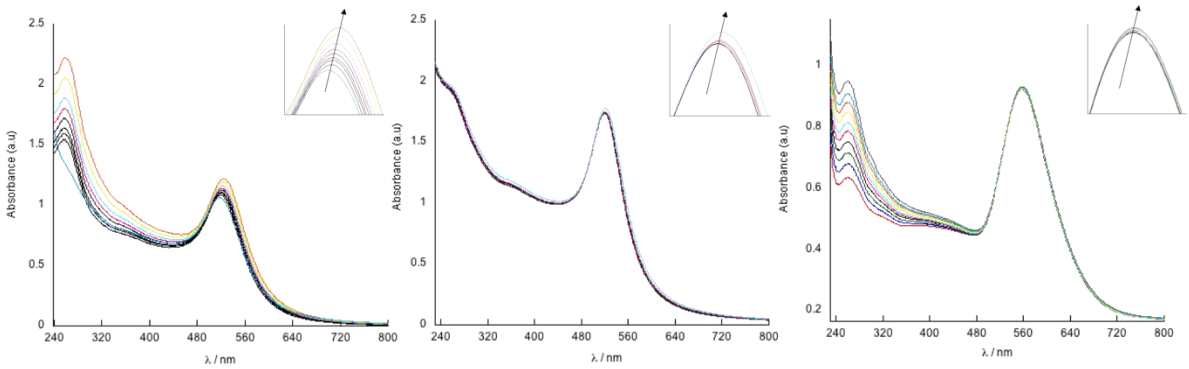

Figure 5.16. UV/Vis titration of IrC_6 into (left) 3.4 nM AbH • AuNP13, (middle) 1 nM AbH • AuNP25 and (right) 24 pM AbH • AuNP100. The SPR region is shown in the inset to highlight the shift in SPR.

The iridium coated nanoparticles were centrifuged three times using a Millipore filter (100 kDa MWCO) for 5 minutes at 2000 *g* giving a final product of 3 nM IrC_6 •AbH •**AuNP13**, 1 nM IrC_6 •AbH •**AuNP25** and 20 pM IrC_6 •AbH •**AuNP100** in water. The absorbance was measured after purification and it was found that the SPR λ_{max} (H_2O) remained unchanged, showing non-aggregation of these particles after centrifugation (Appendix). DLS was carried out to measure the size of these functionalised nanoparticles in solution. The results can be seen in Table 5.2 and Figure 5.17. An increase in size and PDI when coated with **IrC_6** can be seen in which the results showed a 10 nm increase in size in comparison to the antibody coated particles (AbH •**AuNPs**). This increase in size is greater than previously seen with **IrC_6** coated Zonyl particles, where the size increased by a couple of nanometres upon addition of **IrC_6.** This could be because the iridium(III) complex is interacting with the antibody attached to the gold nanoparticle surface causing a large increase in the hydrodynamic size.

Table 5.2. DLS results for IrC_6 •AbH •AuNP13, IrC_6 •AbH •AuNP25 and IrC_6 •AbH •AuNP100 in water. Results displayed are Size by Number Distribution, Size by Intensity Distribution and Polydispersity Index (PDI).

	Number Distribution (nm)	Intensity Distribution (nm)	PDI
IrC_6 •AbH •**AuNP13**	36 ± 12	88 ± 40	0.26
IrC_6 •AbH •**AuNP25**	38 ± 10	62 ± 23	0.22
IrC_6 •AbH •**AuNP100**	127 ± 32	158 ± 40	0.05

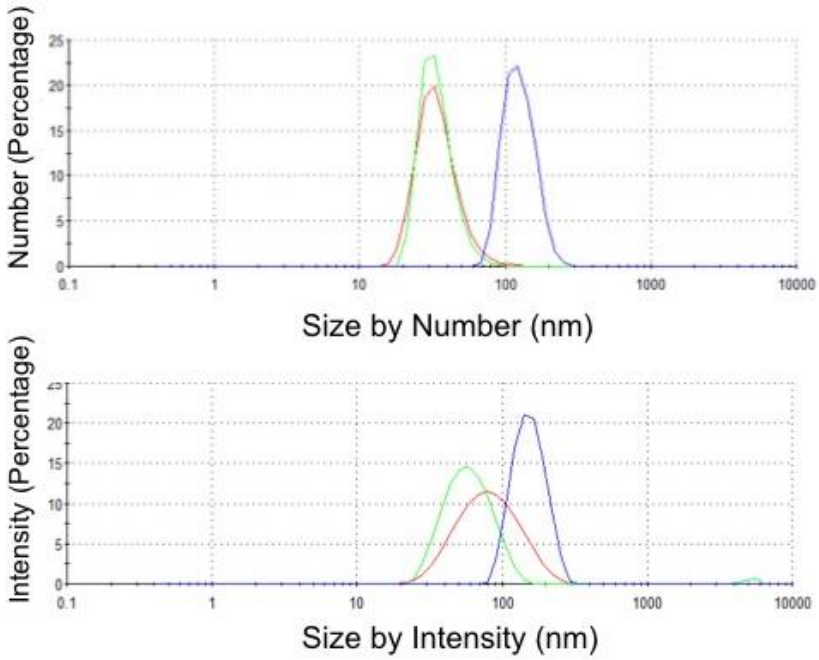

Figure 5.17. Dynamic Light Scattering (DLS) Data showing sizing by Number Distribution (top) and Intensity Distribution (bottom). Results displayed are for IrC_6 •AbH •AuNP13 (red), IrC_6 •AbH •AuNP25 (green) and IrC_6 •AbH •AuNP100 (Blue).

ζ-potential for the IrC_6 •AbH •**AuNPs** were measured and found to be -28 ± 19 mV, -30 ± 11 mV and -31 ± 20 mV for IrC_6 •AbH •**AuNP13**, IrC_6 •AbH •**AuNP25** and IrC_6 •AbH •**AuNP100** respectively (Figure 5.18). The results showed a decrease in negative potential in comparison to the AbH •**AuNPs**, which had a ζ-potential of -39 ± 21 mV, -36 ± 23 mV and -40 ± 26 mV for AbH •**AuNP13**, AbH •**AuNP25** and AbH

•**AuNP100** respectively. This was to be expected as **IrC$_6$** in solution holds an overall positive charge.

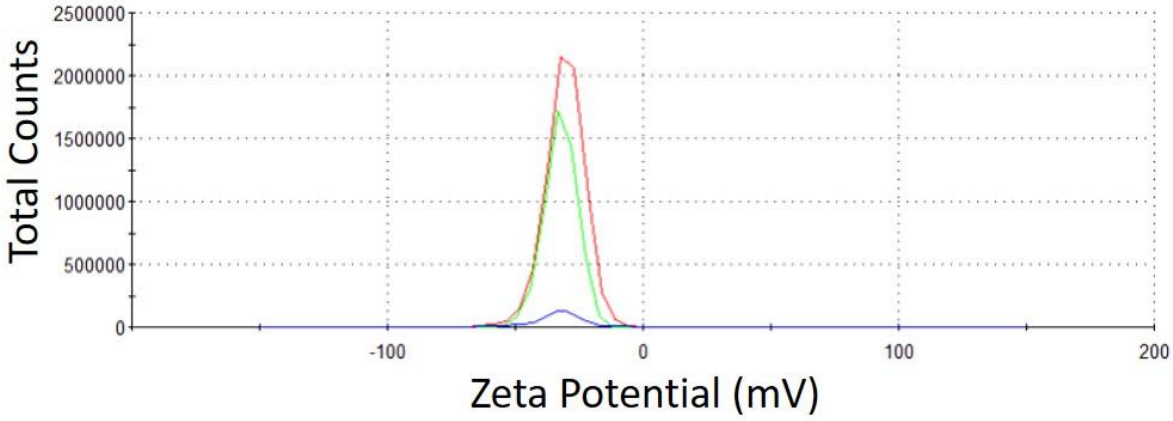

Figure 5.18. DLS data showing the absolute ζ-potential measurements for IrC$_6$ • AbH • AuNP13 (red), IrC$_6$ • AbH • AuNP25 (green) and IrC$_6$ • AbH • AuNP100 (blue) in water.

Elemental composition of the nanoparticles by inductively coupled plasma mass spectroscopy (ICP-MS) was carried out to calculate the number of **IrC$_6$** per AbH• **AuNPs** (Table 5.3). This was done by dissolving the coated AuNPs in ultrapure Aqua Regia, until the nanoparticles were fully digested. The metal content for each iridium(III) functionalised nanoparticles was then calculated from the iridium concentration detected from ICP-MS.

Table 5.3. Elemental composition of nanoparticles by ICP-MS, showing number of IrC$_6$ complexes per AuNP.

Sample	**IrC$_6$** per AbH •**AuNP**
IrC$_6$ •AbH •**AuNP13**	680
IrC$_6$ •AbH •**AuNP25**	800
IrC$_6$ •AbH •**AuNP100**	7550

The results show a high coating of iridium(III) complexes onto AbH •**AuNPs**, with hundreds of **IrC$_6$** being detected. The number of **IrC$_6$** complexes per AbH •**AuNPs** is much less than seen for Zonyl coated particles where thousands of complexes were detected per **AuNP**. This is due to a lower concentration of **IrC$_6$** added to AbH •**AuNPs.** It was found that the concentration of **IrC$_6$** added to Z •**AuNPs** was 11 μM, 20 μM and 15 μM for Z • **AuNP13**, Z • **AuNP25** and Z • **AuNP100** respectively. In comparison, the total concentration of **IrC$_6$** added to AbH •**AuNPs** which was 6 μM, 7 μM and 5 μM for AbH •**AuNP13**, AbH •**AuNP25** and AbH •**AuNP100** respectively. One of the advantages of using multiphoton lifetime imaging over emission based microscopy is detection of the luminescence lifetimes which is independent of probe concentration.

5. 3. 2 Synthesis of IrC$_6$ •SiRNA •AuNPs

5. 3. 2. 1 Conjugation of SiRNA onto AuNPs

The monodisperse AuNPs (13 nm, 25 nm and 100 nm) were coated with **SiRNA** for delivery into cancer endothelial cells for gene silencing applications. **SiRNA** was chemically modified with a thiol group on the 5' end for attachment onto the gold surface (Appendix). The scheme for attaching **SiRNA** onto the surface of gold nanoparticles can be seen below.

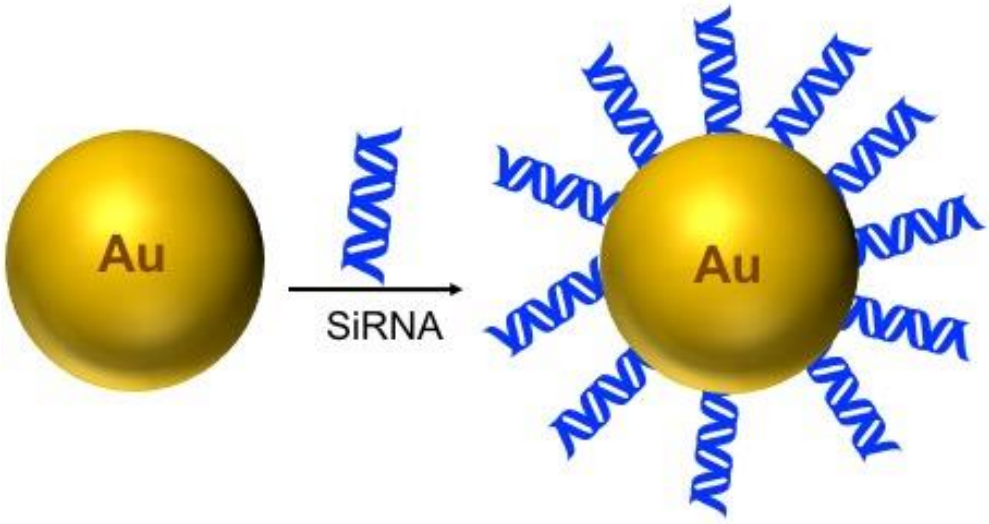

Scheme 5. 6. Schematic for the procedure of coating AuNPs with Thiolated SiRNA to produce SiRNA •AuNPs.

The coating of SiRNA was carried out on a solution of **AuNP13**, **AuNP25** and **AuNP100.** A solution of **SiRNA** (100 μM) was added in 10 μL, 3 μL and 10 μL aliquots for **AuNP13**, **AuNP25** and **AuNP100** respectively. The SiRNA was added to a final volume of 30 μL and a concentration of 1.5 μM for all three sizes. Addition of 30 μL **SiRNA** into **AuNP13**, **AuNP25** and **AuNP100** resulted in a 1 nm shift in λ_{max} (H_2O) for all three sizes. This resulted in a shift from 516 nm to 517 nm, 518 nm to 519 nm and 550 nm to 551 nm for **AuNP13**, **AuNP25** and **AuNP100** respectively (Figure 5.19). Appearance of a peak at 260 nm along with the shift in SPR confirms the presence of **SiRNA** on the gold nanoparticles.

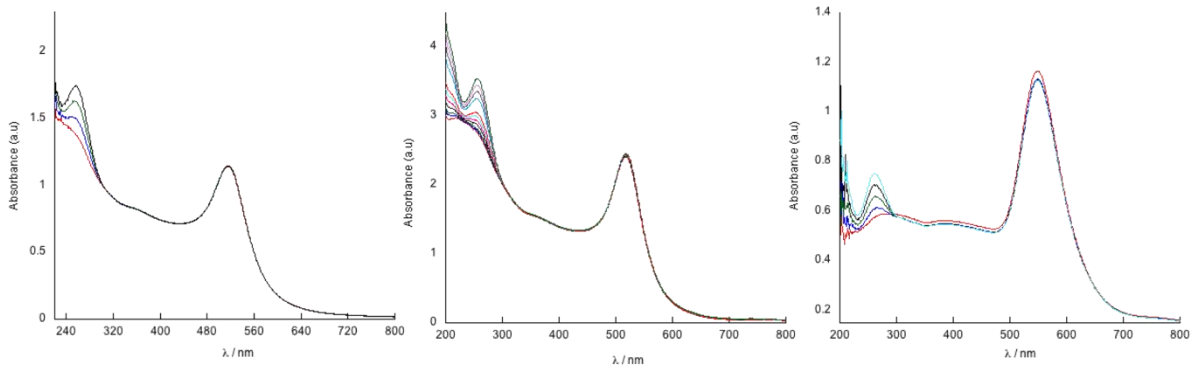

Figure 5.19. UV/Vis titration of SiRNA (100 μM) into (left) 4.5 nM AuNP13, (middle) 1.7 nM AuNP25 and (right) 30 pm AuNP100 in water. Region of interest of at 260 nm showing absorbance from SiRNA.

These **SiRNA** coated nanoparticles were purified three times using Millipore filters (10 kDa MWCO) to produce 4 nM SiRNA •**AuNP13**, 6 nM SiRNA •**AuNP25** and 25 pM SiRNA •**AuNP100**. Upon isolation of the **SiRNA** coated nanoparticles the SPR λ_{max} (H_2O) maximum remained unchanged showing that no aggregation occurred after purification (Appendix). After purification, the absorbance peak at 260 nm remained for all three sizes of nanoparticles, confirming the conjugation of **SiRNA** to the surface of gold nanoparticles (Figure 5.20, arrows).

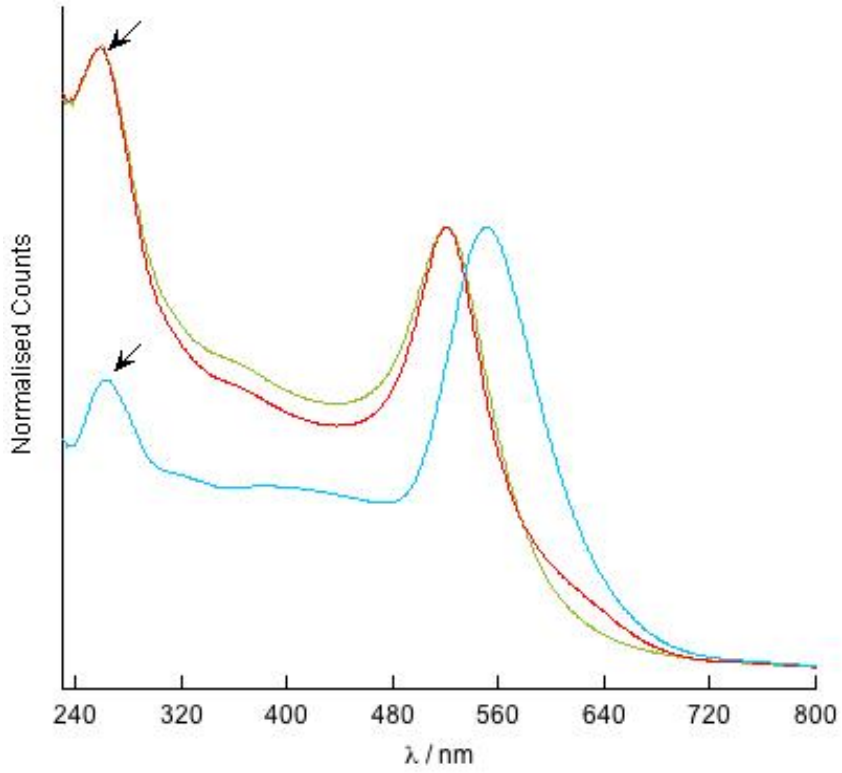

Figure 5.20. Normalised UV/Vis plots of 4 nM SiRNA •AuNP13 (green), 6 nM SiRNA •AuNP25 (red) and 27 pM SiRNA •AuNP100 (blue) after purification. SiRNA absorbance at 260 nm showed with arrows.

The SiRNA •**AuNPs** were sized by DLS to show that coating of the nanoparticles with **SiRNA** did not affect the stability of the nanoparticles. The results can be seen in Table 5.4 and Figure 5.21. The results showed a small increase in hydrodynamic size and PDI which is to be expected upon addition of **SiRNA** into the solution of gold nanoparticles as this confirms conjugation onto the gold surface.

Table 5.4. Dynamic Light Scattering (DLS) for SiRNA •AuNP13, SiRNA •AuNP25 and SiRNA •AuNP100 in water. Results displayed are Size by Number Distribution, Size by Intensity Distribution and Polydispersity Index (PDI).

	Number Distribution (nm)	Intensity Distribution (nm)	PDI
SiRNA •**AuNP13**	22 ± 7	41 ± 15	0.26
SiRNA •**AuNP25**	28 ± 8	60 ± 25	0.21
SiRNA •**AuNP100**	115 ± 28	143 ± 32	0.04

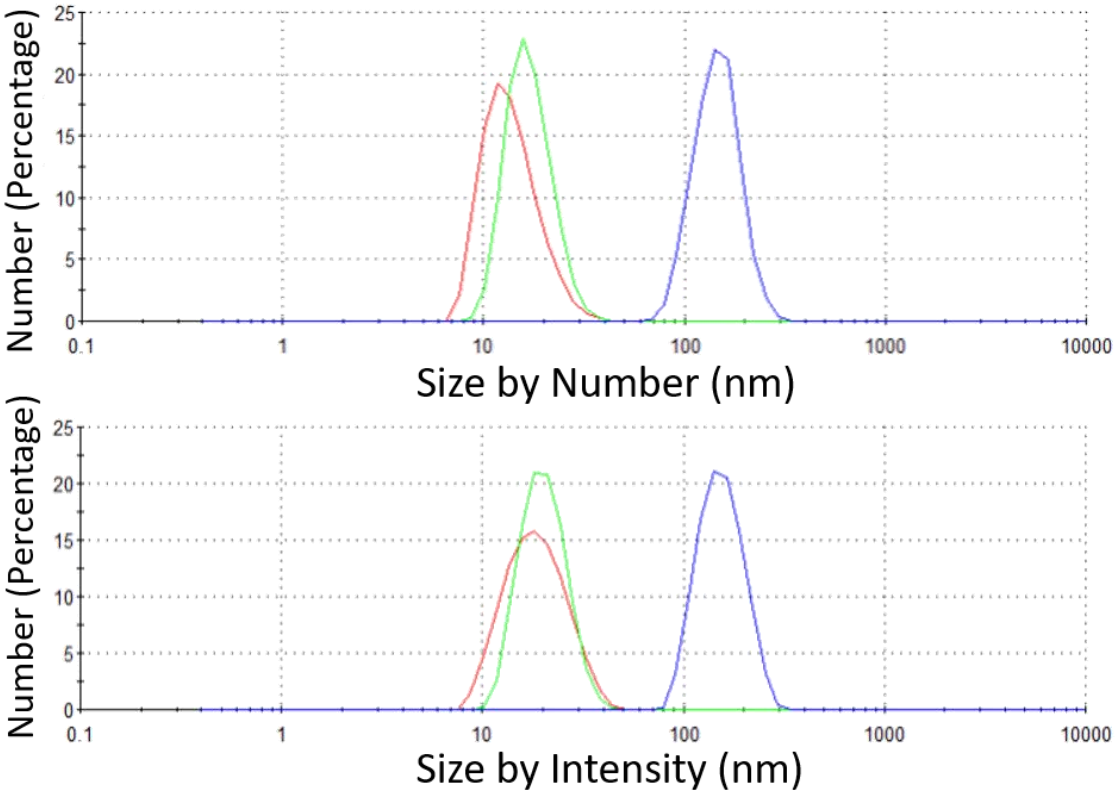

Figure 5.21. Dynamic Light Scattering (DLS) Data showing sizing by Number Distribution (top) and Intensity Distribution (bottom). Results displayed are for SiRNA • AuNP13 (red), SiRNA • AuNP25 (green) and SiRNA • AuNP100 (Blue).

ζ-potential were measured and found to be -68 ± 30 mV, -58 ± 22 mV and -58 ± 28 mV for SiRNA •**AuNP13**, SiRNA •**AuNP25** and SiRNA •**AuNP100** respectively (Figure 5.22). The results showed an increase in negative potential in comparison to the citrate stabilised nanoparticles, which indicates an increase in stability of the nanoparticles in solution. This large increase in negative potential was to be expected due to the high negative charge of the **SiRNA** which were conjugated to the gold nanoparticles. This same increase in negative potential was also seen for the Zonyl coated gold nanoparticles.

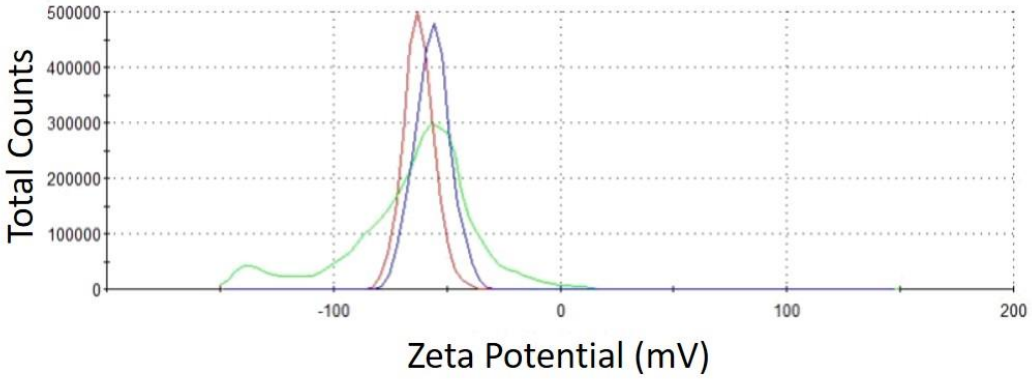

Figure 5.22. DLS data showing the absolute ζ-potential measurements for SiRNA • AuNP13 (red), SiRNA • AuNP25 (green) and SiRNA • AuNP100 (blue) in water.

5. 3. 2. 2 Attachment of IrC_6 onto SiRNA •AuNPs

A solution of **IrC_6** in MeOH (1 mM) was titrated into an aqueous solution of 4 nM SiRNA•**AuNP13**, 6 nM SiRNA •**AuNP25** and 25 pm SiRNA •**AuNP100** in 2 μL, 5 μL and 10 μL aliquots respectively (Scheme 5.7). The shift in SPR showed modifications onto the gold surface.

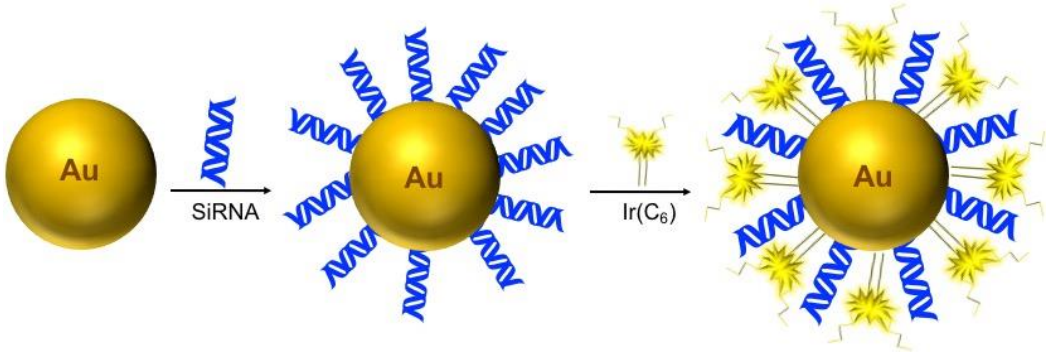

Scheme 5.7. Schematic for the procedure of coating SiRNA •AuNPs with IrC_6 to produce IrC_6 • SiRNA • AuNPs.

IrC_6 (1 mM) was added up to a final concentration of 20 μM, 24 μM and 18 μM for SiRNA •**AuNP13**, SiRNA •**AuNP25** and SiRNA •**AuNP100** respectively (Figure 5.23).

This addition of 1mM **IrC_6** into the colloidal solution of SiRNA •**AuNPs** resulted in an 8 nm (525 nm), 7 nm (526 nm) and 5 nm (556 nm) shift in λ_{max} (H_2O) for SiRNA • **AuNP13**, SiRNA •**AuNP25** and SiRNA •**AuNP100** respectively.

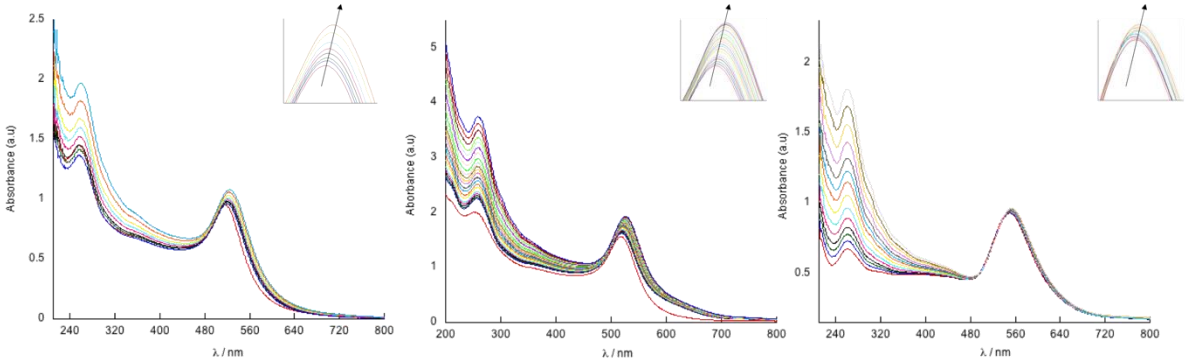

Figure 5.23. UV/Vis titration of IrC_6 (1 mM) into (left) 4 nM AuNP13, (middle) 1.4 nM AuNP25 and (right) 27 pm AuNP100 in water. The SPR region is shown in the inset to highlight the shift in SPR.

These functionalised nanoparticles were purified by centrifuging three times using a Millipore filter (10 kDa MWCO) for 3 minutes at 2000 g to produce 3 nM IrC_6 •SiRNA •**AuNP13**, 4.5 nM IrC_6 •SiRNA •**AuNP25** and 15 pM IrC_6 •SiRNA •**AuNP100** respectively. The SPR was checked after purification and it was found that the SPR λ_{max} (H_2O) remained unchanged, showing non-aggregation of these particles after centrifugation (Appendix). DLS was carried out to measure the hydrodynamic size of the functionalised nanoparticles in solution and to show the stability in solution, the results are shown in Table 5.5 and Figure 5.24. There is an increase in both size by number and intensity for the IrC_6 • SiRNA •**AuNPs** in comparison to the SiRNA •**AuNPs**. This is comparable to the increase in size that was seen when **IrC_6** was added to Zonyl coated nanoparticles. There has been no significant increase in PDI

for the IrC_6 • SiRNA •**AuNPs** showing high stability of the functionalised gold nanoparticles in solution.

Table 5.5. DLS results for IrC_6 •AbH •AuNP13, IrC_6 •AbH •AuNP25 and IrC_6 •AbH •AuNP100 in water. Results displayed are Size by Number Distribution, Size by Intensity Distribution and Polydispersity Index (PDI).

	Number Distribution (nm)	Intensity Distribution (nm)	PDI
IrC_6 • SiRNA •**AuNP13**	32 ± 10	50 ± 23	0.25
IrC_6 • SiRNA •**AuNP25**	36 ± 13	58 ± 29	0.23
IrC_6• SiRNA•**AuNP100**	127 ± 32	163 ± 45	0.05

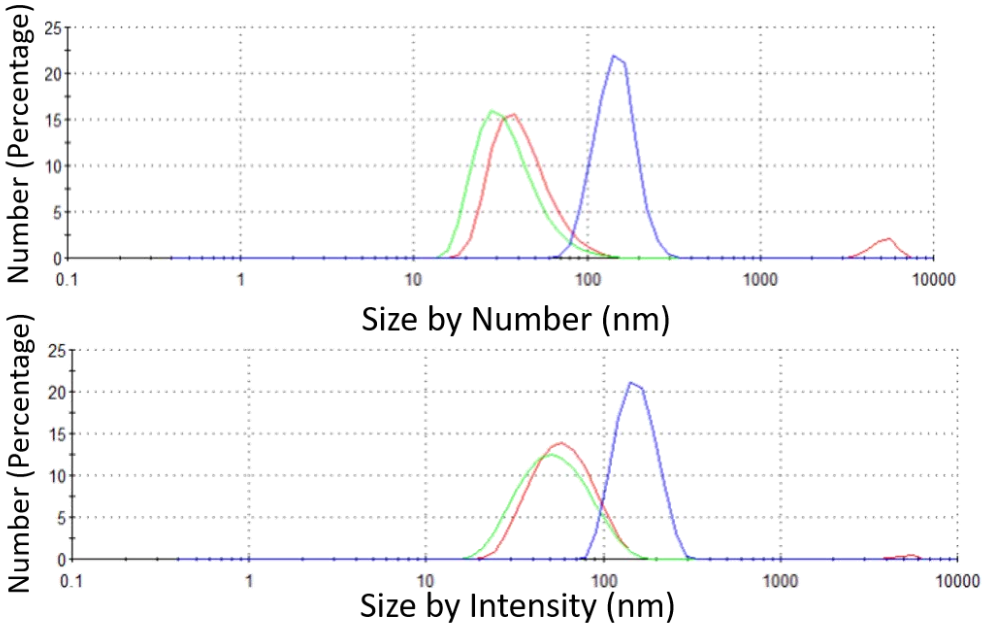

Figure 5.24. Dynamic Light Scattering (DLS) Data showing sizing by Number Distribution (top) and Intensity Distribution (bottom). Results displayed are for IrC_6 •SiRNA •AuNP13 (green), IrC_6 •SiRNA •AuNP25 (red) and IrC_6 •SiRNA •AuNP100 (Blue).

ζ-potentials for IrC_6 • SiRNA •**AuNPs** were measured and found to be -34 ± 25 mV, -35 ± 12 mV and -38 ± 17 mV for IrC_6 • SiRNA •**AuNP13,** IrC_6 • SiRNA •**AuNP25 and** IrC_6 • SiRNA •**AuNP100** respectively (Figure 5.25). The results indicate highly stable nanoparticles in solution with an overall negative charge similar for all three sizes. The results showed a decrease in negative ζ-potential in comparison to the SiRNA •**AuNPs**

in solution, which were found to be -68 ± 30 mV, -58 ± 22 mV and -58 ± 28 mV for SiRNA •**AuNP13**, SiRNA •**AuNP25** and SiRNA •**AuNP100** respectively. This decrease in negative potential was to be expected due to the positive charge of the **IrC$_6$** on the gold nanoparticles, which had an overall positive charge of +1.

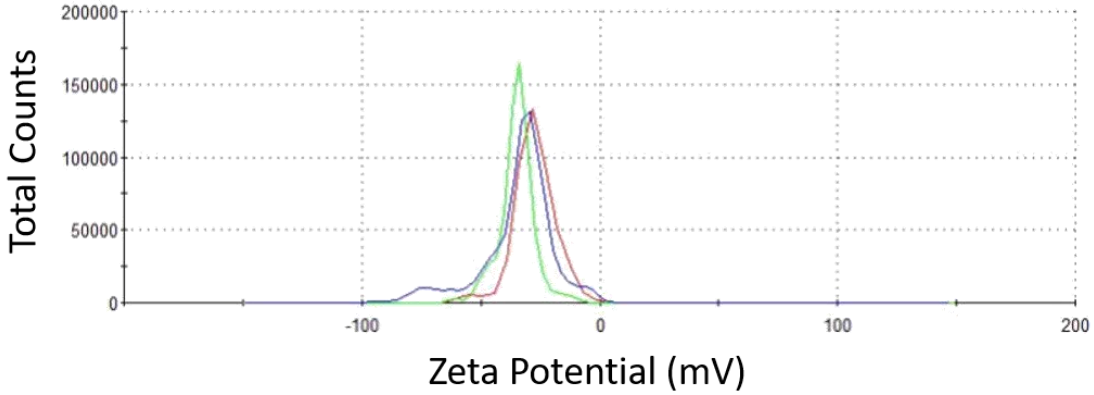

Figure 5.25. DLS data showing the absolute ζ-potential measurements for IrC$_6$ • SiRNA •AuNP13 (red), IrC$_6$ • SiRNA •AuNP25 (green) and IrC$_6$ • SiRNA •AuNP100 (blue) in water.

Elemental composition of IrC$_6$ •SiRNA •**AuNP13** was carried out by inductively coupled plasma mass spectrometry (ICP-MS) to calculate the number of **IrC$_6$** complexes per SiRNA •**AuNPs** (Table 5.6).

Table 5.6. Elemental composition of nanoparticles by ICP-MS, showing number of IrC$_6$ complexes per SiRNA •AuNPs.

Sample ID	**IrC$_6$** per SiRNA •**AuNPs**
IrC$_6$ •SiRNA•**AuNP13**	2400
IrC$_6$ •SiRNA•**AuNP25**	4100
IrC$_6$ •SiRNA•**AuNP100**	27000

The results showed a high coating of **IrC$_6$** onto SiRNA •**AuNPs**, with thousands of **IrC$_6$** complexes per SiRNA •**AuNPs**. This showed an increase in **IrC$_6$** complexes per SiRNA

coated gold nanoparticle in comparison to Zonyl coated gold nanoparticles, which were found to have 1400, 3200 and 22,000 **IrC$_6$** complexes per Z •**AuNP13**, Z •**AuNP25** and Z •**AuNP100** respectively. The higher loading of **IrC$_6$** onto SiRNA coated nanoparticles is due to the increased stability when coating the gold nanoparticle with the negative SiRNA complex. This was also supported by the ζ-potential measurements. The higher negative charge of the aqueous solution of SiRNA •**AuNPs** meant that more positive iridium could be added before the nanoparticles destabilised.

5. 3. 3 Synthesis of IrC$_6$ •AbH/SiRNA •AuNPs

5. 3. 3. 1 Conjugation of AbH onto SiRNA •AuNPs

In this section, monodisperse **AuNPs** (13, 25 and 100 nm) were coated with **AbH** and **SiRNA** before the addition of **IrC$_6$**. Addition of **AbH** onto **SiRNA** coated nanoparticles allows for targeted delivery of **SiRNA** into cancer cells. In theory, these nanoparticles should deliver the SiRNA in a more efficient manner than gold nanoparticle particles coated with just SiRNA. These particles are prone to entrapment into endosomes and lysosomes which would stop SiRNA from being delivered and potentially cause degradation of the SiRNA from the acidic nature of the lysosomes.

Monodisperse **AuNPs** (13 nm, 25 nm and 100 nm) were pre-coated with SiRNA as described in the section 5. 3. 2.1 of this chapter. The **SiRNA** coated gold nanoparticles were purified and isolated to provide 4 nM SiRNA •**AuNP13**, 6 nM SiRNA •**AuNP25** and 25 pm SiRNA •**AuNP100.** A solution of **AbH** (1 mg/ mL^{-1}) was titrated into the SiRNA •**AuNPs**. The attachment of **AbH** on SiRNA •**AuNPs** can be seen in Scheme 5.8.

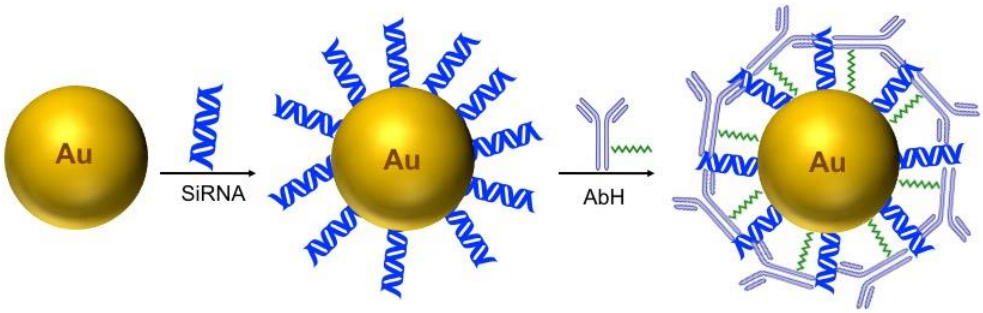

Scheme 5.8. Schematic for the procedure of coating SiRNA •AuNPs with AbH to produce AbH•SiRNA •AuNPs.

A solution of **AbH** (1 mg/ mL^{-1}) was added in 5 μL, 5 μL and 10 μL aliquots for SiRNA **•AuNP13**, SiRNA **•AuNP25** and SiRNA **•AuNP100** respectively. The **AbH** was added to a final volume of 30 μL and a concentration of 30 μg/ mL^{-1} for all three sizes. Addition of 30 μL **AbH** into SiRNA **•AuNP13**, SiRNA **•AuNP25** and SiRNA **•AuNP100** resulted in a 1 nm shift in λ_{max} (H_2O) for all three sizes. This resulted in a shift from 518 to 519 nm, 518 to 519 nm and 557 to 558 nm for SiRNA **•AuNP13**, SiRNA **•AuNP25** and SiRNA **•AuNP100** respectively (Figure 5.26).

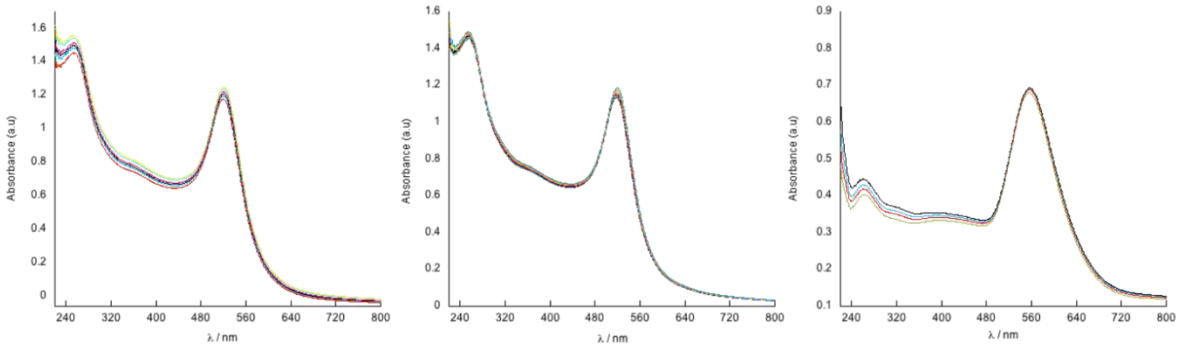

Figure 5.26. UV/Vis titration of AbH (1 mg/ mL^{-1}) into (left) 6 nM SiRNA •AuNP13 (middle) 1.4 nM SiRNA •AuNP25 and (right) 25 pm SiRNA •AuNP100 in water.

These nanoparticles were purified three times using Millipore filters (300 kDa MWCO) to produce 3.5 nM AbH/SiRNA **•AuNP13**, 3.5 nM AbH/SiRNA **•AuNP25** and 17 pM

AbH/SiRNA •**AuNP100**. After purification, the SPR λ_{max} (H_2O) maximum of these functionalised gold nanoparticles remained unchanged showing that no aggregation had occurred during the purification step (Appendix). The particles were sized by DLS to show that coating of the nanoparticles with **AbH/SiRNA** did not affect the overall stability of these nanoparticles in solution (Table 5.7 and Figure 5.27).

Table 5.7. Dynamic Light Scattering (DLS) for AbH •SiRNA•AuNP13, AbH •SiRNA•AuNP25 and AbH •SiRNA•AuNP100 in water. Results displayed are Size by Number Distribution, Size by Intensity Distribution and Polydispersity Index (PDI).

	Number Distribution (nm)	Intensity Distribution (nm)	PDI
AbH/SiRNA •**AuNP13**	32 ± 17	49 ± 20	0.32
AbH/SiRNA •**AuNP25**	35 ± 16	55 ± 24	0.35
AbH/SiRNA •**AuNP100**	129 ± 33	136 ± 33	0.04

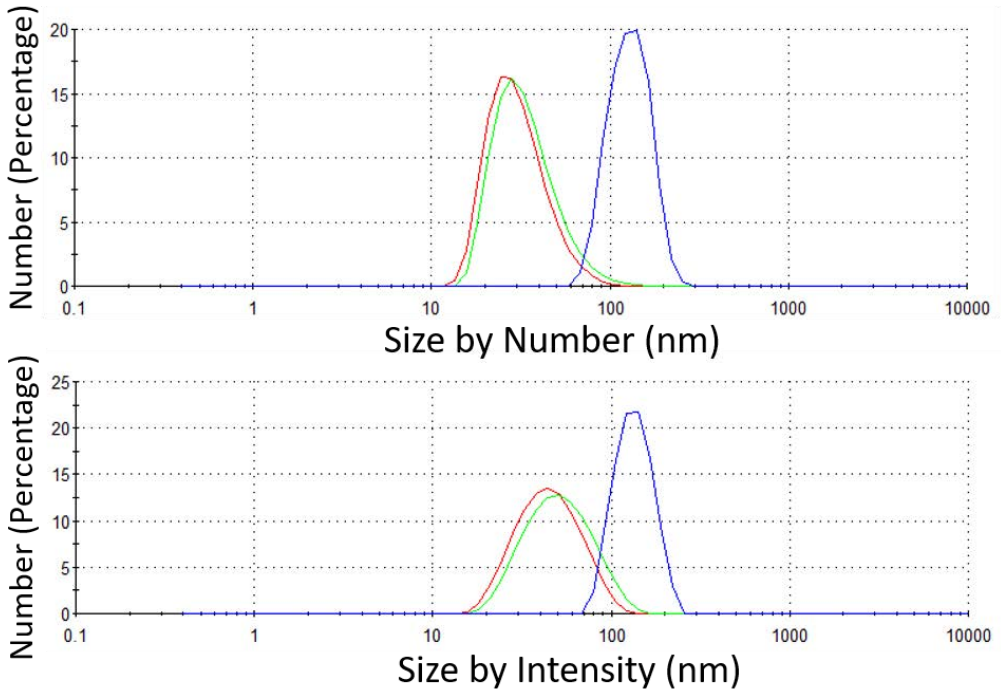

Figure 5.27. Dynamic Light Scattering (DLS) Data showing sizing by Number Distribution (top) and Intensity Distribution (bottom). Results displayed are for AbH •SiRNA•AuNP13 (red), AbH •SiRNA•AuNP25 (green) and AbH •SiRNA•AuNP100 (blue) in water.

The results showed a large increase in size when compared to the SiRNA coated nanoparticles. This is to be expected due to the large size of the monoclonal antibodies. These results showed the largest PDI of 0.32 and 0.35 in comparison to AbH •**AuNPs** and SiRNA •**AuNPs**, which had PDI of <0.3 after coating. This increase in PDI shows that having both SiRNA and the monoclonal antibodies conjugated to the surface of the gold nanoparticles, could lead to faster destabilisation in solution in comparison to the other functionalised nanoparticles.

ζ-potentials were measured and found to be -36 ± 19 mV, -39 ± 20 mV and -43 ± 19 mV for AbH/SiRNA •**AuNP13**, AbH/SiRNA •**AuNP25** and AbH/SiRNA •**AuNP100** respectively (Figure 5.28). The overall negative potential of the AbH/SiRNA •**AuNPs** didn't increase as much as that seen for the SiRNA coated nanoparticles, which displayed ζ-potentials of -68 ± 30 mV, -58 ± 22 mV and -58 ± 28 mV for SiRNA •**AuNP13**, SiRNA •**AuNP25** and SiRNA •**AuNP100** respectively. This could mean that addition of the antibody to the negatively charged solution of SiRNA •**AuNPs** causes displacement of **SiRNA** molecules on the surface of the gold nanoparticles.

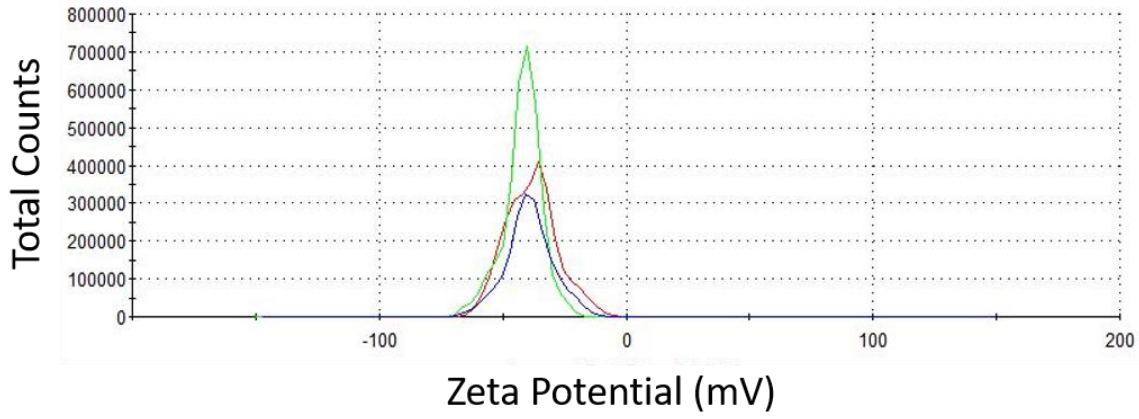

Figure 5.28. DLS data showing the absolute ζ-potentials measurements for IrC_6 • AbH •AuNP13 (red), IrC_6 • AbH •AuNP25 (green) and IrC_6 • AbH •AuNP100 (blue) in water.

5. 3. 3. 2 Attachment of IrC_6 onto AbH/SiRNA •AuNPs

A solution of **IrC_6** in MeOH (1 mM) was titrated into an aqueous solution of 3.5 nM AbH/SiRNA •**AuNP13**, 3.5 nM AbH/SiRNA •**AuNP25** and 17 pM AbH/SiRNA •**AuNP100** (Scheme 5.9). The **IrC_6** was titrated in aliquots of 2 μL, 2 μL and 2.5 μL for AbH/SiRNA •**AuNP13**, AbH/SiRNA •**AuNP25** and AbH/SiRNA •**AuNP100** respectively. The shift in SPR shows modifications onto the gold surface.

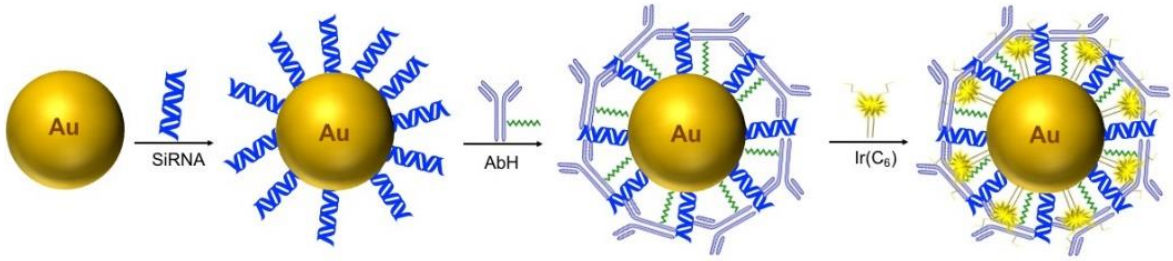

Scheme 5.9. Schematic for the procedure of coating SiRNA •AuNPs with IrC_6 to produce IrC_6 • AbH/SiRNA •AuNPs.

IrC_6 (1 mM) was added up to a final concentration of 9 μM, 21 μM and 12.5 μM for AbH/SiRNA •**AuNP13**, AbH/SiRNA •**AuNP25** and AbH/SiRNA •**AuNP100** respectively (Figure 5.29). This addition of 1mM **IrC_6** into the colloidal solution of AbH/SiRNA •**AuNPs** resulted in a 4 nm (525 nm), 6 nm (525 nm) and 2 nm (560 nm) shift in λ_{max} (H_2O) for AbH/SiRNA •**AuNP13**, AbH/SiRNA •**AuNP25** and AbH/SiRNA •**AuNP100** respectively.

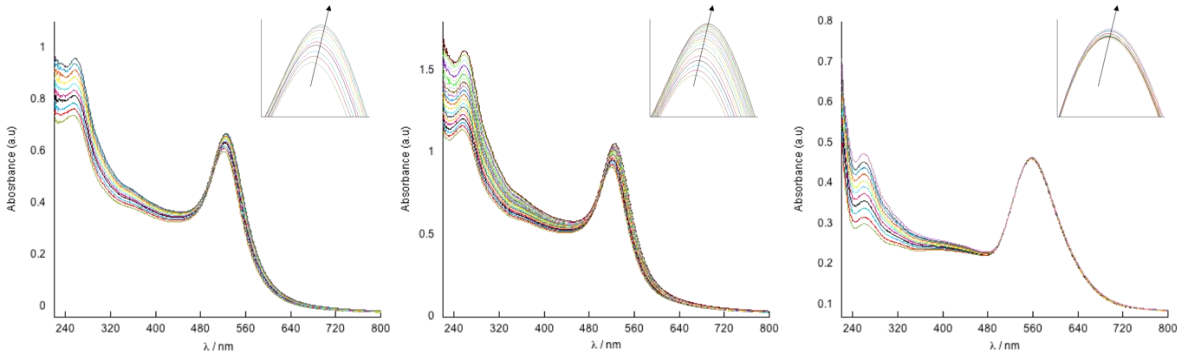

Figure 5.29. UV/Vis titration of IrC_6 (1 mM) into (left) 3.5 nM AbH/SiRNA •AuNP13, (middle) 3.5 nM AbH/SiRNA •AuNP25 and (right) 17 pM AbH/SiRNA•AuNP100 in water. The SPR region is shown in the inset to highlight the shift in SPR.

These functionalised nanoparticles were purified by centrifuging three times using a Millipore filter (300 kDa MWCO) for 3 minutes at 2000 g to produce 3 nM IrC_6 •AbH/SiRNA •**AuNP13**, 2 nM IrC_6 •AbH/SiRNA •**AuNP25** and 12 pM IrC_6 •AbH/SiRNA •**AuNP100** respectively. The SPR was checked after purification and it was found that the SPR λ_{max} (H_2O) remained unchanged, positively identifying that these gold nanoparticles did not aggregate after centrifugation (Appendix). DLS was carried out to measure the size of these functionalised nanoparticles and to identify the stability of in solution, the results are shown in Table 5.8 and Figure 5.30. The results showed an increase in size by both number and intensity in comparison to AbH/SiRNA•**AuNPs** in solution. The increase is significantly larger in comparison to the other two iridium functionalised nanoparticles (SiRNA and AbH). This is to be expected due to both **AbH** and **SiRNA** being conjugated onto gold nanoparticle surface.

Table 5.8. DLS results for IrC_6 • AbH/SiRNA • AuNP13, IrC_6 • AbH/SiRNA • AuNP25 and IrC_6 • AbH/SiRNA • AuNP100 in water. Results displayed are Size by Number Distribution, Size by Intensity Distribution and Polydispersity Index (PDI).

	Number Distribution (nm)	Intensity Distribution (nm)	PDI
IrC_6 •AbH/SiRNA •**AuNP13**	32 ± 13	48 ± 20	0.36
IrC_6 •AbH/SiRNA •**AuNP25**	40 ± 15	54 ± 33	0.36
IrC_6 •AbH/SiRNA •**AuNP100**	147 ± 48	162 ± 52	0.06

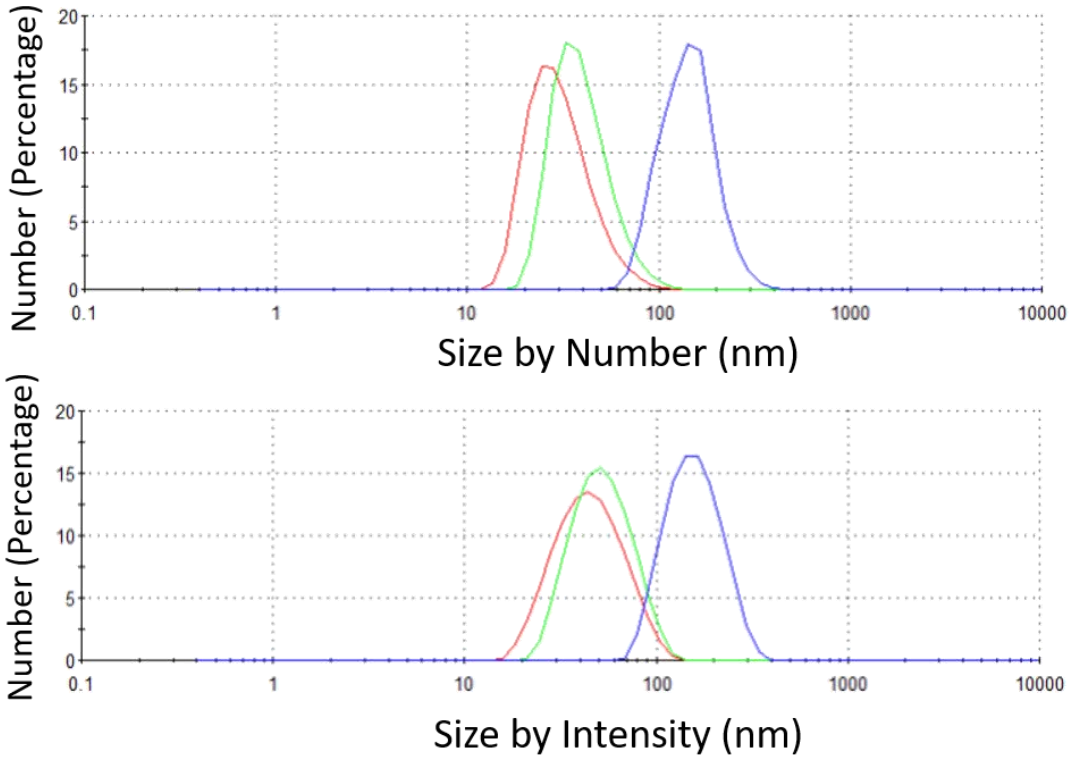

Figure 5.30. Dynamic Light Scattering (DLS) Data showing sizing by Number Distribution (top) and Intensity Distribution (bottom). Results displayed are for IrC_6 •AbH/SiRNA •AuNP13 (red), IrC_6 •AbH/SiRNA •AuNP25 (green) and IrC_6 •AbH/SiRNA •AuNP100 (blue) in water.

There is no significant increase in PDI in comparison to the AbH/SiRNA •**AuNPs**. It should be noted that only a single peak is seen in the distribution graph for size by intensity for these functionalised nanoparticles. A second peak within the intensity distribution graph has previously been seen for Zonyl coated gold nanoparticles when

there has been excess of Zonyl present in the solution (Appendix). Since a second peak has not been detected for these nanoparticles it can be assumed that there is no free antibody or SiRNA present in solution.

ζ-potentials of the IrC_6 •AbH/SiRNA •**AuNPs** were measured and found to be -31 ± 11 mV, -33 ± 16 mV and -39 ± 15 mV for IrC_6 •AbH/SiRNA •**AuNP13**, IrC_6 •AbH/SiRNA •**AuNP25** and IrC_6 •AbH/SiRNA •**AuNP100** respectively (Figure 5.31).

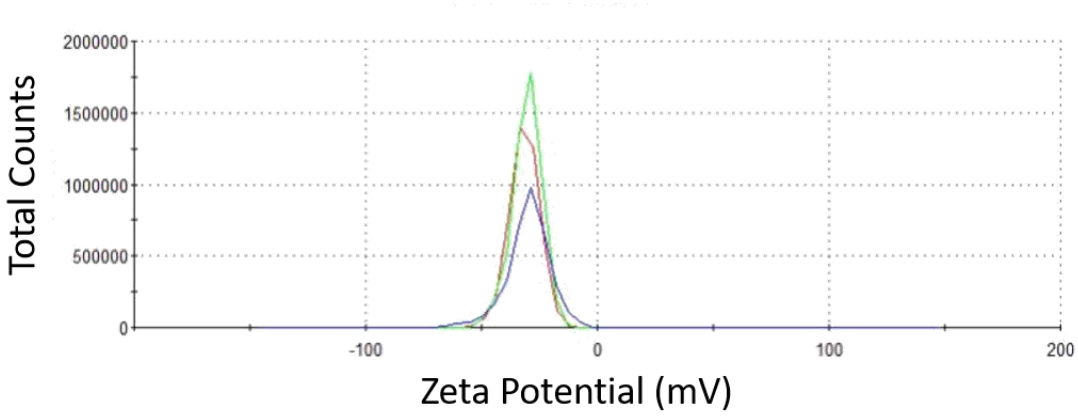

Figure 5.31. DLS data showing the absolute ζ-potentials measurements for IrC_6 •AbH/SiRNA •AuNP13 (red), IrC_6 •AbH/SiRNA •AuNP25 (green) and IrC_6 •AbH/SiRNA •AuNP100 (blue) in water.

These results show highly stable nanoparticles in solution with an overall similar negative charge for all three sizes. The results show a decrease in negative potential in comparison to AbH/SiRNA •**AuNPs,** which had zeta-potentials of -36 ± 19 mV, -39 ± 20 mV and -43 ± 19 mV for AbH/SiRNA •**AuNP13**, AbH/SiRNA •**AuNP25** and AbH/SiRNA •**AuNP100** respectively. This is due to the conjugation of the positive iridium complex onto the gold nanoparticles in the solution which caused an overall decrease in negative potential.

Elemental composition of the nanoparticles by inductively coupled plasma mass spectroscopy (ICP-MS) was carried out to calculate number of **IrC_6** complexes per

AbH/SiRNA •**AuNPs**. The results show a high coating of iridium complexes onto AbH •SiRNA•**AuNPs**, with thousands of iridium complexes per AbH •SiRNA•**AuNPs** (Table 5.9). The amount of **IrC_6** attached to the **AbH/SiRNA** coated gold nanoparticles is similar to that previously seen for IrC_6 •SiRNA •**AuNPs**.

Table 5.9. Elemental composition of nanoparticles by ICP-MS, showing number of IrC_6 complexes per AbH/SiRNA •AuNP13.

Sample	**IrC_6** per AuNPs
IrC_6 •AbH/SiRNA •**AuNP13**	1000
IrC_6 •AbH/SiRNA •**AuNP25**	3500
IrC_6 •AbH/SiRNA •**AuNP100**	25000

This shows that the SiRNA coating provides extra stability for the nanoparticles by increasing the overall negative charge of the aqueous solution. This allows for a higher concentration of positive **IrC_6** to be added to the solution **AbH/SiRNA** coated gold nanoparticles before aggregation occurs.

5. 3. 4 Photophysical characterisations of functionalised nanoprobes

The photophysical properties of gold nanoparticles functionalised with **SiRNA**, **AbH** and **AbH/SiRNA** were investigated. The luminescence properties were characterised by steady state and time resolved spectroscopy. The luminescence spectra of IrC_6 •SiRNA •**AuNPs**, IrC_6 •AbH •**AuNPs** and IrC_6 •AbH/SiRNA •**AuNPs** in water were recorded and the results displayed in Figure 5.32. The results will be compared to Zonyl coated gold nanoparticles (IrC_6 •**AuNPs**) and **IrC_6** in water.

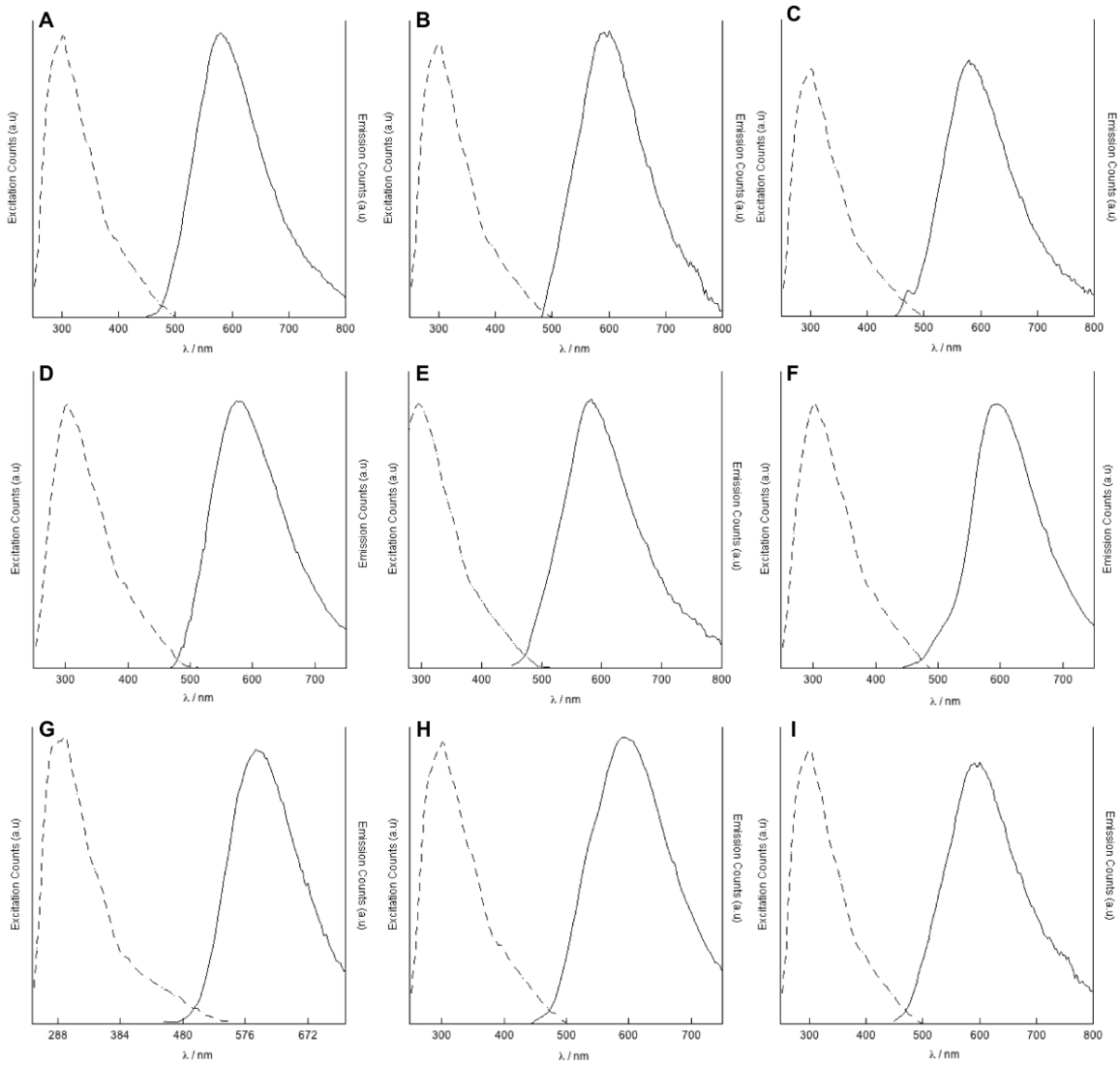

Figure 5.32. Steady-state emission spectrum λ_{exc} = 375 nm (solid line) and excitation spectra (dotted line). (A) 3 nM IrC_6 •SiRNA •AuNP13 (λ_{em} = 595 nm), (B) 3 nM IrC_6 •AbH •AuNP13 (λ_{em} = 580 nm), (C) 3 nM IrC_6 •AbH/SiRNA •AuNP13 (λ_{em} = 580 nm), (D) 3 nM IrC_6 •SiRNA •AuNP25 (λ_{em} = 595 nm), (E) 2 nM IrC_6 •AbH •AuNP25 (λ_{em} = 580 nm), (F) 2 nM IrC_6 •AbH/SiRNA •AuNP25 (λ_{em} = 580 nm), (G) 15 pM IrC_6 •SiRNA •AuNP100 (λ_{em} = 600 nm), (H) 15 pM IrC_6 •AbH •AuNP100 (λ_{em} = 595 nm) and 12 pM IrC_6 •AbH/SiRNA•AuNP100 (λ_{em} = 595 nm). Spectra corrected for PMT and instrument response.

All sets of nanoparticles for all three sizes showed to be highly emissive upon excitation at 375 nm, but differences were seen in the emission λ_{max} between the different surface coatings (Table 5.10). The excitation spectra displayed the characteristic bands of the

iridium complex which are responsible for the observed emission. The excitation spectra are similar for all sets of functionalised nanoparticles and for all three sizes.

Table 5.10. Emission λ_{max} (nm) taken upon excitation at 375 nm for 13 nm, 25 nm and 100 nm AuNPs coated with SiRNA, AbH and SiRNA/AbH.

	AuNP13 (λ_{max} nm)	AuNP25 (λ_{max} nm)	AuNP100 (λ_{max} nm)
IrC_6 •AbH	580	580	595
IrC_6 •SiRNA	595	595	600
IrC_6 •AbH/SiRNA	580	580	595

A surface coating with **AbH** showed an emission λ_{max} of 580 nm for IrC_6 •AbH •**AuNP13** and IrC_6 •AbH •**AuNP25**, and an emission λ_{max} of 595 nm for IrC_6 •AbH •**AuNP100**. The emission λ_{max} for IrC_6 •AbH •**AuNP13** and IrC_6 •AbH •**AuNP25** was found to be the same as the free metal complex in solution. The monoclonal antibody is around 12 nm in size, therefore the fact that no shift in emission λ_{max} was seen could be indicative of the interaction of the antibody with the surface of these smaller sized nanoparticles. This could show that the antibody wraps around the nanoparticles which in turn causes less interaction with the **IrC_6** complexes. This is different for IrC_6 •AbH •**AuNP100** which showed a 15 nm red shift in emission λ_{max} in comparison to the **IrC_6** in solution. It is unlikely that the antibody (12 nm) would be able to wrap around these larger 100 nm nanoparticles, and therefore a shift in emission is seen indicating a greater interaction between the antibody and the **IrC_6** complexes. A surface coating with **SiRNA** showed an emission λ_{max} of 595 nm for IrC_6 •SiRNA •**AuNP13** and IrC_6 •SiRNA •**AuNP25**, and an emission λ_{max} of 600 nm for IrC_6 •SiRNA •**AuNP100**. The emission has red shifted by 15 nm for IrC_6 •SiRNA •**AuNP13** and IrC_6 •SiRNA •**AuNP25** and by 20 nm for IrC_6 •SiRNA •**AuNP100** in comparison to **IrC_6** in water, which has an emission λ_{max} of 580 nm. This same affect was seen when gold

nanoparticles were coated with Zonyl FSA, where a 10 nm shift was seen in the emission λ_{max} in comparison to **IrC$_6$** in solution. When gold nanoparticles were coated with both **AbH** and **SiRNA** there was an emission λ_{max} of 580 nm for IrC$_6$ •AbH/SiRNA **•AuNP13** and IrC$_6$ •AbH/SiRNA **•AuNP25**, again this shows no shift in emission in comparison to **IrC$_6$** in solution. This same affect was seen for the 13 nm and 25 nm particles which were coated with **AbH**. The emission λ_{max} for IrC$_6$ •AbH/SiRNA **•AuNP100** was found to be 595 nm, which showed a 15 nm red shift in emission in comparison to **IrC$_6$** in solution. This same trend was seen for the 100 nm particles coated with **AbH**. The luminescence lifetimes of these functionalised nanoparticles are summarised in the table below (Table 5.11).

Table 5.11. Luminescence lifetimes of iridium(III) functionalised gold nanoparticles coated with SiRNA, AbH or SiRNA/AbH. Iridium functionalised gold nanoparticles coated with Zonyl FSA have been shown for comparison. Luminescence lifetimes were fitted with a χ^2 between 1 and 1.1.

	AuNP13 (τ ns)	**AuNP25** (τ ns)	**AuNP100** (τ ns)
IrC$_6$ •AbH	60 (5 %) 210 (32 %) 720 (63 %)	50 (4 %) 190 (30 %) 700 (65 %)	20 (3 %) 130 (30%) 710 (67 %)
IrC$_6$ •SiRNA	30 (1 %) 110 (42 %) 500 (57 %)	10 (1 %) 170 (33 %) 570 (67 %)	50 (2 %) 240 (34 %) 540 (64 %)
IrC$_6$ •AbH/SiRNA	40 (3 %) 160 (24 %) 640 (72 %)	40 (1 %) 130 (32 %) 620 (67%)	30 (1 %) 180 (21 %) 600 (79 %)
IrC$_6$ •Zonyl	50 (5 %) 180 (48 %) 340 (47 %)	40 (5 %) 160 (42 %) 330 (53 %)	25 (3 %) 140 (43 %) 340 (54 %)

All the lifetimes detected were found to have three lifetime components. The luminescence lifetimes recorded for IrC$_6$ •AbH **•AuNPs** are similar for all three sizes of nanoparticles. A short lifetime component of 20 – 60 ns was observed at a small percentage of 3 – 5 %. The long component was found to be 720 ns, 700 ns and 710

ns for IrC_6 •AbH •**AuNP13,** IrC_6 •AbH •**AuNP25** and IrC_6 •AbH •**AuNP100** respectively. This showed an increase in luminescence lifetimes of 112 %, 112 % and 109 % for IrC_6 •AbH •**AuNP13,** IrC_6 •AbH •**AuNP25** and IrC_6 •AbH •**AuNP100** respectively when compared to the Zonyl coated nanoparticles. In comparison to **IrC_6** in solution ($\tau 3$ = 430 ns) an increase of 67 %, 63 % and 65 % for IrC_6 •AbH •**AuNP13,** IrC_6 •AbH •**AuNP25** and IrC_6 •AbH •**AuNP100**. The coating with **AbH** resulted in the largest increase in luminescence lifetimes when compared to coatings with **SiRNA** and **SiRNA/AbH**. This increase in luminescence lifetimes would indicate interactions between the **IrC_6** with AbH conjugated to the gold nanoparticles, however this doesn't correlate with emission studies which showed no shift in λ_{max}.

The luminescence lifetimes for IrC_6 •SiRNA •**AuNPs** are similar for all three sizes of nanoparticles. A short lifetime component of 10 - 50 ns was observed at a small percentage of 1 – 2 %, which was also present for the lifetime recorded for the Zonyl FSA coated nanoparticles. The long component was found to be 500 ns, 570 ns and 540 ns for IrC_6 •SiRNA •**AuNP13,** IrC_6 •SiRNA •**AuNP25** and IrC_6 •SiRNA• **AuNP100** respectively. This showed an increase in luminescence lifetimes of 47 %, 73 % and 59 % for IrC_6 •SiRNA •**AuNP13,** IrC_6 •SiRNA •**AuNP25** and IrC_6 •SiRNA •**AuNP100** respectively when compared to the Zonyl coated particles. In comparison to **IrC_6** in solution, the luminescence lifetimes increased by 16 %, 33 % and 26 % for IrC_6 •SiRNA •**AuNP13,** IrC_6 •SiRNA •**AuNP25** and IrC_6 •SiRNA •**AuNP100** respectively. This increase in luminescent lifetime shows interactions of the **IrC_6** complex with the SiRNA •**AuNPs.**

The luminescence lifetimes for IrC_6 •AbH/SiRNA •**AuNPs** are similar for all three sizes of nanoparticles. A short lifetime component of 30 – 40 ns was observed at a small percentage of 1 – 3 %. The long component was found to be 640 ns, 620 ns and 600 ns for IrC_6 •AbH/SiRNA •**AuNP13,** IrC_6 •AbH/SiRNA •**AuNP25** and IrC_6 •AbH/SiRNA •**AuNP100** respectively. This showed an increase in luminescence lifetimes of 88 %, 88 % and 76 % for IrC_6 •AbH/SiRNA •**AuNP13,** IrC_6 •AbH/SiRNA •**AuNP25** and IrC_6 •AbH/SiRNA •**AuNP100** respectively when compared to the Zonyl coated particles. In comparison to **IrC_6** in solution, the luminescence lifetimes showed an increase of 49 %, 44 % and 40 % for IrC_6 •AbH/SiRNA •**AuNP13,** IrC_6 •AbH/SiRNA •**AuNP25** and IrC_6 •AbH/SiRNA •**AuNP100** respectively. This increase in luminescent lifetime shows that the iridium complex is interacting with the surfactant, which increases the luminescence lifetime in solution.

5. 3. 5 Mapping localisation and uptake into cancer cells using multiphoton lifetime imaging

Multiphoton fluorescence and phosphorescence lifetime imaging was carried out, in which the short-lived picosecond lifetimes from the gold was detected in one channel and the long-lived iridium signal was detected in the second channel. The lifetimes obtained from the two channels were analysed and the differences between the surface coatings were compared. The long-lived lifetimes detected in the PLIM channel were fitted to three components for all samples and the lifetimes displayed in the resulting PLIM image were taken from the τ_3 lifetime component.

5. 3. 5. 1 Multichannel detection of IrC_6 •AbH •AuNPs in cancer cells

Analysis of the short-lived and long-lived signals of IrC_6 •AbH •**AuNPs** in Hela cells can be seen below for the three different sizes (Figure 5.33, 5.34 and 5.35). The PLIM images revealed strong phosphorescence signal within HeLa cells for all three sizes of **AbH** coated nanoparticles. The uptake of the **AbH** coated nanoparticles show a similar pattern of uptake for all three sizes of nanoparticles, with uptake being mainly within the cytoplasm of the cell. Future work would be carried out to confirm whether these nanoparticles localised within endosomes or lysosomes within the cytoplasm. The luminescence lifetimes detected for IrC_6 •AbH •**AuNP13** in Hela Cells ranged from 620 – 2500 ns. The PLIM images show only green (600 – 690 ns) and red (700 – 1000 ns) lifetimes detected within the cells (Figure 5.33).

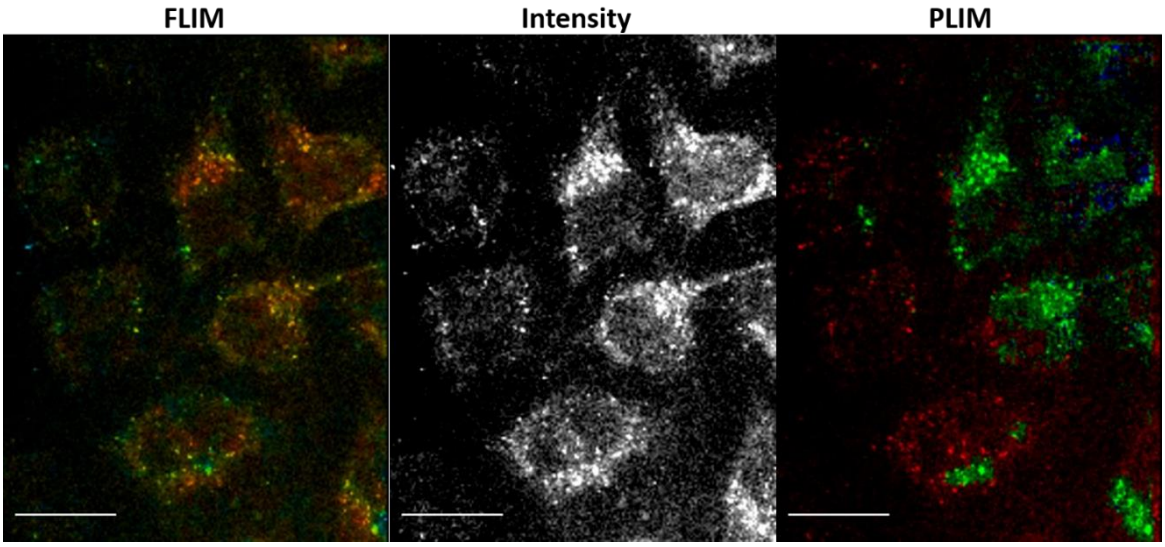

Figure 5.33. Two-photon lifetime images showing detection of the short-lived fluorescence (FLIM) and long-lived phosphorescence (PLIM) lifetimes for multichannel detection. HeLa cells incubated with 0.3 nM IrC_6 •AbH •AuNP13 for 24 hours. (Left) FLIM image showing detection of lifetimes in the range 20 – 1000 ps. (Middle) Intensity image and (Right) Mapped PLIM images showing detection of lifetimes in the range of 700 – 1000 ns (red), 600 – 690 ns (green) and 450 – 590 ns (blue). λ_{exc} = 760 nm, scale bar = 10 µm.

Analysis of the PLIM image shows luminescence lifetimes longer than those recorded for IrC_6 •AbH •**AuNP13** in solution, which had a long component of 720 ns in water. This extension in luminescence lifetimes is present in all the cells (displayed in red) with only some areas showing the shorter nanosecond lifetimes being detected which are displayed in green (600 – 690 ns) and in blue (450 – 590 ns) in the image. This follows a similar trend to that seen for the Zonyl coated nanoparticles (IrC_6 •**AuNP13**), where uptake into the cytoplasm showed long nanosecond lifetimes.

The FLIM image shows detection of short-lived lifetimes in the range of 20 – 1000 ps. The fitting of the lifetime decays suggests this signal is coming from the gold, the characteristic SPR peak is present in the lifetime decay. These results show that the short-lived lifetimes from the gold have been detected within the cytoplasm of the cells and fully co-localise with the long-lived signal from the iridium seen in the PLIM channel. This can be seen for a specific coordinate within the HeLa cells which shows lifetimes detected within the PLIM and FLIM channel fully co-localise with each other, therefore identifying uptake of intact IrC_6 •AbH •**AuNP13** (Appendix). This is due to the high loading and long incubation time of IrC_6 •AbH •**AuNP13**, which was dosed at a concentration of 0.3 nM for 24 hours. The luminescence lifetimes were detected through multichannel lifetime imaging. These lifetime images are shown below for IrC_6 •AbH•**AuNP25** in Hela Cells (Figure 5.34).

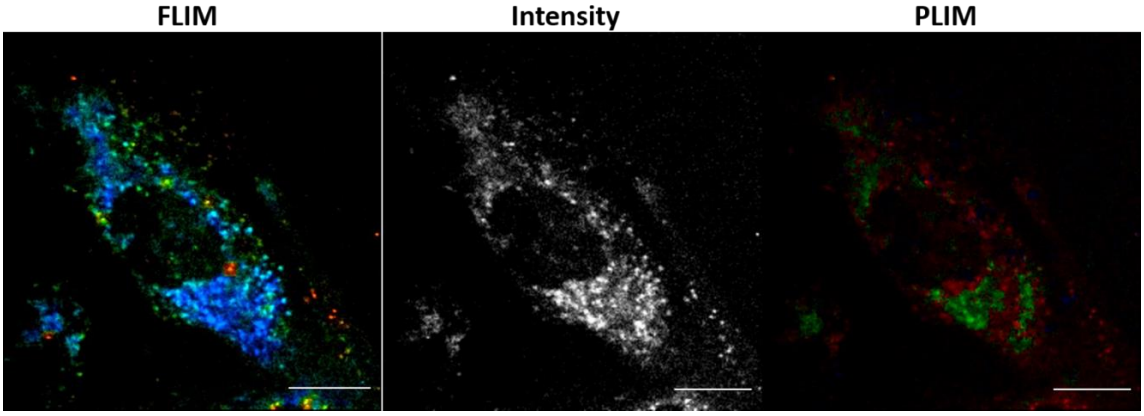

Figure 5.34. Two-photon lifetime images showing detection of the short-lived fluorescence (FLIM) and long-lived phosphorescence (PLIM) lifetimes for multichannel detection. HeLa cells incubated with 0.2 nM IrC_6 •AbH•AuNP25 for 24 hours. (Left) FLIM image showing detection of lifetimes in the range 20 – 1000 ps. (Middle) Intensity image and (Right) Mapped PLIM images showing detection of lifetimes in the range of 700 – 1000 ns (red), 600 – 690 ns (green) and 450 – 590 ns (blue). λ_{exc} = 760 nm, scale bar = 10 µm.

The PLIM image displays all the lifetime ranges detected in HeLa cells from short nanosecond lifetimes in blue (450 – 590 ns) to longer nanosecond lifetimes in green (600 – 690 ns) and red (700 – 1000 ns). However, the lifetimes detected in the sample show mostly longer lifetimes (red) localised throughout the cytoplasm of the HeLa cells. Some lifetimes in the 600 – 690 ns range (green) were detected around the nuclear and inner cell membrane. This is a similar trend to 13 nm AbH coated nanoparticles which showed mostly long nanosecond lifetimes being detected in the cytoplasm (red) and some shorter nanosecond being detected in some cells within the image, displayed in green. Analysis of the PLIM image shows lifetimes which are longer than the IrC_6 •AbH •**AuNP25** in solution, which has a long component of 700 ns in water. This extension of the luminescent lifetime is present in all the cells with most lifetimes being detected in the 700 – 2000 ns range, which appears as red in the image. This shows that upon uptake into cells the probe is interacting with cellular proteins, causing an extension in the luminescent lifetime. This was seen for the Zonyl coated particles

(IrC_6 •**AuNPs**) where long luminescence lifetimes of 650 – 790 ns were detected within the cytoplasm and nucleus of HeLa cells, which was an extension from the luminescent lifetime in solution (~330 ns).

The FLIM image shows detection of short-lived lifetimes in the range of 50 – 1300 ps. The fitting of the lifetime decays suggests this signal is coming from the gold, as there is a characteristic peak from the surface plasmon resonance band seen in the lifetime decay. These results showed that the short-lived lifetimes from the gold have been detected within the cytoplasm of the cells and fully co-localise with the long-lived signal from the iridium seen in the PLIM channel. This can be seen for a specific coordinate within the HeLa cells showing both PLIM and FLIM lifetimes being detected, therefore identifying full localised iridium functionalised nanoparticles (Appendix). The lifetimes detected through multichannel lifetime imaging for IrC_6 •AbH •**AuNP100** in Hela Cells are shown in Figure 5.35.

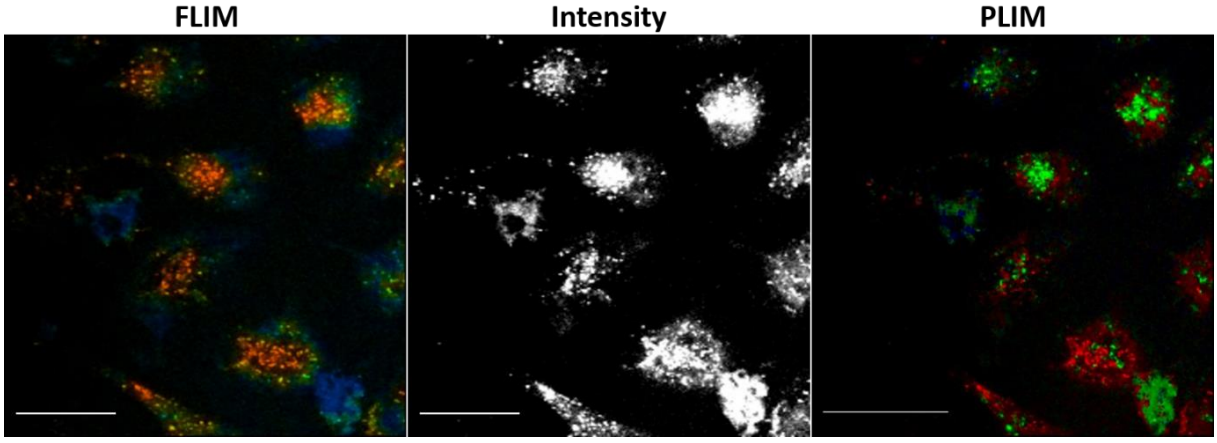

Figure 5.35. Two-photon lifetime images showing detection of the short-lived fluorescence (FLIM) and long-lived phosphorescence (PLIM) lifetimes for multichannel detection. HeLa cells incubated with 1.5 pM IrC_6 •AbH •AuNP100 for 24 hours. (Left) FLIM image showing detection of lifetimes in the range 50 – 1300 ps. (Middle) Intensity image and (Right) Mapped PLIM images showing detection of lifetimes in the range of 700 – 1000 ns (red), 600 – 690 ns (green) and 450 – 590 ns (blue). λ_{exc} = 760 nm, scale bar = 10 µm.

The PLIM image displays all the lifetime ranges detected in HeLa cells from short nanosecond lifetimes in blue (450 – 590 ns) to longer nanosecond lifetimes in green (600 – 690 ns) and red (700 – 1000 ns). The lifetimes detected in the sample show mostly shorter lifetimes displayed in green (600 – 690 ns) localised throughout the cytoplasm and inner cell membranes and some areas of red (700 – 1000 ns) lifetimes being detected in a few HeLa cells. This shows a similar trend to the 13 nm and 25 nm AbH coated nanoparticles. Analysis of the PLIM image shows lifetimes which are longer than the IrC_6 •AbH•**AuNP100** in solution, which has a long component of 710 ns in water. This extension of the luminescent lifetime is present in all the cells with most lifetimes being detected in the 700 – 3000 ns range, which appears as red in the image.

The FLIM image shows detection of short-lived lifetimes in the range of 50 – 1300 ps. The fitting of the lifetime decays suggests this signal is coming from the gold, as there is a characteristic peak from the surface plasmon resonance of the gold. The FLIM image shows clustering of nanoparticles within the cytoplasm of the cells, which can be seen in orange in the FLIM image. These clusters can be seen in all cells within the sample. This visual clustering of nanoparticles was not seen for the 13 nm and 25 nm AbH coated nanoparticles. The analysis of the FLIM lifetimes and the visual clustering seen in the cells, shows that 100 nm particles are easily detected using fluorescence lifetime imaging due to their size and strong plasmon resonance. Uptake of 13 nm and 25 nm particles could show a similar pattern of clustering within the cytoplasm, but since the FLIM signal is much weaker, these clusters are not visually seen in the images. The corresponding PLIM images show that these clusters of nanoparticles have long luminescence lifetimes which are greater than the lifetimes of aggregated

nanoparticles (~300 ns in water), these can be seen in green and red in the PLIM image. The short-lived lifetimes from the gold have been detected within the cytoplasm of the cells and fully co-localise with the long-lived signal from the iridium seen in the PLIM channel. This can be seen for a specific coordinate within the HeLa cells showing both PLIM and FLIM lifetimes being detected, therefore identifying full localised iridium functionalised nanoparticles (Appendix). The same trend was seen for the 13 nm and 25 nm AbH coated nanoparticles and has been attributed to the long 24 hour incubation time which has allowed for accumulation of nanoparticles into cells.

5. 3. 5. 2 Multichannel detection of IrC_6 •SiRNA •AuNPs in cancer cells

Analysis of the short-lived and long-lived signals of IrC_6 •SiRNA •**AuNPs** in Hela cells can be seen below for the three different sizes (Figure 5.36, 5.37 and 5.38). The luminescence lifetimes from the fluorescence channel (FLIM) can be seen on the left-hand side of the intensity image. The short-lived lifetimes detected were similar for all three sizes of nanoparticles. The lifetimes from the phosphorescence channel (PLIM) can be seen to the right of the intensity images, the colour in the images represents a range of lifetimes detected from the sample. The PLIM images revealed strong phosphorescence signal within HeLa cells for all three sizes of **SiRNA** coated nanoparticles. The luminescence lifetimes detected in the PLIM channel were mapped and found to range from short nanosecond lifetimes (blue) to long nanosecond lifetimes (red). The uptake of the **SiRNA** coated nanoparticles show a similar pattern of uptake for all three sizes of nanoparticles, with uptake being mainly within the cytoplasm of the cell. The lifetimes detected for IrC_6 •SiRNA •**AuNP13** in Hela Cells ranged from 620 – 2500 ns. The PLIM images show only green (600 – 690 ns) and red

(700 – 1000 ns) lifetimes detected within the cells, with no shorter lifetimes being detected in the range of 450 – 590 ns (blue) (Figure 5.36).

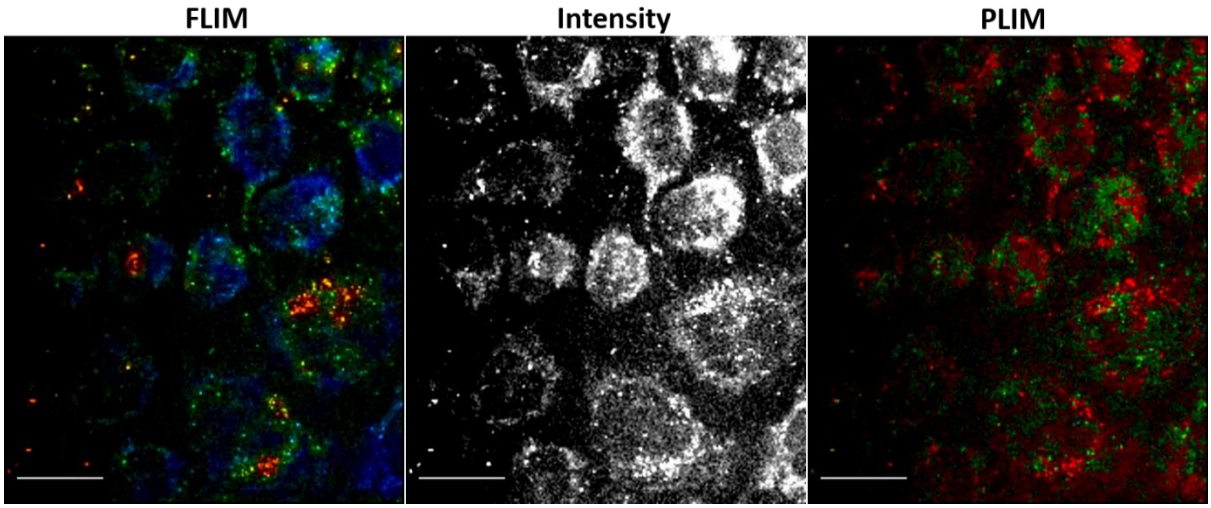

Figure 5.36. Two-photon lifetime images showing detection of the short-lived fluorescence (FLIM) and long-lived phosphorescence (PLIM) lifetimes for multichannel detection. HeLa cells incubated with 0.3 nM IrC_6 •SiRNA •AuNP13 for 24 hours. (Left) FLIM image shows detection of lifetimes in the range 20 – 2500 ps. (Middle) Intensity image and (Right) Mapped PLIM images showing detection of lifetimes in the range of 700 – 1000 ns (red), 600 – 690 ns (green) and 450 – 590 ns (blue). λ_{exc} = 760 nm, scale bar = 10 µm.

Analysis of the PLIM image shows lifetimes which are longer than the IrC_6 •SiRNA •**AuNP13** in solution, which has a long component of 500 ns in water. This extension of the luminescent lifetime is present in all the cells with no short nanosecond lifetimes (450 – 590 ns) being detected in the sample, which would appear blue in the image. The data shows similar uptake and luminescence lifetimes detection within cancer cells in comparison to IrC_6 •AbH •**AuNP13.** However, this does differ from the uptake of Zonyl coated particles, IrC_6 •**AuNP13**, in cancer cells where lifetimes were detected in the range of 450 – 1500 ns and short nanosecond lifetimes (blue) were detected in the cytoplasm of HeLa cells as clusters of nanoparticles. Interactions with cellular proteins could cause an extension in the luminescent lifetime, as previously seen for IrC_6

•**AuNP13** in which the luminescence lifetime increased in cellular culture media and serum.

The FLIM image showed detection of short-lived lifetimes in the range of 20 – 1300 ps. The fitting of the lifetime decays suggests this signal is coming from the gold, as there is a characteristic peak from the surface plasmon resonance of the gold. These results show that the short-lived lifetimes from the gold have been detected within the cytoplasm of the cells and fully co-localise with the long-lived signal from the iridium seen in the PLIM channel. This can be seen for a specific coordinate within the HeLa cells showing both PLIM and FLIM lifetimes being detected, therefore identifying full localised iridium functionalised nanoparticles (Appendix). This is due to the high loading and long incubation time of IrC_6 •SiRNA •**AuNP13**, which was dosed at a concentration of 0.3 nM for 24 hours. These results were similar for IrC_6 •**AuNP13** in Hela cells which showed fully localised FLIM and PLIM signal in the cells which was attributed to high loading of nanoparticles into HeLa cells (0.45 nM for 5 hours). Since strong FLIM and PLIM signal was seen after 5 hours dosing with Zonyl coated particles, these results are expected from a 24-hour incubation time for the SiRNA coated particles. The lifetimes detected for IrC_6 •SiRNA •**AuNP25** in Hela Cells are shown in Figure 5.37.

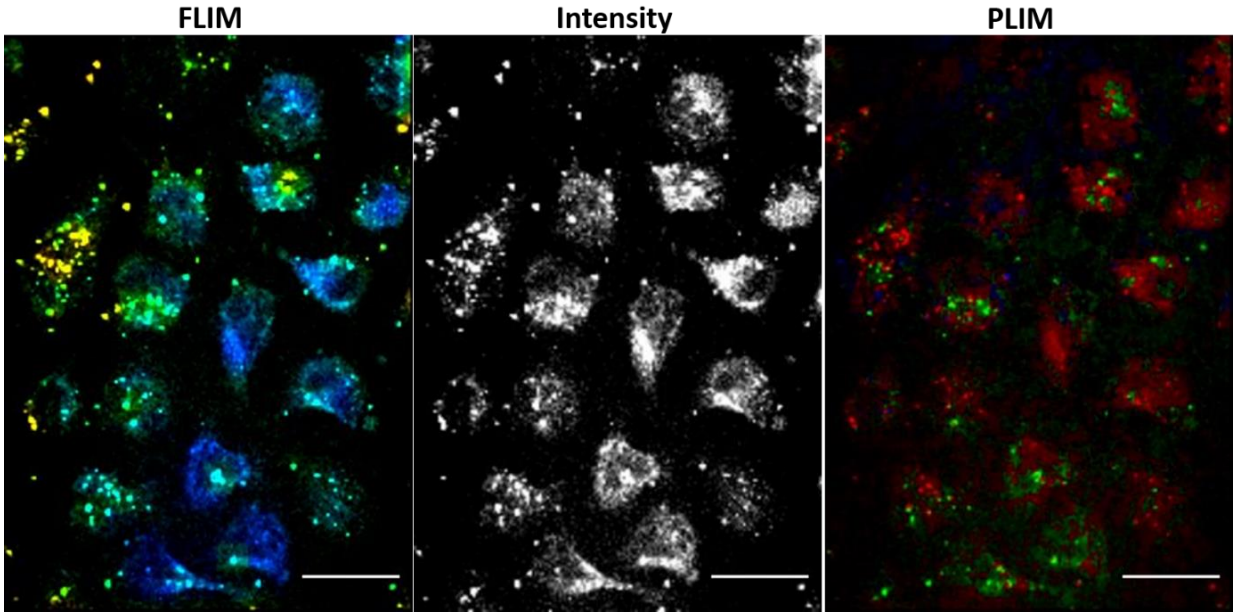

Figure 5.37. Two-photon lifetime images showing detection of the short-lived fluorescence (FLIM) and long-lived phosphorescence (PLIM) lifetimes for multichannel detection. HeLa cells incubated with 0.3 nM IrC_6 •SiRNA •AuNP25 for 24 hours. (Left) FLIM image showing detection of lifetimes in the range 20 – 1300 ps. (Middle) Intensity image and (Right) Mapped PLIM images showing detection of lifetimes in the range of 700 – 2000 ns (red), 600 – 690 ns (green) and 450 – 590 ns (blue). λ_{exc} = 760 nm, scale bar = 10 µm.

The PLIM image displays all the lifetime ranges detected in HeLa cells from short nanosecond lifetimes in blue (450 – 590 ns) to longer nanosecond lifetimes in green (600 – 690 ns) and red (700 – 1000 ns). The luminescence lifetimes detected in the sample show mostly longer lifetimes displayed in red localised throughout the cytoplasm of the cell with areas of green (450 – 590 ns) and blue (600 – 690 ns) lifetimes being detected around the inner cell membrane of HeLa cells. This differs from the lifetimes detected for IrC_6 •SiRNA •**AuN13**, which showed more 600 – 690 ns lifetimes in green throughout the cytoplasm of the cells and no short nanosecond lifetimes detected in the sample. Analysis of the PLIM image shows lifetimes which are longer than the IrC_6 •SiRNA •**AuNP25** in solution, which has a long component of 570 ns in water. This extension of the luminescent lifetime is present in all the cells with

most lifetimes being detected in the 700 – 2000 ns range, which appears as red in the image. This extension in luminescence lifetime has been seen for all the nanoparticles analysis with HeLa cells, and strongly indicates interactions of the iridium probe with cellular proteins. The FLIM image shows detection of short-lived lifetimes in the range of 20 – 1600 ps. The fitting of the lifetime decays suggests this signal is coming the characteristic surface plasmon resonance band of the gold. These results show that the short-lived lifetimes from the gold have been detected within the cytoplasm of the cells and fully co-localise with the long-lived signal from the iridium seen in the PLIM channel. This can be seen for a specific coordinate within the HeLa cells showing both PLIM and FLIM lifetimes being detected, therefore identifying full localised iridium functionalised nanoparticles (Appendix). The same trend was seen for the 13 nm SiRNA coated nanoparticles and has been attributed to the long 24 hour incubation time which has allowed for accumulation of nanoparticles into cells. The lifetimes detected for IrC_6 •SiRNA **•AuNP100** in Hela Cells are shown in Figure 5.38.

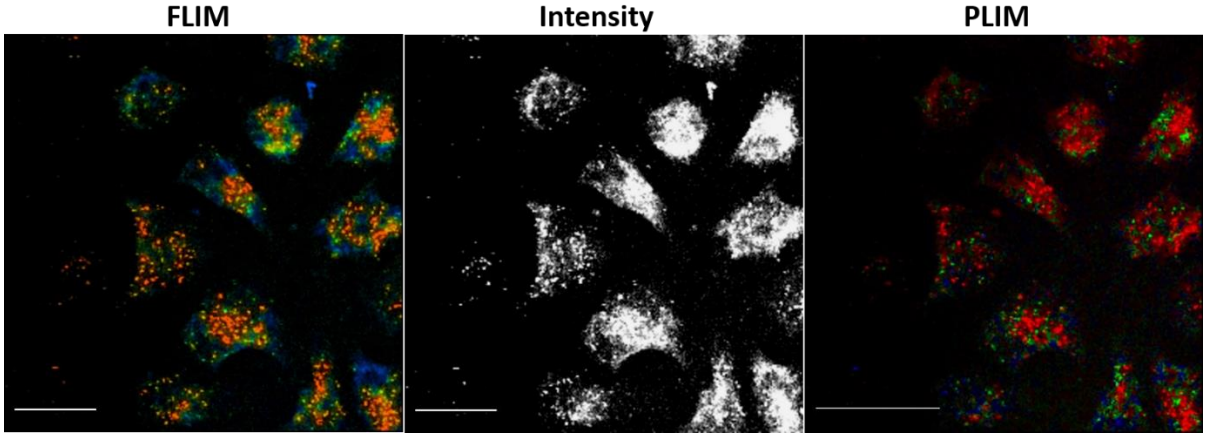

Figure 5.38. Two-photon lifetime images showing detection of the short-lived fluorescence (FLIM) and long-lived phosphorescence (PLIM) lifetimes for multichannel detection. HeLa cells incubated with 1.5 nM IrC_6 •SiRNA•AuNP100 for 5 hours. (Left) FLIM image showing detection of lifetimes in the range 20 – 2500 ps. (Middle) Intensity image and (Right) Mapped PLIM images showing detection of lifetimes in the range of 700 – 1000 ns (red), 600 – 690 ns (green) and 450 – 590 ns (blue). λ_{exc} = 760 nm, scale bar = 10 µm.

The PLIM image displays all the lifetime ranges detected in HeLa cells from short nanosecond lifetimes in blue (450 – 590 ns) to longer nanosecond lifetimes in green (600 – 690 ns) and red (700 – 1000 ns). The lifetimes detected in the sample show mostly longer lifetimes displayed in red localised throughout the cytoplasm which are longer than the IrC_6 •SiRNA •**AuNP100** in solution, which has a long component of 540 ns in water. This extension of the luminescent lifetime is present in all the cells with most lifetimes being detected in the 700 – 2000 ns range. Interestingly, the PLIM images show high uptake of IrC_6 •SiRNA •**AuNP100** in the cytoplasm of the cells, which appear to be non-aggregated nanoparticles since they are coloured in red. This pattern in uptake differs from IrC_6 •**AuNP100**, which saw these 100 nm nanoparticles localising around the outer membrane, with minimal uptake into the cells. This was attributed to the large size of these nanoparticles hindering uptake into HeLa cells. The fact that multichannel lifetime imaging has detected IrC_6 •AbH •**AuNP100** within the cytoplasm of HeLa cells, could be attributed to the SiRNA coating increasing the uptake efficiency of these nanoparticles.

The FLIM image shows clustering of nanoparticles within the cytoplasm of the cells, which can be seen in orange in the FLIM image. These clusters can be seen in all cells within the sample. This amount of clustering of nanoparticles within HeLa cells was not seen for the 13 nm and 25 nm particles. Analysis of the short picosecond lifetimes showed stronger signal detected in comparison to that seen from the 25 nm particles (Appendix). The analysis of the FLIM lifetimes and the visual clustering seen in the cells, shows that these 100 nm particles are easily detected using fluorescence lifetime imaging due to their size and strong plasmon resonance. The corresponding PLIM images show that these clusters of nanoparticles have long luminescence lifetimes

which are greater than the lifetimes of aggregated nanoparticles (~300 ns in water), these can be seen mainly in red within the PLIM image. The short-lived lifetimes from the gold have been detected within the cytoplasm of the cells and fully co-localise with the long-lived signal from the iridium seen in the PLIM channel. This can be seen for a specific coordinate within the HeLa cells showing both PLIM and FLIM lifetimes being detected, therefore identifying fully localised iridium functionalised nanoparticles (Appendix). This trend was seen for IrC_6 •AbH •**AuNP100** where clustering of nanoparticles could be seen within the cytoplasm of HeLa cells, which had short nanosecond lifetimes detected (600 – 690 ns).

5. 3. 5. 3 Multichannel detection of IrC_6 •AbH/SiRNA •AuNPs in cancer cells

Analysis of the short-lived and long-lived signals of IrC_6 •AbH/SiRNA•**AuNPs** in Hela cells can be seen below for the three different sizes (Figure 5.39, 5.40 and 5.41). The PLIM images revealed strong phosphorescence signal within HeLa cells for IrC_6 •AbH/SiRNA•**AuNP25** and IrC_6 •AbH/SiRNA•**AuNP100**, however the PLIM signal detected for IrC_6 •AbH/SiRNA•**AuNP13** was extremely weak. The uptake of the AbH/SiRNA coated nanoparticles show a similar pattern of uptake for IrC_6 •AbH/SiRNA•**AuNP13** and IrC_6 •AbH/SiRNA•**AuNP25**, with uptake being mainly within the cytoplasm of the cell. However, the uptake of IrC_6 •AbH/SiRNA•**AuNP100** appears to be around the cell's outer membrane. The shows a similar pattern of uptake as seen for IrC_6 •**AuNP100** in HeLa cells after only 5 hours of incubation with the nanoparticles. The lifetimes detected for IrC_6 •AbH/SiRNA •**AuNP13** in Hela Cells ranged from 450 – 950 ns. The PLIM signal detected for IrC_6 •AbH/SiRNA •**AuNP13** was extremely weak so to fit the lifetime decay, the binning had to be increased to

maximum (10 binning). Analysis of the PLIM image shows mainly short nanosecond lifetimes being detected (450 – 590 ns), which are coloured in blue in the image (Figure 5.39) This differs from the lifetimes detected for IrC_6 •AbH •**AuNP13** which showed mostly long nanosecond lifetime being detected in red (700 – 1000 ns) and IrC_6 •SiRNA•**AuNP13** which showed long nanosecond lifetimes being detected in green (600 – 690 ns) and red (700 – 1000 ns) throughout the cytoplasm. This shows that there is no extension of lifetimes for the nanoparticles which have been internalised in the HeLa cells for IrC_6 •AbH/SiRNA •**AuNP13**.

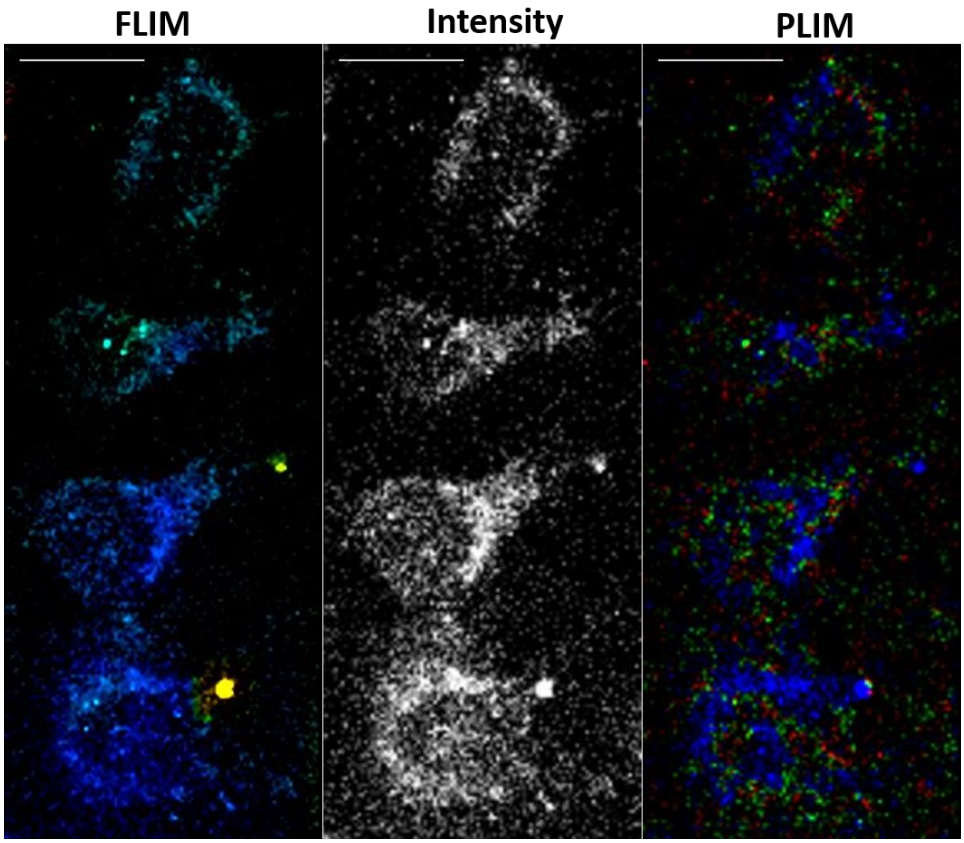

Figure 5.39. Two-photon lifetime images showing detection of the short-lived fluorescence (FLIM) and long-lived phosphorescence (PLIM) lifetimes for multichannel detection. HeLa cells incubated with 0.3 nM IrC_6 •AbH/SiRNA •AuNP13 for 24 hours. (Left) FLIM image showing detection of lifetimes in the range 20 – 1000 ps. (Middle) Intensity image and (Right) Mapped PLIM images showing detection of lifetimes in the range of 700 – 1000 ns (red), 600 – 690 ns (green) and 450 – 590 ns (blue). λ_{exc} = 760 nm, scale bar = 10 µm.

Analysis of the PLIM image shows mainly lifetimes which are shorter than the IrC_6 •AbH/SiRNA •**AuNP13** in solution, which has a long component of 640 ns in water. The predominate lifetimes present in the sample are within the range of 450 – 590 ns (blue). This is the opposite to that seen for IrC_6 •AbH •**AuNP13** and IrC_6 •SiRNA •**AuNP13**, which showed extension of the luminescent lifetimes when internalised into HeLa cells. The presence of both **AbH** and **SiRNA** onto the gold surface, could have slowed the uptake into cells due to steric hindrance. Therefore, the amount of IrC_6 •AbH/SiRNA •**AuNP13** present in the cells is lower than that seen from previous sets of nanoparticles. Since both FLIM and PLIM signal is detected in the cells, it is assumed that there is no free **IrC_6** present within the cells, and that detection of these long and short lived signals are coming from fully coated gold nanoparticles.

The FLIM image shows detection of short-lived lifetimes in the range of 300 – 900 ps. In comparison to the other sets of coated nanoparticles, which displayed strong FLIM signal from the gold nanoparticles, the FLIM signal detected for IrC_6 •AbH/SiRNA •**AuNP13** was extremely weak. However, the characteristic peak from the surface plasmon resonance of the gold was still present within the cells. A comparison of the FLIM and PLIM signal detected for IrC_6 •AbH/SiRNA •**AuNP13** and IrC_6 •SiRNA •**AuNP13**, can be found in the Appendix. However, the short-lived lifetimes that have been detected within the cytoplasm of the cells appear to fully co-localise with the long-lived signal from the iridium seen in the PLIM channel. This can be seen for a specific coordinate within the HeLa cells showing both PLIM and FLIM lifetimes being detected, therefore identifying full localised iridium functionalised nanoparticles (Appendix). Since these nanoparticles were dosed under the same conditions as IrC_6 •SiRNA •**AuNP13** and IrC_6 •AbH •**AuNP13** (0.3 nM or 24 hours), the FLIM and PLIM signal

detected within the cell should be a lot stronger. This could be an indication of the nanoparticle surface coating affecting the mechanism of uptake into the cells. The luminescence lifetimes detected for IrC_6 •AbH/SiRNA •**AuNP25** in Hela Cells are shown in Figure 5.40.

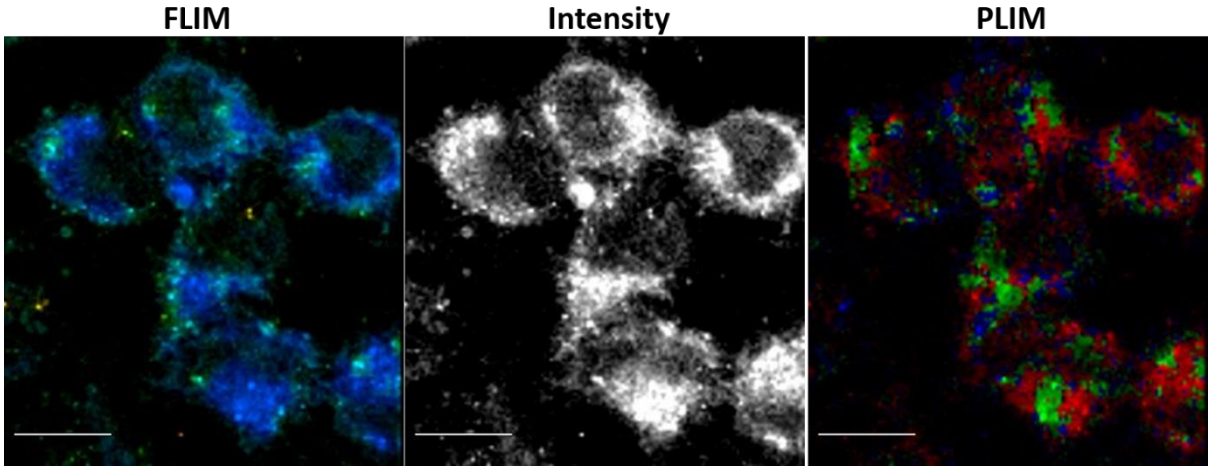

Figure 5.40. Two-photon lifetime images showing detection of the short-lived fluorescence (FLIM) and long-lived phosphorescence (PLIM) lifetimes for multichannel detection. HeLa cells incubated with 0.2 nM IrC_6 •AbH/SiRNA •AuNP25 for 24 hours. (Left) FLIM image showing detection of lifetimes in the range 60 – 1600 ps. (Middle) Intensity image and (Right) Mapped PLIM images showing detection of lifetimes in the range of 700 – 1000 ns (red), 600 – 690 ns (green) and 450 – 590 ns (blue). λ_{exc} = 760 nm, scale bar = 10 µm.

The PLIM image displays all the lifetime ranges detected in HeLa cells from short nanosecond lifetimes in blue (450 – 590 ns) to longer nanosecond lifetimes in green (600 – 690 ns) and red (700 – 1000 ns). The predominant lifetimes detected in the cell appear to be from the long nanosecond lifetimes, displayed in red. The lifetimes detected appear to be localised through the cytoplasm of the cells. Some luminescence lifetimes in the 600 – 690 ns range were detected around the nuclear and inner cell membrane. This pattern of uptake is similar to that seen for IrC_6 •AbH •**AuNP25** and the IrC_6 •AbH •**AuNP13** in HeLa cells, which showed mostly long nanosecond lifetimes being detected in the cytoplasm (red) and some shorter

nanosecond lifetimes being detected around the cell inner and outer membranes (green). Analysis of the PLIM image shows lifetimes which are longer than the IrC_6 •AbH •**AuNP25** in solution, which has a long component of 620 ns in water. This shows that upon uptake into cells the probe is interacting with cellular proteins, causing an extension in the luminescent lifetime. This extension in the luminescent lifetime was seen for the Zonyl coated particles (IrC_6 •**AuNPs**), SiRNA coated particles (IrC_6 •SiRNA •**AuNPs**) and antibody coated nanoparticles (IrC_6 •AbH •**AuNPs**), where long luminescence lifetimes of 650 – 790 ns were detected within the cells. However, this long extension of the luminescent lifetime was not seen for the IrC_6 •AbH/SiRNA •**AuNP13** in HeLa cells. The same trend was seen for IrC_6 •**AuNP25** in HeLa cells in comparison to IrC_6 •**AuNP13**, which showed a higher uptake for 25 nm particles than for the 13 nm particles, which had weaker PLIM and FLIM signals detected in cells. The strong signal detected for both the long and short lived lifetimes within HeLa cells for all sets of 25 nm gold nanoparticles studied, identify these sized nanoparticles as promising candidates for lifetime imaging within cancer cell lines.

The FLIM image shows detection of short-lived lifetimes in the range of 60 – 1500 ps. The fitting of the lifetime decays suggests this signal is coming from the gold, as there is a characteristic peak from the surface plasmon resonance of the gold. These results show that the short-lived lifetimes from the gold have been detected within the cytoplasm of the cells and fully co-localise with the long-lived signal from the iridium seen in the PLIM channel (Appendix). This same trend has been seen for SiRNA coated particles (IrC_6 •SiRNA •**AuNPs**) and antibody coated nanoparticles (IrC_6 •AbH •**AuNPs**). There appears to be no visual clustering of nanoparticles within the cells which is to be expected due to the smaller diameter of the nanoparticles in comparison

to 100 nm nanoparticles. The lifetimes detected for IrC_6 •AbH/SiRNA •**AuNP100** in Hela Cells ranged as shown in Figure 5.41.

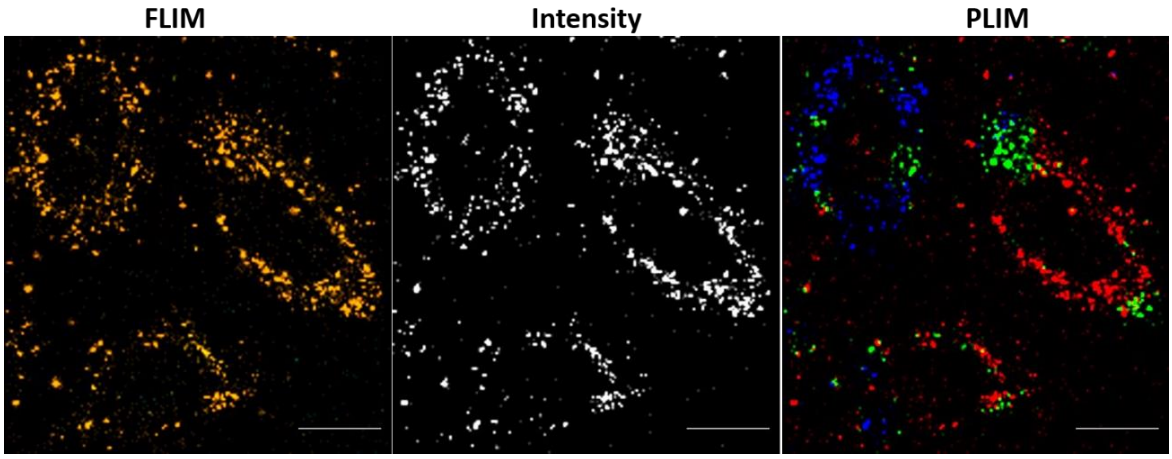

Figure 5.41. Two-photon lifetime images showing detection of the short-lived fluorescence (FLIM) and long-lived phosphorescence (PLIM) lifetimes for multichannel detection. HeLa cells incubated with 1.2 pM IrC_6 •AbH/SiRNA•AuNP100 for 24 hours. (Left) FLIM image showing detection of lifetimes in the range 30 – 3500 ps. (Middle) Intensity image and (Right) Mapped PLIM images showing detection of lifetimes in the range of 700 – 1000 ns (red), 600 – 690 ns (green) and 450 – 590 ns (blue). λ_{exc} = 760 nm, scale bar = 10 µm.

The PLIM image displays all the lifetime ranges detected in HeLa cells from short nanosecond lifetimes in blue (450 - 590 ns) to longer nanosecond lifetimes in green (600-690 ns) and red (700 – 1000 ns). The PLIM signal detected in this sample was weaker than previously seen for IrC_6 •AbH •**AuNP100** and IrC_6 •SiRNA •**AuNP100** in HeLa cells. The pattern of uptake is confined mainly to the cell membranes, which was seen for IrC_6 •SiRNA•**AuNP100** and IrC_6 •AbH•**AuNP100**. There appear to be two cells that have phosphorescence lifetimes detected in the long nanosecond range (700 – 1000 ns) and one cell present that has phosphorescence lifetimes detected in the short nanosecond range (450 – 590 ns) with all nanoparticles being localised around the cell membrane. It is unclear why the pattern of luminescence lifetimes detected is different from one cell to the other, this could be an indication of non-uniform coating

of nanoparticles with iridium due to the large amount of **SiRNA** and **AbH** present on the gold surface. Another reason could be the cultured HeLa cells themselves affecting uptake into one specific cell. The PLIM images show luminescence lifetimes which are longer than the IrC_6 •AbH/SiRNA •**AuNP100** in solution, which had a long component of 600 ns in water. However, this extension of the luminescent lifetime is not present in all the cells, with one cell showing only shorter nanosecond lifetimes (blue).

The FLIM image shows detection of short-lived lifetimes in the range of 30 –3500 ps. The fitting of the lifetime decays suggests this signal is coming from the gold, as there is a characteristic peak from the SPR of the gold nanoparticles. The FLIM image shows that all nanoparticles detected within the sample are present as clusters, which are coloured in orange. These clusters can be seen in all cells within the sample, localised around the cell membrane. This trend was seen for IrC_6 •AbH •**AuNP100** and IrC_6 •SiRNA •**AuNP100** where clustering of nanoparticles could be seen within the cytoplasm of HeLa cells. However, with IrC_6 •AbH •**AuNP100** and IrC_6 •SiRNA •**AuNP100,** short-lived signal from the gold was also present in areas where there was no clustering of nanoparticles visually seen. The corresponding PLIM images show that these clusters of nanoparticles have long luminescence lifetimes which are greater than the lifetimes of aggregated nanoparticles (~300 ns in water). The short-lived lifetimes from the gold have been detected around the cell membrane and fully co-localise with the long-lived signal from the iridium seen in the PLIM channel (Appendix).

5. 3. 5. 4 Lifetime analysis showing nuclear uptake of IrC6 •AbH •AuNP25, IrC6 •SiRNA •AuNP25 and IrC6 •AbH/SiRNA •AuNP25 into cancer cells

Further lifetime analysis was carried out on the nuclear region of HeLa cells dosed with IrC_6 •AbH •**AuNP25**, IrC_6 •SiRNA •**AuNP25** and IrC_6 •AbH/SiRNA •**AuNP25,** to identify whether these functionalised nanoparticles localised within the nucleus. The nucleus of the cells analysed have been highlighted by a red box present on both the phosphorescence and fluorescence lifetime images. Unfortunately, for these preliminary experiments no Z-stacks were acquired for any of the images. To identify true uptake into the nucleus, future work would entail carrying out PLIM and FLIM Z-stacks throughout the cells for all functionalised nanoprobes. Since the outline of the nucleus can be seen in the images, it is assumed that this plane is located somewhere within the nucleus. Analysis of the lifetimes within the nucleus of cells dosed with IrC_6 •AbH •**AuNP25**, can be seen in Figure 5.42 below.

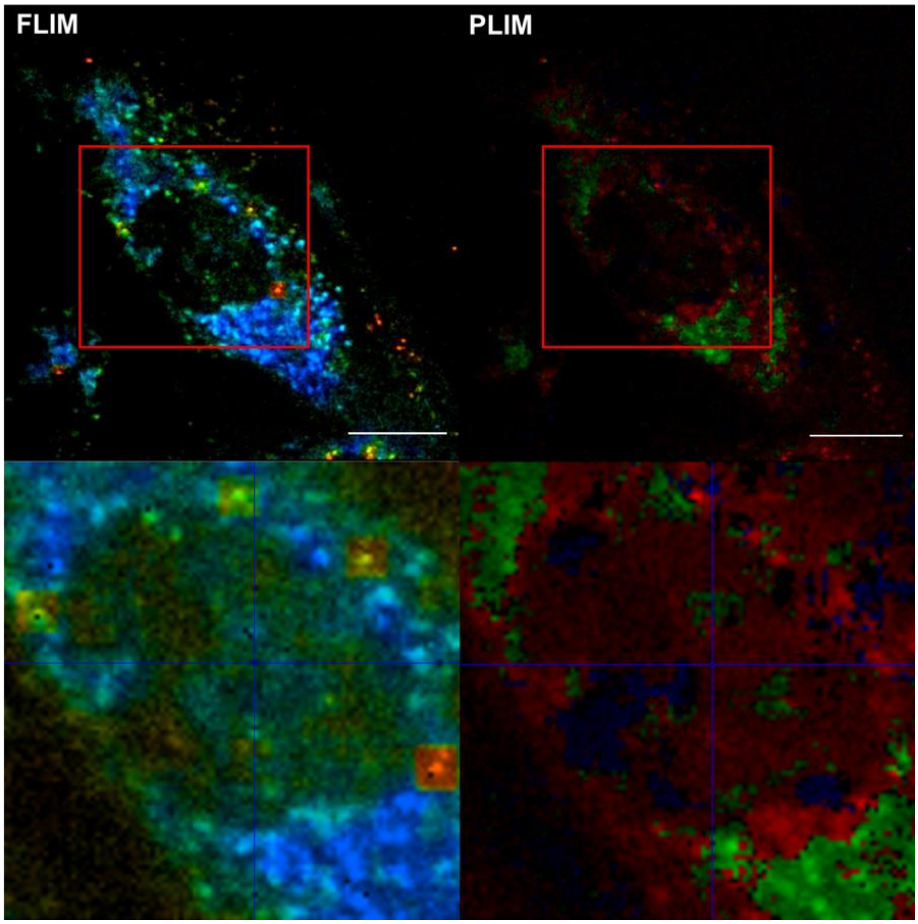

Figure 5.42. Hela cells dosed with 0.2 nM IrC_6 •AbH •AuNP25 for 24 hours, (Top, right) Short-lived lifetimes showing gold signal, t_m: 20 – 1000 ps. (Top, right) Long-lived lifetimes showing iridium signal in nucleus, blue: 450 – 590 ns, green: 600 – 690 ns and red: 700 – 1000 ns. (Bottom, left) Inset of red box on FLIM image showing gold detection in the nucleus. (Bottom, right) Inset of red box on PLIM image showing iridium signal in the nucleus. λ_{exc} = 760 nm, scale bar = 20 µm.

The PLIM images show long-lived signal from the iridium within the nucleus of the cells, which are displayed in red. Shorter lifetimes in green and blue can be seen in patches within the inner nuclear membrane. Lifetimes detected in the range 600 – 690 ns (green) can also be seen around the cell outer nuclear membrane. The long-lived lifetimes appear strongly in the nucleus and co-localise with the short-lived signal from the gold, thus positively identifying fully functionalised gold nanoparticles within the nucleus of HeLa cells. It should be noted that no clusters of nanoparticles can be seen

within the nucleus. The short-lived and long-lived lifetimes were extracted from a specific coordinate within the nucleus of the HeLa cell analysed, this can be found in the Appendix. The results show both the long lifetime decay from the iridium, and the characteristic SPR peak from the gold, both within the same coordinate of the cell. This further confirms uptake of fully coated IrC_6 •AbH •**AuNP25** within the nucleus. The uptake pattern of HeLa cells dosed with IrC_6 •SiRNA •**AuNP25** differs from the nuclear uptake for IrC_6 •AbH •**AuNP25** which can be seen below (Figure 5.43).

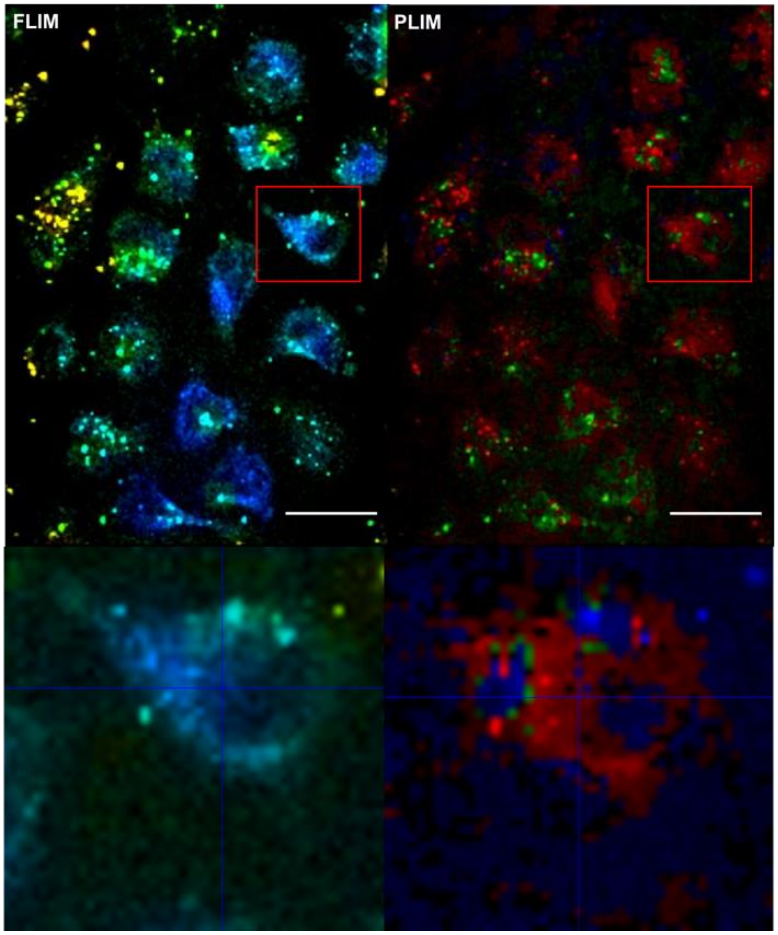

Figure 5.43. Hela cells dosed with 0.3 nM IrC_6 •SiRNA •AuNP25 for 24 hours, (Top, right) Short-lived lifetimes showing gold signal, t_m: 20 – 1300 ps. (Top, right) Long-lived lifetimes showing iridium signal in nucleus, blue: 450 – 590 ns, green: 600 – 690 ns and red: 700 – 1000 ns. (Bottom, left) Inset of red box on FLIM image showing gold detection in the nucleus. (Bottom, right) Inset of red box on PLIM image showing iridium signal in the nucleus. λ_{exc} = 760 nm, scale bar = 20 µm.

The lifetimes detected within the nucleus of cells dosed with 0.3 nM IrC_6 •SiRNA •**AuNP25** for 24 hours, show mostly longer luminescence lifetimes in the range of 700 – 1000 ns (red). There are some areas of shorter lifetimes detected in the range of 450 – 590 ns (blue), however no lifetimes in the range of 600 – 690 ns (green) were detected within the nucleus. The long-lived lifetimes for iridium appear a lot stronger within the nucleus in comparison to cells dosed with IrC_6 •AbH •**AuNP25**. This long-lived signal presented in red can also be seen around the outer nuclear membrane of the cell. The short-lived lifetimes from the gold were detected within the cell and co-localise with the long-lived lifetimes from the iridium complex on the nanoparticles. This co-localisation of the two signals confirms uptake of fully functionalised gold nanoparticles within the nucleus of HeLa cells. The short-lived and long-lived lifetimes were extracted from a specific coordinate within the nucleus of the HeLa cell analysed, this can be found in the Appendix. The results show both the long lifetime decay from the iridium, and the characteristic SPR peak from the gold, both within the same coordinate. This further confirms uptake of fully coated IrC_6 •SiRNA •**AuNP25** within the nucleus. The third set of functionalised nanoparticles (IrC_6 •AbH/SiRNA •**AuNP25**) were found to localise within the nucleus of HeLa cells. The lifetimes detected within the nucleus of HeLa cells for these nanoparticles appears to follow the same pattern as seen for IrC_6 •AbH •**AuNP25** (Figure 5.44).

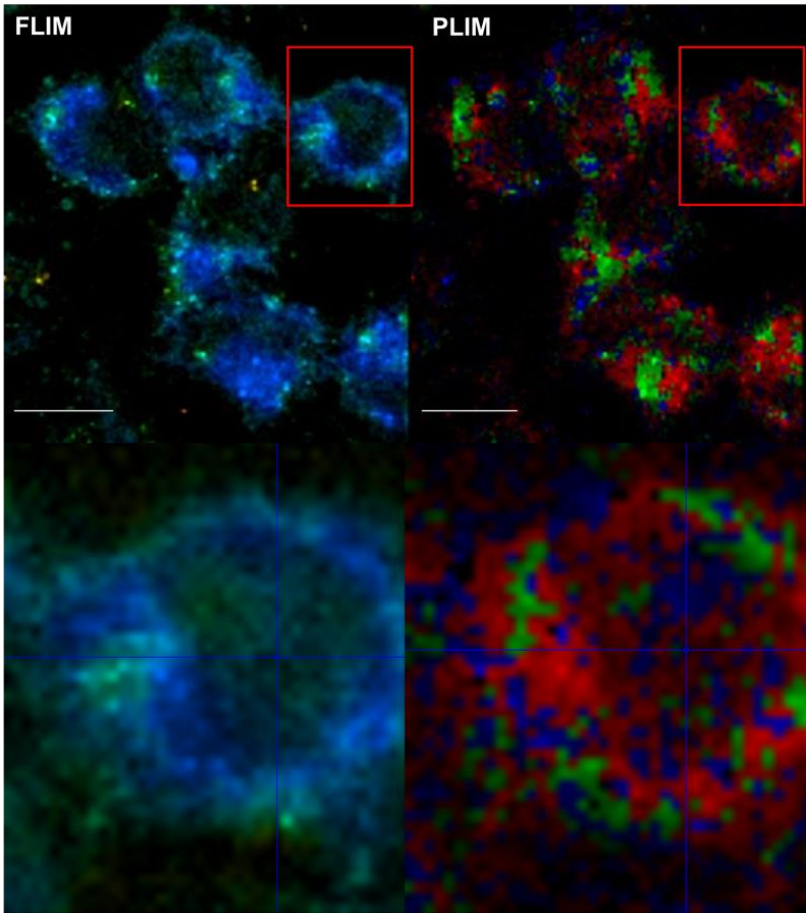

Figure 5.44. Hela cells dosed with 0.2 nM IrC_6 •AbH/SiRNA •AuNP25 for 24 hours, (Top, right) Short-lived lifetimes showing gold signal, t_m: 60 – 1600 ps. (Top, right) Long-lived lifetimes showing iridium signal in nucleus, blue: 450 – 590 ns, green: 600 – 690 ns and red: 700 – 1000 ns. (Bottom, left) Inset of red box on FLIM image showing gold detection in the nucleus. (Bottom, right) Inset of red box on PLIM image showing iridium signal in the nucleus. λ_{exc} = 760 nm, scale bar = 20 µm.

The PLIM images show that most of the lifetimes detected within the HeLa cells are the long luminescence lifetimes from iridium in the range of 700 – 1000 ns, presented in red. Shorter lifetimes in green and blue were detected within certain areas of the nucleus. This is similar to the uptake of IrC_6 •AbH •**AuNP25** into the nucleus of HeLa cells based on the lifetime analysis. This is to be expected since both nanoparticles have been functionalised with the monoclonal antibody. The PLIM images showed

lifetimes within the range of 500 – 690 ns being detected around the nuclear outer membrane. The FLIM images show short-lived lifetimes detected from the gold nanoparticles within the nucleus of HeLa cells. These short-lived lifetimes appear to fully co-localise with the long-lived signal from the iridium, thus positively identifying fully functionalised gold nanoparticles within the nucleus of HeLa cells. The short-lived and long-lived lifetimes were extracted from a specific coordinate within the nucleus of the HeLa cell analysed, this can be found in the Appendix. The results show both the long lifetime decay from the iridium, and the characteristic SPR peak from the gold, both within the same coordinate. This further confirms uptake of fully coated IrC_6 •AbH/SiRNA •**AuNP25** within the nucleus. This work has allowed for multichannel detection of iridium functionalised gold nanoparticles within the nucleus of cancer cells, which has currently have been investigated.

5. 3. 6 Selective targeting of functionalised nanoprobes into endothelial cells

These gold nanoparticles have been functionalised with monoclonal antibodies that selectively target CLEC14a which is a known tumour endothelial marker. The targeting abilities of these functionalised nanoprobes were assessed using multiphoton lifetime imaging by monitoring the lifetime changes upon uptake into HUVEC cells. HUVEC cells were used in these experiments due to the presence of CLEC14a on their surface.[7] Multiphoton lifetime imaging was carried out on live HUVEC cells dosed with functionalised nanoparticles and the localisation patterns were assessed by detecting the lifetime changes within the cells. This was done by looking at the uptake of IrC_6 •AbH •**AuNP25** into HUVEC cells and identifying whether the antibody conjugated

onto the surface of gold nanoparticles has any affect up the uptake into these endothelial cells. The results can be seen in Figure 5.45 below.

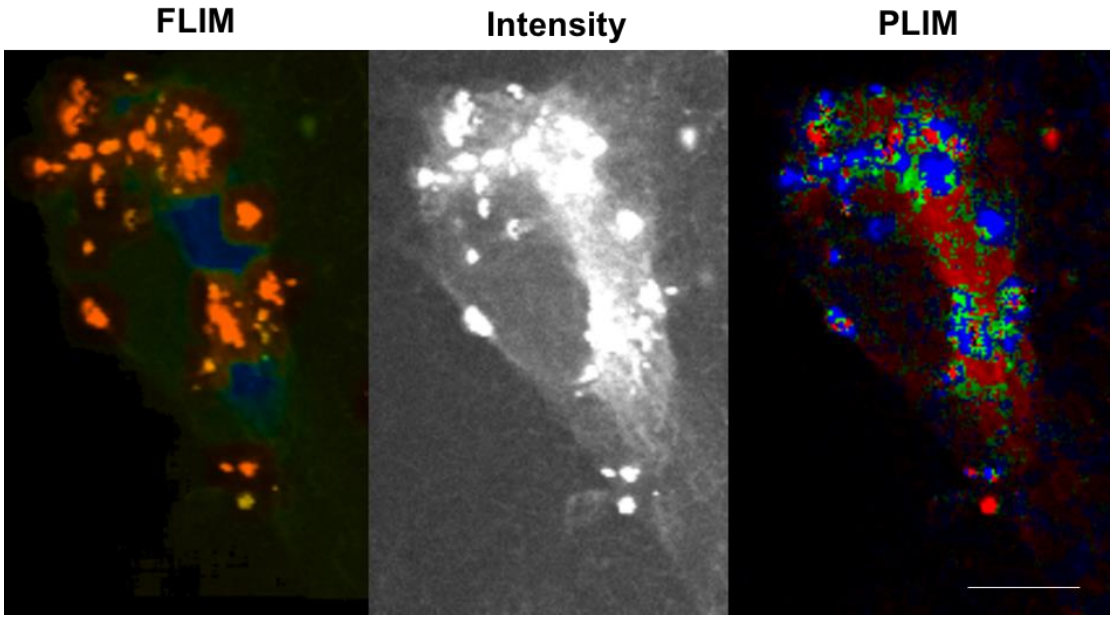

Figure 5.45. Two-photon lifetime images showing detection of the short-lived fluorescence (FLIM) and long-lived phosphorescence (PLIM) lifetimes for multichannel detection in HUVEC cells. HUVEC cells were incubated with 0.2 nM IrC_6 •AbH •AuNP25 for 24 hours. (Left) FLIM image showing detection of lifetimes in the range 100 – 2300 ps. (Middle) Intensity image and (Right) Mapped PLIM images showing detection of lifetimes in the range of 700 – 1000 ns (red), 600 – 690 ns (green) and 450 – 590 ns (blue). λ_{exc} = 760 nm, scale bar = 10 µm.

The phosphorescence lifetime images show uptake of IrC_6 •AbH •**AuNP25** into HUVEC cells, with mostly long-lived luminescence lifetimes in the range of 700 – 1000 ns being detected. This follows the same trend as seen for IrC_6 •AbH •**AuNP25** into HeLa cells under the same dosing conditions, where most lifetimes detected were present in this range. Interestingly, there appears to be a lot more clusters of nanoparticles around the cell inner and outer membrane, which was not seen for IrC_6 •AbH •**AuNP25** in HeLa cells. The lifetimes for these clusters can be seen in blue and have been detected in the range of 450 – 590 ns, identifying these as non-aggregated nanoparticles. The fluorescence lifetime images show detection of the short-lived

lifetimes from the gold, which co-localises with the long-lived signal from the iridium(III) complexes. The clustering of nanoparticles can be seen in bright orange in the FLIM image, showing strong signal detected from the gold, which is confirmed by the lifetime decay plot showing the SPR band of the gold. The uptake into HeLa cells for these antibody functionalised nanoprobes showed no clustering of nanoparticles and no lifetimes were detected within the range of 450 – 590 ns. This shows that the uptake of IrC_6 •AbH •**AuNP25** into HUVEC is specific to these endothelial cells. This high clustering around the cell surface could be an indication of selective targeting of the antibody with the CLEC14a, tumour endothelial marker, since this pattern of uptake is only seen within HUVEC cells. Next, the uptake of IrC_6 •SiRNA •**AuNP25** into HUVEC cells was assessed through multiphoton lifetime imaging, to confirm their potential as delivery carriers for gene silencing applications (Figure 5.46).

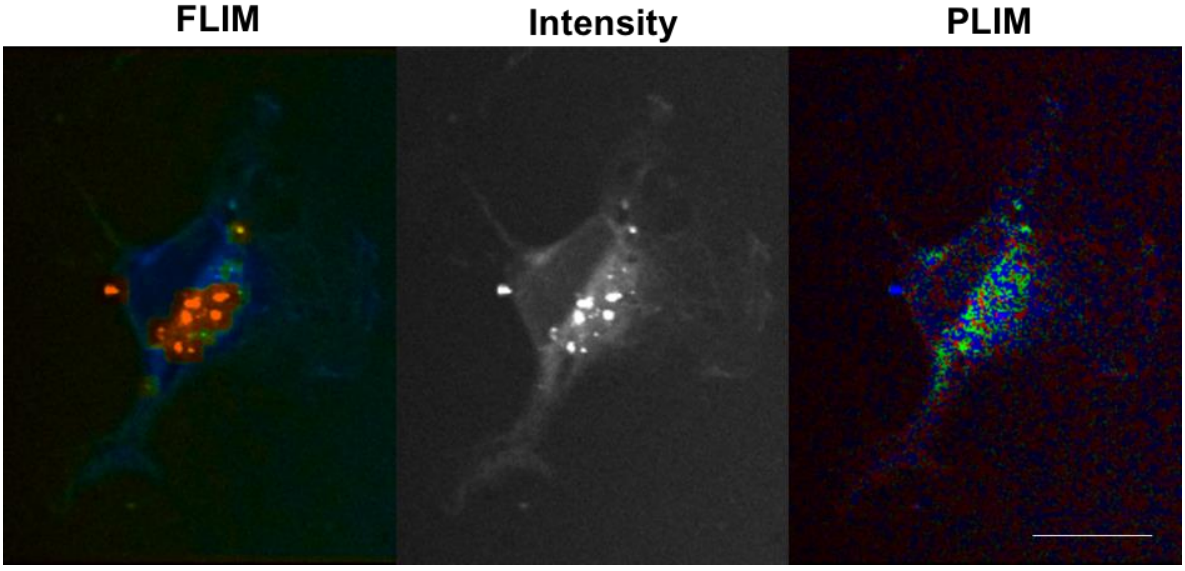

Figure 5.46. Two-photon lifetime images showing detection of the short-lived fluorescence (FLIM) and long-lived phosphorescence (PLIM) lifetimes for multichannel detection in HUVEC cells. HUVEC cells were incubated with 0.3 nM IrC_6 •SiRNA •AuNP25 for 24 hours. (Left) FLIM image showing detection of lifetimes in the range 50 – 2100 ps. (Middle) Intensity image and (Right) Mapped PLIM images showing detection of lifetimes in the range of 700 – 1000 ns (red), 600 – 690 ns (green) and 450 – 590 ns (blue). λ_{exc} = 760 nm, scale bar = 10 µm.

The phosphorescence lifetime images show uptake of IrC_6 •SiRNA •**AuNP25** into HUVEC cells, with mostly long-lived luminescence lifetimes in the range of 450 – 590 ns being detected in the cells. The phosphorescence lifetimes detected were very weak and the binning had to be increased to the maximum to fit the lifetime decays. This differs for the uptake and signal found for IrC_6 •AbH •**AuNP25** in HeLa cells under the same dosing conditions, where strong signal was detected, and lifetimes were mostly in the range of 700 -1000 ns. There appears to be some clusters of nanoparticles within the cytoplasm of HUVEC cells, which can be seen on the fluorescence lifetime image. Analysis of these cluster reveal lifetimes in the range of 450 – 590 ns. This is different for the uptake of IrC_6 •SiRNA •**AuNP25** into HeLa cells were the clusters of nanoparticles showed longer lifetimes in the range of 600 – 690 ns and 700 – 1000 ns. The fluorescence lifetime images show detection of the short-lived lifetimes from the gold, which co-localises with the long-lived signal from the iridium(III) complexes. This confirms uptake of fully functionalised nanoparticles into cancer cells. The clustering of nanoparticles can be seen in bright orange in the FLIM image, and appears to by localised within a small section of the cytoplasm of HUVEC cells. The weak PLIM signal detected for these SiRNA coated nanoparticles suggests ineffective uptake into HUVEC cells after 24 hours. This differs from the uptake seen in HeLa cells where strong PLIM signal could be seen after 24 hours suggesting high uptake into these cells. The inefficient uptake into cancer endothelial cells could be due to the high negative charge on the IrC_6 •SiRNA •**AuNP25,** which was found to be -58 mV in solution. It is known that the surface of vascular endothelial cells is negatively charged,[52] and therefore the inefficient uptake into HUVEC cells could be due to electrostatic repulsion. This has previously been shown where the internalisation of

magnetite nanoparticles into human endothelial cells (HUVEC) was shown to be dependent on the nanoparticles surface charge.[53] They found that the uptake of positively charged nanoparticles into HUVEC cells was much greater than nanoparticles containing a negative surface change. They also found that normal cancer cells the uptake was indifferent to surface charge. This agrees with the results seen for the uptake of IrC_6 •SiRNA •**AuNP25** into HUVEC cells. The last experiment focuses of the uptake of IrC_6 •AbH/SiRNA •**AuNP25** into HUVEC cells, to identify the selective delivery of SiRNA into endothelial cells. (Figure 5.47). However, to fully prove this process is selective, future work would include using positive and negative controls for CLEC14a expressing and non-expressing cells which would be dosed with these nanoparticles.

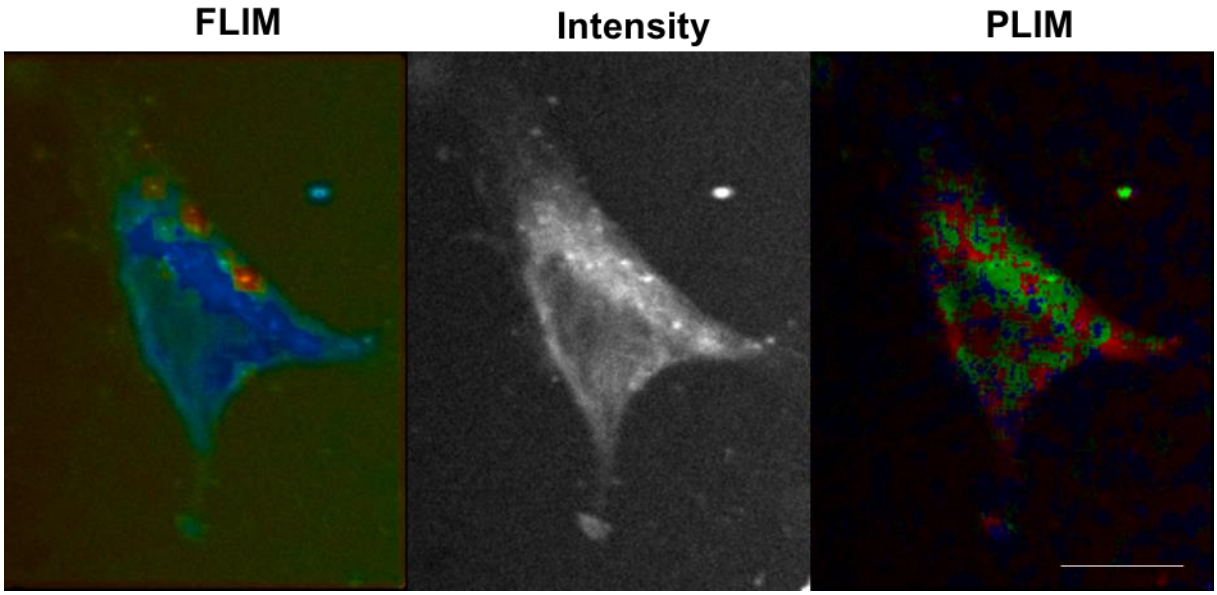

Figure 5.47. Two-photon lifetime images showing detection of the short-lived fluorescence (FLIM) and long-lived phosphorescence (PLIM) lifetimes for multichannel detection in HUVEC cells. HUVEC cells were incubated with 0.2 nM IrC_6 •AbH/SIRNA •AuNP25 for 24 hours. (Left) FLIM image showing detection of lifetimes in the range 40 – 1600 ps. (Middle) Intensity image and (Right) Mapped PLIM images showing detection of lifetimes in the range of 700 – 1000 ns (red), 600 – 690 ns (green) and 450 – 590 ns (blue). λ_{exc} = 760 nm, scale bar = 10 µm.

The phosphorescence lifetime images show uptake of IrC_6 •AbH/SiRNA •**AuNP25** into HUVEC cells, with mostly long-lived luminescence lifetimes in the range of 600 – 690 ns being detected in the cells. There are some areas containing the longer luminescence lifetimes in the range for 700 – 1000 ns (red) within the cell. There are also some shorter lifetimes detected which can be seen in blue. This is similar to the uptake pattern found for IrC_6 •AbH/SiRNA •**AuNP25** in HeLa cells under the same dosing conditions, where the predominant lifetimes in the cells were found to be in the range of 600 – 690 ns. The lifetime images show no clustering of nanoparticles within the HUVEC cells, which was the same for IrC_6 •AbH/SiRNA •**AuNP25** in HeLa cells. However, this is different from the results seen for both IrC_6 •AbH •**AuNP25** and IrC_6 •SiRNA •**AuNP25** in HUVEC cells where visual clustering could be seen in the FLIM images. This could show that SiRNA hinders the antibodies ability to selectively target CLEC14a and therefore the mechanism is not through receptor-mediated internalisation but rather through normal endocytosis of nanoparticles as seen for IrC_6 •AbH/SiRNA •**AuNP25** in HeLa cells. The fluorescence lifetime images show detection of the short-lived lifetimes from the gold, which co-localises with the long-lived signal from the iridium(III) complexes. This confirms uptake of fully functionalised nanoparticles into cancer cells. The lifetime analysis from both the FLIM and PLIM channels revealed strong signal detected for both gold and iridium. This shows efficient uptake of nanoparticles into the HUVEC cells, though not through selective uptake. Since these were preliminary experiments, further work would need to be carried out to identify the true selective targeting abilities of these functionalised nanoparticles into cancer vasculature.

5. 4 Conclusions

Gold nanoparticles were functionalised with monoclonal antibodies and SiRNA for selective targeting of cancer cells. The nanoparticles were synthesised and functionalised with iridium(III) complexes, which have shown to undergo multiphoton excitation and contain long-luminescence lifetimes desirable to lifetime imaging techniques. The photophysical properties of the iridium(III) functionalised nanoprobes revealed long-luminescence lifetimes and high photostability. Their uptake into cancer cells was monitored by multiphoton lifetime imaging where the gold and iridium signal could be detected separately in two channels. The uptake of IrC_6 •AbH •**AuNPs**, IrC_6 •SiRNA •**AuNP25** and IrC_6 •AbH/SiRNA •**AuNP25** into cancer cells was found to be within the cytoplasm of the cells, with high signal detected for both the gold and iridium. Future experiments would have to be designed to identify whether these functionalised gold nanoparticles are localising within endosomes or lysosomes within the cytoplasm. This could be done through confocal and lifetime microscopy by using endosomal and lysosomal cellular stains to look at co-localisation in the fluorescence signal and the lifetime changes within these vesicles. The PLIM images showed long-lived lifetimes mainly present in the range of 700 – 1000 ns and lifetimes which were longer than the functionalised nanoprobes in solution. Investigation of the lifetime was carried out to reveal nuclear uptake of IrC_6 •AbH •**AuNP25,** IrC_6 •SiRNA •**AuNP25** and IrC_6 •AbH/SiRNA •**AuNP25** within HeLa cells. The targeting abilities of these functionalised nanoprobes were investigated within HUVEC cells, which contain CLEC14a on their surface. The results showed uptake of IrC_6 •AbH•**AuNP25**, which showed long-lived luminescence lifetime detected in the cytoplasm of cells. A high degree of clustering could be seen around the cell inner and outer membrane suggesting a difference in

uptake mechanism when compared with IrC_6 •AbH •**AuNP25** in HeLa cells. It was found that the uptake of IrC_6 •SiRNA •**AuNP25** into HUVEC cells was inefficient with weak PLIM signal detected inside the endothelial cells. Lastly, uptake of IrC_6 •AbH/SiRNA •**AuNP25** into HUVEC cells showed similar patterns to that seen for IrC_6 •AbH/SiRNA •**AuNP25** in HeLa cells. There was no clustering of nanoparticles seen around the cell membranes, suggesting the addition of SiRNA to the AbH coated gold nanoparticles, changes the uptake mechanism. These were preliminary experiments to assess uptake into these endothelial cells. This work would be continued to assess the true targeting abilities by looking at uptake of IrC_6 •AbH •**AuNP25** in both HUVEC cells and HUVEC cells over-expressing CLEC14a on their surface membrane. Secondly, live cell time-lapse experiments and lifetime z-stacks would be taken to identify uptake mechanisms and localisation patters within HUVEC cells. To assess delivery of SiRNA into endothelial cells gene knockdown experiments would be carried out. To complete this work, uptake into angiogenic vasculature would be carried out by injecting nanoparticles into tumour bearing mice and two-photon lifetime imaging would be carried out on tumour tissue sections to positively identify selective targeting of tumour vasculature.

5. 5 Experimental section

5. 5. 1 Synthesis of AbH

The method for conjugation of a hydrazide linker to a monoclonal antibody (**AbH**) was based on the nature protocol by Kumar *et al*.[49] CRT3 monoclonal antibody (100μL, 1 mg/ mL^{-1}) was centrifuged in a Vivaspin®6 filter (10 kDa) at 2000 *g* for 3 minutes. Sodium Phosphate (Na_2PO_4, pH 7.5) was added to a final volume of 100 μL. The

antibody was oxidised by adding 10 μL $NaIO_4$ (100 mM) to the solution and left to stir in the dark for 30 minutes at room temperature. The reaction was quenched with PBS (500 μL, 0.1 M, pH 7). A Purpald test was done to confirm oxidation of the carbohydrate. 10 mg Purpald was dissolved in 1mL NaOH (1 mM). The antibody solution (20□μL) was mixed with freshly prepared Purpald solution (60 μL). The solution turned purple after 5 minutes, confirming presence of aldehyde.

Hydrazide linker (2 μL, 46.5 mM) was added to the antibody solution and left to stir in the dark for 1 hour at room temperature. HEPES buffer (1 mL, 40 mM) was added and the entire volume filtered in a Vivaspin®6 tube (10 kDa MWCO) for 5 minutes at 2,000 *g*. The solution was centrifuged in a Vivaspin®6 filter for 5 minutes at 2000 *g*. HEPES buffer (40 mM) was added to a volume of 1 mL and centrifuged at the same conditions, this was repeated 3 times. The remaining solution was made to a final volume of 100 μL in 40 mM HEPES buffer, giving 100 μL/ mL^{-1} **AbH solution**.

5. 5. 2 Synthesis of IrC_6 •AbH •AuNPs

PEG •**AuNP13**. 28 μM PEG-SH (230 mW) in ultrapure water (20μL) was added to 4.5 nM **AuNP13** (2 mL) and sonicated for 15 minutes. This was centrifuged at 10, 000 *g* for 20 minutes, the supernatant was decanted, and the pellet was resuspended in ultrapure water (2 mL) to form PEG •**AuNP13**. $\lambda_{max}(H_2O)$: 520 nm (SPR). Diameter 19 ± 3 nm (DLS number distribution), PDI = 0.21. ζ-potential = - 43 ± 21 mV.

AbH •**AuNP13**. 100 μL/ mL^{-1} **AbH** in HEPES buffer (100μL) was added to 4.5 nM PEG •**AuNP13** (2 mL) and incubated at RT for 1 hour whilst stirring. These nanoparticles were purified using Vivaspin®20 tube (300 kDa MWCO) for 20 minutes at 2, 000 *g.* The supernatant was removed from the bottom of the tube and 1 mL HEPES buffer

added. This was repeated three times to remove any excess antibody in solution, and left in a final volume of 2 mL. This formed 4 nM AbH •**AuNP13**. $\lambda_{max}(H_2O)$: 524 nm (SPR). Diameter 22 ± 7 nm (DLS number distribution), PDI = 0.26. ζ-potential = - 39 ± 21 mV.

IrC_6 •AbH •**AuNP13**. IrC_6 (8 μL, 1 mM) was titrated into 4 nM solution of AbH •**AuNP13** (2 mL) with stirring in between. These nanoparticles were purified using Vivaspin®20 tube (300 kDa MWCO) for 20 minutes at 2, 000 *g.* The supernatant was removed from the bottom of the tube and 1 mL HEPES buffer added. This was repeated three times to remove any excess probe in solution, and left in a final volume of 2 mL forming 3 nM IrC_6 •AbH •**AuNP13**. $\lambda_{max}(H_2O)$: 528 nm (SPR). Diameter 36 ± 12 nm (DLS number distribution), PDI = 0.26. ζ-potential = -28 ± 19 mV. ICP-MS results show 680 complexes per AbH •**AuNP13.**

PEG •**AuNP25**. 28 μM PEG-SH (230 mW) in ultrapure water (20μL) was added to 8 nM **AuNP25** (2 mL) and sonicated for 15 minutes. This was centrifuged at 10, 000 *g* for 20 minutes, the supernatant was decanted and the pellet was resuspended in ultrapure water (2 mL) to form PEG •**AuNP25**. $\lambda_{max}(H_2O)$: 519 nm (SPR). Diameter 21 ± 9 nm (DLS number distribution), PDI = 0.130. ζ-potential = - 44 ± 19 mV.

AbH •**AuNP25**. 100 μL/ mL^{-1} **AbH** in HEPES buffer (100μL) was added to 8 nM PEG •**AuNP13** (2 mL) and incubated at RT for 1 hour whilst stirring. These nanoparticles were purified using Vivaspin®20 tube (300 kDa MWCO) for 20 minutes at 2, 000 *g.* The supernatant was removed from the bottom of the tube and 1 mL HEPES buffer added. This was repeated three times to remove any excess antibody in solution, and left in a final volume of 2 mL. This formed 6 nM AbH •**AuNP25**. $\lambda_{max}(H_2O)$: 521 nm

(SPR). Diameter 28 ± 8 nm (DLS number distribution), PDI = 0.21. ζ-potential = - 36 ± 23 mV.

IrC_6 •AbH •**AuNP25**. IrC_6 (8 μL, 1 mM) was titrated into 6 nM solution of AbH •**AuNP25** (2 mL) with stirring in between. These nanoparticles were purified using Vivaspin®20 tube (300 kDa MWCO) for 20 minutes at 2, 000 *g.* The supernatant was removed from the bottom of the tube and 1 mL HEPES buffer added. This was repeated three times to remove any excess probe in solution, and left in a final volume of 2 mL forming 2 nM IrC_6 •AbH •**AuNP25**. $\lambda_{max}(H_2O)$: 528 nm (SPR). Diameter 38 ± 10 nm (DLS number distribution), PDI = 0.22. ζ-potential = -30 ± 11 mV. ICP-MS results show 800 complexes per AbH •**AuNP25.**

PEG •**AuNP100**. 28 μM PEG-SH (230 mW) in ultrapure water (20μL) was added to 30 pM **AuNP100** (2 mL) and sonicated for 15 minutes. This was centrifuged at 10, 000 *g* for 20 minutes, the supernatant was decanted and the pellet was resuspended in ultrapure water (2 mL) to form PEG •**AuNP100**. $\lambda_{max}(H_2O)$: 554 nm (SPR). Diameter 107 ± 27 nm (DLS number distribution), PDI = 0.025. ζ-potential = - 41 ± 27 mV.

AbH •**AuNP100**. 100 μL/ mL^{-1} **AbH** in HEPES buffer (100μL) was added to 30 pM PEG •**AuNP13** (2 mL) and incubated at RT for 1 hour whilst stirring. These nanoparticles were purified using Vivaspin®20 tube (300 kDa MWCO) for 20 minutes at 2, 000 *g.* The supernatant was removed from the bottom of the tube and 1 mL HEPES buffer added. This was repeated three times to remove any excess antibody in solution, and left in a final volume of 2 mL. This formed 25 pM AbH •**AuNP100**. $\lambda_{max}(H_2O)$: 556 nm (SPR). Diameter 115 ± 28 nm (DLS number distribution), PDI = 0.04. ζ-potential = - 40 ± 26 mV.

IrC_6 •AbH •**AuNP100**. IrC_6 (9 μL, 1 mM) was titrated into 25 pM solution of AbH •**AuNP100** (2 mL) with stirring in between. These nanoparticles were purified using Vivaspin®20 tube (300 kDa MWCO) for 20 minutes at 2, 000 *g.* The supernatant was removed from the bottom of the tube and 1 mL HEPES buffer added. This was repeated three times to remove any excess probe in solution, and left in a final volume of 2 mL forming 15 pM IrC_6 •AbH •**AuNP100**. $\lambda_{max}(H_2O)$: 558 nm (SPR). Diameter 127 ± 32 nm (DLS number distribution), PDI = 0.05. ζ-potential = -40 ± 26 mV. ICP-MS results show 7550 complexes per AbH •**AuNP100.**

5. 5. 3 Synthesis of IrC_6 •SiRNA •AuNPs

SiRNA •**AuNP13**. 100 μM **SiRNA** in HEPES buffer (30μL) was added to 4.5 nM **AuNP13** (2 mL) and incubated at RT for 30 minutes whilst stirring. These nanoparticles were purified using Vivaspin®6 tube (10 kDa MWCO) for 20 minutes at 2, 000 *g.* The supernatant was removed from the bottom of the tube and 1 mL HEPES buffer pH 7.4 was added and centrifuged. This was repeated three times to remove any excess SiRNA in solution, and left in a final volume of 2 mL. This formed 4 nM SiRNA •**AuNP13**. $\lambda_{max}(H_2O)$: 517 nm (SPR). Diameter 24 ± 5 nm (DLS number distribution), PDI = 0.24. ζ-potential = - 68 ± 30 mV.

IrC_6 •SiRNA •**AuNP13**. IrC_6 (20 μL, 1 mM) was titrated into 4 nM solution of SiRNA •**AuNP13** (2 mL) with stirring in between. These nanoparticles were purified using Vivaspin®6 tube (10 kDa MWCO) for 20 minutes at 2, 000 *g.* The supernatant was removed from the bottom of the tube and 1 mL HEPES buffer pH 7.4 was added and centrifuged. This was repeated three times to remove any excess probe in solution, and left in a final volume of 2 mL forming 3 nM IrC_6 •SiRNA •**AuNP13**. $\lambda_{max}(H_2O)$: 525

nm (SPR). Diameter 34 ± 10 nm (DLS number distribution), PDI = 0.25. ζ-potential = -34 ± 25 mV. ICP-MS results show 2400 complexes per AbH •**AuNP13.**

SiRNA •**AuNP25**. 100 μM **SiRNA** in HEPES buffer (30μL) was added to 8 nM **AuNP13** (2 mL) and incubated at RT for 30 minutes whilst stirring. These nanoparticles were purified using Vivaspin®6 tube (10 kDa MWCO) for 20 minutes at 2, 000 *g.* The supernatant was removed from the bottom of the tube and 1 mL HEPES buffer pH 7.4 was added and centrifuged. This was repeated three times to remove any excess SiRNA in solution, and left in a final volume of 2 mL. This formed 6 nM SiRNA •**AuNP25**. $\lambda_{max}(H_2O)$: 519 nm (SPR). Diameter 26 ± 7 nm (DLS number distribution), PDI = 0.19. ζ-potential = - 58 ± 22 mV.

IrC_6 •SiRNA •**AuNP25**. IrC_6 (24 μL, 1 mM) was titrated into 6 nM solution of SiRNA •**AuNP25** (2 mL) with stirring in between. These nanoparticles were purified using Vivaspin®6 tube (10 kDa MWCO) for 20 minutes at 2, 000 *g.* The supernatant was removed from the bottom of the tube and 1 mL HEPES buffer pH 7.4 was added and centrifuged. This was repeated three times to remove any excess probe in solution, and left in a final volume of 2 mL forming 3 nM IrC_6 •SiRNA •**AuNP25**. $\lambda_{max}(H_2O)$: 526 nm (SPR). Diameter 36 ± 13 nm (DLS number distribution), PDI = 0.23. ζ-potential = -35 ± 12 mV. ICP-MS results show 4100 complexes per AbH •**AuNP25.**

SiRNA •**AuNP100**. 100 μM **SiRNA** in HEPES buffer (30μL) was added to 30 pM **AuNP100** (2 mL) and incubated at RT for 30 minutes whilst stirring. These nanoparticles were purified using Vivaspin®6 tube (10 kDa MWCO) for 20 minutes at 2, 000 *g.* The supernatant was removed from the bottom of the tube and 1 mL HEPES buffer pH 7.4 was added and centrifuged. This was repeated three times to remove any excess SiRNA in solution, and left in a final volume of 2 mL. This formed 25 pM

SiRNA •**AuNP100**. $\lambda_{max}(H_2O)$: 551 nm (SPR). Diameter 103 ± 21 nm (DLS number distribution), PDI = 0.04. ζ-potential = - 58 ± 28 mV.

IrC_6 •SiRNA •**AuNP100**. IrC_6 (18 μL, 1 mM) was titrated into 25 pM solution of SiRNA •**AuNP100** (2 mL) with stirring in between. These nanoparticles were purified using Vivaspin®6 tube (10 kDa MWCO) for 20 minutes at 2, 000 *g.* The supernatant was removed from the bottom of the tube and 1 mL HEPES buffer pH 7.4 was added and centrifuged. This was repeated three times to remove any excess probe in solution, and left in a final volume of 2 mL forming 15 pM IrC_6 •SiRNA •**AuNP100**. $\lambda_{max}(H_2O)$: 556 nm (SPR). Diameter 127 ± 32 nm (DLS number distribution), PDI = 0.05. ζ-potential = -38 ± 17 mV. ICP-MS results show 27, 000 complexes per SiRNA •**AuNP100.**

5. 5. 4 Synthesis of IrC_6 •AbH/SiRNA •AuNPs

AbH/SiRNA •**AuNP13**. 100 μL/ mL^{-1} **AbH** in HEPES buffer (30μL) was added to 4 nM SiRNA •**AuNP13** (2 mL) and incubated at RT for 1 hour whilst stirring. These nanoparticles were purified using Vivaspin®20 tube (300 kDa MWCO) for 20 minutes at 2, 000 *g.* The supernatant was removed from the bottom of the tube and 1 mL HEPES buffer added. This was repeated three times to remove any excess antibody in solution, and left in a final volume of 2 mL. This formed 3.5 nM AbH/SiRNA •**AuNP13**. $\lambda_{max}(H_2O)$: 519 nm (SPR). Diameter 35 ± 7 nm (DLS number distribution), PDI = 0.35. ζ-potential = - 36 ± 19 mV.

IrC_6 •AbH/SiRNA •**AuNP13**. IrC_6 (9 μL, 1 mM) was titrated into 3.5 nM solution of AbH/SiRNA •**AuNP13** (2 mL) with stirring in between. These nanoparticles were purified using Vivaspin®20 tube (300 kDa MWCO) for 20 minutes at 2, 000 *g.* The

supernatant was removed from the bottom of the tube and 1 mL HEPES buffer added. This was repeated three times to remove any excess antibody in solution, and left in a final volume of 2 mL forming 3 nM IrC_6 •AbH/SiRNA •**AuNP13**. $\lambda_{max}(H_2O)$: 525 nm (SPR). Diameter 35 ± 7 nm (DLS number distribution), PDI = 0.36. ζ-potential = -31 ± 11 mV. ICP-MS results show 1,000 complexes per AbH/SiRNA •**AuNP13.**

AbH/SiRNA •**AuNP25**. 100 μL/ mL^{-1} **AbH** in HEPES buffer (30μL) was added to 6 nM SiRNA •**AuNP25** (2 mL) and incubated at RT for 1 hour whilst stirring. These nanoparticles were purified using Vivaspin®20 tube (300 kDa MWCO) for 20 minutes at 2, 000 *g.* The supernatant was removed from the bottom of the tube and 1 mL HEPES buffer added. This was repeated three times to remove any excess antibody in solution, and left in a final volume of 2 mL. This formed 3.5 nM AbH/SiRNA •**AuNP25**. $\lambda_{max}(H_2O)$: 519 nm (SPR). Diameter 37 ± 6 nm (DLS number distribution), PDI = 0.32. ζ-potential = - 39 ± 20 mV.

IrC_6 •AbH/SiRNA •**AuNP25**. IrC_6 (21 μL, 1 mM) was titrated into 3.5 nM solution of AbH/SiRNA •**AuNP25** (2 mL) with stirring in between. These nanoparticles were purified using Vivaspin®20 tube (300 kDa MWCO) for 20 minutes at 2, 000 *g.* The supernatant was removed from the bottom of the tube and 1 mL HEPES buffer added. This was repeated three times to remove any excess antibody in solution, and left in a final volume of 2 mL forming 2 nM IrC_6 •AbH/SiRNA •**AuNP25**. $\lambda_{max}(H_2O)$: 525 nm (SPR). Diameter 33 ± 16 nm (DLS number distribution), PDI = 0.36. ζ-potential = -33 ± 16 mV. ICP-MS results show 4,100 complexes per AbH/SiRNA •**AuNP25.**

AbH/SiRNA •**AuNP100**. 100 μL/ mL^{-1} **AbH** in HEPES buffer (30μL) was added to 25 pM SiRNA •**AuNP100** (2 mL) and incubated at RT for 1 hour whilst stirring. These

nanoparticles were purified using Vivaspin®20 tube (300 kDa MWCO) for 20 minutes at 2, 000 *g.* The supernatant was removed from the bottom of the tube and 1 mL HEPES buffer added. This was repeated three times to remove any excess antibody in solution, and left in a final volume of 2 mL. This formed 17 pM AbH/SiRNA •**AuNP100**. $\lambda_{max}(H_2O)$: 558 nm (SPR). Diameter 113 ± 21 nm (DLS number distribution), PDI = 0.36. ζ-potential = - 43 ± 19 mV.

IrC_6 •AbH/SiRNA •**AuNP100**. IrC_6 (12.5 μL, 1 mM) was titrated into 17 pM solution of AbH/SiRNA •**AuNP100** (2 mL) with stirring in between. These nanoparticles were purified using Vivaspin®20 tube (300 kDa MWCO) for 20 minutes at 2, 000 *g.* The supernatant was removed from the bottom of the tube and 1 mL HEPES buffer added. This was repeated three times to remove any excess antibody in solution, and left in a final volume of 2 mL forming 12 pM IrC_6 •AbH/SiRNA •**AuNP100**. $\lambda_{max}(H_2O)$: 560 nm (SPR). Diameter 145 ± 32 nm (DLS number distribution), PDI = 0.06. ζ-potential = -39 ± 15 mV. ICP-MS results show 27,000 complexes per AbH/SiRNA •**AuNP100.**

5. 5. 5 Cell culture and nanoparticle dosing

5. 5. 5. 1. HeLa cells

Human cervical epithelioid cancer cells (HeLa cells) obtained from Public Health England (catalogue number 93021013) were used in all experiments. HeLa cells were maintained and grown in complete Dulbecco's Modified Eagle Medium (DMEM) without phenol red supplemented with 10% Fetal Bovine Serum (FBS), 2 mM glutamine, 100 units/mL penicillin and 0.4 mg/mL streptomycin. Cells were grown as monolayer in vented cap T75 flasks at 37 °C in a humidified atmosphere of 5 % CO_2 incubator. A day prior to dosing with nanoparticles, HeLa cells were counted with

Biorad automated cell counter and viability determined by trypan blue exclusion. Cells were seeded at a density of 100,000 cells per 35 mm MaTek glass dishes and allowed to attach overnight in a humidified 5 % CO_2 atmosphere. For nanoparticle dosing, cell media was removed and the dishes washed twice with phosphate buffered saline (PBS) at pH 7. HeLa cells were dosed for 24 hours for IrC_6 •AbH •**AuNP13** (0.3 nM), IrC_6 •SiRNA •**AuNP13** (0.3 nM), IrC_6 •AbH/SiRNA •**AuNP13** (0.3 nM) IrC_6 •AbH •**AuNP25** (0.2 nM), IrC_6 •SiRNA •**AuNP25** (0.3 nM), IrC_6 •AbH/SiRNA •**AuNP25** (0.2 nM), IrC_6 •AbH •**AuNP100** (1.5 pM), IrC_6 •SiRNA •**AuNP100** (1.5 pM) and IrC_6 •AbH/SiRNA •**AuNP100** (1.2 pM). At the end of each time point, cells were rinsed three times with PBS and imaging was carried out in imaging buffer (HEPES, pH 7).

5. 5. 5. 2. HUVEC cells

HUVEC cells were isolated from umbilical cords. HUVEC cells were extracted, maintained and grown in complete M199 complete media without phenol red and supplemented with 10% Fetal Calf Serum (FCS), 4 mM glutamine, 100 units/mL penicillin, 0.4 mg/mL streptomycin and 10 % endothelial cell growth supplement. HUVEC cells were grown as monolayer in vented cap T75 flasks coated with 1 % gelatin at 37 °C in a humidified atmosphere of 5 % CO_2 incubator. HUVEC cells were passaged 1 in 3 upon reaching 70 – 80 % confluency. A day prior to dosing with nanoparticles, HUVEC cells were seeded at a density of 300,000 cells per 35 mm MaTek glass dishes and allowed to attach overnight in a humidified 5 % CO_2 atmosphere at 37 °C. For nanoparticle dosing, cell media was removed and the dishes washed twice with phosphate buffered saline (PBS) at pH 7. HeLa cells were dosed for 24 hours for IrC_6 •AbH •**AuNP13** (0.3 nM), IrC_6 •SiRNA •**AuNP13** (0.3 nM), IrC_6

•AbH/SiRNA •**AuNP13** (0.3 nM) IrC_6 •AbH •**AuNP25** (0.2 nM), IrC_6 •SiRNA •**AuNP25** (0.3 nM), IrC_6 •AbH/SiRNA •**AuNP25** (0.2 nM), IrC_6 •AbH •**AuNP100** (1.5 pM), IrC_6 •SiRNA •**AuNP100** (1.5 pM) and IrC_6 •AbH/SiRNA •**AuNP100** (1.2 pM). At the end of each time point, cells were rinsed three times with PBS and imaging was carried out in imaging buffer (HEPES, pH 7).

5. 6 References

1 J. Folkman, *Nat. Rev. Drug. Discov.* **2007**, *6*, 273-86.

2 J. Folkman, *J. Pediatr. Surg.* **2007**, *42*, 1-11.

3 A. F. Karamysheva, *Biochem. (Mos) +.* **2008**, *73*, 751-762.

4 N. Nishida, H. Yano, T. Nishida, T. Kamura and M. Kojiro, *Vasc. Health. Risk. Manag.* **2006**, *3*, 213-219.

5 E. B. Brown, R. B. Campbell, Y. Tsuzuki, L. Xu, P. Carmeliet, D. Fukumura and R. K. Jain, *Nat. Med.* **2001**, *7*, 1069-1069.

6 K. A. Khan, J. L. McMurray, F. Mohammed and R. Bicknell, *FEBS. J.* **2019**.

7 S. S. Rho, H. J. Choi, J. K. Min, H. W. Lee, H. Park, H. Park, Y. M. Kim and Y. G. Kwon, *Biochem. Biophys. Res. Commun.* **2011**, *404*, 103-8.

8 S. Krishna Priya, K. Kumar, K. R. Hiran, M. R. Bindhu, R. P. Nagare, D. K. Vijaykumar and T. S. Ganesan, *Int. J. Clin. Oncol.* **2017**, *22*, 107-117.

9 C. W. Lin, M. H. Tsai, S. T. Li, T. I. Tsai, K. C. Chu, Y. C. Liu, M. Y. Lai, C. Y. Wu, Y. C. Tseng, S. S. Shivatare, C. H. Wang, P. Chao, S. Y. Wang, H. W. Shih, Y. F. Zeng, T. H. You, J. Y. Liao, Y. C. Tu, Y. S. Lin, H. Y. Chuang, C. L. Chen, C. S. Tsai, C. C. Huang, N. H. Lin, C. Ma, C. Y. Wu and C. H. Wong, *Proc. Natl. Acad. Sci. U. S. A.* **2015**, *112*, 10611-6.

10 H. Attarwala, *J. Nat. Sci. Biol. Med.* **2010**, *1*, 53-6.

11 M. Boyiadzis and K. A. Foon, *Expert. Opin. Biol. Ther.* **2008**, *8*, 1151-8.

12 Thermofisher in *Vol.* **2019**.

13 D. Banerjee, R. Harfouche and S. Sengupta, *Vasc. Cell.* **2011**, *3*, 3.

14 M. Arruebo, M. Valladares and A. Gonzalez-Fernandez, *J. Nanomater.* **2009**.

15 G. D'Errico, H. L. Machado and B. Sainz, Jr., *Clin. Transl. Med.* **2017**, *6*, 3.

16 K. L. Brogan, K. N. Wolfe, P. A. Jones and M. H. Schoenfisch, *Anal. Chim. Acta.* **2003**, *496*, 73-80.

17 A. K. Trilling, J. Beekwilder and H. Zuilhof, *Analyst.* **2013**, *138*, 1619-27.

18 Nanohybrids in *Antibody conjugation*, *Vol.* **2019**.

19 M. H. Jazayeri, H. Amani, A. A. Pourfatollah, H. Pazoki-Toroudi and B. Sedighimoghaddam, *Sens. Biosensing. Res.* **2016**, *9*, 17-22.

20 R. G. Rayavarapu, W. Petersen, C. Ungureanu, J. N. Post, T. G. van Leeuwen and S. Manohar, *Int J Biomed. Imaging.* **2007**, *2007*, 29817.

21 K. Sokolov, M. Follen, J. Aaron, A. Malpica, R. Lotan and R. Richards-Kortum, *Cancer. Res.* **2003**, *63*, 1999-2004.

22 J. O. Tam, H. de Puig, C. W. Yen, I. Bosch, J. Gomez-Marquez, C. Clavet, K. Hamad-Schifferli and L. Gehrke, *J. Immunoassay. Immunochem.* **2017**, *38*, 355-377.

23 R. F. Dutra and L. T. Kubota, *Clin. Chim. Acta.* **2007**, *376*, 114-20.

24 N. A. Taranova, A. E. Urusov, E. G. Sadykhov, A. V. Zherdev and B. B. Dzantiev, *Microchimica. Acta.* **2017**, *184*, 4189-4195.

25 Z. Alhalili, J. Shapter, D. Figueroa and B. Sanderson, *Drug. Deliv. Lett.* **2018**, *8*, 217-225.

26 X. Gao, Y. Cui, R. M. Levenson, L. W. Chung and S. Nie, *Nat. Biotechnol.* **2004**, *22*, 969-76.

27 R. R. Wakaskar, *Int. J. Drug. Dev. Res.* **2017**, *9*, 37-41.

28 F. Yuan, M. Dellian, D. Fukumura, M. Leunig, D. A. Berk, V. P. Torchilin and R. K. Jain, *Cancer. Res.* **1995**, *55*, 3752-6.

29 W. Li, X. Zhao, B. Du, X. Li, S. Liu, X. Y. Yang, H. Ding, W. Yang, F. Pan, X. Wu, L. Qin and Y. Pan, *Sci. Rep.* **2016**, *6*, 30619.

30 A. Mohajeri, S. Sanaei, F. Kiafar, A. Fattahi, M. Khalili and N. Zarghami, *Adv. Pharm. Bull.* **2017**, *7*, 21-34.

31 W. Li, X. Li, S. Liu, W. Yang, F. Pan, X. Y. Yang, B. Du, L. Qin and Y. Pan, *Int. J. Nanomedicine.* **2017**, *12*, 3509-3520.

32 P. Mukherjee, R. Bhattacharya, P. Wang, L. Wang, S. Basu, J. A. Nagy, A. Atala, D. Mukhopadhyay and S. Soker, *Clin. Cancer. Res.* **2005**, *11*, 3530-4.

33 R. Bazak, M. Houri, S. E. Achy, W. Hussein and T. Refaat, *Mol. Clin. Oncol.* **2014**, *2*, 904-908.

34 I. H. El-Sayed, X. Huang and M. A. El-Sayed, *Nano. Lett.* **2005**, *5*, 829-34.

35 D. Bartczak, O. L. Muskens, T. Sanchez-Elsner, A. G. Kanaras and T. M. Millar, *ACS. Nano.* **2013**, *7*, 5628-36.

36 L. Brannon-Peppas and J. O. Blanchette, *Adv. Drug. Deliv. Rev.* **2004**, *56*, 1649-59.

37 M. A. Behlke, *Oligonucleotides.* **2008**, *18*, 305-319.

38 G. J. Hannon, *Nature.* **2002**, *418*, 244-51.

39 R. Majumdar, K. Rajasekaran and J. W. Cary, *Front. Plant. Sci.* **2017**, *8*, 200.

40 Y. K. Oh and T. G. Park, *Adv. Drug. Deliv. Rev.* **2009**, *61*, 850-862.

41 H. Dana, G. M. Chalbatani, H. Mahmoodzadeh, R. Karimloo, O. Rezaiean, A. Moradzadeh, N. Mehmandoost, F. Moazzen, A. Mazraeh, V. Marmari, M. Ebrahimi, M. M. Rashno, S. J. Abadi and E. Gharagouzlo, *Int. J. Biomed. Sci.* **2017**, *13*, 48-57.

42 Y. Wang, Z. Li, Y. Han, L. H. Liang and A. Ji, *Curr. Drug. Metab.* **2010**, *11*, 182-96.

43 J. Li, Y. C. Chen, Y. C. Tseng, S. Mozumdar and L. Huang, *J. Control. Release.* **2010**, *142*, 416-21.

44 A. M. Ji, D. Su, O. Che, W. S. Li, L. Sun, Z. Y. Zhang, B. Yang and F. Xu, *Nanotechnology.* **2009**, *20*, 405103.

45 K. A. Howard, S. R. Paludan, M. A. Behlke, F. Besenbacher, B. Deleuran and J. Kjems, *Mol. Ther.* **2009**, *17*, 162-8.

46 D. A. Giljohann, D. S. Seferos, A. E. Prigodich, P. C. Patel and C. A. Mirkin, *J. Am. Chem. Soc.* **2009**, *131*, 2072-3.

47 K. Zhang, L. Hao, S. J. Hurst and C. A. Mirkin, *J. Am. Chem. Soc.* **2012**, *134*, 16488-91.

48 Y. Ding, Z. Jiang, K. Saha, C. S. Kim, S. T. Kim, R. F. Landis and V. M. Rotello, *Mol. Ther.* **2014**, *22*, 1075-1083.

49 S. Kumar, J. Aaron and K. Sokolov, *Nat. Protoc.* **2008**, *3*, 314-320.

50 F. Schulz, T. Homolka, N. G. Bastus, V. Puntes, H. Weller and T. Vossmeyer, *Langmuir.* **2014**, *30*, 10779-10784.

51 G. Frens, *Nature-Phys. Sci.* **1973**, *241*, 20-22.

52 F. F. Vargas, M. H. Osorio, U. S. Ryan and M. De Jesus, *Membr. Biochem.* **1989**, *8*, 221-7.

53 T. Osaka, T. Nakanishi, S. Shanmugam, S. Takahama and H. Zhang, *Colloids. Surf. B. Biointerfaces.* **2009**, *71*, 325-30

CHAPTER 6. GENERAL CONCLUSIONS AND FUTURE WORK

IrC_6 was designed based on a previously synthesised iridium(III) complex (**IrbpySS**) in which the phenyl pyridine ligand was modified with a hexyl chain to increase the hydrophobicity of the complex. These iridium(III) complexes were synthesised and characterised by NMR and MS. These iridium(III) complexes showed desirable photophysical properties such as long-lived luminescence lifetimes, emission in the visible range and high photostability. The **IrC_6** complex was found to undergo multiphoton excitation with high two-photon absorption cross-sections. It was found that the complex without the hydrophobic chain (**IrbpySS**) did not undergo multiphoton excitation. The reasons for this are unclear since both complexes displayed similar photophysical properties for absorption, excitation and luminescence lifetimes. This would be fully investigated in future work, to identify the properties of **IrC_6** that causes it to undergo multiphoton excitation whilst **IrbpySS** did not. Since **IrbpySS** did not undergo multiphoton excitation, **IrC_6** was chosen for the multiphoton lifetime imaging experiments and was conjugated to the surface of monodisperse 13 nm, 25 nm and 100 nm gold nanoparticles. The photophysical properties of these luminescent nanoparticles revealed long luminescence lifetimes in the hundreds of nanosecond range, showed emission in the visible range and high photostability in solution.

These iridium(III) coated nanoparticles were investigated as multiphoton lifetime imaging probes. Multiphoton lifetime imaging revealed uptake of these luminescent nanoprobes into cancer cell lines. It was found that detection of the long-lived iridium signal could be completely gated from background autofluorescence. These experiments revealed changes in lifetimes of the iridium(III) coated nanoparticles

depending on where they localised within the cell. This allowed for mapping of localisation patterns based on the long-lived lifetimes from iridium being sensitive to the cell microenvironment. The multiphoton lifetime images showed localisation of the iridium(III) functionalised nanoparticles was mainly within the cytoplasm of cells, but some nuclear localisation was also seen. It was not determined during these experiments if these functionalised nanoparticles were localising within vesicles (endosomes or lysosomes) or free within the cytoplasm of the cells. For future work, this would be investigated using endosomal and lysosome markers, which would allow for visualisation of the uptake of nanoparticles into these cellular compartments through changes in the iridium(III) lifetimes (multiphoton lifetime imaging) or co-localisation in fluorescence (confocal microscopy).

The fluorescence lifetime images revealed strong signal from the gold, by detecting the SPR band in the lifetime decay. This allowed for detection of the iridium signal in one channel, and the gold signal in a separate channel. This is the first time multichannel detection of short-lived and long-lived signals has been done. With this technique, the short-lived lifetimes from the gold and the long-lived lifetimes from the iridium(III) complex could be overlaid to reveal uptake of fully coated nanoprobes into cancer cells. The phosphorescence lifetime images showed longer lifetimes detected within the cells than seen for the metal complex and luminescent nanoprobes in solution. Lifetime analysis revealed the extension in luminescence lifetime was due to the nanoprobes interactions with biomolecules such as proteins within the cells.

Upon successful application of these iridium(III) coated nanoprobes as multiphoton lifetime imaging probes, their targeting abilities were assessed. For these experiments

gold nanoparticles were functionalised with monoclonal antibodies which selectively targeted the tumour endothelial marker, CLEC14A and SiRNA molecules for targeted delivery into endothelial cells. Lifetime imaging revealed uptake of these functionalised nanoprobes into both cancer cells and endothelial cells. Long luminescence lifetimes were detected within the cytoplasm and nucleus of the cancer cells. Investigation of the selective targeting towards CLEC14A on the surface of endothelial cells was done on 25 nm gold nanoparticles. These preliminary results looked promising with long and short lived signals being detected in two separate channels. The lifetime images revealed that the uptake of gold nanoparticles was mainly within the cytoplasm of the endothelial cells with no aggregation occurring upon uptake. The antibody functionalised nanoprobes showed localisation around the membrane, proposing interactions of the antibody with CLEC14A present on the surface of the endothelial cells. Nanoprobes coated with SiRNA showed weak signal detected within the cells, possibly due to the high negative charge of the nanoparticles. The nanoprobes functionalised with both biomolecules showed a different pattern of uptake in comparison to the antibody only functionalised nanoprobes. This could be due to the SiRNA molecule hindering the antibodies selectivity towards the endothelial marker. Further work would need to be carried out to assess the true targeting and delivery mechanism of these functionalised nanoprobes. To investigate the selective delivery of SiRNA, SiRNA gene knockdown experiments would need to be designed. To assess these nanoparticles targeting abilities, uptake into angiogenic tumour vasculature would also need to be carried out. This would involve tumour bearing mice being injected with iridium(III) functionalised gold nanoparticles and two-photon lifetime imaging being carried out on tumour tissue sections to positively identify selective

targeting of tumour vasculature. The ability for multiphoton lifetime imaging to detect extensions in the long-lived iridium signal based on changes in the microenvironment, alongside detection of the short-lived signal from the gold in a separate channel proves the power of using this technique for multichannel detection of luminescent nanoprobes.

7. APPENDIX

NMR and Mass Spectra

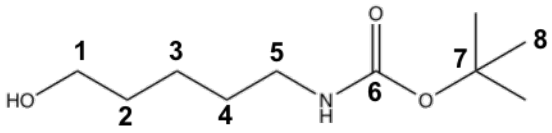

Figure 7.1. Structure of N-(Boc)-5-amino-1-pentanol

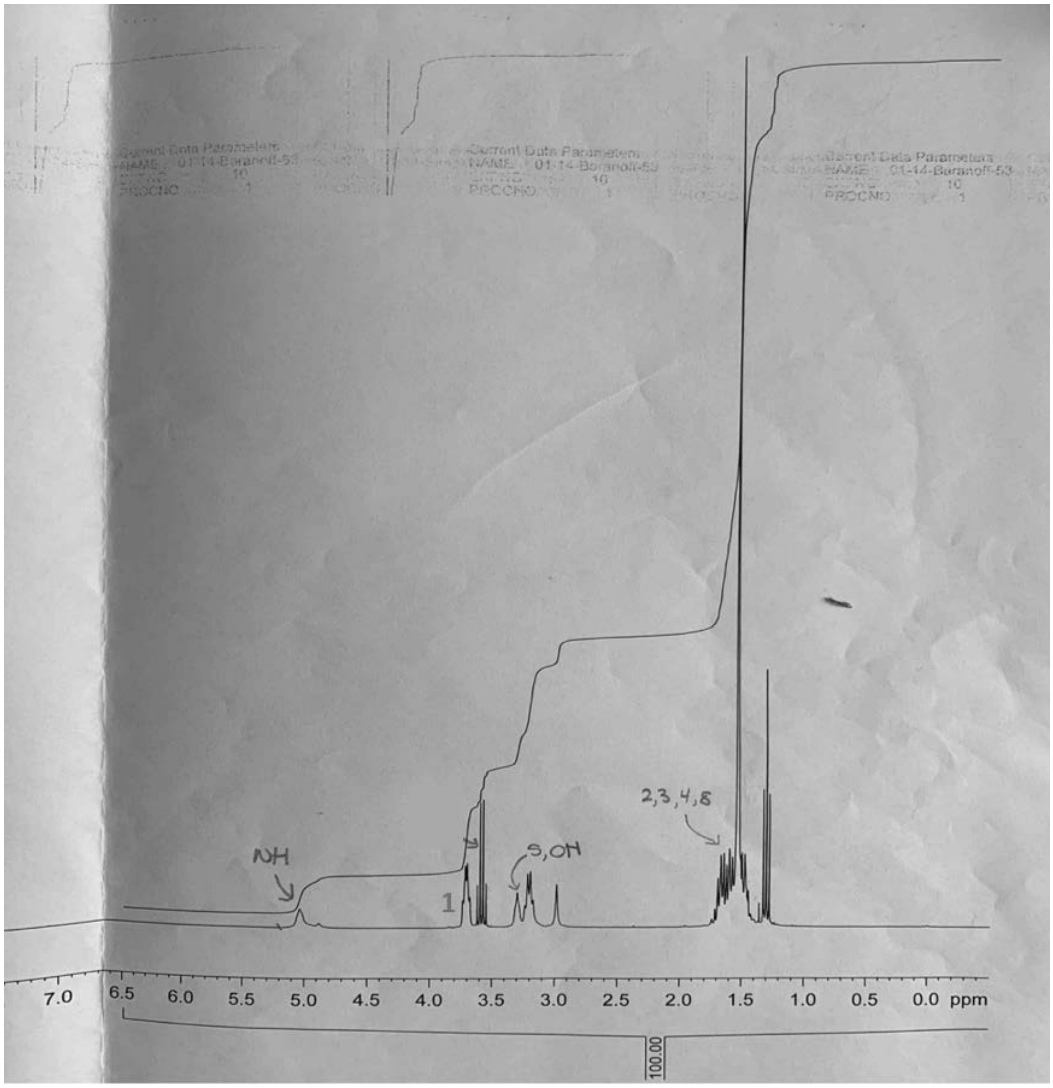

Figure 7.2. ^{1}H NMR N-Boc-5-amino-1-pentanol ($CDCl_3$).

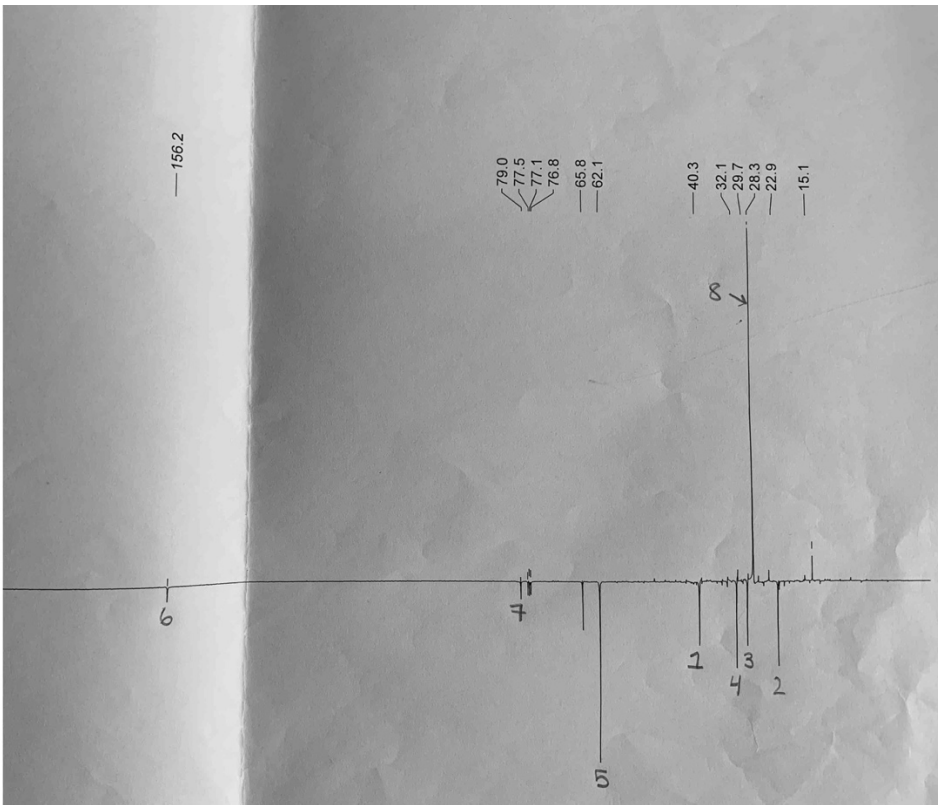

Figure 7.3. ^{13}C NMR N-Boc-5-amino-1-pentanol ($CDCl_3$).

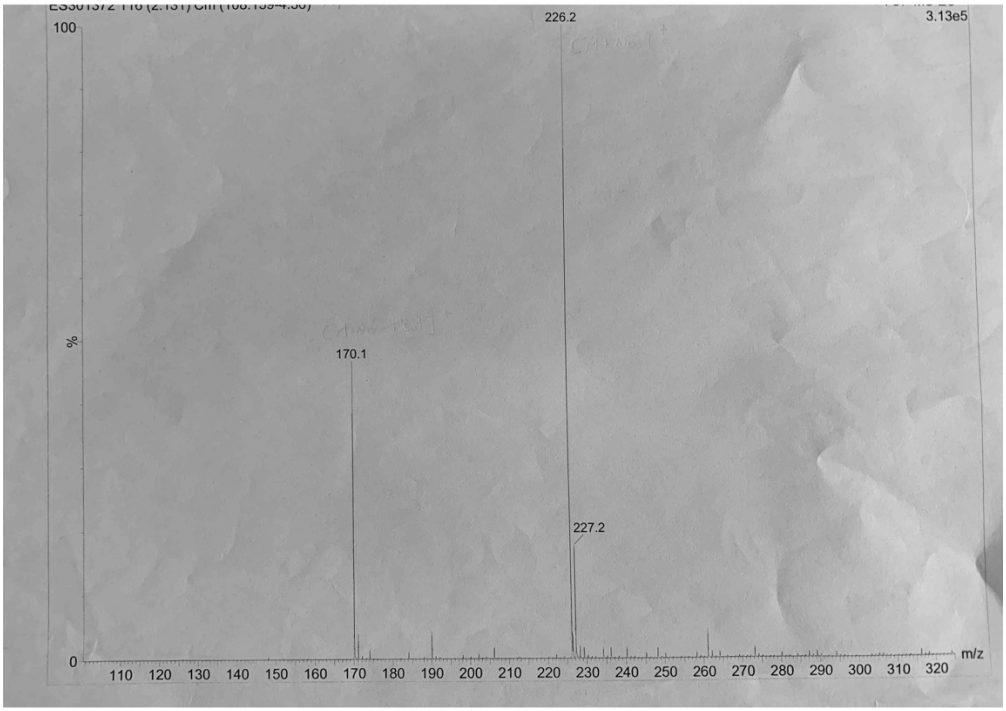

Figure 7.4. MS N-Boc-5-amino-1-pentanol.

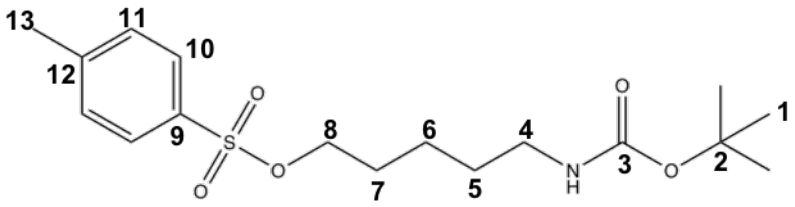

Figure 7.5. Structure of N-(Boc)-5-amino-1-tosylpentane

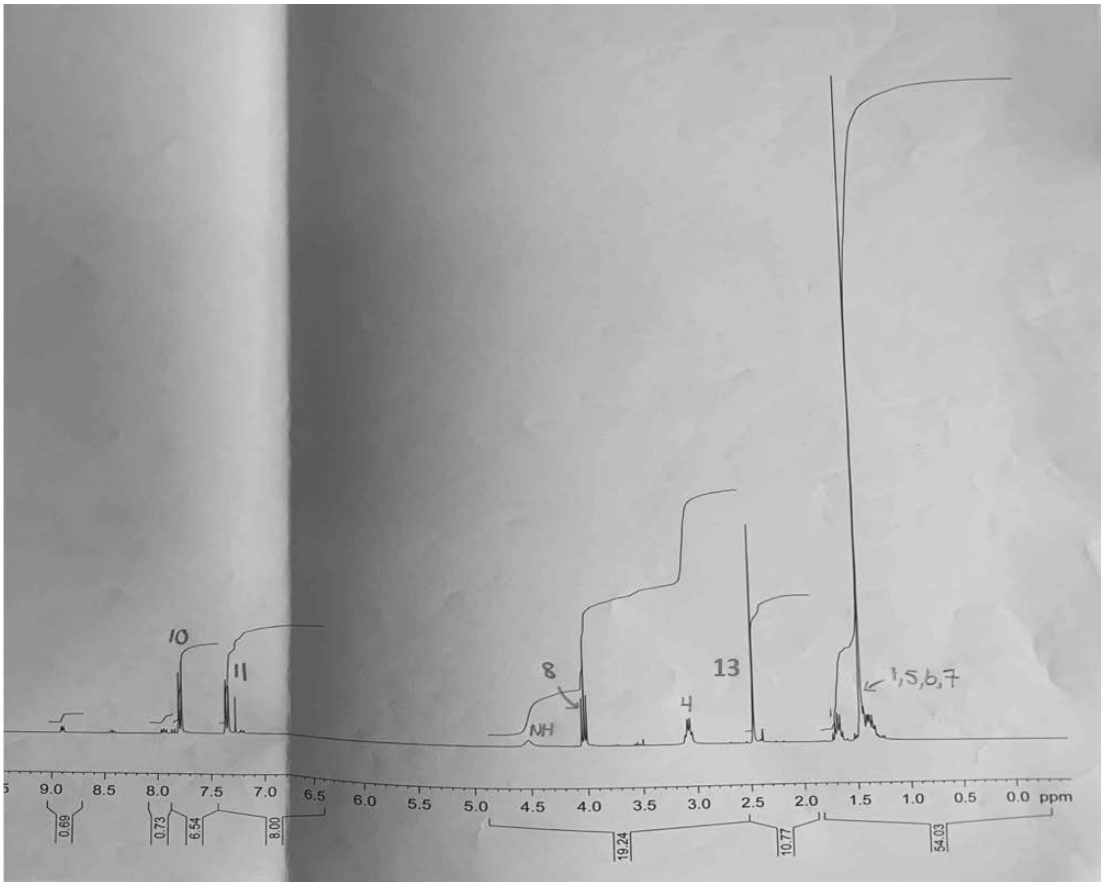

Figure 7.6. ^{1}H NMR N-(Boc)-5-amino-1-tosylpentane ($CDCl_3$).

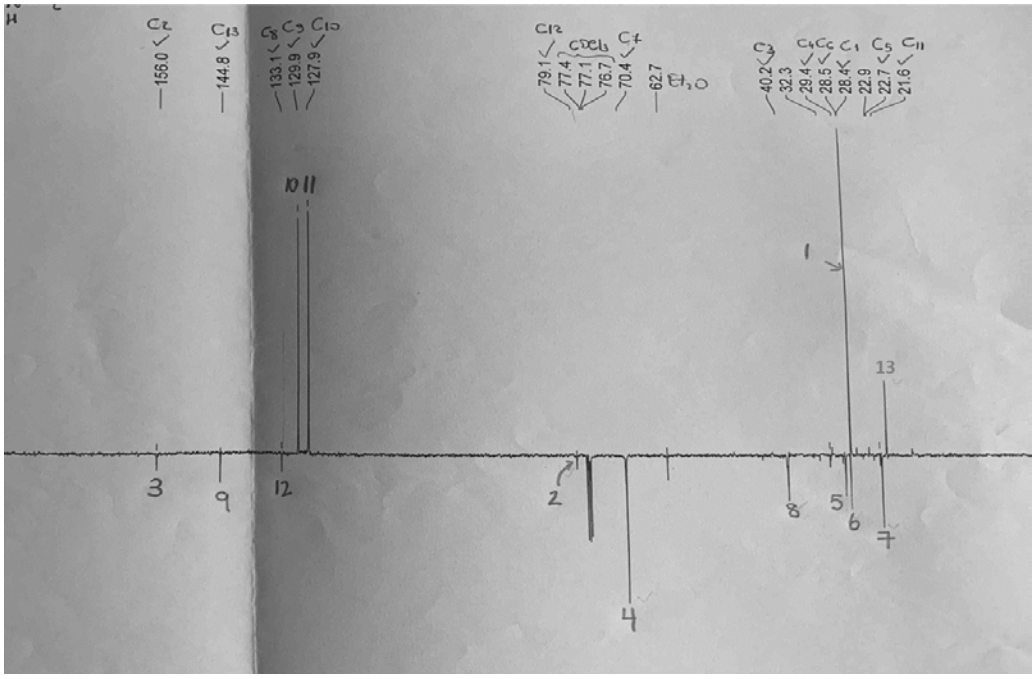

Figure 7.7. ^{13}C NMR N-(Boc)-5-amino-1-tosylpentane ($CDCl_3$).

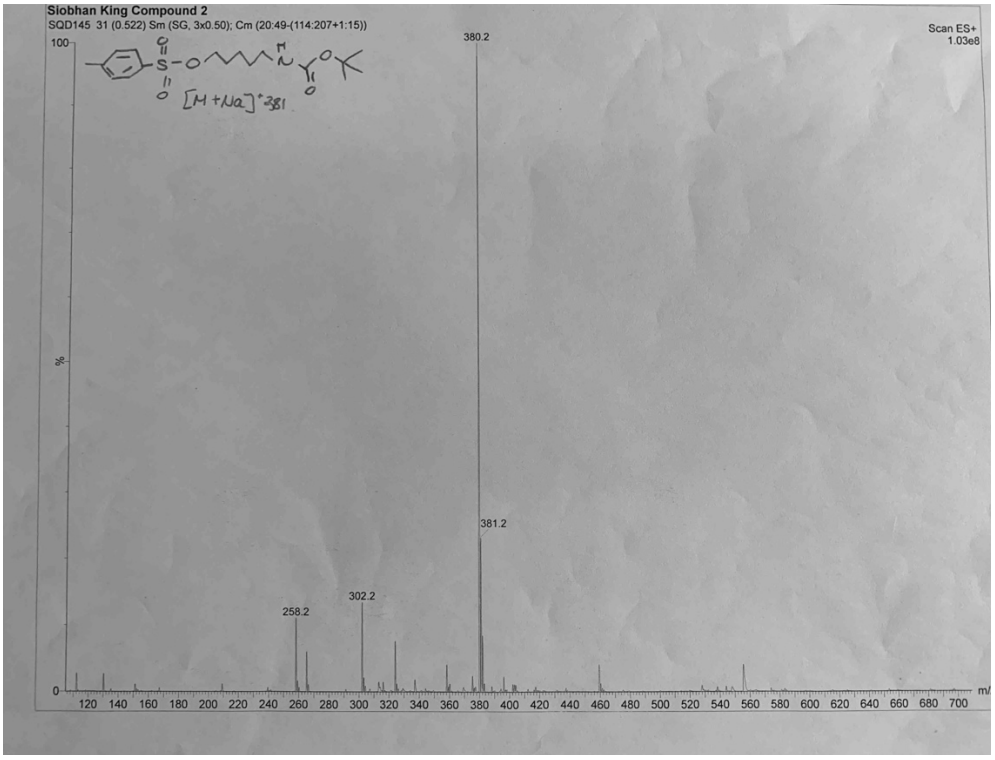

Figure 7.8. MS N-(Boc)-5-amino-1-tosylpentane

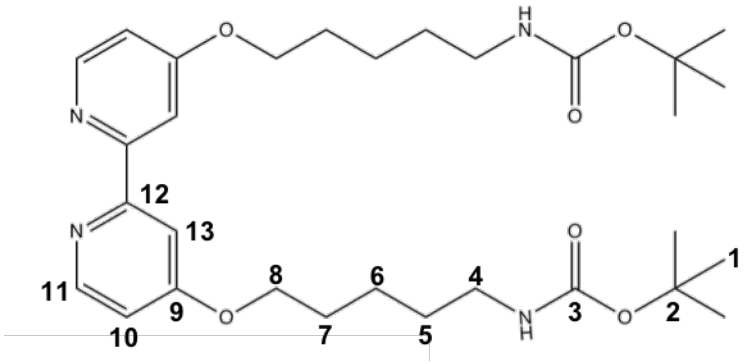

Figure 7.9. Structure of 4,4'-di-(N-(Boc)-5-amino-1-pentoxy)-2,2'-bipyridine

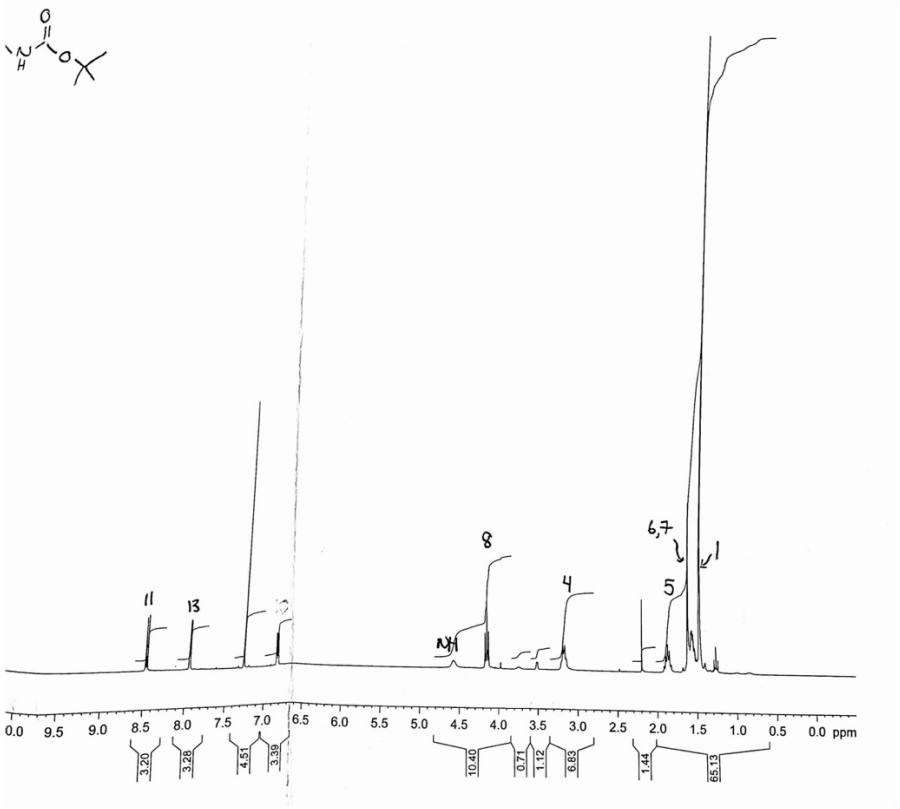

Figure 7.10. ^{1}H NMR 4,4'-di-(N-(Boc)-5-amino-1-pentoxy)-2,2'-bipyridine ($CDCl_3$).

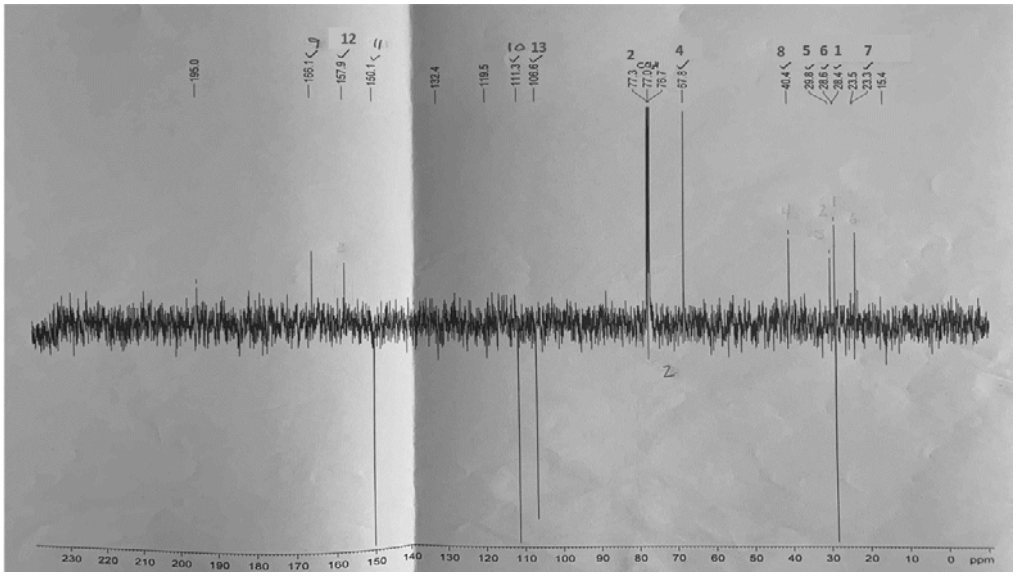

Figure 7.11. ^{13}C NMR 4,4'-di-(N-(Boc)-5-amino-1-pentoxy)-2,2'-bipyridine ($CDCl_3$).

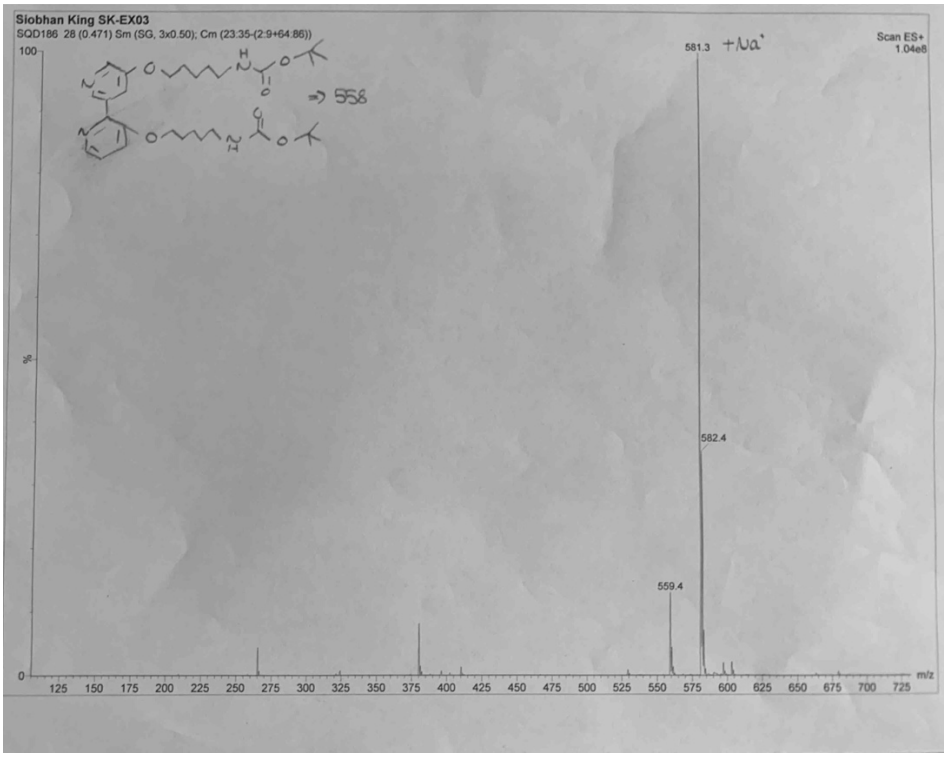

Figure 7.12. MS 4,4'-di-(N-(Boc)-5-amino-1-pentoxy)-2,2'-bipyridine

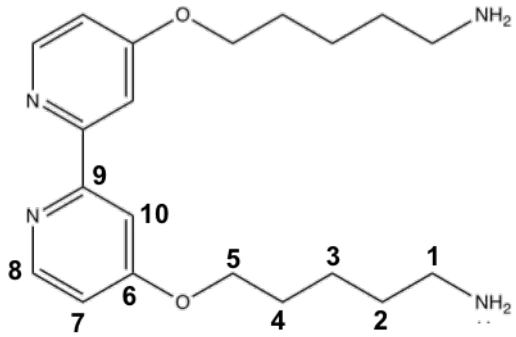

Figure 7.13. Structure of 4,4'-di-(5-amino-1-pentoxy)-2,2'-bipyridine

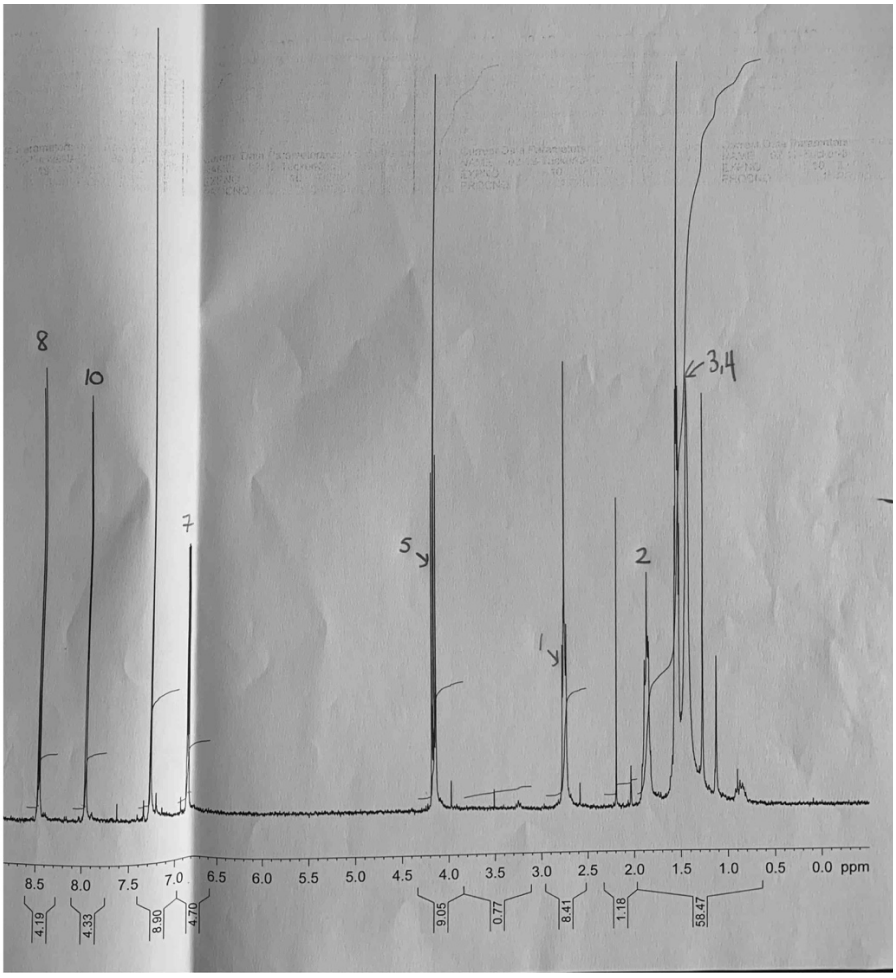

Figure 7.14. ^{1}H NMR 4,4'-di-(5-amino-1-pentoxy)-2,2'-bipyridine ($CDCl_3$).

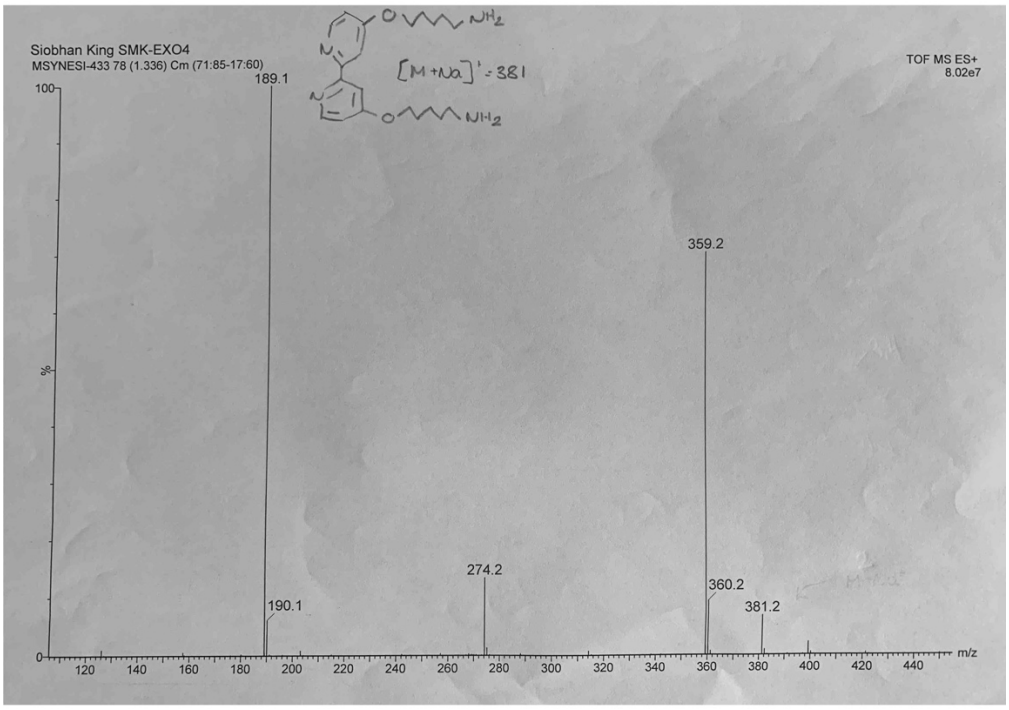

Figure 7.15. MS 4,4'-di-(5-amino-1-pentoxy)-2,2'-bipyridine ($CDCl_3$).

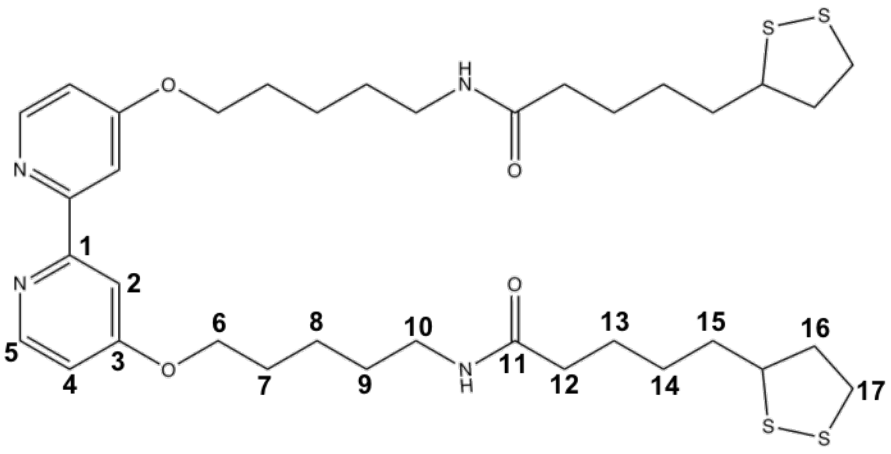

Figure 7.16. Structure of 4,4'-di-(5-lipoamido-1-pentoxy)-2,2'-bipyridine (bpySS)

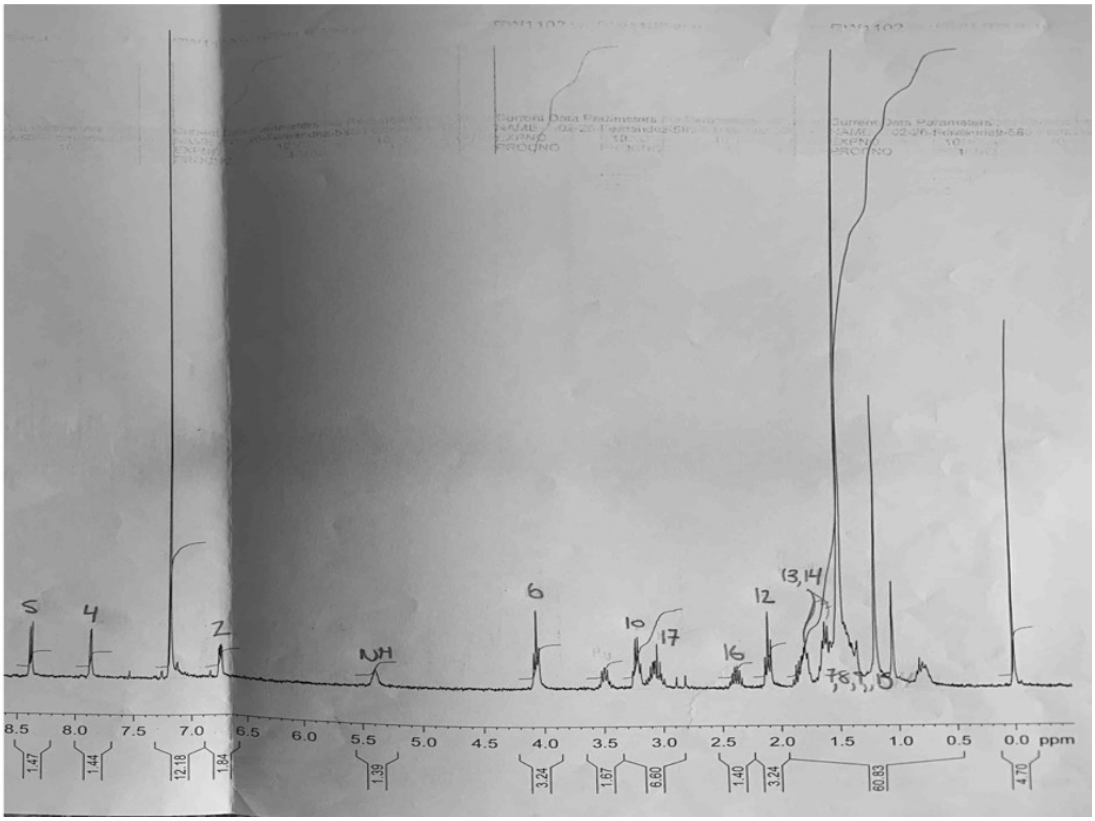

Figure 7.17. ^{1}H NMR 4,4'-di-(5-lipoamido-1-pentoxy)-2,2'-bipyridine (bpySS) ($CDCl_3$).

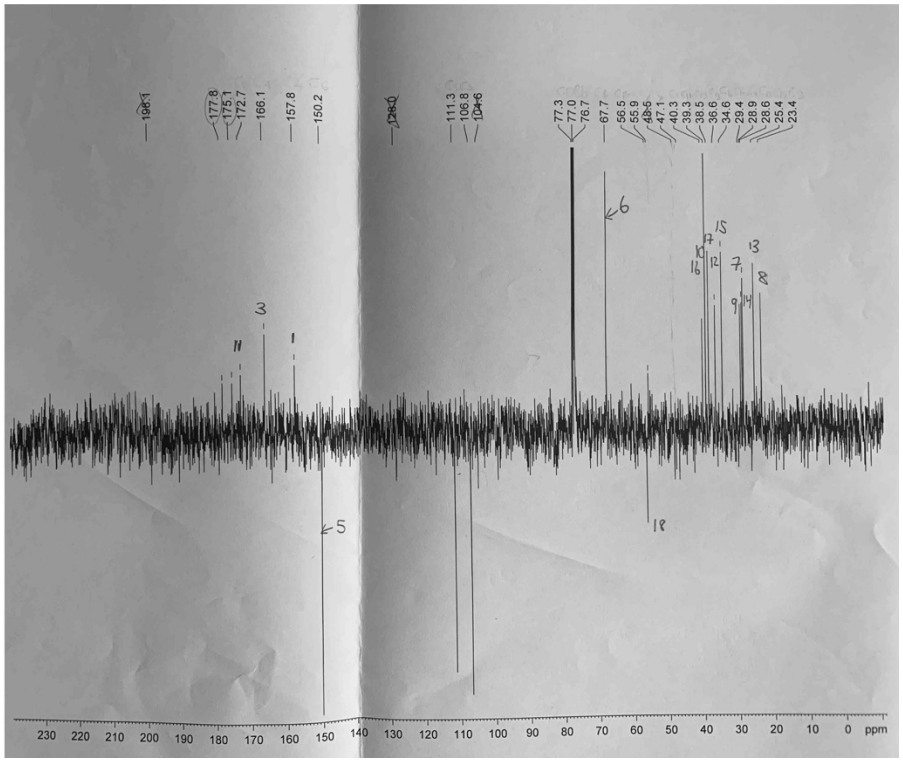

Figure 7.18. ^{13}C NMR 4,4'-di-(5-lipoamido-1-pentoxy)-2,2'-bipyridine (bpySS) ($CDCl_3$).

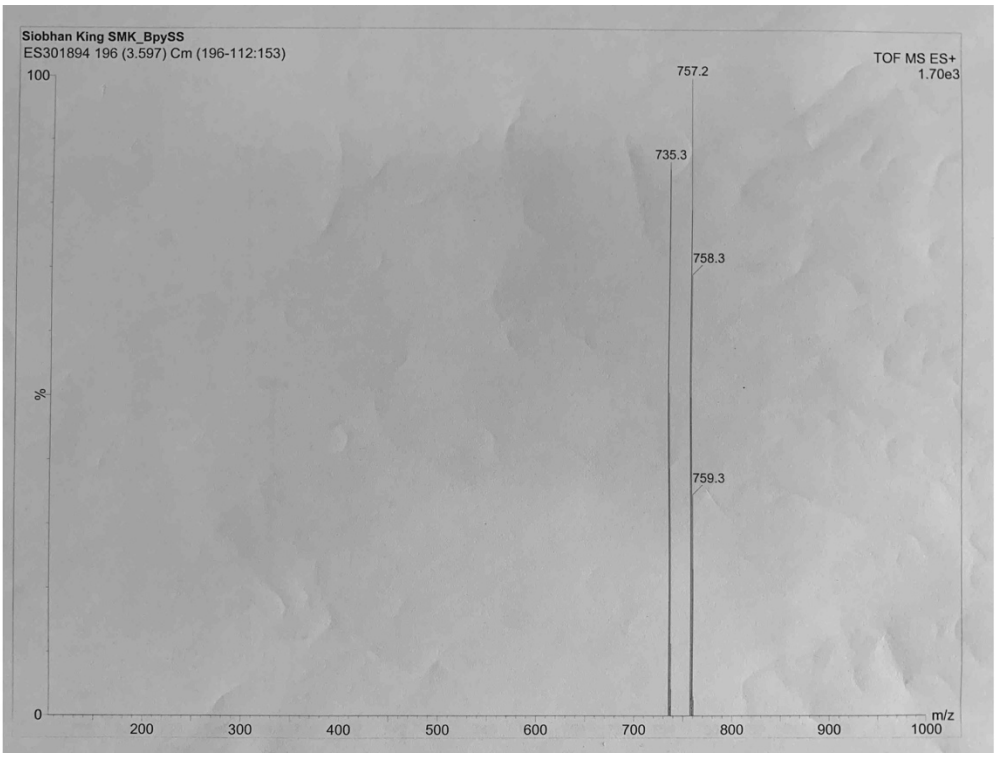

Figure 7.19. MS 4,4'-di-(5-lipoamido-1-pentoxy)-2,2'-bipyridine (bpySS) ($CDCl_3$).

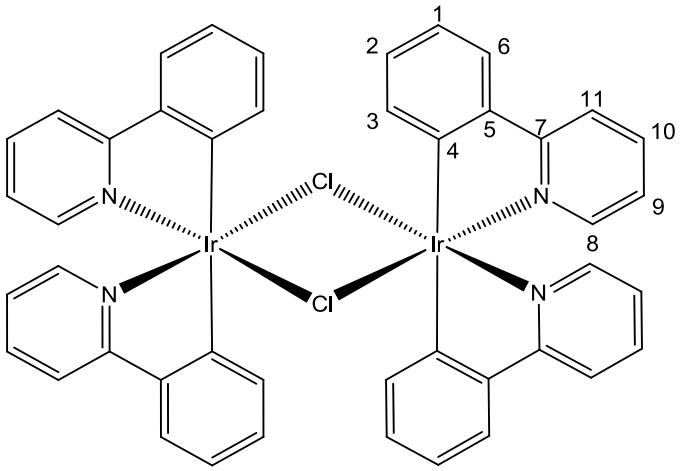

Figure 7.20. Structure of Tetrakis(2-phenylpyridine-*C2,N'*)(μ-dichloro)diiridium (Iridium dimer)

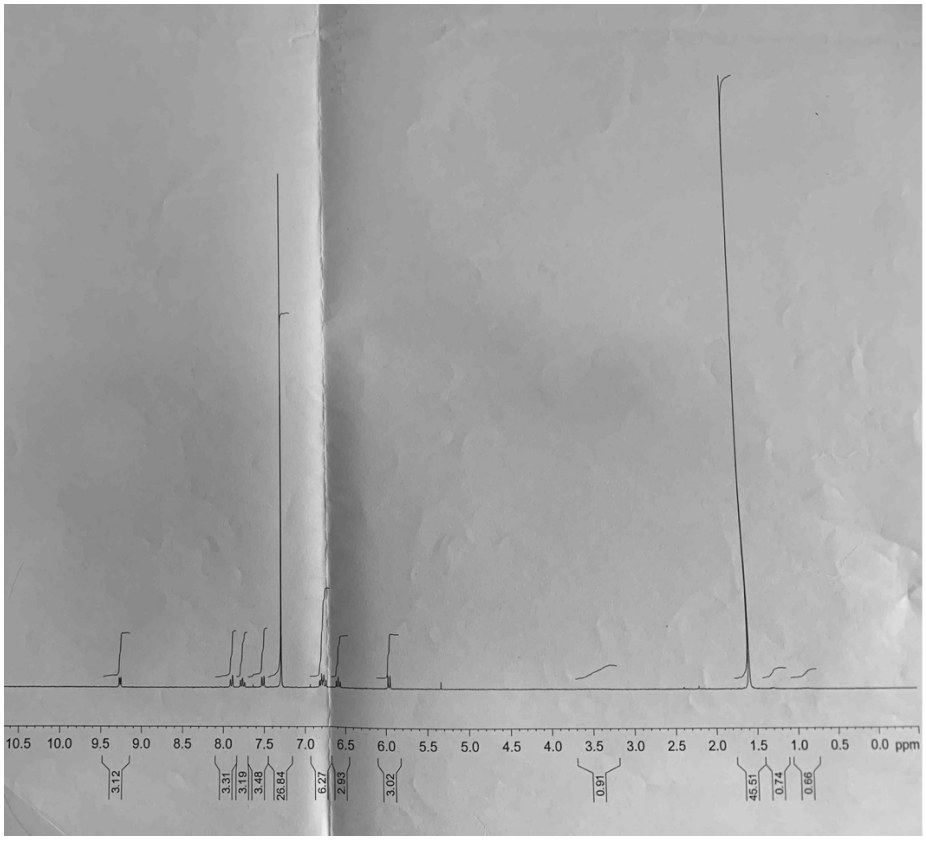

Figure 7.21. ^{1}H NMR iridium dimer ($CDCl_3$).

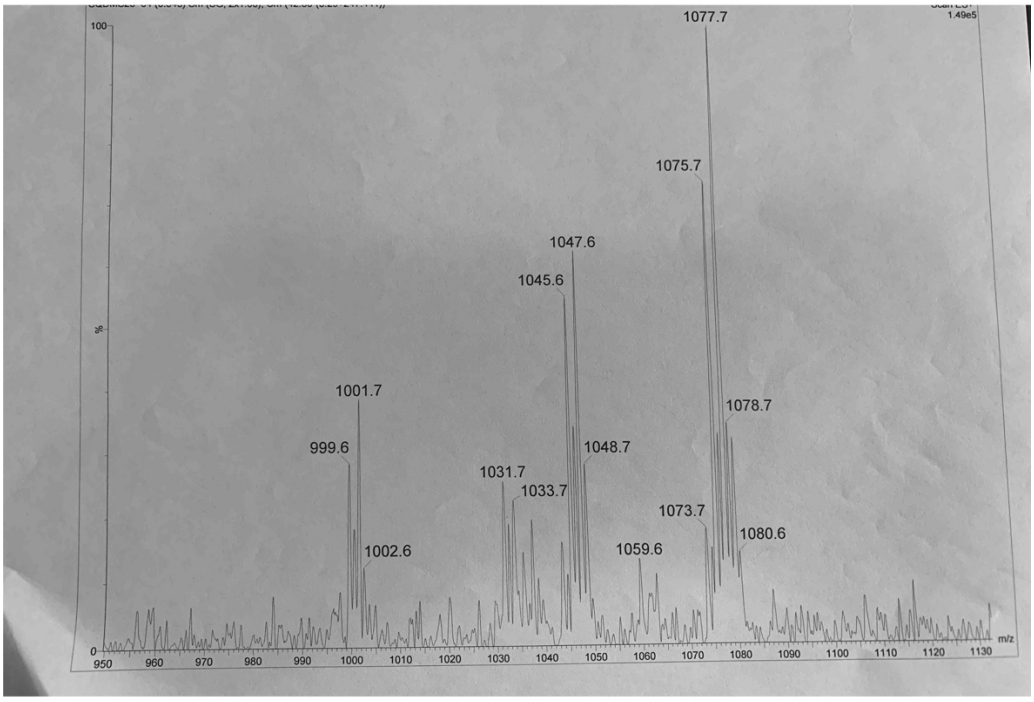

Figure 7.22. MS iridium dimer ($CDCl_3$).

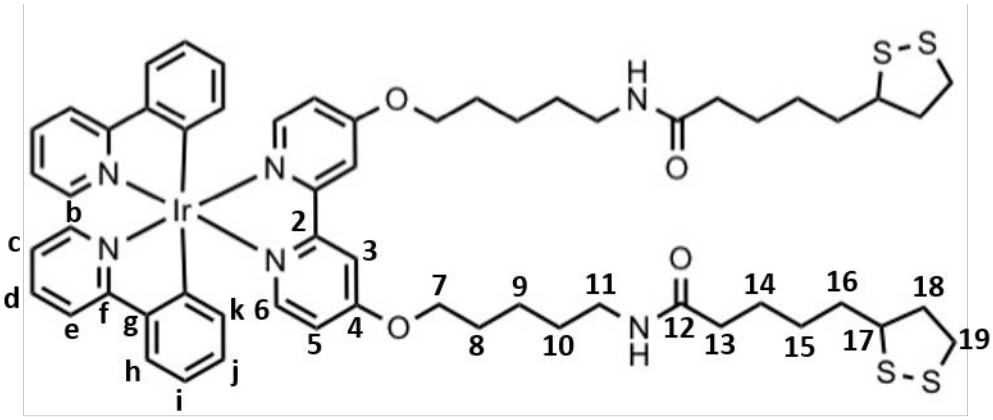

Figure 7.23. Structure of IrbpySS

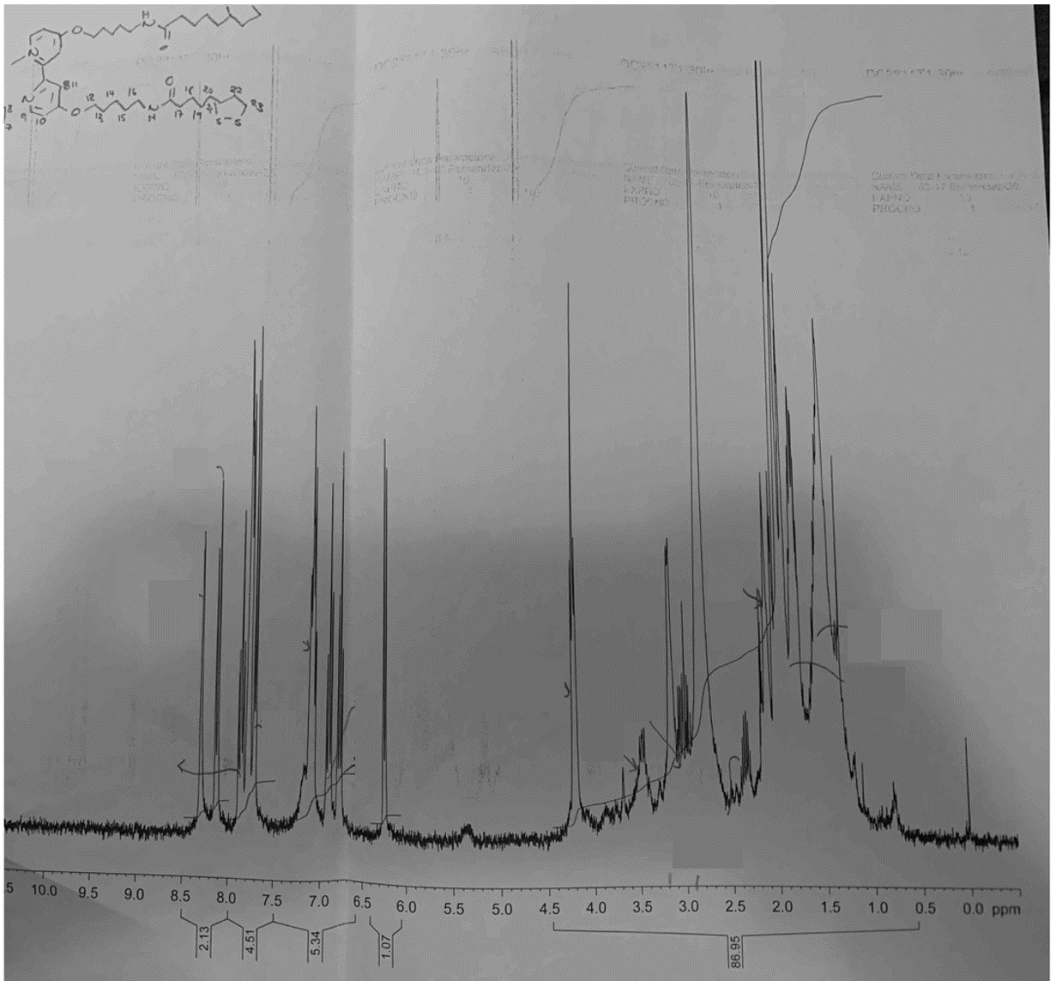

Figure 7.24. ^{1}H NMR IrbpySS (d^{6}-acetone).

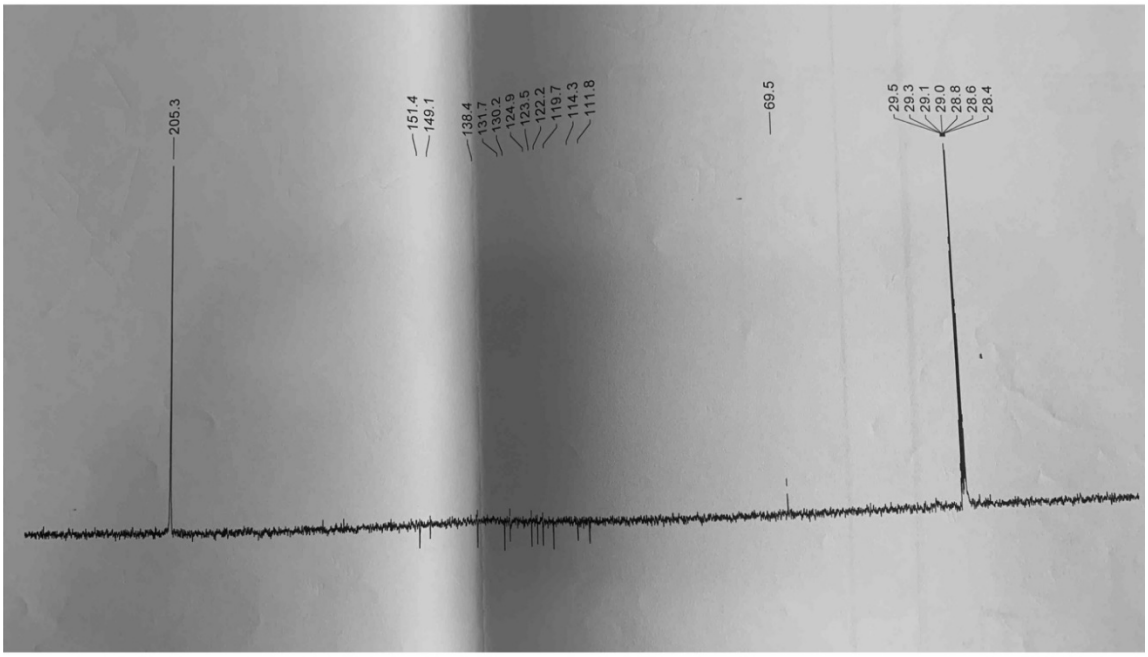

Figure 7.25. ^{13}C NMR IrbpySS (d^6-acetone).

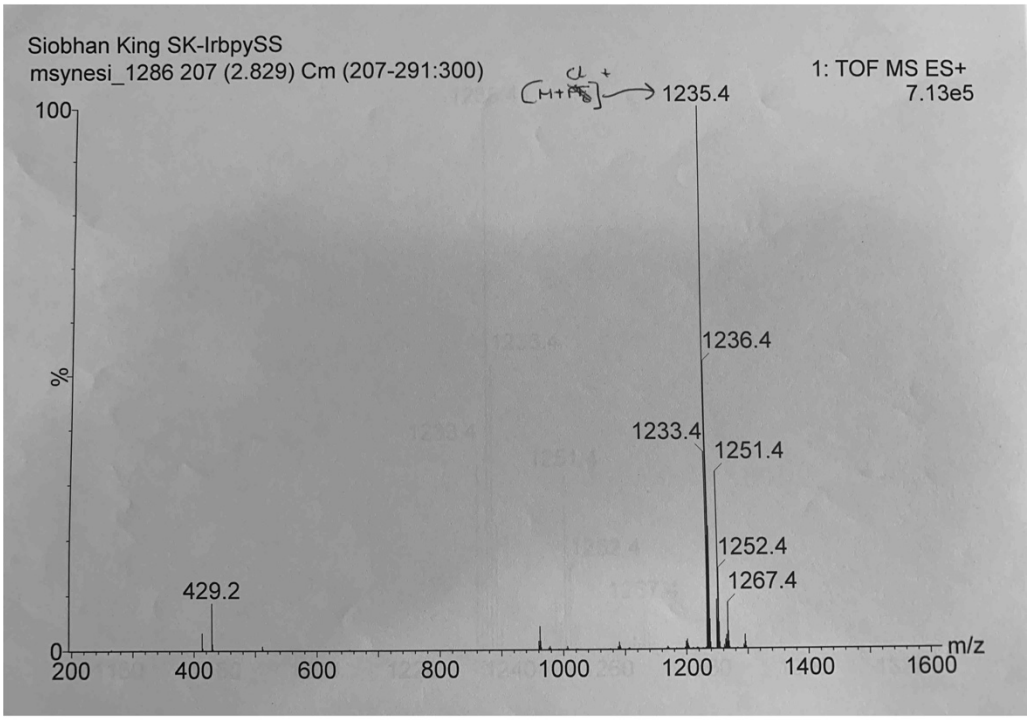

Figure 7.26. MS NMR IrbpySS

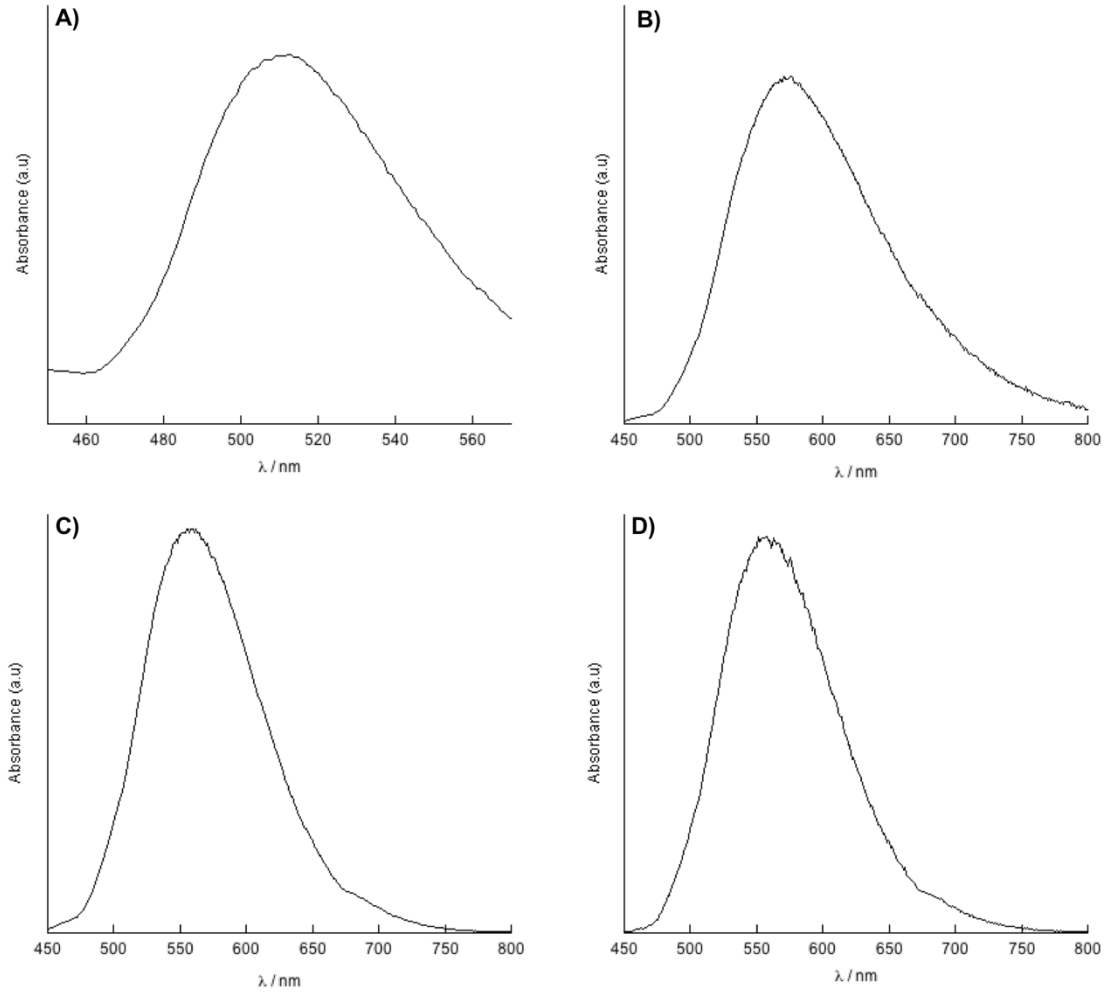

Figure 7.27. Steady-state emission spectrum (A) 30 μM IrbpySS λ_{exc} = 375 nm, (B) 30 μM IrbpySS λ_{exc} = 405 nm, (C) 30 μM IrC_6 λ_{exc} = 375 nm and (D) 30 μM IrC_6 λ_{exc} = 405 nm. Spectra corrected for PMT and instrument response.

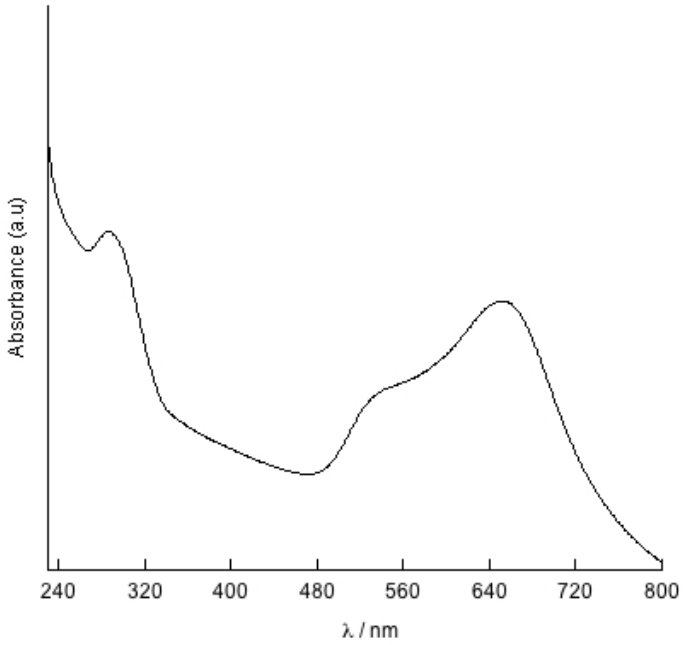

Figure 7.28. Aggregated nanoparticles. Absorption spectra of IrC_6 •AuNP25 in water after visual aggregation in solution by turning from red to purple. Particles show clear aggregation with the SPR λ_{max} shifting from 525 nm to 654 nm along with peak broadening.

Figure 7.29. Calculation of Number of AuNP per cell using ICPMS[5-6]

$$N = \frac{\pi}{6} \frac{(\rho D^3)}{M} N_A$$

$$N = 30.89602\ D^3$$

Where:

N is the number of Atoms per AuNP

ρ is the density of gold (19.3 g/cm^3)

D is the core diameter of the AuNPs taken from TEM (nm)

M is the atomic weight of gold (197 g/mol[1])

N_A is Avogadro constant (6.02 x 10^{23} mol^{-1})

Nanoparticle Diameter (nm)	Number of Gold atoms per AuNP (N)
15	1.04×10^5
25	4.82×10^5
95	2.64×10^7

Calculating number of AuNPs per HeLa cell using data from ICP-MS

Concentrations detected in ICP-MS were 77 μg/L, 172 μg/L and 1485 μg/L for IrC_6 •**AuNP13**, IrC_6 •**AuNP25** and IrC_6 •**AuNP100** respectively.

$$Number\ of\ Gold\ atoms = \left(\frac{concentration\ (g/ml)}{atomic\ weight\ (g/mol)}\right) x\ N_A$$

Number of gold atoms calculated: 7.04×10^{14}, 1.57×10^{15} and 1.36×10^{16} for IrC_6 •**AuNP13**, IrC_6 •**AuNP25** and IrC_6 •**AuNP100** respectively.

Number of gold atoms to for one AuNP:

$$Number\ of\ AuNPs = \frac{Number\ of\ Gold\ Atoms}{N}$$

Number of AuNPs calculated: 6.7×10^9, 3.26×10^9 and 5.13×10^8 for IrC_6 •**AuNP13**, IrC_6 •**AuNP25** and IrC_6 •**AuNP100** respectively.

Number of AuNPs per cell:

$$Number\ of\ AuNPs\ per\ cell = \frac{Number\ of\ AuNPs}{1\ x\ 10^5}$$

Number of AuNPs per cell (1×10^5) was calculated: 67,000, 26,000 and 5100 for IrC_6 •**AuNP13**, IrC_6 •**AuNP25** and IrC_6 •**AuNP100** respectively.

Figure 7.30. Quantum Yield Calculations

Spectral scans of the emission region (E), recorded from 450 – 700 nm and excitation scatter region (S), recorded from 365 – 385 nm of the sample (s) and reference standard or solvent (r).

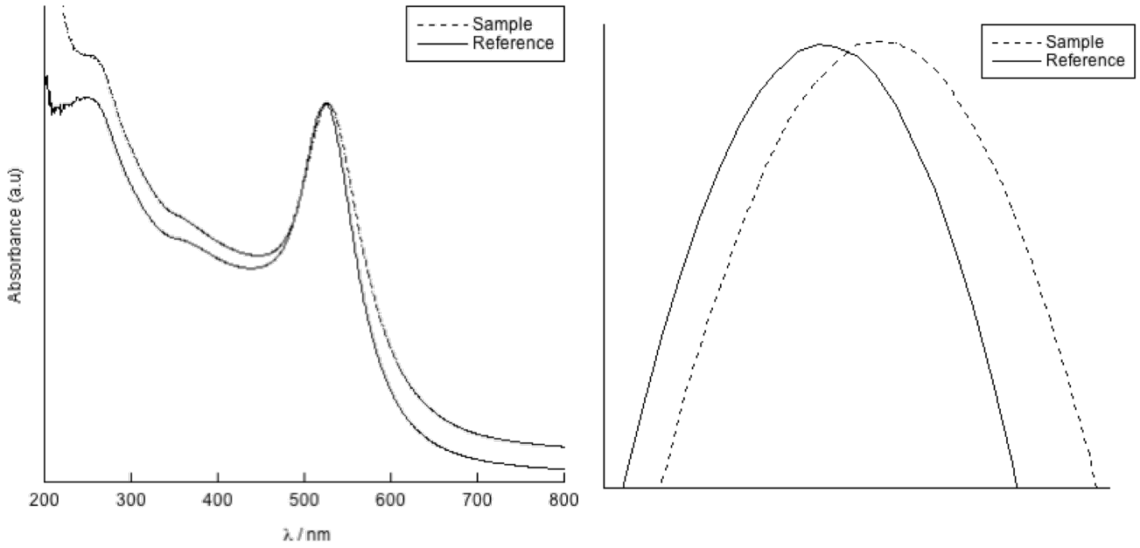

Figure 7.31. Absorption spectra of (left) sample, IrC_6 •AuNP25 (dotted line) and reference, Z •AuNP25 (solid line). (Right) Expanded region showing SPR overlap of sample and reference.

Quantum yield experiments were carried out using an integrated sphere attachment on Edinburgh Instruments FLS920 spectrometer, the equation above is applied for calculating the Quantum Yield. For molecular complex a sample of IrC_6 in water (1% MeOH in water) and reference solvent of 1% MeOH in water was used. A different method was applied for the functionalised gold nanoparticles. A sample of IrC_6 •**AuNPs** and a reference standard of Z •**AuNP2**5 was used. The reference standard was diluted until the SPR peak of the gold matched that of the sample SPR peak, which was confirmed by UV/Vis absorption.

$$\eta = \frac{E_s - E_r}{S_r - S_s}$$

Spectral scans of the emission region (E), recorded from 450 – 700 nm and excitation scatter region (S), recorded from 365 – 385 nm of the sample (s) and reference standard or solvent (r).

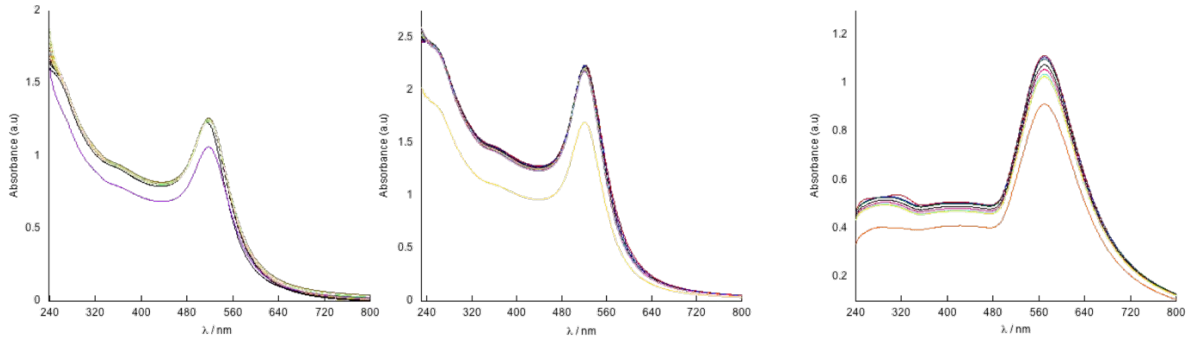

Figure 7.32. UV/Vis showing purified AbH •AuNPs for (left) 4 nM AbH •AuNP13, (middle) 6 nM AbH •AuNP25 and (right) 25 pm AbH •AuNP100 in water.

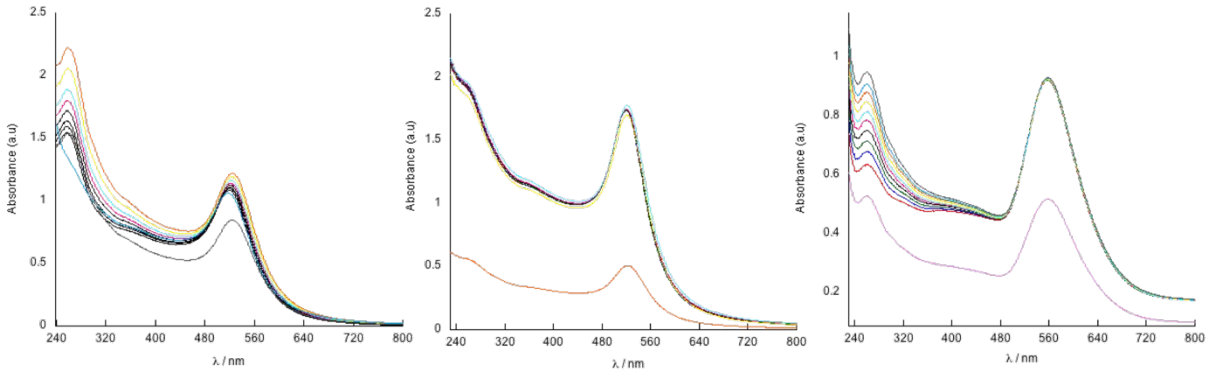

Figure 7.33. UV/Vis showing purified IrC_6 •AbH •AuNPs for (left) 3 nM IrC_6 •AbH •AuNP13, (middle) 2 nM IrC_6 •AbH •AuNP25 and (right) 15 pm IrC_6 •AbH •AuNP100 in water.

Eurogentec
Experience true partnership

DUPLEX OLIGONUCLEOTIDE
Technical Data Sheet (TDS)

For Research Use Only

YOUR ORDER	SON	DATE
805888 - 483.15 GBP	1000836240	29-May-17

CUSTOMER	ADDRESS / INSTITUTION
Bicknell Roy	UNITED KINGDOM Birmingham B15 2TT

OLIGO ① NAME	BATCH	SCALE	CHEMISTRY	BASES
SCLEC14A	6355515	40 nmol	RNA	21

SEQUENCE ① (5' → 3') * Phosphorothioate linkage

1 GAA-CAA-GAC-AAU-UCA-GUA-A55

OLIGO ② NAME	BATCH	SCALE	CHEMISTRY	BASES
ACLEC14A	6355516	40 nmol	RNA	21

SEQUENCE ② (5' → 3') * Phosphorothioate linkage

1 UUA-CUG-AAU-UGU-CUU-GUU-C55

BACKBONE (BASES + LINKAGES)

	①	②		①	②		
A	10	3	MW ($g.mol^{-1}$)[/]	6904.4	6546.9	Quantity	
C	3	3					
G	3	3	Ext. coeff.	226500	204400		
U / T	3 / 0	10 / 0	($l.mol^{-1}.cm^{-1}$)[/]				
Other	2	2				(nmol)	22.0
Wobbles	0	0			[/] Theoretical values	(µg)	295.93

MODIFICATION(S)	OLIGO ①			MODIFICATION(S)	OLIGO ②		
Mod 3'				Mod 3'			
Mod 5'	Thiol Modifier C6	196.20		Mod 5'			
Mod 1			0	Mod 1			0
Mod 2			0	Mod 2			0
Mod 3			0	Mod 3			0
Mod 4			0	Mod 4			0
Mod 5	dT	304.20	2	Mod 5	dT	304.20	2
Mod 6			0	Mod 6			0
Mod 7			0	Mod 7			0
Mod 8			0	Mod 8			0
Mod 9			0	Mod 9			0
Mod 0			0	Mod 0			0

PURIFICATION(S)
SePOP

ADDITIONAL SERVICE(S)

FORMAT	Dried	ALIQUOTING	
		Number of Aliquots	0

QUALITY CONTROL(S)

①	Passed	②	Passed

DELIVERY CONDITION
Room Temperature

RECONSTITUTION
To Make up to 100 µM concentration add 220 µl of recommended buffer.
To Make up to 20 µM concentration add 1.10 ml of recommended buffer.
To Make up to 5 µM concentration add 4.40 ml of recommended buffer.

LONG-TERM STORAGE
DNA -20 °C / RNA -70 °C

COMMENTS
General:
Specific: Annealing buffer used is 50 mM TRIS-HCl, 100 mM NaCl, pH 7.6

HELP

EUROPE
If you have any questions feel free to call our Oligo Centre depending on your location: [Belgium, France, Germany, Luxembourg, The Netherlands, United Kingdom, Switzerland, Austria] 00 800 666 00 123 (European toll free number), or send an email to oligo@eurogentec.com

NORTH AMERICA
If you have questions, please contact our Technical Support Team at +1 858 793 2661 or send an e-mail to ivd.na@egt-biotech.com

Kaneka Eurogentec S.A. Liège Science Park - Rue Bois Saint-Jean 5 - 4102 SERAING BELGIUM
Tel: +32(0)4 372 74 00 - Fax: +32(0)4 264 07 88 E-mail: info@eurogentec.com
RPM Liège T.V.A.-(BE)-0427.348.346 - Web: www.eurogentec.com

EGT North America, Inc.
34801 Campus Drive - Fremont, CA 94555
Tel.: +1 (510) 896 -1350 * Fax: +1 (510) 791-9572
E-mail: ivd.na@egt-biotech.com * Web: www.egt-biotech.com

Figure 7.34. Thiolated SiRNA

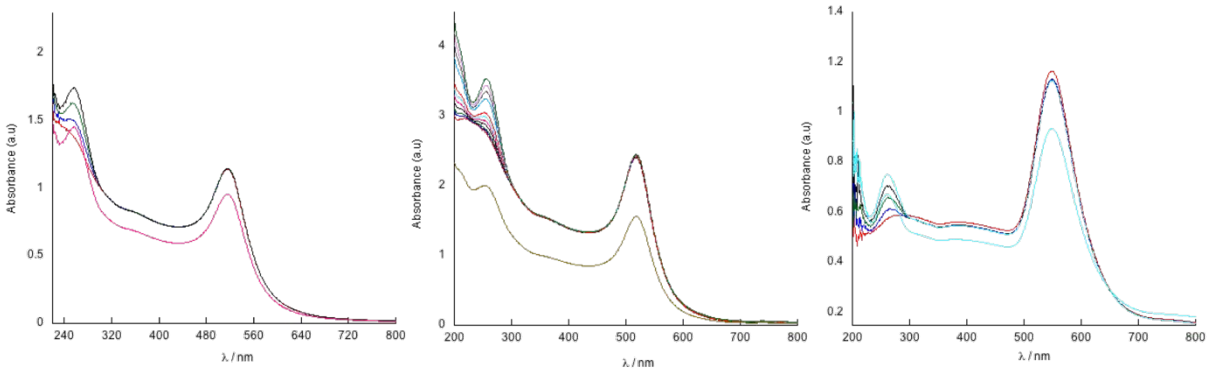

Figure 7.35. UV/Vis showing purified SiRNA •AuNPs for (left) 4 nM SiRNA •AuNP13, (middle) 6 nM SiRNA •AuNP25 and (right) 25 pm SiRNA •AuNP100 in water.

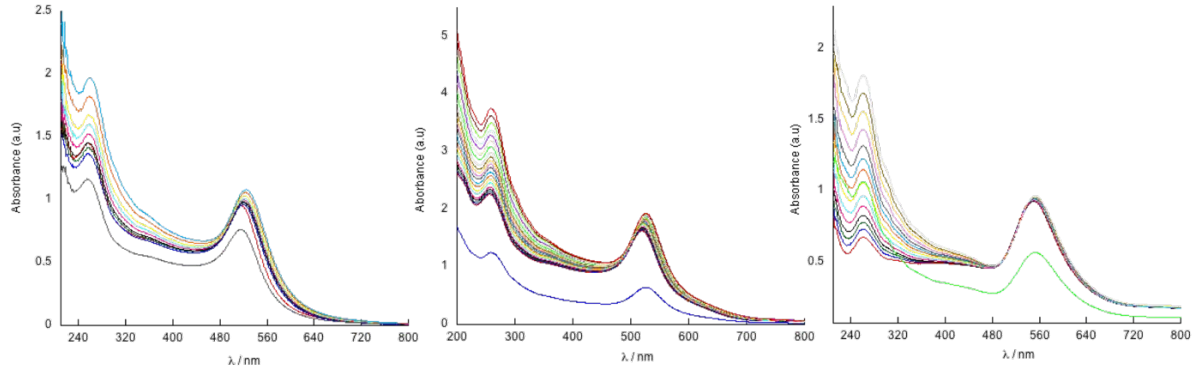

Figure 7.36. UV/Vis showing purified IrC_6 •SiRNA •AuNPs for (left) 3 nM IrC_6 •SiRNA •AuNP13, (middle) 3 nM IrC_6 •SiRNA •AuNP25 and (right) 15 pm IrC_6 •SiRNA •AuNP100 in water.

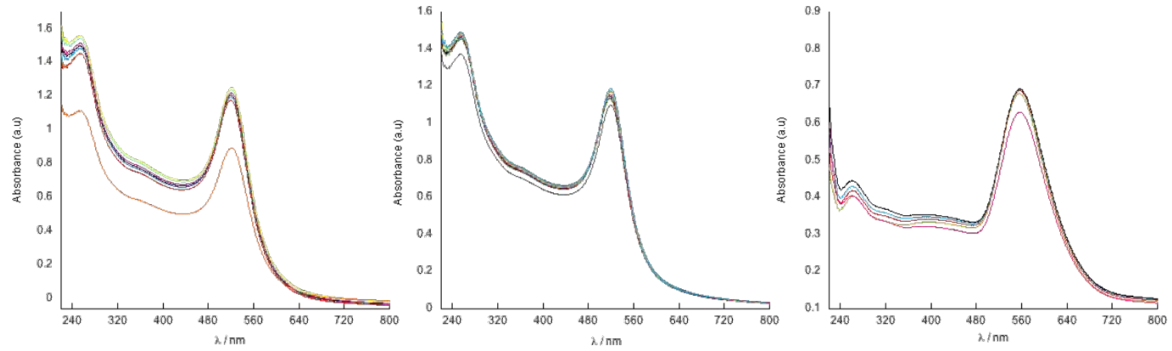

Figure 7.37 UV/Vis showing purified AbH/SiRNA •AuNPs for (left) 3.5 nM AbH/SiRNA •AuNP13, (middle) 3.5 nM AbH/SiRNA •AuNP25 and (right) 17 pm AbH/SiRNA •AuNP100 in water.

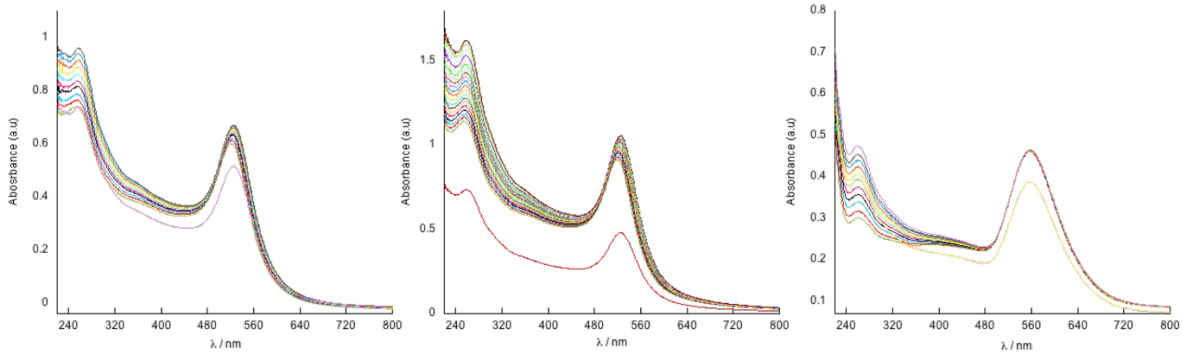

Figure 7.38 UV/Vis showing purified IrC_6 •AbH/SiRNA •AuNPs for (left) 3 nM IrC_6 •AbH/SiRNA •AuNP13, (middle) 2 nM IrC_6 •AbH/SiRNA •AuNP25 and (right) 12 pm IrC_6 •AbH/SiRNA •AuNP100 in water.

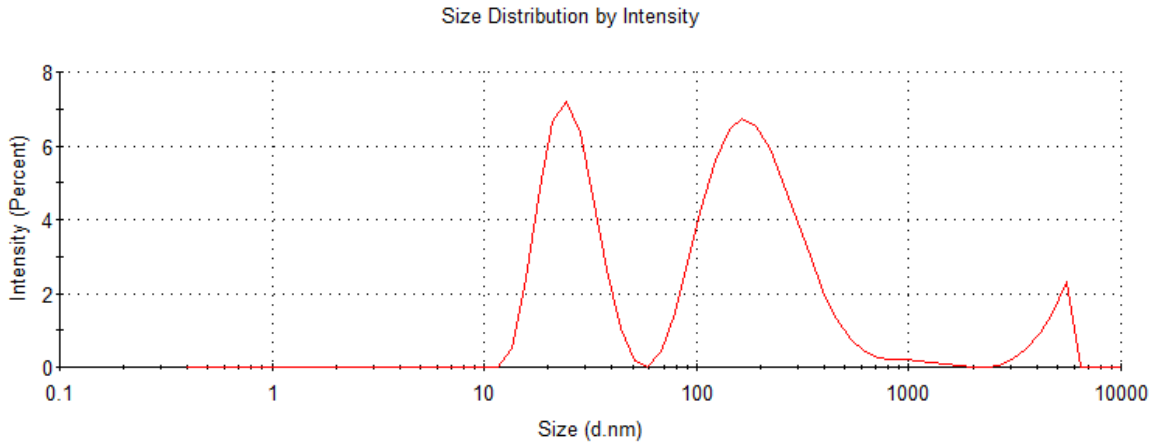

Figure 7.39. Dynamic Light Scattering (DLS) showing size by intensity for IrC_6 •AuNP25. Two peaks have been intentified in the size distribution graph. The presence of this second larger peak is due to excess Zonyl FSA in solution.

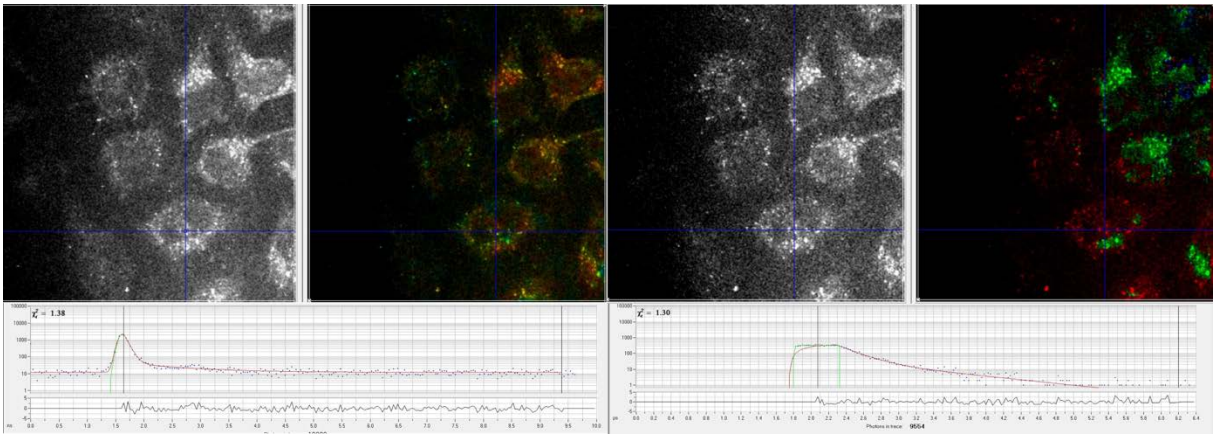

Figure 7.40. Two-photon fluorescence and phosphorescence lifetimes of IrC_6 •AbH •AuNP13 analysed on SPCImage (Becker & Hickl software, version 5.0). Blue cross hairs showing iridium gold nanoparticles. Intensity images can be seen in grey, left of both the FLIM and PLIM images. (Left) FLIM image shows a sharp peak in the lifetime decay plot which is attributed to the short-lived signal from the gold. Lifetime decay is fitted to one component to give a χ^2 of 1.38. (Right) PLIM image shows lifetime decay characteristic of the long-lived signal from the iridium complex. Lifetime decay is fitted to three components to give a χ^2 of 1.30.

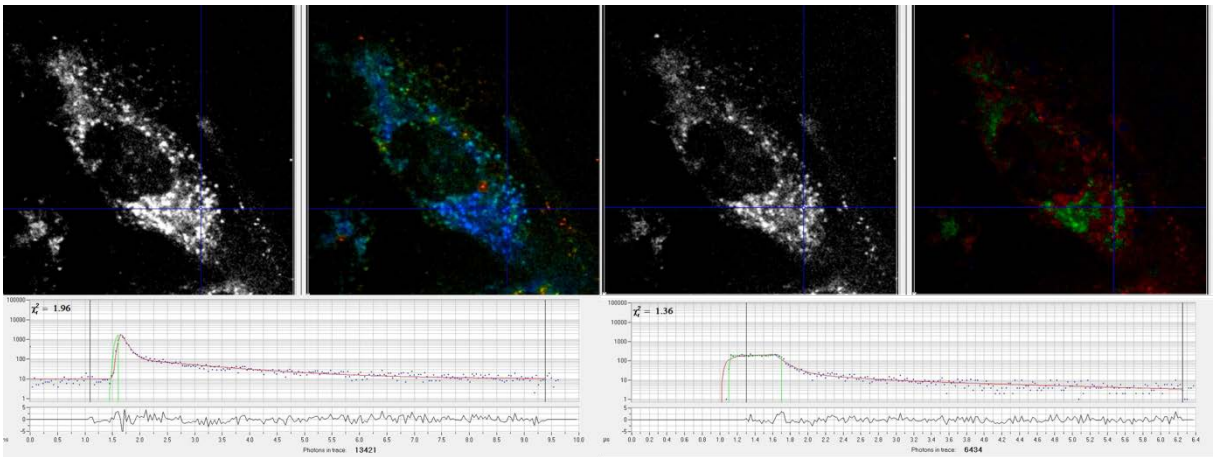

Figure X.17 Two-photon fluorescence and phosphorescence lifetimes of IrC_6 •AbH •AuNP25 analysed on SPCImage (Becker & Hickl software, version 5.0). Blue cross hairs showing iridium gold nanoparticles. Intensity images can be seen in grey, left of both the FLIM and PLIM images. (Left) FLIM image shows a sharp peak in the lifetime decay plot which is attributed to the short-lived signal from the gold. Lifetime decay is fitted to one component to give a χ^2 of 1.96. (Right) PLIM image shows lifetime decay characteristic of the long-lived signal from the iridium complex. Lifetime decay is fitted to three components to give a χ^2 of 1.36.

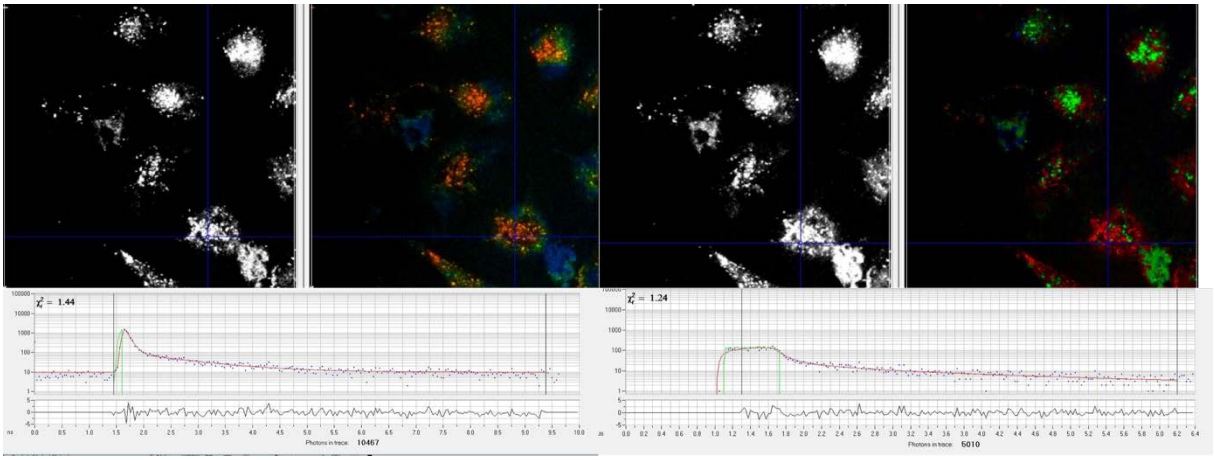

Figure X.18 Two-photon fluorescence and phosphorescence lifetimes of IrC_6 •AbH •AuNP100 analysed on SPCImage (Becker & Hickl software, version 5.0). Blue cross hairs showing iridium gold nanoparticles. Intensity images can be seen in grey, left of both the FLIM and PLIM images. (Left) FLIM image shows a sharp peak in the lifetime decay plot which is attributed to the short-lived signal from the gold. Lifetime decay is fitted to one component to give a χ^2 of 1.44. (Right) PLIM image shows lifetime decay characteristic of the long-lived signal from the iridium complex. Lifetime decay is fitted to three components to give a χ^2 of 1.24.

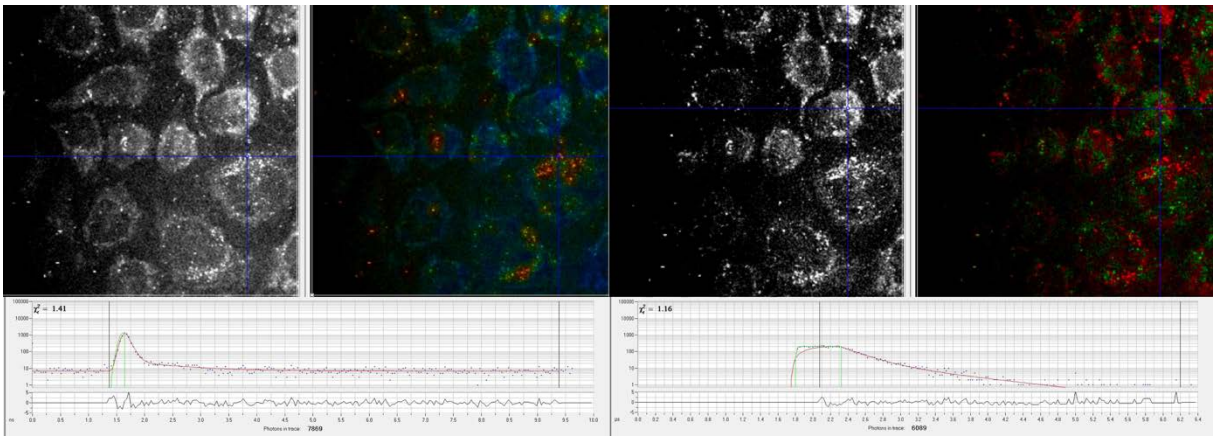

Figure 7.41 Two-photon fluorescence and phosphorescence lifetimes of IrC_6 •SiRNA •AuNP13 analysed on SPCImage (Becker & Hickl software, version 5.0). Blue cross hairs showing iridium gold nanoparticles. Intensity images can be seen in grey, left of both the FLIM and PLIM images. (Left) FLIM image shows a sharp peak in the lifetime decay plot which is attributed to the short-lived signal from the gold. Lifetime decay is fitted to one component to give a χ^2 of 1.41. (Right) PLIM image shows lifetime decay characteristic of the long-lived signal from the iridium complex. Lifetime decay is fitted to three components to give a χ^2 of 1.16.

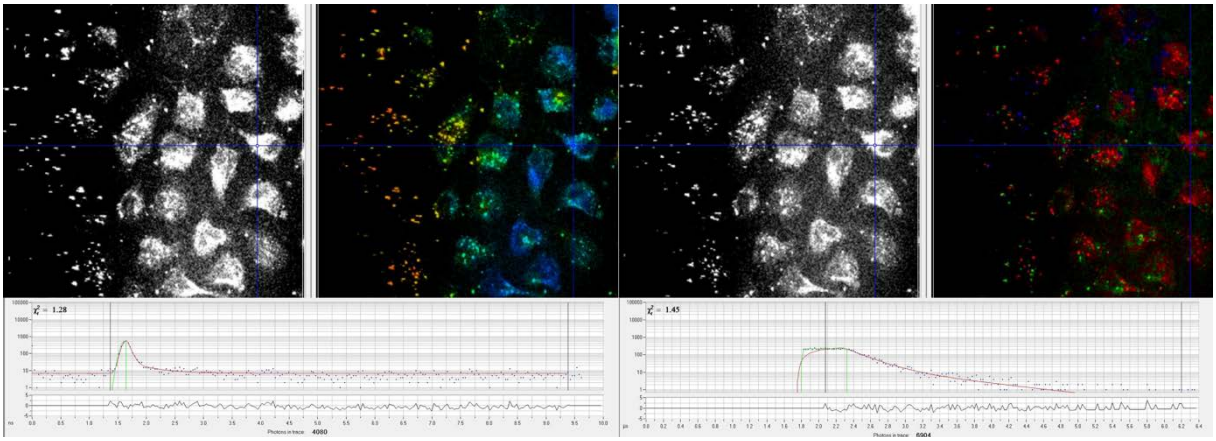

Figure 7.42 Two-photon fluorescence and phosphorescence lifetimes of IrC_6 •SiRNA •AuNP25 analysed on SPCImage (Becker & Hickl software, version 5.0). Blue cross hairs showing iridium gold nanoparticles. Intensity images can be seen in grey, left of both the FLIM and PLIM images. (Left) FLIM image shows a sharp peak in the lifetime decay plot which is attributed to the short-lived signal from the gold. Lifetime decay is fitted to one component to give a χ^2 of 1.28. (Right) PLIM image shows lifetime decay characteristic of the long-lived signal from the iridium complex. Lifetime decay is fitted to three components to give a χ^2 of 1.45.

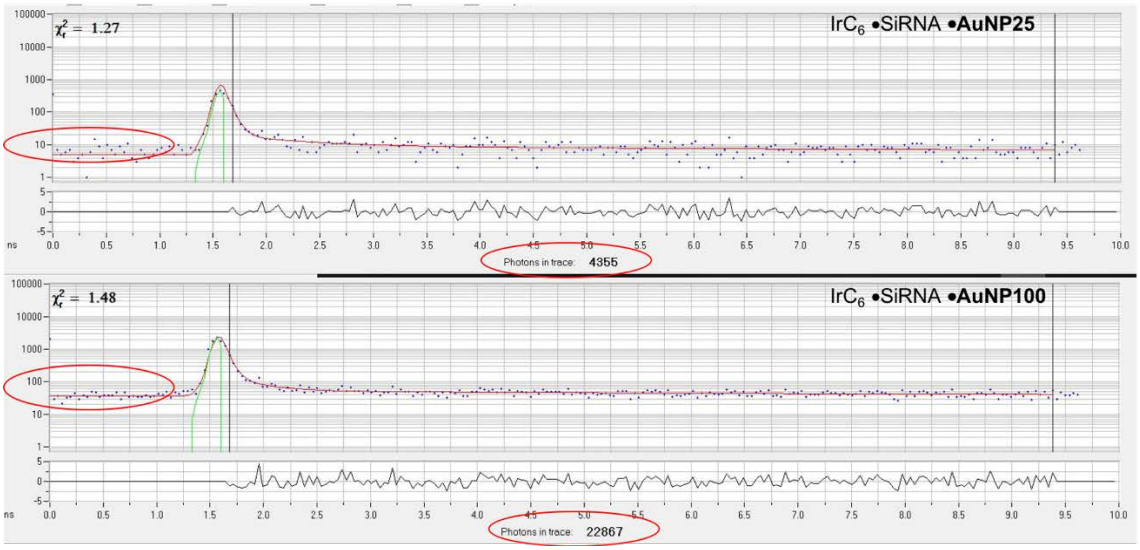

Figure 7.43 Two-photon fluorescence lifetimes of IrC_6 •SiRNA •AuNP25 and IrC_6 •SiRNA •AuNP100 analysed on SPCImage (Becker & Hickl software, version 5.0). Binning had to be increased to 10 to fit lifetimes detected for IrC_6 •SiRNA •AuNP25, in comparison to IrC_6 •SiRNA •AuNP100. Red boxes are drawn over areas showing weak vs strong signal from the gold. Both the lifetime decays show a sharp peak in the lifetime decay plot which is attributed to the short-lived signal from the gold. (Top) Lifetime decay for IrC_6 •SiRNA •AuNP25 is fitted to one component to give a χ^2 of 1.27. (Bottom) Lifetime decay for IrC_6 •SiRNA •AuNP100 is fitted to one component to give a χ^2 of 1.48.

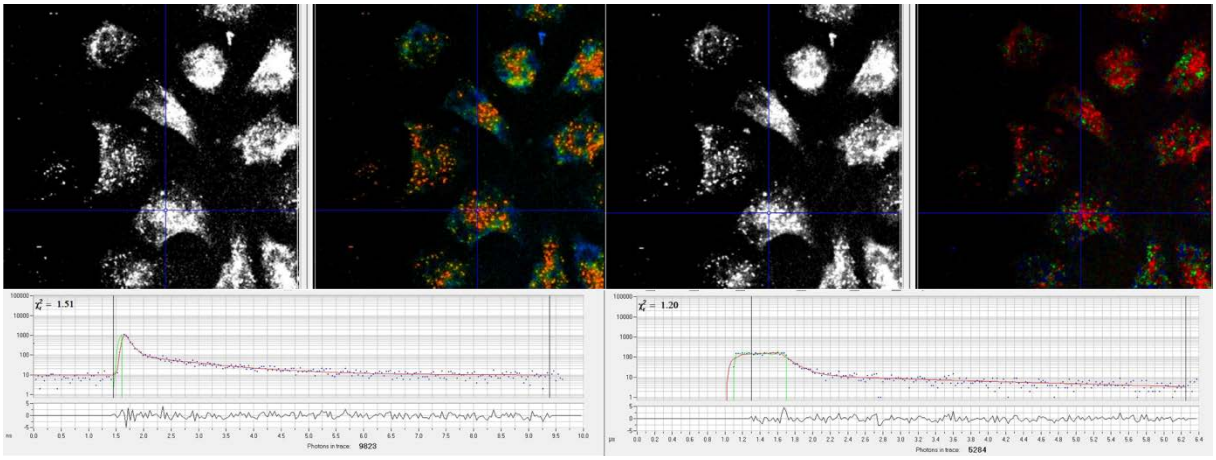

Figure 7.44 Two-photon fluorescence and phosphorescence lifetimes of IrC_6 •SiRNA •AuNP100 analysed on SPCImage (Becker & Hickl software, version 5.0). Blue cross hairs showing iridium gold nanoparticles. Intensity images can be seen in grey, left of both the FLIM and PLIM images. (Left) FLIM image shows a sharp peak in the lifetime decay plot which is attributed to the short-lived signal from the gold. Lifetime decay is fitted to one component to give a χ^2 of 1.51. (Right) PLIM image shows lifetime decay characteristic of the long-lived signal from the iridium complex. Lifetime decay is fitted to three components to give a χ^2 of 1.20.

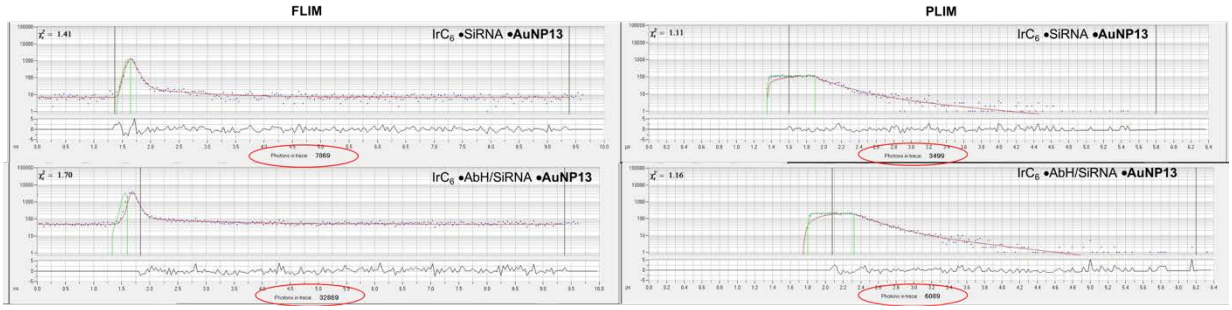

Figure 7.45 Two-photon fluorescence and phosphorescence lifetimes of IrC_6 •SiRNA •AuNP13 and IrC_6 •AbH/SiRNA •AuNP13 analysed on SPCImage (Becker & Hickl software, version 5.0). Red boxes are drawn over areas showing weak vs strong signal from the gold and iridium. (Left) Fluorescence lifetime decays for (Top) IrC_6 •SiRNA •AuNP13 and (Bottom) IrC_6 •AbH/SiRNA •AuNP13.Both the lifetime decays show a sharp peak in the lifetime decay plot which is attributed to the short-lived signal from the gold. (Left) Phosphorescence Lifetime decay for (Top) IrC_6 •SiRNA •AuNP13 and (Bottom) IrC_6 •AbH/SiRNA •AuNP13.

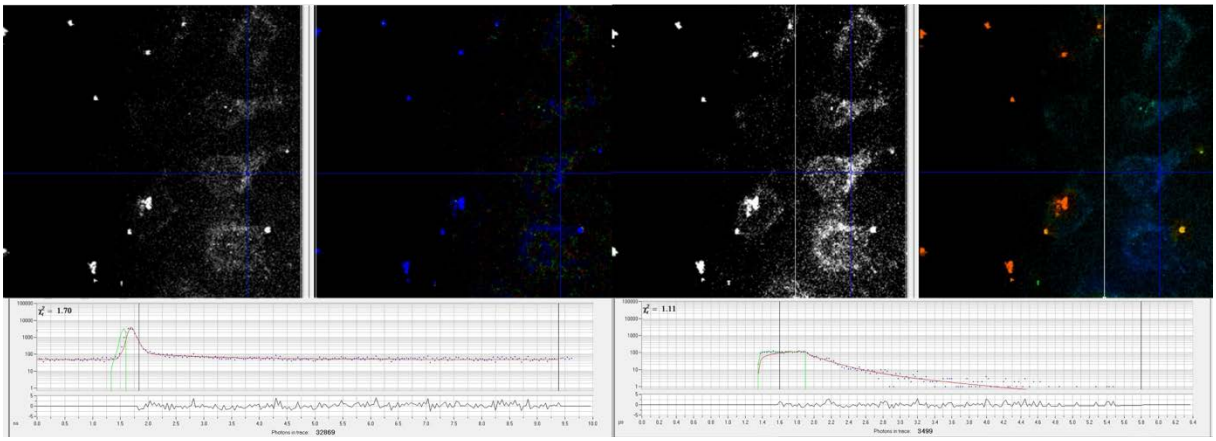

Figure 7.46 Two-photon fluorescence and phosphorescence lifetimes of IrC_6 •AbH/SiRNA •AuNP13 analysed on SPCImage (Becker & Hickl software, version 5.0). Blue cross hairs showing iridium gold nanoparticles. Intensity images can be seen in grey, left of both the FLIM and PLIM images. (Left) FLIM image shows a sharp peak in the lifetime decay plot which is attributed to the short-lived signal from the gold. Lifetime decay is fitted to one component to give a χ^2 of 1.70. (Right) PLIM image shows lifetime decay characteristic of the long-lived signal from the iridium complex. Lifetime decay is fitted to three components to give a χ^2 of 1.11.

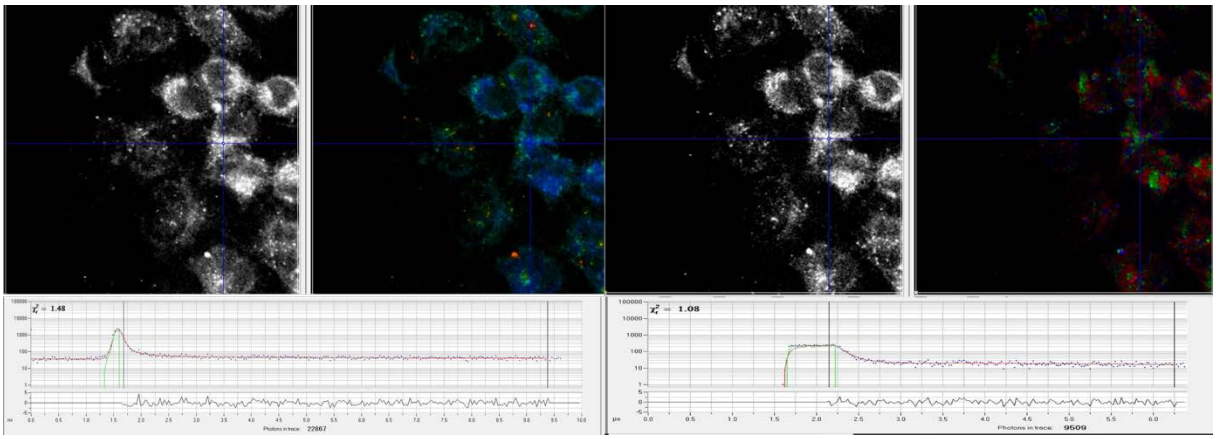

Figure 7.47 Two-photon fluorescence and phosphorescence lifetimes of IrC_6 •AbH/SiRNA •AuNP25 analysed on SPCImage (Becker & Hickl software, version 5.0). Blue cross hairs showing iridium gold nanoparticles. Intensity images can be seen in grey, left of both the FLIM and PLIM images. (Left) FLIM image shows a sharp peak in the lifetime decay plot which is attributed to the short-lived signal from the gold. Lifetime decay is fitted to one component to give a χ^2 of 1.48. (Right) PLIM image shows lifetime decay characteristic of the long-lived signal from the iridium complex. Lifetime decay is fitted to three components to give a χ^2 of 1.08.

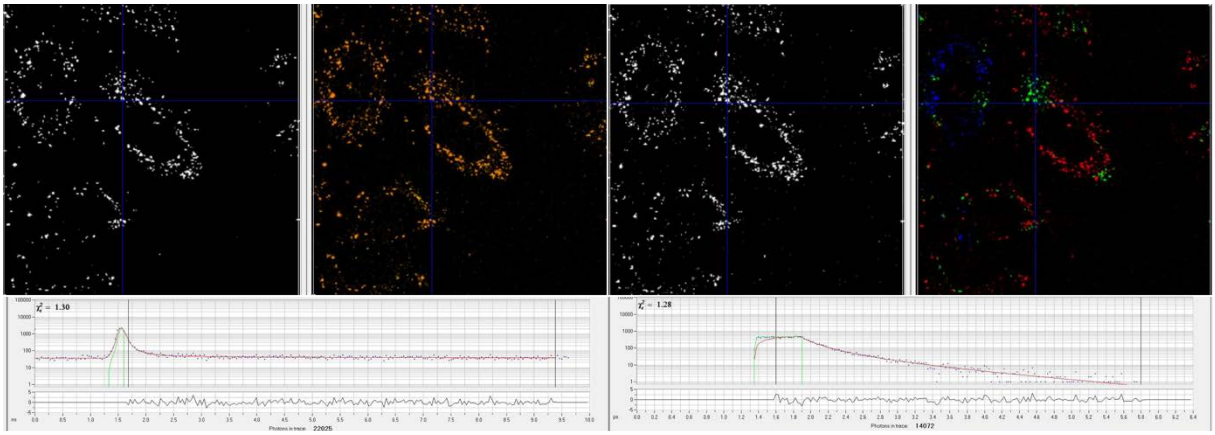

Figure 7.48 Two-photon fluorescence and phosphorescence lifetimes of IrC_6 •AbH/SiRNA •AuNP100 analysed on SPCImage (Becker & Hickl software, version 5.0). Blue cross hairs showing iridium gold nanoparticles. Intensity images can be seen in grey, left of both the FLIM and PLIM images. (Left) FLIM image shows a sharp peak in the lifetime decay plot which is attributed to the short-lived signal from the gold. Lifetime decay is fitted to one component to give a χ^2 of 1.30. (Right) PLIM image shows lifetime decay characteristic of the long-lived signal from the iridium complex. Lifetime decay is fitted to three components to give a χ^2 of 1.28.